Substitution and Analysis of Additional Heteroatoms in 1,2λ^5-Azaphosphinines

by

J. Nolan McNeill

A dissertation accepted and approved in partial fulfillment of the

requirements for the degree of

Doctor of Philosophy

in Chemistry

Dissertation Committee:

Ramesh Jasti, Chair

Michael Haley, Advisor

Darren Johnson, Co-Advisor

Michael Pluth, Core Member

Marian Hettiaratchi, Institutional Representative

University of Oregon

Summer 2024

DISSERTATION ABSTRACT

J. Nolan McNeill

Doctor of Philosophy in Chemistry

Title: Substitution and Analysis of Additional Heteroatoms in 1,2λ^5-Azaphosphinines

Azaphosphinines are, simply put, six-membered heterocycles containing one nitrogen and one phosphorus atom. While garnering more attention in the last couple decades, they are still decidedly understudied. This lack of research is primarily due to the difficult and often intense reaction conditions required to synthesize them. This is especially true for the azaphosphinine moiety's early iterations. In the Haley and Johnson groups we have found a facile synthetic pathway that allows us to circumvent these issues. In this dissertation I will discuss not only a history of the azaphosphinine functional group but also the results of my independent research. The main body of my Ph.D. work is concerned with the substitution of additional heteroatoms into our thoroughly studied azaphosphinines. These substitutions result in dramatic changes to both the supramolecular and photophysical properties of the heterocycles. While most of the work I will discuss is related to different orientations of pyrido-fused azaphosphinines, I also include a study on the thionation of the ubiquitous phosphoryl group.

Chapter I is a holistic review of azaphosphinines. I begin by discussing the nomenclature and unusual electronic properties of these heterocycles before detailing a chronological progression of the literature concerning the three isomers and both valencies of the azaphosphinine functional group. In Chapter II I describe the synthesis and unexpected tautomerization effects observed in pyrido[2,3-*e*]-1,2λ^5-azaphosphinines. Chapter III continues to explore the electronic effects of a pyrido-fusion, but in this case, we are now considering the internal charge transfer present in

pyrido[3,4-*e*]-1,2λ^5-azaphosphinines. And lastly Chapter IV examines the thionating effect of Lawesson's Reagent on our heterocycles and the dramatic impacts this transformation has on their photophysical properties.

This dissertation includes previously published co-authored material.

CURRICULUM VITAE

NAME OF AUTHOR: J. Nolan McNeill

GRADUATE AND UNDERGRADUATE SCHOOLS ATTENDED:

University of Oregon, Eugene
University of Maryland, College Park

DEGREES AWARDED:

Doctor of Philosophy, Chemistry, 2024, University of Oregon
Master of Science, Chemistry, 2021, University of Oregon
Bachelor of Science, Chemistry, 2019, University of Maryland

AREAS OF SPECIAL INTEREST:

Organic Chemistry
Heterocyclic Small Molecules
Physical Organic Chemistry
Mesodimerization and Supramolecular Assembly

PROFESSIONAL EXPERIENCE:

Graduate Employee, University of Oregon, 2019–2024

GRANTS, AWARDS, AND HONORS:

Best Lecture, Exploration of Tautomerization in Pyridine-Bearing PN-Heterocycles, Organic pi-Electron Molecules and Materials Meetings, 2023

Semester Academic Honors, University of Maryland, 2018

Semester Academic Honors, University of Maryland, 2017

PUBLICATIONS:

Rizzi, A.; Murkli, S.; McNeill, J. N.; Yao, W.; Sullivan, M.; Gilson, M. K.; Chiu, M. W.; Isaacs, L.; Gibb, B. C.; Mobley, D. L.; Chodera, J. D. Overview of the SAMPL6 host-guest binding affinity prediction challenge. *J. Comput. Aided. Mol. Des*. **2018**, *32*, 937–963.

Murkli, S.; McNeill, J. N.; Isaacs, L. Cucurbit[8]uril•guest complexes: blinded dataset for the SAMPL6 challenge. *Supramol. Chem.* **2018**, *31*, 150–158.

Bard, J. P.; McNeill, J. N.; Zakharov, L. N.; Johnson, D. W.; Haley, M. M. Thionation of the 2-λ^5-Phosphaquinolin-2-one Scaffold with Lawesson's Reagent. *Isr. J. Chem.* **2021**, *61*, 217–221.

McNeill, J. N.; Karas, L. J.; Bard, J. P.; Fabrizio, K.; Zakharov, L. N.; MacMillan, S. N.; Brozek, C. K.; Wu, J. I.; Johnson, D. W.; Haley, M. M. Controlling Tautomerization in Pyridine-Fused Phosphorus-Nitrogen Heterocycles. *Chem. Eur. J.* **2022**, *28*, e202200472.

McNeill, J. N.; Melanie, A. K.; Karas, L. J.; Zakharov, L. N.; Wu, J. I.; Johnson, D. W.; Haley, M. M. Impact of Internal Charge Transfer on the Photophysical Properties of Pyridine-Fused Phosphorus-Nitrogen Heterocycles. *Chem. Eur. J.* **2023**, *29*, e202203918.

Bard, J. P.; Bolton, S. G.; Howard, H. J.; McNeill, J. N.; de Faria, T. P.; Zakharov, L. N.; Johnson, D. W.; Pluth, M. D.; Haley, M. M. 2-λ^5-Phosphaquinolin-2-ones as Non-cytotoxic, Targetable, and pH-Stable Fluorophores. *J. Org. Chem.* **2023**, *21*, 15516–15522.

McNeill, J. N.; Bard, J. P.; Johnson, D. W.; Haley, M. M. Azaphosphinines and their derivatives. *Chem. Soc. Rev.*, **2023**, *52*, 8599–8634.

ACKNOWLEDGMENTS

First and foremost, I need to acknowledge my partner, Rachel. We have been together since before this whole crazy experience. When it was decided that I was going to move from Maryland to Oregon for a 5-year degree, she packed up and came with me without hesitation. We drove across the country together with our two cats (Boots and Smallcat) and lived in a lofted shoebox. We weathered the challenges of living together for the first time while 3000 miles away from any family, a global pandemic, and countless other obstacles. But through all that she supported this dream of mine and I could not have done this without her.

I would like to express my gratitude to Profs. Michael Haley and Darren Johnson. They have helped to stoke my scientific curiosity and blossom as a chemist while being infinitely patient with me. A Ph.D. program is a daunting task and cannot be finished without advisors supporting you every step of the way. Organized and regular group meetings, opportunities to give lectures, and networking with colleagues are just some of the ways that Mike and Darren have facilitated my growth as a scientist. For this I will always be grateful. My research on the azaphosphinine project was funded by the National Science Foundation (CHE-1607214 & 2107425).

When I was an undergraduate, I was told that you could have two of three things in graduate school: engaging research, a good lab, or a good boss. I am happy to say that this is not the case. While I did enjoy my research and both of my advisors, the best part of this experience was certainly the people I was here with. During the first year of the program things could get chaotic with deadlines, cumulative exams, and teaching all swirling about. But finding a group of friends among my classmates grounded and made it all bearable.

In the later years of the program, the Haley Lab became my greatest asset. Countless hours of engaging and friendly discussion about chemistry, life, and foie gras helped to enrich my time here. The mentors I had in the lab (Dr. Josh Barker, Dr. Gabrielle Warren, and especially Prof. Jeremy Bard) kept me on track with constructive criticism and reminders about deadlines. Meanwhile, my colleagues in the lab (Prof. Joe Workman, Efrain Vidal, Bella Demachkie, Michael Miller, Nathan Boone, and Megan Rammer) provided an environment I was excited to work in every day. Of course, there are countless other chemists who have conspired to make this dissertation possible. From my high school chemistry teacher Mrs. Balimtas who first encouraged my interests, to my undergraduate mentor Dr. Steven Murkli and advisor Prof. Lyle Isaacs.

And finally, I need to thank my family. My parents Chris and Patti my brother Henry, my grandparents Mimi and Pop, and everyone else too. They supported and encouraged me every step of the way from high school to here. I really cannot express how grateful I am to them, so hopefully this dissertation will stand in place of even sappier language.

Dedicated to my family, without whom none of this would have been possible.

TABLE OF CONTENTS

Chapter Page

I. AZAPHOSPHININES AND THEIR DERIVATIVES 21

1.1 Introduction 21

1.2 Azaphosphinine origins 28

1.3 1,2-Azaphosphinines 31

1.3.1 Reactivity with Alkynes 31

1.3.1.1 Pericyclic / Cycloadditions 31

1.3.1.2 Transition Metal-Catalyzed C–H Activation 36

1.3.2 Intramolecular Cyclization Reactions 51

1.4 1,3-Azaphosphinines 88

1.4.1 Heteroatom Exchange 88

1.4.2 Pericyclic / Cycloadditions 89

1.4.3 Intramolecular Cyclization Reactions 96

1.5 1,4-Azaphosphinines 98

1.6 Comparing Electronic Properties of the Azaphosphinine Isomers 103

1.7 Conclusions 110

II. CONTROLLING TAUTOMERIZATION IN PYRIDINE-FUSED PHOSPHORUS-NITROGEN HETEROCYCLES 115

2.1 Introduction 115

2.2 Results and Discussion 118

2.2.1 Synthesis of PN-pyridines 118

2.2.2 X-ray Crystallography 120

2.2.3 Heterocycle Alkylation 121

2.2.4 NMR Shift Comparison 123

2.2.5 UV-Vis Spectroscopy Comparison 125

2.2.6 Solid-state UV-Vis Comparison 126

2.2.7 Calculations 127

2.3 Conclusion 128

III. IMPACT OF INTERNAL CHARGE TRANSFER ON THE PHOTOPHYSICAL PROPERTIES OF PYRIDINE-FUSED PHOSPHORUS-NITROGEN HETEROCYCLES 130

3.1 Introduction 130

3.2 Results and Discussion 133

3.2.1 Synthesis of 3-pyridine PNs 135

3.2.2 Absorption and Emission Data 142

3.2.3 X-ray Crystallography 146

3.3 Conclusions 146

IV. THIONATION OF THE 2-λ^5-PHOSPHAQUINOLIN-2-ONE SCAFFOLD WITH LAWESSON'S REAGENT 148

4.1 Introduction 148

4.2 Results and Discussion 150

4.3 Conclusions 156

APPENDICES 157

A. SUPPLEMENTARY INFORMATION FOR CHAPTER II 157

B. SUPPLEMENTARY INFORMATION FOR CHAPTER III 216

C. SUPPLEMENTARY INFORMATION FOR CHAPTER IV 271

REFERENCES CITED 303

LIST OF FIGURES

Figure Page

1. **Figure 1.1.** Phosphorus nomenclature commonly referred to in Chapter I. 22

2. **Figure 1.2** Examples of (top) ionic nature in hexachlorophosphazene and (bottom) ylidic nature in P^V phosphinine 24

3. **Figure 1.3** Examples of (top) 1,2- (**1a**), 1,3- (**1b**) and 1,4-azaphosphinines (**1c**) and (bottom) benzo[*c*]- (**2a**) and benzo[*b*]azaphosphinine (**2b**) isomers. 27

4. **Figure 1.4** Examples of nomenclature rules applied to more complex azaphosphinine derivatives such as **3** and **4**. 27

5. **Figure 1.5** Representative *meso*-dimer of **98g**. Blue dashed lines represent hydrogen bonds between phosphonamidate moieties. Nonparticipating hydrogen atoms omitted for clarity. 76

6. **Figure 1.6** Benzo[*e*]-1,2-dihydro-1,2λ^5-azaphosphinine 2-oxide cellular imaging dyes. 84

7. **Figure 2.1** Phosphaquinolinone and analogous heterocycles (top), as well as previously derivatized PN-motif **1** and new pyridine-PN scaffold **2** (bottom). 116

8. **Figure 2.2** (a) The two tautomeric forms of heterocycle **2a**; colors represent aromatic (blue) core vs nonaromatic (pink) core. (b) Hydrogen-bonding nature of the aromatic (left) and quinoidal (right) tautomers. 117

9. **Figure 2.3** X-ray crystal structures (173 K; ellipsoids at 30% probability) and corresponding ChemDraw representations of the pyridine-fused PN-heterocycles. Heterocycles **2a'** and **2c'** display quinoidal tautomerization in the solid state whereas **2e** remains as the aromatic form. N1-C4 and N2-C4 bond lengths (Å) are shown inside the rings 119

10. **Figure 2.4** X-ray crystal structure (100 K; ellipsoids at 30% probability) of **6a**, displaying the pyridyl-nitrogen N-alkylation. N1-C4 and N2-C4 bond lengths (Å) are shown inside the rings and are the average of the values from two independent molecules 122

11. **Figure 2.5** Comparison of heterocycle absorbance (solid line) and emission (dashed line) data of pre- (**2**) and post-alkylation (**6**) of PN-heterocycles. 125

12. **Figure 2.6** Computed relative free energies (ΔG, kcal mol^{-1}) and NICS(0) (ppm) values for **2a** vs. **2a'** (top) and their protonated analogues (bottom) 127

13. **Figure 3.1** Coumarin, carbostyril, and phosphaquinolinone scaffolds 131

14. **Figure 3.2**. a) 2-Pyridine PN (**1**) and its key tautomeric form **1'**.[12] b)

3-Pyridine PN (**2**) and the highly-polarized quinoidal resonance form **2'**. c) Comparison between imidate (**I**) and amidate (**A**) forms of the PN-heterocycle scaffold..... 133

15. **Figure 3.3** Electronic absorption spectra of imidates **6** (top) and amidates **2** (bottom) in $CHCl_3$ (~10^{-5} M) at room temperature..... 136

16. **Figure 3.4** Absorption (solid) and emission (dashed) spectra of a solvatochromic study on **6d** (top) and **2d** (bottom) taken at room temperature .. 138

17. **Figure 3.5** Emission spectra of **6** (top) and **2** (bottom) in $CHCl_3$ at room temperature. 140

18. **Figure 3.6** Example of *para*-substituted stilbazole (left) and the motif superimposed on imidate PN **6** and amidate PN **2**..... 140

19. **Figure 3.7** Crystal structures of imidate **6d** (top) and amidate **2d** (bottom) with labeled atoms; ellipsoids drawn at the 30% probability level 144

20. **Figure 3.8** Computed molecular electrostatic potential maps for **2a-2d** at B3LYP-D3/6-311+G(d,p); the pyridine N atom is on the left..... 145

21. **Figure 4.1** Lawesson's Reagent and a sampling of commonly prepared thiocarbonyl compounds. 149

22. **Figure 4.2** ORTEP drawing of the thioheterocycle **2e** mesodimer; thermal ellipsoids drawn at 30% probability level..... 152

23. **Figure 4.3** Stacked absorption and emission spectra of heterocycles **2** 154

LIST OF TABLES

Table Page

1. **Table 1.1** Experimental details for reactions of *rac*-**36** with various internal alkynes. Ar = 3,5-$(CF_3)_2C_6H_3$ 41

2. **Table 1.2** Emission data for measured heterocycles **49**. 50

3. **Table 1.3** Substrate scope of cyclization of **74** to afford **75**..... 57

4. **Table 1.4** Cyclization and subsequent allylation of give azaphosphinines **77** 58

5. **Table 1.5** Phosphite cyclization of *ortho*-ethynylanilines..... 68

6. **Table 1.6** Fluorescence properties of selected **97**, **98**, and deprotonated **98** in $CHCl_3$. 69

7. **Table 1.7** Photophysical properties of selected **100**. 71

8. **Table 1.8** Photophysical properties of selected heterocycles **101**–**106**..... 74

9. **Table 1.9** VC ^1H and ^{31}P NMR–measured dimerization constant for select azaphosphinines. 76

10. **Table 1.10** Photophysical properties of selected **109**. 78

11. **Table 1.11** Photophysical properties of selected **114** and **115**. 80

12. **Table 1.12** Association constants[a] (K_a, M^{-1}) of receptors **117** with various anions in 10 vol% DMSO-d_6/$CDCl_3$ at room temperature 82

13. **Table 1.13** Computed NICS values of relevant heterocycles computed by Le Floch (left) and Elguero (right)..... 111

14. **Table 1.14** Comparison of selected ^1H and ^{31}P NMR chemical shifts across selected azaphosphinine systems 113

15. **Table 2.1** Changes in the ^1H NMR chemical shifts (ppm) before and after the alkylation reaction to give **6a**-**d** 123

16. **Table 2.2** Photophysical properties of heterocycles **2a**, **2e**, **6a**, and **6d** 126

17. **Table 3.1** Experimental and computational photophysical properties of amidates **2** and imidates **6**. 137

18. **Table 3.2** Solvatochromic photophysical measurements of **6d** and **2d**..... 139

19. **Table 3.3** Selected bond lengths (Å) and dihedral angle (°) of **2a-d**, **2d'**, and **6d** 141

20. **Table 4.1** Photophysical properties of heterocycles **2**. 153

LIST OF SCHEMES

Scheme Page

1. **Scheme 1.1** Schenk and Michaelis' first reported synthesis of a PN-heterocycle scaffold, dibenzo[*b,e*]1,4-dihydro-1,4λ^5-azaphosphinine 4-oxide 28

2. **Scheme 1.2** Synthesis of Dewar and Kubba's early dibenzo[*c,e*]-1,2-dihydro-1,2λ^3-azaphosphinine **9** and comparison to the previously prepared boron-containing species **7** 29

3. **Scheme 1.3** Oxidation products of Dewar and Kubba's azaphosphinine **9** with aromatic resonance structures 30

4. **Scheme 1.4** Campbell and Way's synthesis of early azaphosphinines **9** and oxidation to **11** 31

5. **Scheme 1.5** Synthesis of 1,2-azaphosphinine **14** using the Staudinger reaction and subsequent Diels-Alder cycloaddition 32

6. **Scheme 1.6** Preparation of heterocycles **16** using phosphazene **17** and formation of azaphosphininium salts **18** 33

7. **Scheme 1.7** Synthesis of 2,2-diphenyl-1,2λ^5-azaphosphinin-6-ones **20** through cycloaddition with DMAD 33

8. **Scheme 1.8** (top) Synthesis of 1,2-azaphosphinines **24** through the formation and cycloaddition of a 1,3,2-diazaphosphinine. (bottom) Substrate scope of the heterocycles prepared in this way 34

9. **Scheme 1.9** Preparation of tripodal 1,2λ^3-azaphosphinine heterocycles (top) **27** and (bottom) **28** 36

10. **Scheme 1.10** Aryl phosphonamide directed C–H activation to furnish **30** 37

11. **Scheme 1.11** Formation of [*c*]-fused 1,2-dihydro-1,2λ^5-azaphosphinine-2-oxide **32** 38

12. **Scheme 1.12** Proposed mechanism for chiral C–H activation heteroannulation of achiral phosphinamide 39

13. **Scheme 1.13** Chiral C–H activation heteroannulation to afford **36**. For every entry, Ar = 3,5-$(CF_3)_2C_6H_3$ 40

14. **Scheme 1.14** Enantiospecific reduction to chiral azaphosphinine **36p'** 41

15. **Scheme 1.15** Reactivity of bis-aryl functionalized chiral phosphinamide. Ar = 3,5-$(CF_3)_2C_6H_3$ 43

16. **Scheme 1.16** Asymmetric reductive aldol condensation of enone **40** and benzaldehyde using chiral benzo[*c*]-1,2-dihydro-1,2λ^3-azaphosphinine additives as Lewis base (LB). Ar = 3,5-$(CF_3)_2C_6H_3$ 44

17. **Scheme 1.17** Enantioselective reduction of **37a** and its use as a chiral ligand in an asymmetric hydrogenation reaction. Ar = 3,5-$(CF_3)_2C_6H_3$ 44

18. **Scheme 1.18** Chiral C–H activation and heteroannulation using Co^{III} to afford **43** 46

19. **Scheme 1.19** Chiral resolution of phosphinamide **44** under standard reaction conditions. Ar = 8-quinolinyl 46

20. **Scheme 1.20** Heteroannulation with allene coupling partners. Ar = 8-quinolinyl 47

21. **Scheme 1.21** Ni^0-mediated heteroannulation to afford azaphosphinines **49** and **51** 49

22. **Scheme 1.22** Asymmetric [4 + 2] heteroannulation starting from chiral phosphanamines. Standard conditions of phosphanamine (1 equiv.), alkyne (2 equiv.), $Ni(COD)_2$ (10 mol%), LiCl (1 equiv.), Cs_2CO_3 (3 equiv.), DMF, 130 °C 50

23. **Scheme 1.23** Synthesis of indole-fused azaphosphinine 2-oxide **56** 51

24. **Scheme 1.24** Proposed pathway to 1,2-dihydro-1,2λ^3-azaphosphinines **57**. No yield reported (*n.y.r.*) 52

25. **Scheme 1.25** Oxidation and hydrolysis of heterocycles **57m** and **57n** 53

26. **Scheme 1.26** H_2O_2 and S_8 oxidations of azaphosphinines **57** 53

27. **Scheme 1.27** Thermolytic synthesis of 1,2λ^3-azaphosphinine **61** and its dihydro products **62**-**64** from attack of various nucleophiles 54

28. **Scheme 1.28** Synthesis of benzo[*e*]-1,4-dihydro-1,2λ^5-azaphosphinines **66** 55

29. **Scheme 1.29** Synthesis of 1,2λ^3-azaphosphinine **69** and subsequent hydrolysis/oxidation 55

30. **Scheme 1.30** Phosphete and isothiocyanate cyclization into azaphosphinine **73** 56

31. **Scheme 1.31** Palladium catalyzed C–H activated heteroannulation to furnish chiral azaphosphinines **79**. Conditions A: $Pd(OAc)_2$ (5 mol%), **L2** (10 mol%), K_3PO_4 (1.5 equiv.), PivOH (30 mol%), toluene, 80 °C. Conditions B: $Pd(dba)_2$. (8 mol%), **L3** (10 mol%), Cs_2CO_3 (1.5 equiv.), PivOH, (40 mol%), hexanes, 60 °C. [a]Reaction performed at room temperature 60

32. **Scheme 1.32** P–N bond cleavage to furnish chiral phosphane oxides **80** 62
33. **Scheme 1.33** Transition-metal free heteroannulation reaction to give azaphosphinines **81** 63

34. **Scheme 1.34** Proposed mechanism for radical C–H activation heteroannulation and subsequent iodination 64

35. **Scheme 1.35** Cleavage of P–N bond and racemization at different temperatures 65

36. **Scheme 1.36** CAN-mediated heteroannulation to afford **88**. [a]10 equiv. of water added. [b]5 equiv. of CAN added and conducted at 60 °C. [c]Run for 2 h 66

37. **Scheme 1.37** Post-synthetic modification of **88a** to furnish chiral acyclic species **90** and **91**, and P^{III} species **93** 67

38. **Scheme 1.38** Asymmetric catalyst **88a** used in condensation reaction 68

39. **Scheme 1.39** Difunctionalized azaphosphinines **100** 70

40. **Scheme 1.40** Scope of arene-core extended azaphosphinines.....72

41. **Scheme 1.41** *P*-phenyl substitution to afford azaphosphinines **105**.....72

42. **Scheme 1.42** *P*-phenyl substituted PN-fused pyrenes **106**.....73

43. **Scheme 1.43** Lawesson's reagent-mediated thionation.....77

44. **Scheme 1.44** Pyrido-fused azaphosphinines **111** and their trapped tautomeric forms **112** 79

45. **Scheme 1.45** Pyrido[3,4-*e*]-fused azaphosphinines.....80

46. **Scheme 1.46** Synthesis of azaphosphinine-based anion receptors **117**.....81

47. **Scheme 1.47** Synthesis of azaphosphinine **125**.....85

48. **Scheme 1.48** Pd-catalyzed heteroannulation of achiral phosphanamines **126** to furnish dibenzo[*c*,*e*]-1,2λ^5-azaphosphinines **127**.....86

49. **Scheme 1.49** Retention of stereogenic P-center in heteroannulation of phosphanamine **128** 87

50. **Scheme 1.50** Conversion of azapyrilium tetrafluoroborate salts to 1,3λ^3-azaphosphinines **131** 89

51. **Scheme 1.51** Probing the reactivity of azaphosphinine **131a**.....89

52. **Scheme 1.52** Diels-Alder route to 1,3λ^3-azaphosphinines **136** 90

53. **Scheme 1.53** Complex synthetic pathway leading to either 1,3λ^3- or 1,4λ^3-azaphosphinines 91

54. **Scheme 1.54** Diels-Alder mediated synthesis of amine-bearing 1,3λ^3-azaphosphinine **145**.....91

55. **Scheme 1.55** Consecutive cycloaddition / cycloreversion pathway to furnish heavily substituted 1,3λ^3-azaphosphinines **148**. No yields reported for **148**.....92

56. **Scheme 1.56** Post-synthetic modification of **148** to either phosphinine **149** (left) or azaphosphabarrelene **150** (right) 92

57. **Scheme 1.57** Generation of heavily substituted **153** via zwitterionic intermediate.....93

58. **Scheme 1.58** Oxidation of **131** to P^V heterocycle **154** (left) or conversion to polycyclic **155** (right).....93

59. **Scheme 1.59** Conversion of triazine **149** to mixture of corresponding 1,3λ^3- and 1,4λ^3-azaphosphinines.....95

60. **Scheme 1.60** Use of 2-pyridyl directing group to dramatically favor 1,4λ^3 product **158** 95

61. **Scheme 1.61** Reversed trend in selectivity for azaphosphinine isomer based on substitution pattern of starting triazine **156** 96

62. **Scheme 1.62** Use of 1,2,3-triazine **159** to give exclusively 1,3λ^3 product **160** 96

63. **Scheme 1.63** Synthetic pathway to π-extended 1,3λ^3 azaphosphinine **167** and corresponding 1,3λ^5 azaphosphinine sulfide **168**.....97

64. **Scheme 1.64** Synthesis of dimethoxy **169** (left) and consecutive Diels-Alder / oxidation to give product **171** (right).....98

65. **Scheme 1.65** Synthesis of 1,4-dihydro-1,4λ^5-azaphosphinine 4-oxide **174**.....99

66. **Scheme 1.66** Synthesis of 2,6-diphenyl-1,4λ^3-azaphosphinine **178**.....100

67. **Scheme 1.67** Dihydro-products resulting from attack of various nucleophiles ...100

68. **Scheme 1.68** Synthesis of 2,4,4,6-tetraphenyl-1,4λ^5-azaphosphinine **184**.....101

69. **Scheme 1.69** Ozonolysis-based approach to 1,4-dihydro-1,4λ^5-azaphosphinine 4-oxides **174a** and **187**.....102

70. **Scheme 1.70** Additional examples of ring-fused 1,4-dihydro-1,4λ^5-azaphosphinine 4-oxides 102

71. **Scheme 1.71** Synthesis of azaphosphinines **194** 103

72. **Scheme 1.72** One-pot cyclization to form 1,4-dihydro-1,4λ^5-azaphosphinines **196**.....104

73. **Scheme 1.73** Synthesis of secondary 1,4λ^5-azaphosphinine 4-oxide **196'**.....104

74. **Scheme 1.74** Cycloaddition/intramolecular cyclization route to 2-oxo-1,4λ^5-azaphosphinines **201**. R^3 is either Me or Et 105

75. **Scheme 1.75** Proposed general mechanism to generate tetrahydro species **204**..106

76. **Scheme 1.76** Phosphazene **205** heteroannulation with benzyne to give azaphosphinines **206** 106

77. **Scheme 1.77** Phosphete route to benzo[*b*]-1,4λ^5-azaphosphinine **207**.....107

78. **Scheme 1.78** Pd-catalyzed heteroannulation to give 1,2,4,6-tetraphenyl-1,4-dihydro-1,4λ^3-azaphosphinine **209** 108

79. **Scheme 1.79** Intramolecular cyclization of *o*-diarylphosphinoaryl isocyanide ylides 109

80. **Scheme 1.80** Cyclization of isocyanide **213a** into dicationic **216**.....110

81. **Scheme 2.1** Synthetic pathway for the preparation of pyridine-containing PN heterocycles (a) **2a-d** and (b) **2e** 119

82. **Scheme 2.2** Synthesis of alkylated pyridine-PNs **6a-d** 122

83. **Scheme 3.1.** Synthesis of 3-Pyridine PNs 134

84. **Scheme 3.2** Synthesis of *N*-methyl pyridinium PN heterocycle **2d'** 144

85. **Scheme 4.1** Conversion of oxo-heterocycles **1** to thio-heterocycles **2** with Lawesson's Reagent (LR).....150

CHAPTER I

AZAPHOSPHININES AND THEIR DERIVATIVES

This chapter includes previously published and co-authored materials from McNeill, J. N.; Bard, J. P.; Johnson, D. W.; Haley, M. M. Azaphosphinines and their derivatives. *Chem. Soc. Rev.* **2023**, *52*, 8599–8634. This manuscript was written by J. Nolan McNeill with assistance from Dr. Jeremy P. Bard, Prof. Darren W. Johnson, and Prof. Michael M. Haley.

1.1 Introduction

Historically, heterocycle chemistry is inseparable from organic chemistry. The first isolated heterocyclic species, alloxan, discovered by Gaspare Brugnatelli in 1818,[1] predates the Kekulé model of benzene by roughly 50 years. These humble beginnings of a small nitrogenous poison isolated from uric acid kicked off an intense interest that has yet to subside. In the last 200 years, heterocycles have spread and flourished into every facet of chemistry—organic, medicinal, metal coordination, and otherwise. Much of the heavy lifting done in the field of heterocycles is done by pnictogen-based species. Simple five- and six-membered nitrogen-containing ring systems such as pyrrole, piperidine, and pyridine commonly act as solvents and/or bases in synthetic processes as well as fundamental building blocks to all manner of pharmaceuticals, dyes, ligands, and pesticides.[2–12] In comparison to their 2nd row counterparts, phosphorus heterocycles are considerably less common in the literature. However, this is not to say that these molecules do not find important uses in the modern world. A few specific examples include the use of phospholes in optoelectronic applications and phosphinines in catalysis and photophysical applications.[13–21] Nitrogen and phosphorus together serve

as an interesting pair in heterocycles as well. In particular, the nature of the P^V=N bond has been a hotly researched phenomenon.

This review will reference phosphorus-specific nomenclature extensively. Many of the functional groups have alternative common names that have risen and fallen out of popularity in the last few decades or even centuries. For the sake of consistency, the nomenclature applied in the review will adhere to the following guide (Figure 1.1). This is not an exhaustive list of phosphorus nomenclature but rather establishes the naming for the functional groups referred to frequently in this review. More elaborate descriptions of azaphosphinine nomenclature are found below (Figures 1.3 and 1.4). It should be noted that the term phosphine is generally used interchangeably with phosphane in the current literature; however, over a decade ago IUPAC decided that phosphane is the preferential term for the PR_3 functional group. For the sake of standardizing phosphorus nomenclature in this review, phosphane naming is used exclusively. This also extends to the pentavalent $P(O)R_3$, dubbed phosphane oxides.

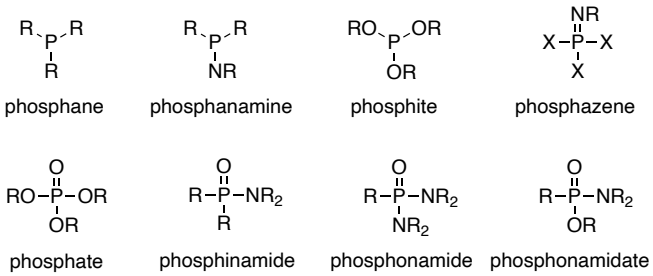

Figure 1.1 Phosphorus nomenclature commonly referred to in this chapter.

An intriguing example of what makes the P^V=N bond so unique are cyclophosphazenes.[22–24] They are cyclic species with the chemical formula $(X_2PN)_n$ (Figure 1.2, top), that at first glance, present the qualities one would expect in an aromatic ring. Prepared by Liebig et al. in 1834, hexachlorophosphazene is one of the

best examples, with the ring being totally planar, containing 6π electrons, and all ring bond-lengths being uniform.[25] For many years following its discovery, it was assumed that these qualities resulted from true delocalization of π-electrons from the nitrogen atoms into the participating 3d orbitals of the adjacent phosphorus atoms. However, it has become well understood in recent decades that a pentavalent phosphorus species has little-to-no participation of the 3d orbitals in its bonding. Instead, the nature of the P^V=N bond can be better described as highly polarized, bordering on ionic. The electronegativity difference in nitrogen and phosphorus atoms results in a transfer of the π electron to the nitrogen atom which can then participate in negative hyperconjugation. Popularized by Schleyer and Kos in 1983, negative hyperconjugation is the donation of π orbitals into adjacent σ* orbitals. This ultimately results in a stabilizing effect for the π-bond and a weakening of the σ-bond.[26] In the context of cyclophosphazenes, the lone pair orbitals of the nitrogen donate back into the $\sigma^*_{P–N}$ and $\sigma^*_{P–X}$. In total, this ionic character of each P^V=N bond and the consistent negative hyperconjugation from each nitrogen into each adjacent σ* creates a facsimile of aromaticity despite there being no delocalization through the phosphorus center (Figure 1.2, top). However, the heterocycles discussed in this review are not the inorganic cyclophosphazenes but are rather azaphosphinines containing just one nitrogen and phosphorus atom each. This difference adds two levels of complexity that must be addressed. While it would be appropriate to translate the cyclophosphazene example to 1,2λ^5-azaphosphinines with a P^V=N bond, we must also consider the other isomers.

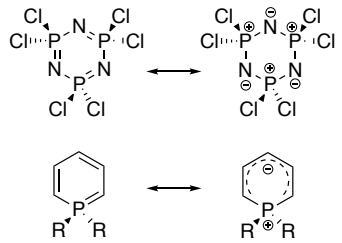

Figure 1.2 Examples of (top) ionic nature in hexachlorophosphazene and (bottom) ylidic nature in P^V phosphinine.

It is commonly recognized that P^{III} phosphinines are aromatic heterocycles in the same vein as pyridine. However, P^V phosphinines are just as commonly understood to be nonaromatic. Several publications[27–29] have addressed the cyclic-phosphonium ylide nature of P^V phosphinines (Figure 1.2, bottom), describing the partial negative charge buildup on the 2-, 4-, and 6-carbons with corresponding positive charge on the phosphorus. The result is a nonaromatic system that does not delocalize through the phosphorus like cyclophosphazenes. This situation would apply directly to the 1,4λ^5-azaphosphinines discussed in this review as there is no direct bond between the phosphorus and nitrogen in these cases, yet the electronegative nitrogen atom would be even more accepting of the negative character of the ylide. In this case it would be appropriate to conclude that the isolated 1,4λ^5-azaphosphinine ring could not be aromatic.

The last consideration to address is the phosphonyl (P^V=O) bond found in many of the heterocycles discussed in this review. Like the P^V=N bond, the phosphonyl bond is known to be extremely polarized[30] and exhibits negative hyperconjugation from the oxygen lone pairs back into the adjacent σ* of the other phosphorus bonds. While there are no thorough computational investigations into the electronics of azaphosphinines with exocyclic P^V=O bonds, we can imagine the resultant heterocycle shares the combined properties of phosphinines and phosphane oxides in which all the bonds to the phosphorus exhibit a high degree of ionic character while simultaneously being

stabilized by negative hyperconjugation from not only the oxygen but also the nitrogen atom. The conclusion of these considerations being that ultimately no P^V azaphosphinine ring of any form could truly be considered aromatic because of the consistent lack of π-delocalization through the phosphorus atom. Despite this, many of the species discussed in this review have aromatic rings fused to the azaphosphinine rings, which result in an overall aromatic structure.

Azaphosphinines have a history that spans back 135 years, yet for much of their existence they have remained little more than a synthetic curiosity (e.g., Scheme 1.1).[31] Early work on these molecules was generally fueled by a desire to explore the definition of aromaticity and its existence in unusual heteroaromatic environments. However, the initial synthetic pathways that were developed by the likes of Campbell, Dewar, Märkl, and more provided the necessary groundwork for translating azaphosphinines into modern heterocyclic chemistry.[32–36] Since the start of the 21st century, azaphosphinines have begun to find increasingly diverse uses in the fields of asymmetric catalysis, supramolecular association, cellular imaging, and even medicinal chemistry.[37–39]

The primary goal of this review is to shed light on where the science of azaphosphinines originated, illustrate both older fundamental studies and numerous recent advances, and offer insights of what is yet to come. Most of the research done on this class of molecules comes from the last 25-30 years. The compounds surveyed in this review will contain at least one six-membered ring with no more than one endocyclic phosphorus and nitrogen atom. Only compounds with high degrees of unsaturation in the PN ring will be considered. Heterocycles with partial saturation will be included as necessary to give useful counterpoints and context when discussing reactivities or properties of the heterocycles such as aromaticity. Despite the propensity for P^V-azaphosphinines to be *P*-stereogenic, stereochemistry will typically only be

shown for chiral centers (i.e., non-identical P-substituents) generated by asymmetric reactions where the enantiomeric or diastereomeric excess can be determined.

A secondary goal of this review is to provide a standardized nomenclature for azaphosphinines. While several names have been used to describe the same general system, it is the opinion of the authors that the terminology of azaphosphinine should be used to describe any six-membered ring containing one phosphorus and one nitrogen atom. This can be further divided into the isomers of 1,2-, 1,3-, and 1,4-azaphosphinine **1a-c** (Figure 1.3, top), where the "1-" is in reference to the position of the nitrogen atom and the second number refers to the position of the phosphorus atom. The commonly observed *benzo* fusion aptly results in the name benzo[*x*]azaphosphinines **2a-b** (Figure 1.3, bottom). The bracketed letter refers to the bond (Figure 1.3, top) on which ring fusion occurs, with the N–X bond being "a", where x is either the phosphorus atom or the closest carbon to it. In the case of naming fused ring systems, Hantzch-Widman nomenclature rules should be used.[40] Further π-extension via ring fusion will continue appropriately. The phosphorus atom in every compound discussed will exist in one of two valences, either P^{III} or P^{V}. This is denoted by the superscript number on the λ inserted into the chemical name. Examples of this nomenclature system are given below (Figure 1.4) for compounds **3** and **4**. As apparent, while these naming conventions are accurate, they rapidly become encumbered with substituents and substitution patterns. As such, when referring to libraries of synthesized azaphosphinines, the authors of this review will typically refer to them as azaphosphinines or benzo[*x*]azaphosphinines with key substituents as appropriate.

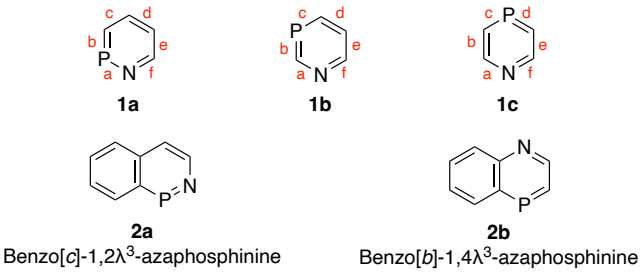

Figure 1.3 Examples of (top) 1,2- (**1a**), 1,3- (**1b**) and 1,4-azaphosphinines (**1c**) and (bottom) benzo[*c*]- (**2a**) and benzo[*b*]azaphosphinine (**2b**) isomers.

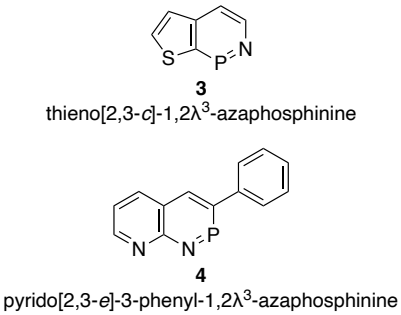

Figure 1.4 Examples of nomenclature rules applied to more complex azaphosphinine derivatives such as **3** and **4**.

This review is divided primarily into three sections concerned with the three isomeric forms of azaphosphinine. The 1,2-isomer is by far the most studied of the three, likely because of the wealth of reactions that have been developed to afford this scaffold. The inherent difference in electronegativities between the phosphorus and nitrogen atoms increases their electrophilicity and nucleophilicity, respectively. This increased reactivity aids reactions such as heteroannulation and C–H activation. These factors could help explain why there are several more publications for the 1,4-isomer than 1,3-isomers, with the latter being quite rare in the current literature. For the purposes of organization, each isomer's section will be divided into subcategories to distinguish between the different methods of synthesis applied to form the azaphosphinine ring.

1.2 Azaphosphinine origins

The first published example of a six-membered PN-heterocycle dates to 1888 with the work of Schenk and Michaelis on what are commonly referred to as dihydrophenophosphazines (Scheme 1.1).[31] This heterocyclic scaffold could also be classified as dibenzo[*b,e*]-1,4-dihydro-1,4λ^5-azaphosphinine under the naming scheme used in this review. The synthesis proceeds through an addition of PCl_3 to diphenylamine at elevated temperatures. This reaction yields the *P*-chloro species **5**, which can be subsequently hydrolyzed/oxidized into the corresponding 1,4λ^5-azaphosphinine 4-oxide **6**. Due to technological constraints, the structure of **6** was not definitively confirmed until nearly a century later thanks to the work of Häring.[41] The dihydrophenophosphazine scaffold stands somewhat alone among azaphosphinine derivatives, as the 1970s and 1980s saw three excellent review articles detailing the chemistry of these species, which we encourage those with further interest to read.[42–44] Since then, the literature has been extremely sparse on publications concerning these chemicals.[45,46] Due to the wealth of previously compiled research and a dearth of recent studies, dihydrophenphosphazines will be excluded from the remainder of this review.

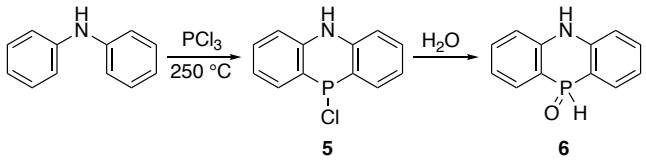

5 **6**

Scheme 1.1 Schenk and Michaelis' first reported synthesis of a PN-heterocycle scaffold, dibenzo[*b,e*]1,4-dihydro-1,4λ^5-azaphosphinine 4-oxide.

The oldest example of a 1,2-azaphosphinine comes from Dewar and Kubba in 1960.[47] Their synthesis follows a similar pathway to that laid out by Schenk and

Michaelis nearly a century before.[31] This team had released a publication two years earlier describing aromatic resonance forms in boron-containing **7** and were interested in developing analogous PN species.[48] The work was aimed at trying to develop a phenanthrene-like dibenzo[*c,e*]-1,2-dihydro-1,2λ^3-azaphosphinine **9a** with hypothetical resonance structure **9a'**, in which the lone pair of the nitrogen atom would resonate through phosphorus to give some additional π-delocalization through the hypervalent P resonance structure **9a'** (Scheme 1.2). Starting from 2-aminobiphenyl, the authors generated an acyclic intermediate by reacting with phosphorus trichloride in benzene. This was then cyclized crude with $AlCl_3$ at elevated temperatures to furnish **8a**. Finally, replacement of the chlorine with PhMgBr resulted in the desired compound **9a**.

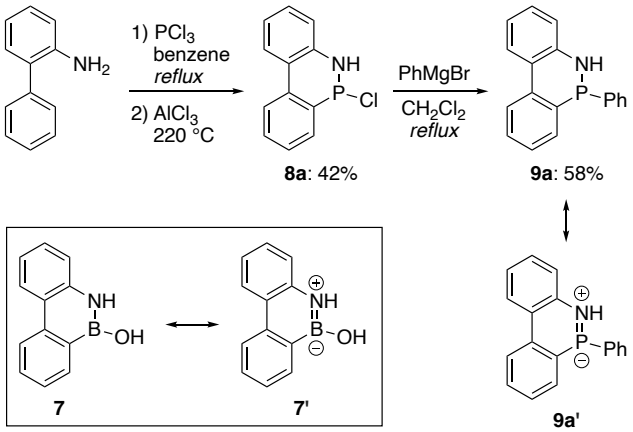

Scheme 1.2 Synthesis of Dewar and Kubba's early dibenzo[*c,e*]-1,2-dihydro-1,2λ^3-azaphosphinine **9** and comparison to the previously prepared boron-containing species **7**.

Comparison of UV-Vis spectra of **7** and **9a** indicated that while the electronic structures of the two species were similar, they were not identical. However, the authors noted that when left exposed to air for extended periods of time, two oxidation products (**10** and **11a**) were generated from **9a** (Scheme 1.3). Interestingly, the spectra of these

oxidation products were nearly identical when compared to that of **7**. This emergent electron delocalization was rationalized by Dewar and Kubba through proposed resonance structures **10'** and **11a'**. By convention, P^V-oxo compounds are represented as P=O double bonds; however, due to the nature of the hypervalent bonding of these atoms, it can be argued that the phosphonyl moiety exists as P^+–O^- in most cases. As discussed previously, it is unlikely any true aromaticity is occurring in these P^V heterocycles, but rather electron delocalization from the lone pairs of the oxygen and nitrogen to adjacent bonds via negative hyperconjugation. Further consideration of aromaticity in different azaphosphinine isomers is discussed at the end of the review. A majority of the azaphosphinines discussed in this review will feature this negative hyperconjugation phenomenon.

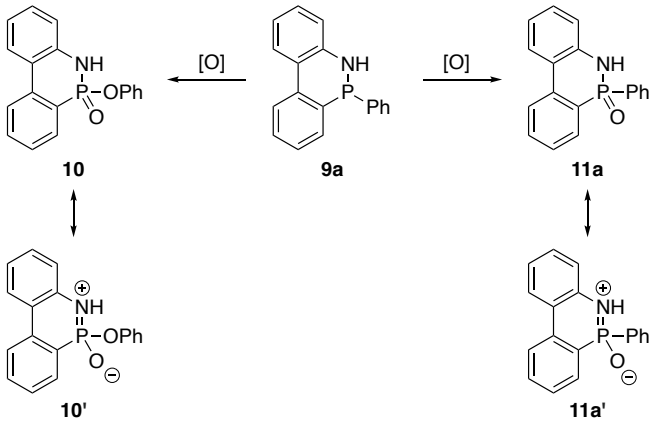

Scheme 1.3 Oxidation products of Dewar and Kubba's azaphosphinine **9** with aromatic resonance structures.

That same year, Campbell and Way significantly expanded upon the previous work laid out by Dewar and Kubba.[49] Starting from one of two *P*-chloro species **8** (R=H or Me), they arylated the system directly with several different aryl lithiates to furnish a family of corresponding azaphosphinines **9**. The authors found that they could induce the oxidation observed by Dewar and Kubba by exposing the heterocycles to a mixture

of H_2O_2 and EtOH at room temperature (Scheme 1.4). No yields were reported for the final oxidation to furnish **11**.

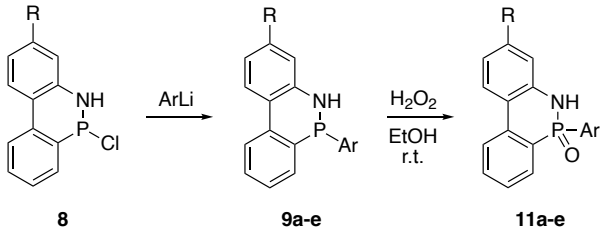

8 **9a-e** **11a-e**

9a: R = H, Ar = Ph, 11%
9b: R = Me, Ar = Ph, 25%
9c: R = H, Ar = *p*-MeC_6H_4, 5%
9d: R = H, Ar = *p*-BrC_6H_4, 9%
9e: R = H, Ar = *p*-$(NMe_2)C_6H_4$, 23%

11a: R = H, Ar = Ph
11b: R = Me, Ar = Ph
11c: R = H, Ar = *p*-MeC_6H_4
11d: R = H, Ar = *p*-BrC_6H_4
11e: R = H, Ar = *p*-$(NMe_2)C_6H_4$

Scheme 1.4 Campbell and Way's synthesis of early azaphosphinines **9** and oxidation to **11**.

1.3 1,2-Azaphosphinines

1.3.1 Reactivity with Alkynes

1.3.1.1 *Pericyclic / Cycloadditions*

When considering the different synthetic approaches used in the development of 1,2-azaphosphinines, few are as prevalent in the early literature as the [4 + 2] cycloaddition, more commonly known as the Diels-Alder reaction. The earliest example of this reaction being applied to the 1,2-isomer of azaphosphinine is from Kobayashi and Nitta in 1985 to furnish three 1,2λ^5-azaphosphinine derivatives.[34] While not the first reported synthesis of this family of heterocycle, it did lay the groundwork for what would become a very typical method. The researchers used an *N*-vinyl-phosphazene (**13**) as their diene (Scheme 1.5), which was generated through the Staudinger reaction of azidostyrene **12** and trimethyl phosphite. The Diels-Alder reaction was then carried out using various substituted alkynes to yield 2,2-dimethoxy-1,2λ^5-azaphosphinines **14** in modest to good yields. The observed regioselectivity of

14b is ascribed to the ylidic nature of the phosphazene diene and the comparatively electrophilic β-carbon of the ester dienophiles. When heated to high temperatures, azaphosphinines **14a-b** underwent a methyl shift to yield the corresponding dihydro derivatives **15** in excellent yields.

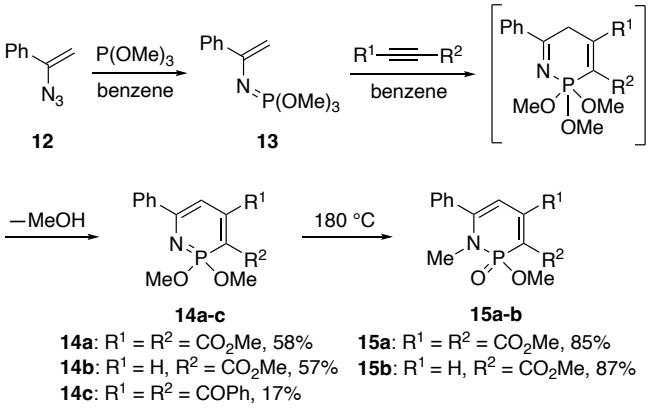

Scheme 1.5 Synthesis of 1,2-azaphosphinine **14** using the Staudinger reaction and subsequent Diels-Alder cycloaddition.

Over a decade later, Nitta and coworkers returned to their work on the cycloadditions of *N*-vinyl-phosphazenes and substituted alkynes to explore further modifications.[50] They synthesized a similar series of 2,2-diphenyl-1,2λ^5-azaphosphinines **16** in modest yields by using phosphazene **17** as the phosphorus source for diene preparation (Scheme 1.6). Besides the new azaphosphinines, this paper also served to demonstrate potential post-synthetic modifications to these heterocycles. Unlike **14**, azaphosphinines **16** did not rearrange but instead could be reversibly protonated to give the corresponding azaphosphininium tetrafluoroborate salts **18**.

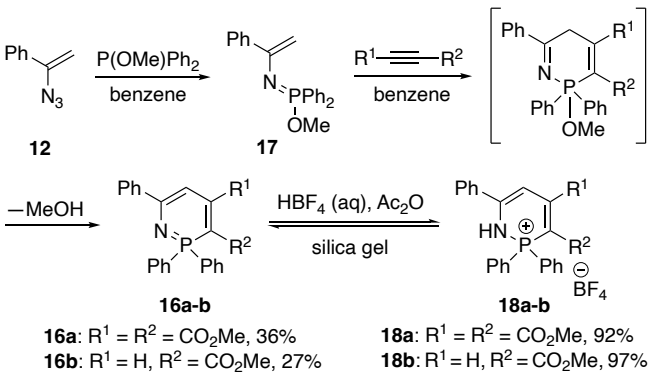

Scheme 1.6 Preparation of heterocycles **16** using phosphazene **17** and formation of azaphosphininium salts **18**.

In 1996, López-Ortiz and coworkers published an interesting alternative pathway to the 2,2-diphenyl-1,2λ^5-azaphosphinine scaffold by using *N*-methoxycarbonyl alkyldiphenylphosphazenes **19** as the pnictogen source in the cycloaddition.[51] The key difference in this procedure from previous work was the generation of a stable ylide by deprotonation of the phosphazene with *n*-BuLi. The ylide then cyclized with dimethyl acetylenedicarboxylate (DMAD) to form the corresponding 2,2-diphenyl-1,2λ^5-azaphosphinin-6-one **20** in very good to excellent yields (Scheme 1.7). The authors concluded that only alkyldiphenylphosphazenes will react accordingly, as the substitution of a hydrogen inhibits the process. The authors noted that they had no explanation for the lack of reactivity in their system when R = H.

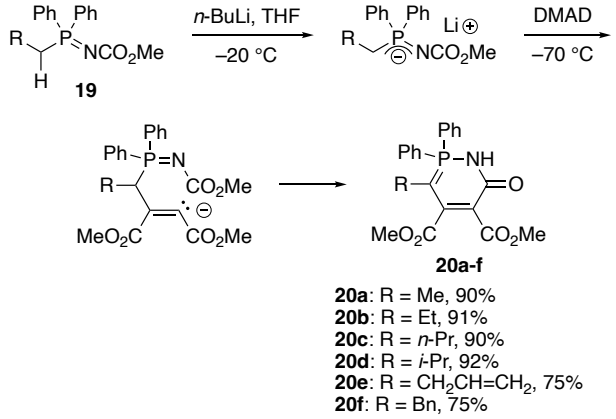

Scheme 1.7 Synthesis of 2,2-diphenyl-1,2λ^5-azaphosphinin-6-ones **20** through cycloaddition with DMAD.

Following this work from López-Ortiz, the chemistry of 1,2λ^3-azaphosphinines began to flourish with the seminal 1996 publication from Mathey and coworkers in which 1,3,2-diazatitana-cyclohexa-3,6-dienes **21** were reacted with an equivalent of PCl_3 at low temperature to furnish the corresponding 1,3,2-diazaphosphinines **22** (Scheme 1.8, top).[52] These diazaphosphinines can then be subjected to [4 + 2] cycloaddition conditions to yield a diazaphosphabarrelene intermediate **23**, which undergoes a subsequent [4 + 2] cycloreversion to extrude an equivalent of *t*-BuCN to yield 1,2λ^3-azaphosphinines **24**. Interestingly, this reaction can be repeated through the same conditions and extrude another equivalent of *t*-BuCN and furnish the corresponding phosphinine. This finding was similar to that of Märkl several years earlier who observed similar nitrile-extrusion properties in 1,3λ^3-azaphosphinines, as will be discussed in a later section of this review.[53] This mild synthesis offered several distinct advantages in the forms of regioselectivity, functional group tolerance, and high yields.

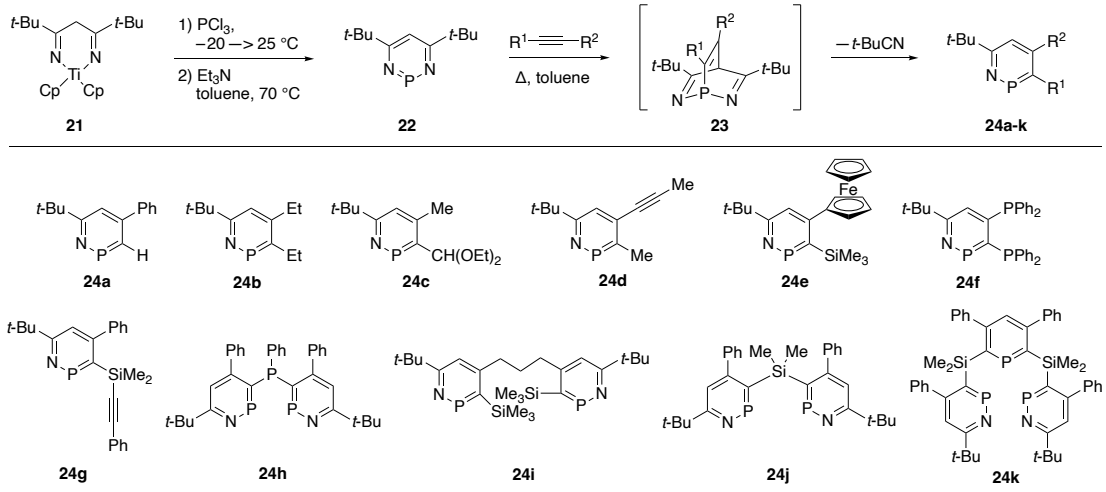

Scheme 1.8 (top) Synthesis of 1,2-azaphosphinines **24** through the formation and cycloaddition of a 1,3,2-diazaphosphinine. (bottom) Substrate scope of the heterocycles prepared in this way.

In 1997, Mathey and coworkers released a follow-up publication that dramatically expanded the substrate scope.[54] Despite demonstrating how titanocenes with either diphenyl or di-*t*-butyl substitution could be applied to the initial cycloaddition-cycloreversion reaction, the authors only used the di-*t*-butyl substituted derivative for the sake of purification. This resulted in a library of diverse 6-*t*-butyl-1,2λ^3-azaphosphinine derivatives **24**, highlighting the benefits of this synthetic approach (Scheme 1.8, bottom). The previously inaccessible derivatives include ferrocene, exocyclic phosphane, and silane-containing species. An interesting facet of the synthesis was discovered when comparing conjugated vs. nonconjugated diynes in the reaction. The authors found that use of conjugated diynes such as 2,4-butadiyne only facilitated a reaction from one of the triple bonds, leading to a 4-ethynyl azaphosphinine. Conversely, by using nonconjugated diynes, the reaction occurs at both alkyne sites resulting in bisazaphosphines (**24h-k**). It should be noted that every azaphosphinine generated through this method can be further transformed into the corresponding phosphinine as described above. Unfortunately, only the yields of the terminal phosphinines are reported. Application of this cycloaddition-cycloreversion strategy with nonconjugated diynes to generate more complex bisazaphosphinine heterocycles begged the question as to whether it could be extended to higher order systems. In 2000, Le Floch and coworkers provided the answer by performing the same reaction on tripodal species **25** and **26** to generate 1,2λ^3-azaphosphinine heterocycles **27** and **28** (Scheme 1.9).[55]

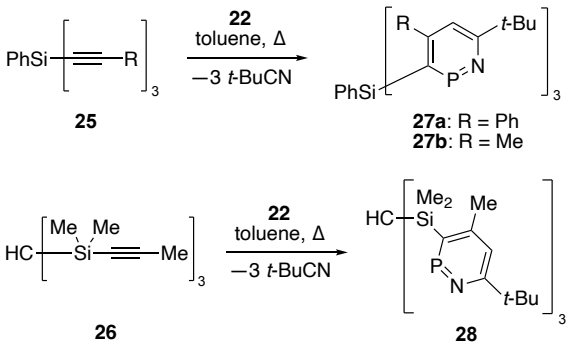

Scheme 1.9 Preparation of tripodal 1,2λ^3-azaphosphinine heterocycles (top) **27** and (bottom) **28**.

1.3.1.2 *Transition Metal-Catalyzed C–H Activation*

While the preparation of azaphosphinines via cycloaddition reactions was the most popular method in the 1980s and 1990s, this route has been supplanted by more modern techniques in recent years. One of the biggest synthetic advances across all of organic chemistry has been the advent and popularization of transition metal-mediated reactions stemming from pioneering works of Heck, Suzuki, Sonogashira, and more. One popular recent advance is transition-metal based C–H activation. A common technique for such reactions is the use of *ortho*-directing groups in aryl systems. By having an appropriate functional handle, specific aryl C–H bonds can be selected and reacted upon. In 2013, Glorius and coworkers published their work using phosphoryl-related directing groups in Rh^{III}-catalyzed C–H activation.[56] They reasoned that because there was a plethora of carbonyl-based directing groups for C–H activation, phosphonyl-based systems may work as well. After screening conditions, the authors found that the catalyst $RhCp^*(MeCN)_3(SbF_6)_2$ was able to effect C–H activation reactions directed by different aryl phosphonamides. Within the scope of this review, when this reaction was performed on phosphonamide **29** and various bis-functionalized alkynes, the corresponding benzo[*c*]-1,2-dihydro-1,2λ^5-azaphosphinines **30** were furnished in good yields (Scheme 1.10). There was no apparent preference in electronic character of the

alkyne. While the authors note that the desire to synthesize **30** was fueled by the biological relevance of the analogous isoquinolinone, this paper served more as a foray into phosphonyl-directed C–H activation and was not focused on the azaphosphinines outside of their application in reaction scope.

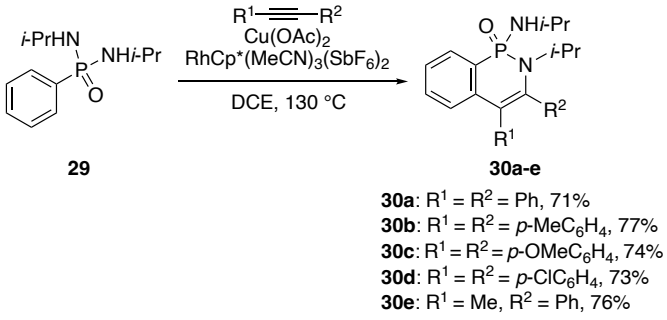

Scheme 1.10 Aryl phosphonamide directed C–H activation to furnish **30**.

In the same year as the work from Glorius, Lee and coworkers sought to use phosphinamides for C–H activation and heteroannulation using a different Rh catalyst.[57] Unlike the work from Glorius and coworkers, this publication was entirely focused on the construction of azaphosphinines. The goal was to use the lone pair of the phosphinamide as a directing group for the heteroannulated benzo[*c*]-1,2-dihydro-1,2λ^5-azaphosphinine 2-oxides. After optimizing the reaction conditions, Lee and coworkers examined a variety of phosphinamide substrates **31** (Scheme 1.11) and generated several derivatives of azaphosphinine **32** in good to excellent yields. There was no apparent preference for electron density or steric bulk in the alkyne coupling partner, and they observed excellent functional group tolerance. In several instances, they obtained heterocycles containing aryl chlorides and bromides that are available for further manipulation. They also proceeded to show how more complex, heterocyclic phosphinamides tolerate the reaction as with *P*-thiophene derivatives **32o** and **32p**.

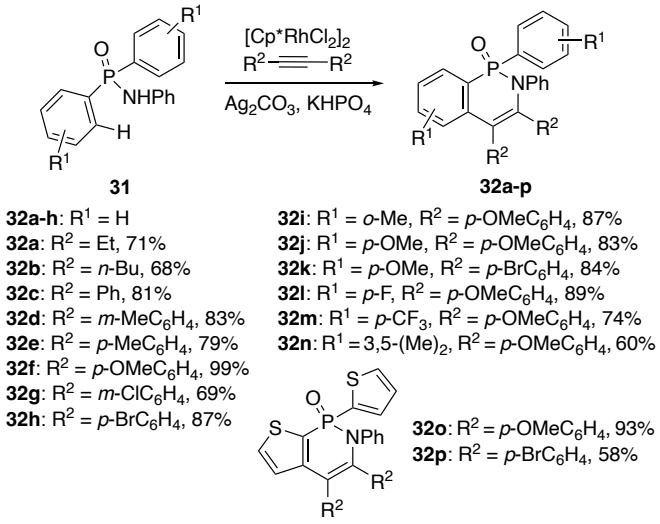

Scheme 1.11 Formation of [*c*]-fused 1,2-dihydro-1,2λ^5-azaphosphinine-2-oxide **32**.

Electron lone pairs, particularly those on pnictogen atom centers, are commonly used to effect ligation. However, while many pnictogen-based ligands exist, the phosphinamide motif is rarely accessed for this purpose. Despite underutilization, the propensity of P^V to form chiral centers combines well with an adjacent directing lone pair. In 2017, Cramer and coworkers aimed to take the previous work from Lee and use it to develop a new class of benzo[*c*]-1,2-dihydro-1,2λ^5-azaphosphinine 2-oxide based *P*-stereogenic ligands.[58] To accomplish this, Cramer took advantage of prochiral molecule **33** to carry out the transition metal-catalyzed heteroannulation reaction. By using the nitrogen to direct the chiral catalyst to one of the two ortho aryl C–H bonds **34**, chiral intermediate **35** is formed, which is then carried through the reaction to give chiral benzo[*c*]-1,2-dihydro-1,2λ^5-azaphosphinine 2-oxide **36** (Scheme 1.12).

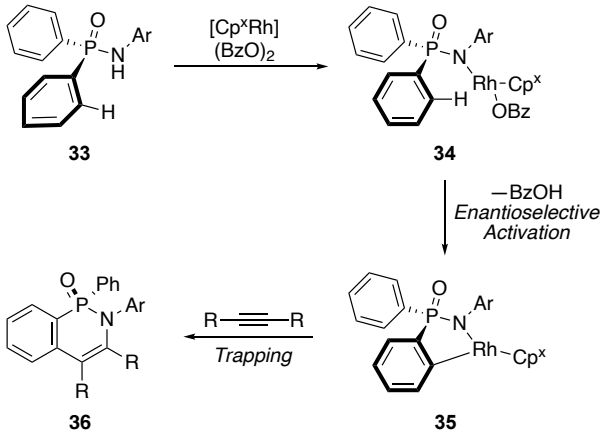

Scheme 1.12 Proposed mechanism for chiral C–H activation heteroannulation of achiral phosphinamide.

Optimization experiments determined that **Rh1** was the most appropriate catalyst for good enantioselectivity of the products, and thus a wide substrate scope was examined (Scheme 1.13). From the results of the synthetic trials, there does not seem to be a large electronic preference of substrate. Regardless, the high enantioselectivity of the reaction is undeniable, with enantiomeric excess being greater than 10:1 (*S:R*) for every derivative of **36** synthesized.

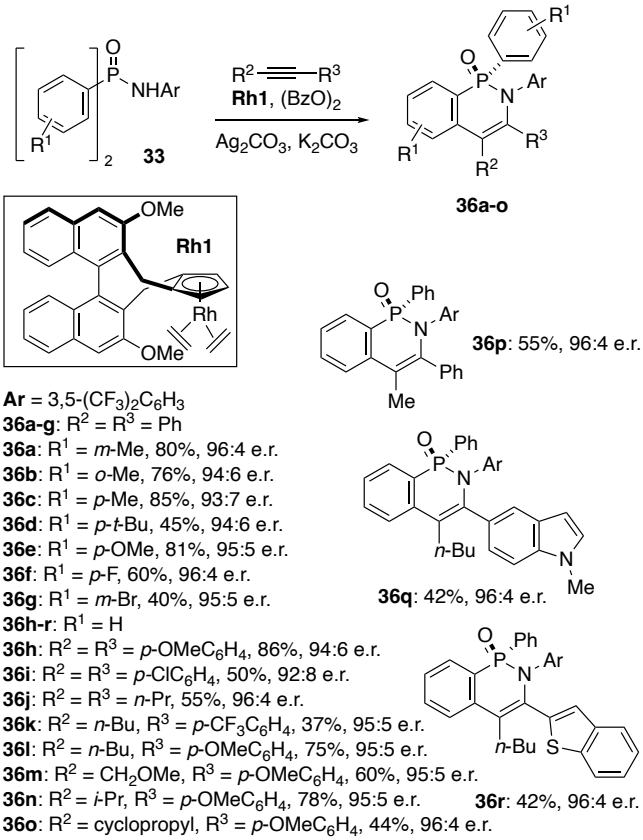

Scheme 1.13 Chiral C–H activation heteroannulation to afford **36**. For every entry, Ar = 3,5-$(CF_3)_2C_6H_3$.

Because the primary aim of the Cramer paper was to generate useful chiral phosphinamide ligands for further chemistry, they also reported reducing the benzo[*c*]azaphosphinine from P^V to P^{III}. Although the authors found that the heterocycles were prone to racemization under certain conditions, the optimal method (Scheme 1.14) used 1,8-diazabicyclo[5.4.0]undec-7-ene (DBU) and trichlorosilane, resulting in 92% yield of P^{III} product and 97% retention of the initial configuration. The authors concluded this is a feasible pathway to enantiospecific benzo[*c*]-1,2-dihydro-1,2λ^3-azaphosphinines ligands **36'**; however, they have not reported additional studies on this system to date.

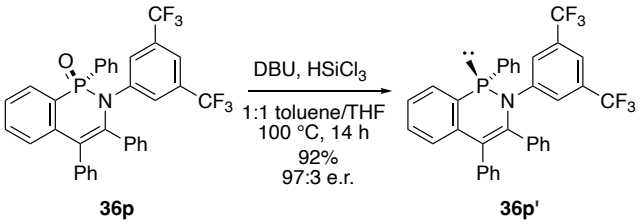

36p **36p'**

Scheme 1.14 Enantiospecific reduction to chiral azaphosphinine **36p'**.

In 2018, Cramer and Sun published a follow-up study that revealed a promising application for their system.[38] Previously, the syntheses of chiral azaphosphinines **36** via this method were limited to the desymmetrization of achiral phosphinamides with two identical aryl *P*-substituents **33**. The authors hypothesized that if the selectivity for the reactive enantiomer could be great enough, then one would be able to take a racemic mixture of chiral phosphinamide and generate two enantiomerically-pure materials, the heteroannulated reactive enantiomer **37** and the purified unreactive enantiomer of the starting racemate **38** (Table 1.1). In this study the chiral catalyst **Rh1** did not give sufficient selectivity, so Rh complexes with bulky trisubstituted Cp^x ligands (to deactivate reactivity on the mismatched substrate) were screened, with **Rh2** proving to be the most effective.

Table 1.1 Experimental details for reactions of *rac*-**36** with various internal alkynes. Ar = 3,5-$(CF_3)_2C_6H_3$.

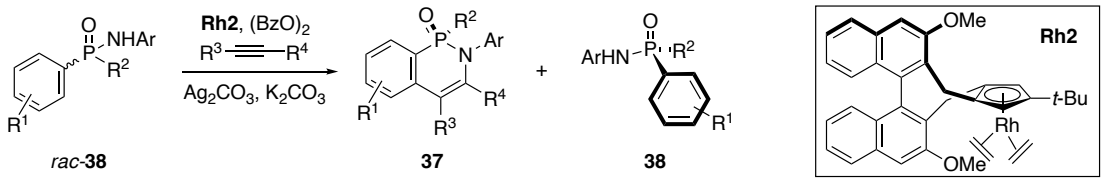

rac-**38** **37** **38**

rac-**38**	R^1	R^2	R^3	R^4	Time [h]	Conv. [%]	e.r **37** (% yield)	e.r. **38** (% yield)
rac-**38a**	H	Me	Ph	Ph	8.5	51	93:7 (46)	95:5 (46)

rac-**38b**	*p*-Me	Me	Ph	Ph	10.5	55	89:11 (50)	98:2 (42)
rac-**38c**	*p*-F	Me	Ph	Ph	10.5	55	90:10 (48)	98:2 (40)
rac-**38d**	*p*-Cl	Me	Ph	Ph	10.5	55	89:11 (45)	97:3 (40)
rac-**38e**	*p*-OMe	Me	Ph	Ph	8.5	54	91:9 (48)	99:1 (42)
rac-**38f**	*p*-NMe_2	Me	Ph	Ph	9.5	42	95:5 (36)	83:17 (50)
rac-**38g**	*m*-Me	Me	Ph	Ph	10.5	58	85:15 (53)	99:1 (38)
rac-**38h**	*m*-Br	Me	Ph	Ph	14	55	91:9 (42)	99:1 (38)
rac-**38i**	*o*-Me	Me	Ph	Ph	10	53	77:23 (42)	79:21 (44)
rac-**38j**	H	Bn	Ph	Ph	4	59	84:16 (53)	99.5:0.5 (37)
rac-**38k**	H	$(CH_2)_2OBn$	Ph	Ph	6.5	51	93:7 (47)	93:7 (44)
rac-**38l**	H	*N*-pyrrolidinyl	Ph	Ph	5	57	79:21 (52)	89:11 (40)
rac-**38m**	H	*N*-morpholinyl	Ph	Ph	3.5	61	79:21 (55)	95:5 (37)
rac-**38n**	H	OMe	Ph	Ph	24	60	81:19 (55)	97:3 (37)
rac-**38o**	H	OPh	Ph	Ph	14	53	86:14 (48)	91:9 (44)
rac-**38p**	H	Me	*p*-$OMeC_6H_4$	*p*-$OMeC_6H_4$	8.5	51	89:11 (46)	95:5 (46)
rac-**38q**	H	Me	*n*-Bu	*p*-$OMeC_6H_4$	8.5	50	95:5 (46)	90:10 (46)
rac-**38r**	H	Me	*i*-Pr	*p*-$OMeC_6H_4$	8.5	43	94:6 (37)	82:18 (52)

rac-**38s**	H	Me	*n*-Bu	5-indolo	8.5	54	96:4 (48)	98:2 (43)

Much like their previous publication, this 2018 Cramer paper featured a large library of derivatives to emphasize the efficacy of their system. Varying the electronic and steric properties of both the alkyne and chiral phosphinamide led to moderate but consistent yields (36-55%) and enantioselectivities, in some cases exceeding 99:1. This included the use of various heterocycles and alkyl chains on both stating materials. The reaction was also performed on achiral diaryl phosphinamide **38t** to explore any possible regioselectivity for which ring results in the *benzo* fusion (Scheme 1.15). The authors found that there was an almost 1:1 distribution between the two possible products with an excellent overall yield for the transformation.

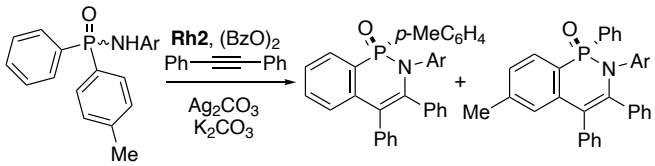

Scheme 1.15 Reactivity of bis-aryl functionalized chiral phosphinamide. Ar = 3,5-$(CF_3)_2C_6H_3$.

To investigate the application of this newly synthesized series as chiral phosphorus-based reagents for asymmetric catalysis, **37a** and **39** were added as a Lewis base (LB) to a reductive aldol condensation of chalcone **40** and benzaldehyde to furnish **41** (Scheme 1.16). Interestingly, the methyl-bearing **37a** gave not only a higher overall yield (95%) of product but also a dramatically improved enantioselectivity (96:4 e.r. of major diastereomer) compared to less selective **39**.

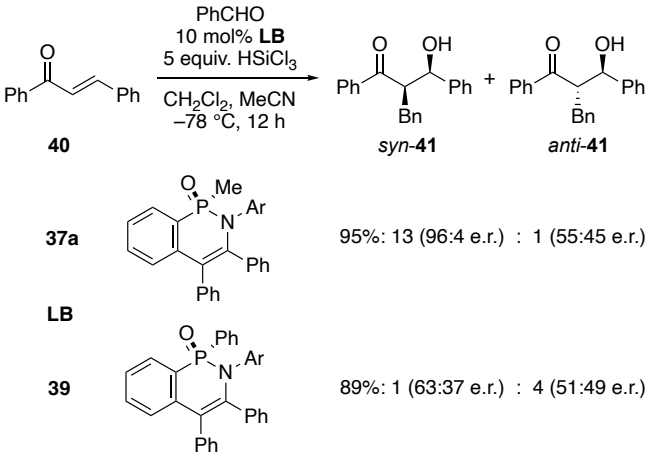

Scheme 1.16 Asymmetric reductive aldol condensation of enone **40** and benzaldehyde using chiral benzo[*c*]-1,2-dihydro-1,2λ^3-azaphosphinine additives as Lewis base (LB). Ar = 3,5-$(CF_3)_2C_6H_3$.

Continuing their investigation into asymmetric applications of their materials, the authors reduced **37a** from the P^V to P^{III} valence via thionation to **37a'** and reduction to **37a''**, which was then used as a ligand for asymmetric hydrogenation (Scheme 1.17). This hydrogenation reaction proceeded with quantitative yield and decent enantioselectivity, suggesting promising future applications for azaphosphinines in the field of organic catalysis.

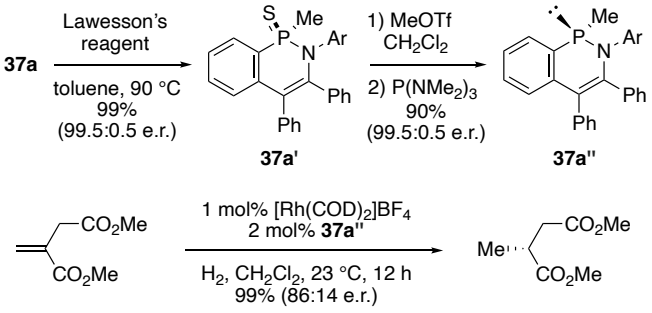

Scheme 1.17 Enantioselective reduction of **37a** and its use as a chiral ligand in an asymmetric hydrogenation reaction. Ar = 3,5-$(CF_3)_2C_6H_3$.

While these studies generated a large body of work that furthered the science of azaphosphinines considerably, the one potential drawback was the reliance on

expensive Rh^{I} catalysts. In 2022, Shi and coworkers reported the design and application of a *in situ*-generated Co^{III} catalyst for the asymmetric heteroannulation of achiral phosphinamides **42** to benzo[*c*]-1,2-dihydro-1,2λ^5-azaphosphinine 2-oxides **43**.[59] Similar to Cramer's initial work, the early substrates are diphenylphosphinamides that rely on the enantiotopic aryl C–H bonds to generate a chiral intermediate.[57] Much of this work is dedicated to the logical design of an appropriate chiral ligand. Previous research suggested that monoanionic bidentate ligands were necessary for the *in situ*-generation of chiral Co^{III} active species.[60,61] After screening a number of ligands, the authors eventually decided upon salicyloxazoline (Salox) *(S)*-**L1**. This ligand, along with the $Co(OAc)_2•4H_2O$ precatalyst and $Mn(OAc)_2•4H_2O$ oxidant, were applied to many substrates where both the achiral phosphinamide and alkyne were varied to form **43** (Scheme 1.18). In the case of every substrate, the aryl substituent is an 8-quinolinyl motif.

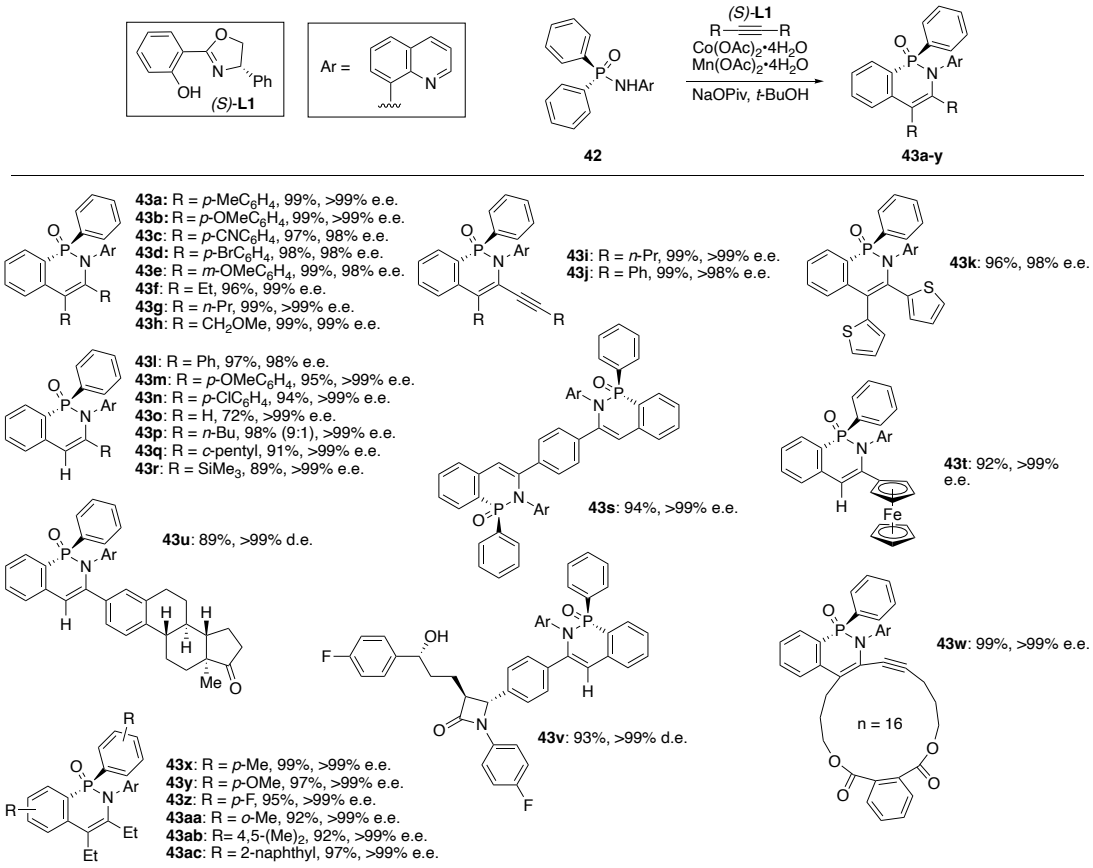

Scheme 1.18 Chiral C–H activation and heteroannulation using Co^{III} to afford **43**.

Shi and coworkers then performed a kinetic resolution experiment like Cramer, reacting a racemic mixture of compound **44** with phenylacetylene under conditions identical to the above trials (Scheme 1.19). The experimental results were excellent, with a near-quantitative overall yield and high enantioselectivity in forming just the (*S)*-enantiomer of the product **45** while ignoring the unreactive enantiomer of the starting phosphinamide (*R)*-**44**.

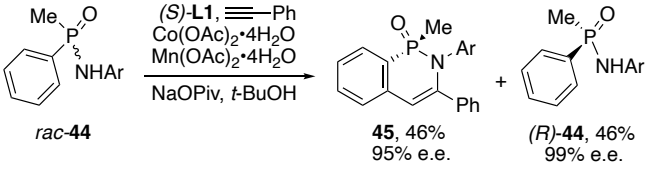

Scheme 1.19 Chiral resolution of phosphinamide **44** under standard reaction conditions. Ar = 8-quinolinyl.

Shi and coworkers also showed that the heteroannulation would proceed when the alkyne was replaced with a variety of allene coupling partners **46** (Scheme 20), affording **47** in good to excellent yields with high e.e. values.

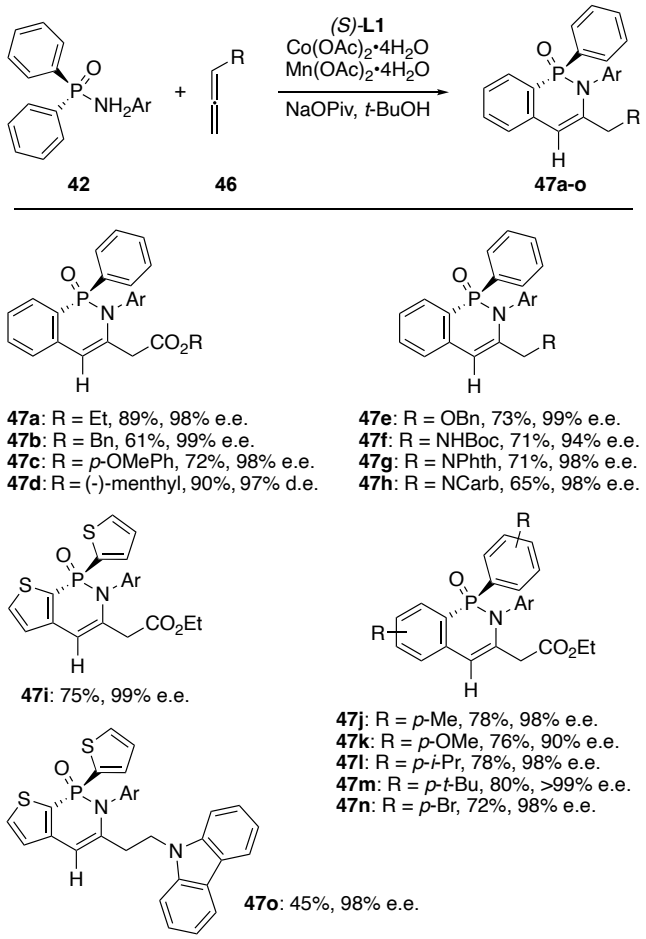

Scheme 1.20 Heteroannulation with allene coupling partners. Ar = 8-quinolinyl.

Very recently in 2023, Shi and coworkers reported similar transition-metal catalyzed [4 + 2] heteroannulation reactions on phosphanamines **48** and functionalized alkynes.[62] There are several important distinctions that separate this work from earlier publications. The design of the starting material is quite different, notably that the

phosphorus atom of the phosphanamines is trivalent and is oxidized to pentavalence during the reaction. Secondly, the heteroannulation is conducted on *ortho*-halo-phosphanamines where the reactive bond is adjacent to the nitrogen instead of the phosphorus. This results in an inversion of the product atom geometry relative to the other species in similar publications. Although initially probed using tris(dibenzylideneacetone)dipalladium(0) (Pd_2dba_3) as the catalyst, screening studies revealed that $Ni(COD)_2$ gave dramatically improved yields. Further optimization of conditions showed that stoichiometric amounts of LiCl aided in the reduction of the Ni catalyst, and that elevated temperatures were required for optimal yield. The main body of explored substrates comprised of achiral phosphanamines with two identical alkyl or aryl substituents to furnish benzo[*e*]-1,2λ^5-azaphosphinines **49** (Scheme 1.21, top). The scope of functionalized alkynes includes not only aryl but also heteroaryl and alkyl substituents, indicating the wide degree of functional group tolerance. A dual heteroannulation was also conducted on **50** to furnish **51** with good to excellent yields (Scheme 1.21, bottom).

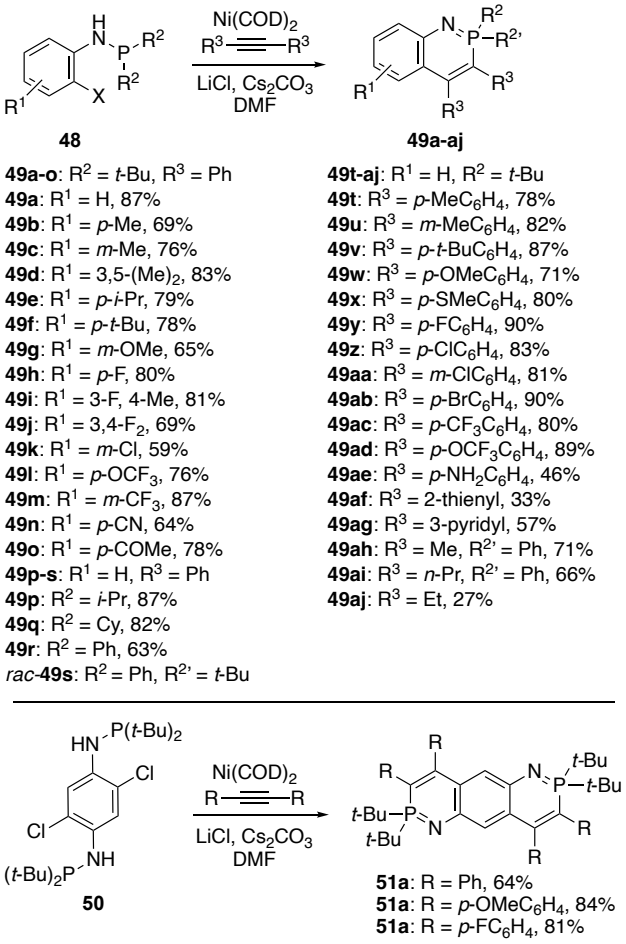

Scheme 1.21 Ni^0-mediated heteroannulation to afford azaphosphinines **49** and **51**.

Shi and coworkers continued to explore the heteroannulation of *P*-stereogenic phosphanamines as well by protecting the P^{III} as borane complexes **52** and **53**. The starting materials were deprotected in situ and proceeded with moderate yields but excellent enantioselectivities for retention of the geometry of the chiral center in heterocycles **49s** and **49ak-an** (Scheme 1.22). Unlike most of the azaphosphinines covered in this review, this paper does provide analysis of the photophysical properties of the molecules. Density functional theory (DFT) provided the computed HOMO and LUMO energy levels of **49a**, which showed a clear distinction between HOMO and LUMO localization, with the HOMO predominantly on the benzo[*c*]azaphosphinine core while the LUMO is distributed across all the aromatic rings. This reasoning led to

the conclusion that the LUMO and subsequent photophysical properties could be modulated through the identity of the aryl-substituent. Six heterocycles with varied aryl-substituents were measured for their emission in both solution and the solid state (Table 1.2). While the solution-state quantum yields of the analyzed species were rather low (4%-13%), the solid-state quantum yields were comparatively quite high with **49y** reaching 90%.

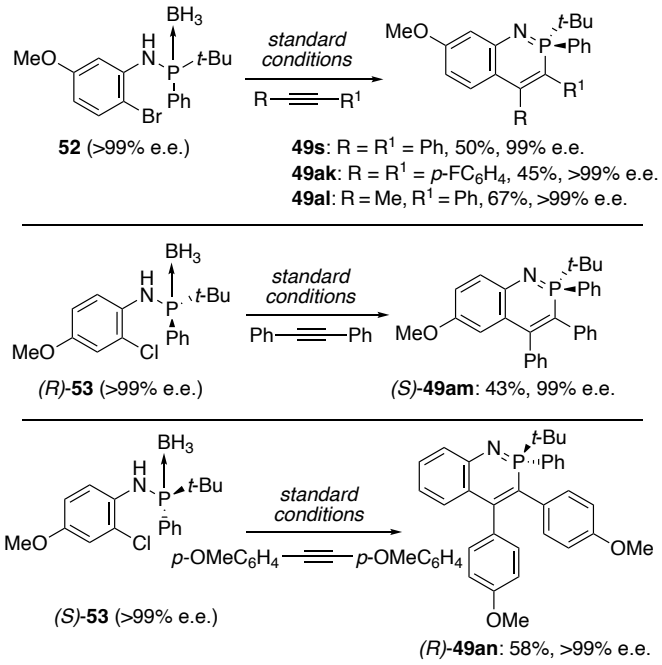

Scheme 1.22 Asymmetric [4 + 2] heteroannulation starting from chiral phosphanamines. Standard conditions of phosphanamine (1 equiv.), alkyne (2 equiv.), $Ni(COD)_2$ (10 mol%), LiCl (1 equiv.), Cs_2CO_3 (3 equiv.), DMF, 130 °C.

Table 1.2 Emission data for measured heterocycles **49**.

Substrate	Aryl group	λ_{em} (nm)[a,b]	φ (%)[b]	λ_{em} (nm)[a,c]	φ (%)[c]
49a	Ph	514	40	547	5
49t	*p*-MeC_6H_4	530	30	539	4
49w	*p*-$OMeC_6H_4$	518	11	536	4
49y	*p*-FC_6H_4	515	90	543	13
49ab	*p*-BrC_6H_4	561	66	560	7

49ac	*p*-$CF_3C_6H_4$	551	24	582	6

[a]Emission maxima upon excitation at maximum absorption wavelength. [b]Measured in solid state. [c]Measured in CH_2Cl_2.

1.3.2 Intramolecular cyclization reactions

Intermolecular heteroannulation reactions, particularly those catalyzed by transition metals, have the decided benefit of extremely varied substrate scopes and in many cases enantioselectivity. However, in terms of published methods, intramolecular cyclization reactions to form benzo[x]azaphosphinine systems remains the most popular. Like cycloaddition reactions, these intramolecular cyclizations are generally transition-metal free. Besides this, lack of reliance on an added alkyne allows for different substitutions made directly on the PN-heterocycle such as *O*- and *N*-substitutions, as well as fusion to larger conjugated systems. In 1966, a very early example of an azaphosphinine synthesis from Shavel and coworkers was the intramolecular Bischler-Napieralski cyclization of indole derivative **54** via dichloro intermediate **55**, ultimately furnishing 1,2-dihydro-1,2λ^5-azaphosphinine 2-oxide **56** (Scheme 1.23).[63] Due to the time period, there is little analytical data for **56**, but it is one of the earliest examples of a PN-heterocycle prepared by an intramolecular route.

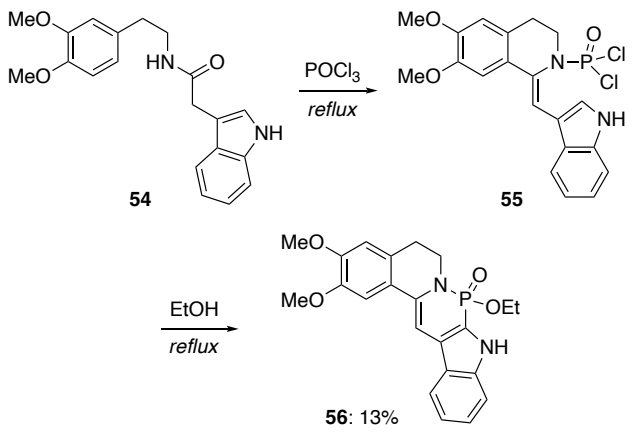

Scheme 1.23 Synthesis of indole-fused azaphosphinine 2-oxide **56**.

Twenty years later, Bourdieu and Foucaud reported in 1986 a concise synthesis to several 1,2-dihydro-1,2λ^3-azaphosphinines **57**.[33] This pathway was influenced by an earlier study from Nurtdinov et al. that prepared 2-oxo-1,2-azaphospholenes using dichlorophosphanes and *N*-butylimines.[64] In their adaption, Foucaud combined dichlorophenylphosphane with two equivalents of various alkyl imines **58** to furnish 1,2-dihydro-1,2λ^3-azaphosphinines **57** (Scheme 1.24). Several of these compounds featuring different alkyl substituents were synthesized in low to very good yields, with the corresponding azaphosphole generated as a side product. In a follow-up study the authors incorporated much larger number of *N*-alkylimines.[65] Overall, variation of chain length led to little discernable trend in the yields of the products.

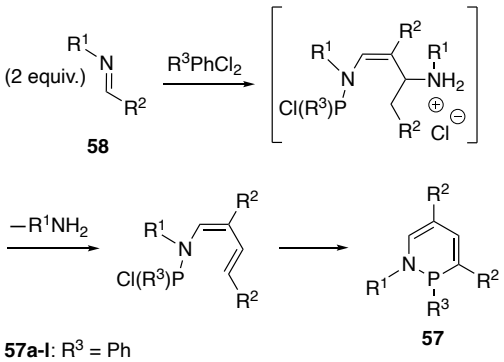

57a-l: R^3 = Ph
57a: R^1 = *t*-Bu, R^2 = Me, 64%
57b: R^1 = *i*-Bu, R^2 = Me, 5%
57c: R^1 = *t*-Oct, R^2 = Me, 70%
57d: R^1 = *i*-Pr, R^2 = Me, 42%
57e: R^1 = Bn, R^2 = Me, 25%
57f: R^1 = *n*-Bu, R^2 = Et, 6%
57g: R^1 = *t*-Bu, R^2 = Et, 60%
57h: R^1 = *i*-Bu, R^2 = Et, 8%
57i: R^1 = *t*-Bu, R^2 = *n*-Pr, 68%
57j: R^1 = *i*-Bu, R^2 = *n*-Pr, 10%
57k: R^1 = *t*-Bu, R^2 = *n*-Bu, 63%
57l: R^1 = *i*-Bu, R^2 = *n*-Bu, 8%
57m: R^1 = *t*-Bu, R^2 = Me, R^3 = Bn, *n.y.r.*
57n: R^1 = *t*-Bu, R^2 = Me, R^3 = OMe, *n.y.r.*

Scheme 1.24 Proposed pathway to 1,2-dihydro-1,2λ^3-azaphosphinines **57**. No yield reported (*n.y.r.*)

Bourdieu and Foucaud also performed several experiments with alternative phosphane and phosphinite reagents, namely $P(CH_2Ph)Cl_2$ and $P(OMe)Cl_2$, respectively; however, neither of the desired P^{III} heterocycles (**57m** and **57n**) were

stable enough to be isolated and instead underwent oxidation in air to furnish the corresponding P^V oxo-compounds **57m'** and **57n'** (Scheme 1.25). Compound **57n** would also hydrolyze in the presence of acid to give **57n''**. Finally, the authors also showed how the P^{III} heterocycles could be intentionally oxidized to P^V using either H_2O_2 or S_8 to form the corresponding oxide **59** or sulfide **60** (Scheme 1.26).

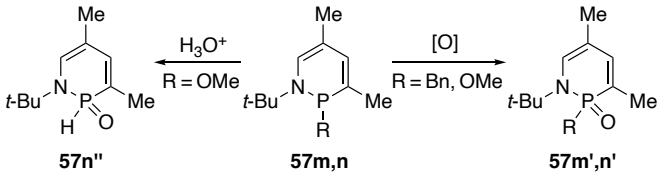

Scheme 1.25 Oxidation and hydrolysis of heterocycles **57m** and **57n**.

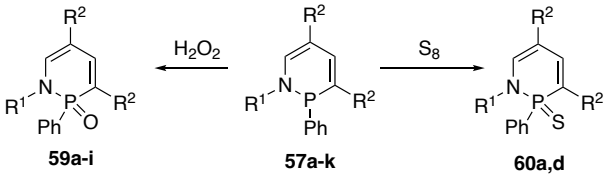

59a: R^1 = *t*-Bu, R^2 = Me, 83%
59b: R^1 = *i*-Bu, R^2 = Me, 78%
59c: R^1 = *t*-Oct, R^2 = Me, 86%
59d: R^1 = *i*-Pr, R^2 = Me, 75%
59e: R^1 = Bn, R^2 = Me, 70%
59f: R^1 = *n*-Bu, R^2 = Et, *n.y.r.*
59f: R^1 = *n*-Bu, R^2 = Et, *n.y.r.*
59g: R^1 = *t*-Bu, R^2 = Et, *n.y.r.*
59h: R^1 = *t*-Bu, R^2 = *n*-Pr, *n.y.r.*
59i: R^1 = *t*-Bu, R^2 = *n*-Bu, *n.y.r.*
60a: R^1 = *t*-Bu, R^2 = Me, 49%
60d: R^1 = *i*-Pr, R^2 = Me, 44%

Scheme 1.26 H_2O_2 and S_8 oxidations of azaphosphinines **57**.

A third paper from Bourdieu and Foucaud in 1987 rounded out the story by briefly describing a protocol for the conversion of the dihydro heterocycles to the corresponding fully conjugated azaphosphinine **61** (Scheme 1.27).[66] Pyrolysis of 1,2-dihydro-1,2λ^3-azaphosphinine **57c** at 600 °C thermolytically cleaved the substituents on both the 1 and 2 positions; however, product **61** was highly electrophilic and added a variety nucleophiles (water, isopropylamine, or methylmercaptan) across the reactive P=N bond, affording heterocycles **62**-**64**. Interestingly, both *P*-amino **63** and *P*-thio **64**

also hydrolyzed to furnish **62** when exposed to water. No yields were reported for the reactions.

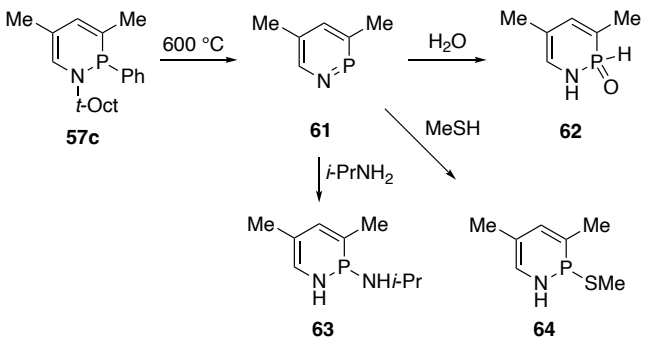

Scheme 1.27 Thermolytic synthesis of 1,2λ^3-azaphosphinine **61** and its dihydro products **62-64** from attack of various nucleophiles.

Also in 1987, Barluenga et al. published their work on the first example of benzo[*e*]-1,4-dihydro-4-oxo-1,2λ^5-azaphosphinines, which was achieved via intramolecular cyclization of *N*-aryl phosphazene (Scheme 1.28).[67] These imides were prepared via Staudinger reaction of methyl *o*-azidobenzoate **65** with various alkyldiphenylphosphanes. The phosphazenes were then cyclized with KH under mild temperatures to furnish the final heterocycles **66**. The authors found that the benzo[*e*]azaphosphinine resulting from a *P*-methylphosphazene was unstable and could not be isolated. Similar to previously discussed early works, this brief publication provides little-to-no subsequent analysis of the new compounds besides NMR chemical shifts. Despite that, the Barluenga study proved to be a key publication that opened the door for several additional reports to further develop the scaffold.

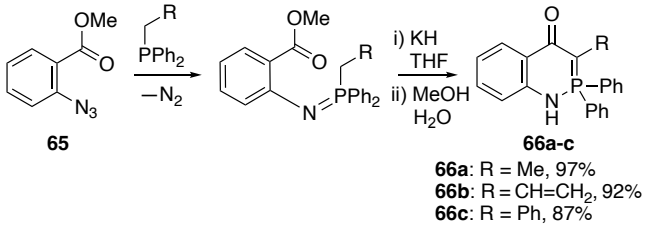

Scheme 1.28 Synthesis of benzo[*e*]-1,4-dihydro-1,2λ^5-azaphosphinines **66**.

In 1991, Bedel and Foucaud published the oxidation of their previously prepared 1,2-dihydro-1,2λ^3-azaphosphinines from P^{III} to P^V,[68] building upon the knowledge gained from their thermolysis of these heterocycles.[66] Methylation of azaphosphinines **57** generated *P*-methyl phosphonium salts **67**, which afforded **68** after thermolysis at 210-230 °C (Scheme 1.29). This system was deprotonated under mildly basic conditions to furnish 1,2λ^5-azaphosphinines **69** in good-to-excellent yields. Upon exposure to air and/or water, the azaphosphinines slowly decomposed to give one equivalent of formamide and the corresponding phosphane oxide **70**.

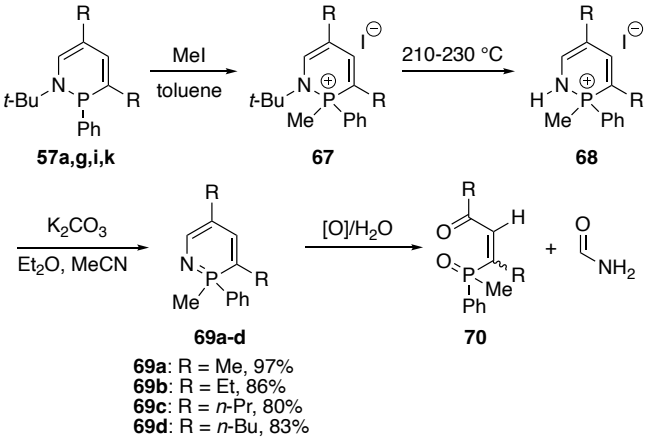

Scheme 1.29 Synthesis of 1,2λ^3-azaphosphinine **69** and subsequent hydrolysis/oxidation.

Fluck et al. published an entirely novel approach to the synthesis of 1,2λ^5-azaphosphinines in 1995, exploring the reactions between isothiocyanates **71** and

1,1,3,3-tetrakis(dimethylamino)-1λ^5,3λ^5-diphosphete **72** (Scheme 1.30).[69] Depending on the molar ratio of starting materials used, exotic azaphosphinine derivatives **73** are furnished. Despite not having an apparent application, this synthesis stands as a unique example of reactivity to obtain the typical azaphosphinine core. The resultant heavily substituted 1,2λ^5-azaphosphinines are notably stable with melting points near or at 200 °C.

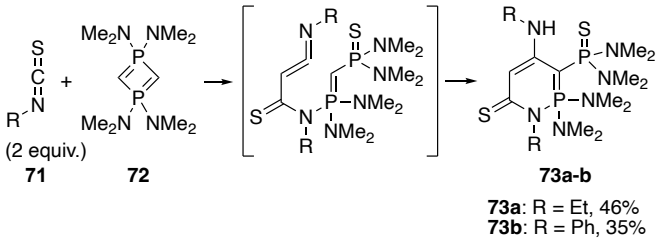

Scheme 1.30 Phosphete and isothiocyanate cyclization into azaphosphinine **73**.

The first example of benzo[*c*]-1,2-dihydro-1,2λ^5-azaphosphinine 2-oxides were published by Tang and Ding in 2006.[37] Their goal was to explore the azaphosphinine analogues of isoquinolin-1-ones, which they termed phosphaisoquinolin-1-ones. To generate these species, the authors first synthesized a library of *o*-(1-alkynyl)phenylphosphonamidate **74**. These were prepared in two steps by chlorinating the starting *o*-(1-alkynyl)phosphonic acid monoester with thionyl chloride and subsequently aminating with various primary amines. The phosphonamidates were then cyclized in a Pd-catalyzed reaction to yield **75** (Table 1.3). Because this was the first reported instance of the P^V–NH intramolecular heteroannulation, a variety of transition metals and temperatures were investigated, revealing the use of $PdCl_2(MeCN)_2$ at 80 °C as optimal. Although, the reaction times varied from entry to entry, there was little notable effect on yield resulting from the R group identities. One noted exception was

for **75k** where only 15% yield was isolated under normal optimized conditions, but the addition of a few drops of AcOH led to the dramatically improved yield of 65%. The authors proposed that this was a result of an external proton source aiding the cleavage of the vinylpalladium intermediate and regeneration of the $PdCl_2(MeCN)_2$. For these reactions only the six-membered product was generated, which is consistent with a 6-endo-dig cyclization. A potential explanation for the regioselectivity of cyclization is that the long C–P and P–N bonds would favor the transition state that leads into the six-membered product. The authors studied the antitumor properties of **75** in vitro, noting at high concentrations these species had very high inhibition ratios of A-549 lung cells in SRB (sulforhodamine B) assay; however, this inhibition fell off dramatically at lower concentrations, so further analysis is warranted.

Table 1.3 Substrate scope of cyclization of **74** to afford **75**.

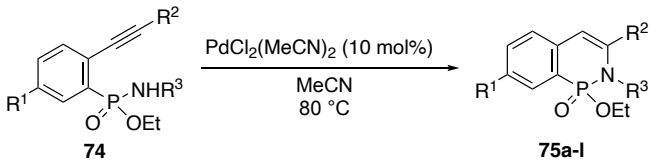

R^1	R^2	R^3	Product	Yield [%]
H	Ph	Bn	**75a**	80
H	Ph	H	**75b**	68
H	Ph	*n*-Pr	**75c**	72
H	*n*-Bu	Bn	**75d**	87
Cl	Ph	Bn	**75e**	85
Cl	Ph	*n*-Pr	**75f**	67
Cl	*n*-Bu	Bn	**75g**	85
Cl	*p*-EtC_6H_4	Bn	**75h**	72
Cl	*p*-EtC_6H_4	*n*-Pr	**75i**	70
Cl	cyclopropyl	Bn	**75j**	90
Cl	CH_2OMe	*n*-Pr	**75k**	65
OMe	Ph	Bn	**75l**	79

In 2008, Ding and coworkers published a follow-up study that now included added allyl halide **76** in stoichiometric excess.[70] This reaction yielded the same benzo[c]1,2-dihydro-1,2λ^5-azaphosphinine scaffold as previously observed but with a 4-allyl substitution leading to series **77** (Table 1.4). A screen of reaction conditions showed that with excess methyloxirane the desired product **77** was formed in very good yield, with **75** generated in small amounts. Increasing the equivalents of both methyloxirane and allyl halide improved the yield of **77** and decreased formation of **75**. The reaction is decidedly robust with a large functional group tolerance and good yields. Much like the previous entry from Ding, it appears that the electron density of the phosphonamidate starting material has little bearing on the yield of the product. This reaction also tolerates *N*-unsubstituted phosphonamidates, as is the case with **77b**. It is also worth noting that the reactivity of the system is selective for the allyl halide over the aryl halide even when both are the same (e.g., **77i-l**). The authors do note that the use of the substituted allyl chlorides (e.g., 3-chloro-1-butene) leads to an internal alkene in the final heterocycle with a consistent 77:23 distribution of *E* to *Z* isomers across all such products.

Table 1.4 Cyclization and subsequent allylation of give azaphosphinines **77**.

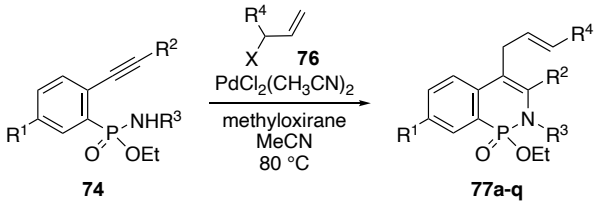

R^1	R^2	R^3	R^4	X	Product	Yield [%]
H	Ph	Bn	H	Br	**77a**	90
H	Ph	H	H	Br	**77b**	69

Cl	Ph	Bn	H	Br	**77c**	92
Cl	Ph	*n*-Pr	H	Br	**77d**	87
Cl	*p*-EtC_6H_4	Bn	H	Br	**77e**	88
Cl	*n*-Bu	Bn	H	Br	**77f**	82
OMe	Ph	Bn	H	Br	**77g**	85
H	Ph	Bn	Me	Cl	**77h**	85[a]
H	*n*-Bu	Bn	Me	Cl	**77i**	78[a]
Cl	Ph	Bn	Me	Cl	**77j**	86[a]
Cl	Ph	*n*-Pr	Me	Cl	**77k**	81[a]
Cl	*p*-EtC_6H_4	*n*-Pr	Me	Cl	**77l**	83[a]
H	Ph	Ph	H	Br	**77m**	83
Cl	Ph	Ph	H	Br	**77n**	80
OMe	Ph	Ph	H	Br	**77o**	78
H	Ph	CH_2CO_2Et	H	Br	**77p**	82
Cl	Ph	CH_2CO_2Et	H	Br	**77q**	85

[a]Products isolated as (*E*/*Z*= 77:23).

As with their previous work, the authors also tested the biological properties of nine derivatives of **77**. At a concentration of 20 μg/mL, the enzyme Src homology 2-containing phosphatase-1 (SHP-1) inhibition ratios varied from 20.2% (**77a**) to 54.3% (**77i**). The heterocycles were then tested against melanin-concentrating hormone receptor-1 (MCH-1R) with IC_{50} values varying from 3.78 (**77d**) to 10.23 μmol (**77e**). The benzo[*c*]-4-allyl-1,2-dihydro-1,2λ^5-azaphosphinine 2-oxides showed no MCH-1R activities and are reported in the publication as the first example of using phosphorus analogues of heterocyclic natural products as MCH-1R inhibitors. An in-depth screen of a variety of antagonists of MCH-1R by Wang and coworkers in 2008[71] showed that of the derivatives of **75** and **77** tested, only **75a'** (Cl on C(4)) showed significant binding affinity (K_i = 115.7 nmol/L) and potent antagonism (K_B = 23.8 nmol/L). The authors note that the benzo[*c*]-2-ethoxy-1,2λ^5-azaphosphinine 2-oxide core may prove to be a

powerful motif in MCH-1R binding in the future despite being structurally quite different from previously found MCH-1R modulators.

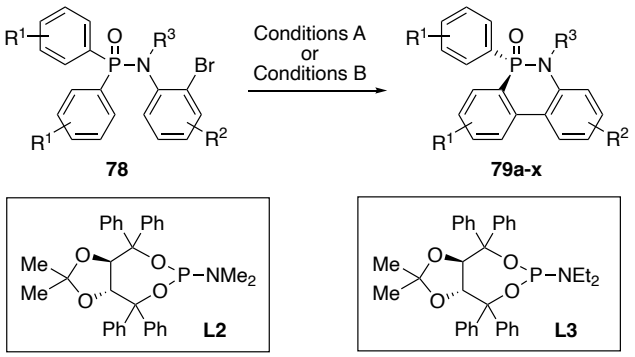

Conditions A (Duan)
79a-l: R^3 = Me
79a: R^1 = H, R^2 = H, 94%, 90% e.e.
79b: R^1 = H, R^2 = *p*-Me, 88%, 93% e.e
79c: R^1 = H, R^2 = *p*-OMe, 80%, 91% e.e
79d: R^1 = H, R^2 = *m*-F, 94%, 90% e.e
79e: R^1 = H, R^2 = *m*-CF_3, 92%, 92% e.e.
79f: R^1 = H, R^2 = *p*-Cl, 88%, 93% e.e.
79g: R^1 = *p*-OMe, R^2 = H, 88%, 89% e.e.
79h: R^1 = *p*-Cl, R^2 = H, 87%, 91% e.e.[a]
79i: R^1 = *p*-CF_3, R^2 = H, 91%, 91% e.e.[a]
79j: R^1 = *o*-Me, R^2 = H, 62%, 85% e.e.
79k: R^1 = 3,5-$(CF_3)_2$, R^2 = H, 79%, 83% e.e.
79l: R^1 = 3,5-$(CF_3)_2$, R^2 = *m*-Me, 58%, 86% e.e.
79m: R^1 = H, R^2 = H, R^3 = *p*-$OMeC_6H_4$, 81%, 91% e.e.

Conditions B (Ma)
79b: R^1 = H, R^2 = *p*-Me, 99%, 95% e.e.
79d: R^1 = H, R^2 = *m*-F, 99%, 95% e.e.
79e: R^1 = H, R^2 = *m*-CF_3, 99%, 95% e.e.
79f: R^1 = H, R^2 = *p*-Cl, 98%, 95% e.e.
79n-u: R^1 = H
79n: R^2 = H, R^3 = Et, 94%, 89% e.e.
79o: R^2 = H, R^3 = *n*-Bu, 61%, 88% e.e.
79p: R^2 = *m*-Me, R^3 = Me, 72%, 92% e.e.
79q: R^2 = *p*-*t*-Bu, R^3 = Me, 99%, 97% e.e.
79r: R^2 = *p*-Ph, R^3 = Me, 68%, 93% e.e.
79s: R^2 = *p*-CN, R^3 = Me, 64%, 96% e.e.
79t: R^2 = *p*-CF_3, R^3 = Me, 83%, 96% e.e.
79u: R^2 = H, R^3 = Bn, 12%, 92% e.e.
79v: R^1 = *p*-Ph, R^2 = H, R^3 = Me, 90%, 95% e.e.
79w: R^1 = *p*-Me, R^2 = H, R^3 = Me, 92%, 96% e.e.
79x: R^1 = *m*-OMe, R^2 = H, R^3 = Me, 54%, 91% e.e.

Scheme 1.31 Palladium catalyzed C–H activated heteroannulation to furnish chiral azaphosphinines **79**. Conditions A: $Pd(OAc)_2$ (5 mol%), **L2** (10 mol%), K_3PO_4 (1.5 equiv.), PivOH (30 mol%), toluene, 80 °C. Conditions B: $Pd(dba)_2$ (8 mol%), **L3** (10 mol%), Cs_2CO_3 (1.5 equiv.), PivOH, (40 mol%), hexanes, 60 °C. [a]Reaction performed at room temperature.

In 2015, Duan and coworkers and Ma and coworkers kicked off what would become a period of great activity for azaphosphinine chemistry.[72,73] The two groups submitted

and published their papers within a week of one another and the content of both is very similar, with some identical derivatives being prepared. These works were conceptual continuations of the studies of not only Lee[57] and Cramer[38,58] but also the very early systems from Dewar[47] and Campbell,[49] with the aim being the generation of chiral, dibenzo[*c*,*e*]1,2-dihydro-1,2λ^5-azaphosphinine 2-oxide species via transition-metal catalyzed C–H activation. Starting from achiral phosphinamide **78** (Scheme 1.31), one of the identical *P*-aryl substituents would be converted to a biphenyl derivative, generating a stereogenic phosphorus center. Interestingly, the two groups of authors screened the same exact pool of chiral phosphorus ligands and decided upon a ligand that only differed in chain length of the dialkylamino group. Whereas Duan used *N,N*-dimethyl ligand **L2**, Ma chose *N,N*-diethyl ligand **L3** and that their choices likely arise from the different reaction conditions, i.e., Conditions A (Duan) vs. Conditions B (Ma) in Scheme 31. Cyclization of a variety of achiral phosphinamide **78** furnished the corresponding dibenzo[*c*,*e*]1,2-dihydro-1,2λ^5-azaphosphinine **79** with both reactions showing excellent yields across the substrates studied. While the results suggest the conditions of Duan and coworkers were more consistent, Ma and coworkers used a wider substrate scope particularly in terms of *N*-substituents. Heterocycles **79b**, **79d**, **79e**, and **79f** were synthesized by both groups with Conditions B performing slightly better in the identical transformation.

Duan and coworkers also explored the generation of chiral phosphane oxides **80** from the P–N bond cleavage of **79** using MeLi, *i*-PrLi, and *t*-BuLi (Scheme 1.32). The former two yielded nearly racemic mixtures of the alkyl addition product, whereas the *t*-BuLi reaction resulted in a complex mixture of products that was not identified. This is a convenient route to chiral phosphane oxides that may find further use in catalysis.

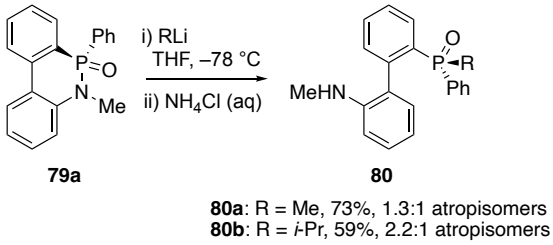

Scheme 1.32 P–N bond cleavage to furnish chiral phosphane oxides **80**.

In early 2017, Yang and coworkers published their work on the transition-metal free *P*-stereogenic dibenzo[*c,e*]-1,2-dihydro-1,2λ^5-azaphosphinine derivatives **81** (Scheme 1.33).[74] In the aim of making the cyclization more economical, the authors decided to investigate the potential for transition-metal free oxidative C–H activation instead. An added benefit of this system would be stability under ambient atmosphere. After screening a variety of oxidants, the authors settled on hypervalent iodine species $PhI(OAc)_2$ with added I_2 in MeCN at 80 °C as the optimal conditions, which were applied to a library of phosphinamides **82** with various aryl and *N*-alkyl functional groups, giving the dibenzo[*c,e*]-8-iodo-1,2λ^5-azaphosphinine 2-oxides **81**. They found that the reaction proceeded better with less sterically demanding *N*-substituents, but having any *N*-alkyl group (46–78% yield) worked better than a hydrogen (20% yield). Electron-withdrawing R-groups (e.g., tosyl or pentafluorobenzene) resulted in C–H hydroxylation and instead gave **83** as product in moderate yields. In every case, excellent diastereoselectivities for the *P*-stereogenic center and the axial chirality of the aryl linking unit were obtained for **81** and **83**. It was also observed that substitution of KBr for I_2 in the reaction furnished the corresponding 5'-bromo heterocycle but did not work with NaCl to yield the corresponding 5'-chloro species.

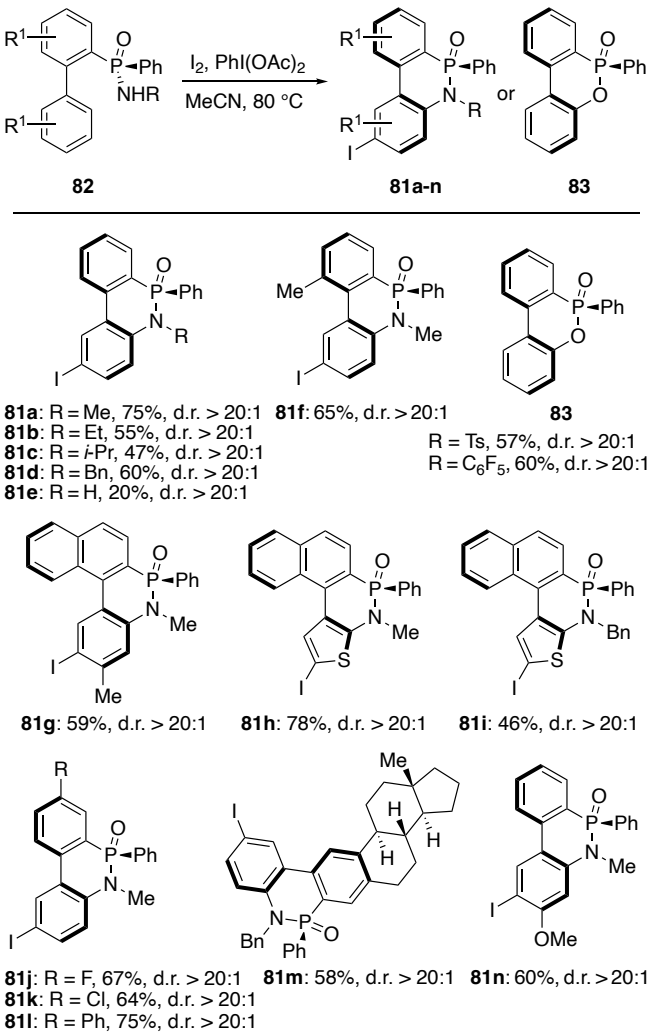

Scheme 1.33 Transition-metal free heteroannulation reaction to give azaphosphinines **81**.

To probe the mechanism of their hypervalent iodine-mediated heteroannulation, Yang and coworkers attempted the reaction in the presence of radical scavengers 2,2,6,6-tetramethylpiperidin-1-yl)oxyl (TEMPO) and butylated hydroxytoluene (BHT). The addition of either inhibited the reaction. Next, a noniodinated analogue **84** was reacted with $PhI(OAc)_2$ and I_2 under standard conditions and the corresponding product **81a** was isolated. This led the researchers to conclude that the iodination step occurs after the annulation. Their proposed radical mechanism for the transformation is shown in Scheme 1.34. The reaction is initiated by the homolytic cleavage of a weak N–I bond to generate a radical species, which is subsequently trapped by the nearby

arene. This is rearomatized via $PhI(OAc)_2$ to give electron-rich **84**, which can rapidly iodinate to furnish the final heterocycle **81a**.

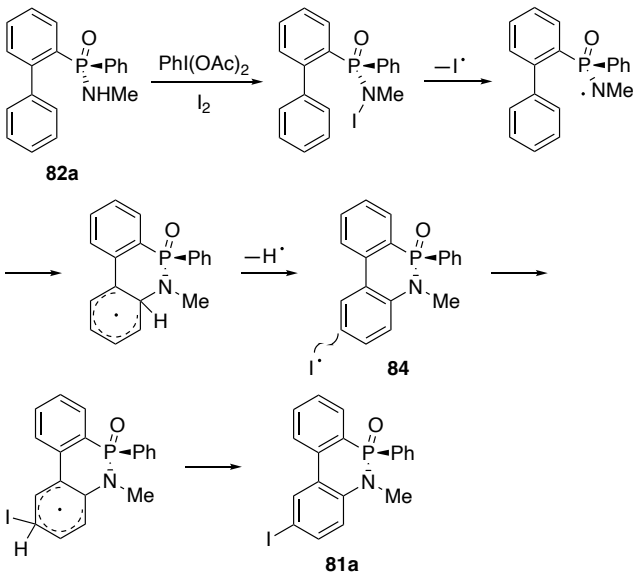

Scheme 1.34 Proposed mechanism for radical C–H activation heteroannulation and subsequent iodination.

Yang and coworkers showed that the aryl iodide generated during the heteroannulation could undergo typical cross-coupling reactions, providing examples of **81a** acting as a substrate in Heck, Suzuki-Miyaura, azidation, phosphination, and Cu(I)-catalyzed azide-alkyne cycloaddition (CuAAC) 'click' reactions in moderate to excellent yields and the typical high degree of diastereoselectivity. Finally, to prove the existence of the axial chirality component in their system, the P–N bond of **85** was selectively cleaved via addition of *n*-BuLi at –78 °C (Scheme 1.35). Once the rigidity of the aryl system was severed, racemization began, but at low temperatures the diastereomers **86** and **86'** were still detected, indicating axial chirality was preserved with a persistent *P*-stereogenic center. It was proposed that the inflexibility of the fully cyclized heterocycle retains the axial chirality under ambient conditions.

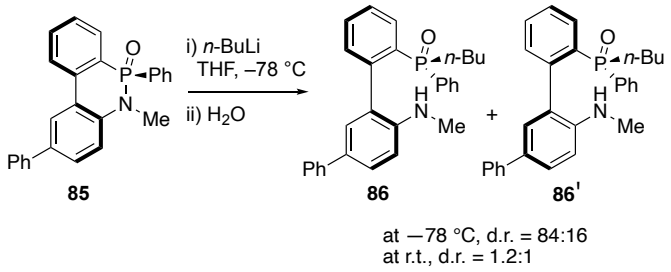

Scheme 1.35 Cleavage of P–N bond and racemization at different temperatures.

Han and coworkers published in 2017 a study that took a somewhat different approach to the dibenzo[*c,e*]-1,2-dihydro-1,2λ^5-azaphosphinine 2-oxide core.[75] As noted previously, the heteroannulation developed by Yang and coworkers did not tolerate electron-deficient *N*-protecting groups, the use of which resulted in oxygen substitution into the heterocycle. The authors proposed this lack of desired reactivity to be a result of difficulty in generating the necessary nitrogen radical. The Han study focused exclusively on the heteroannulation of *P*-stereogenic phosphinamide **87** with a strongly electron-deficient *N*-pentafluorophenyl group (Scheme 1.36). To circumvent the issues found by Yang, the authors found an alternative method of radical oxidative heteroannulation using 2.2 equivalents of $Ce(NH_4)_2(NO_3)_6$ (CAN) at 40 °C to generate the desired heterocycles **88** in excellent yield with high enantiomeric excess, with several examples being prepared on the gram scale. At increased temperature and additional equivalents of CAN, they could also generate a nitrated analogue **89**, much in the same way Yang and coworkers iodinated their molecules. Both electron-rich and electron-deficient substituents were tolerated in the R^1 position; however, incorporating an electron-donating methoxy group into the R^2 position resulted in a high yield of the nitrated byproduct. This side reaction could be inhibited by addition of 10 equivalents of water to the reaction.

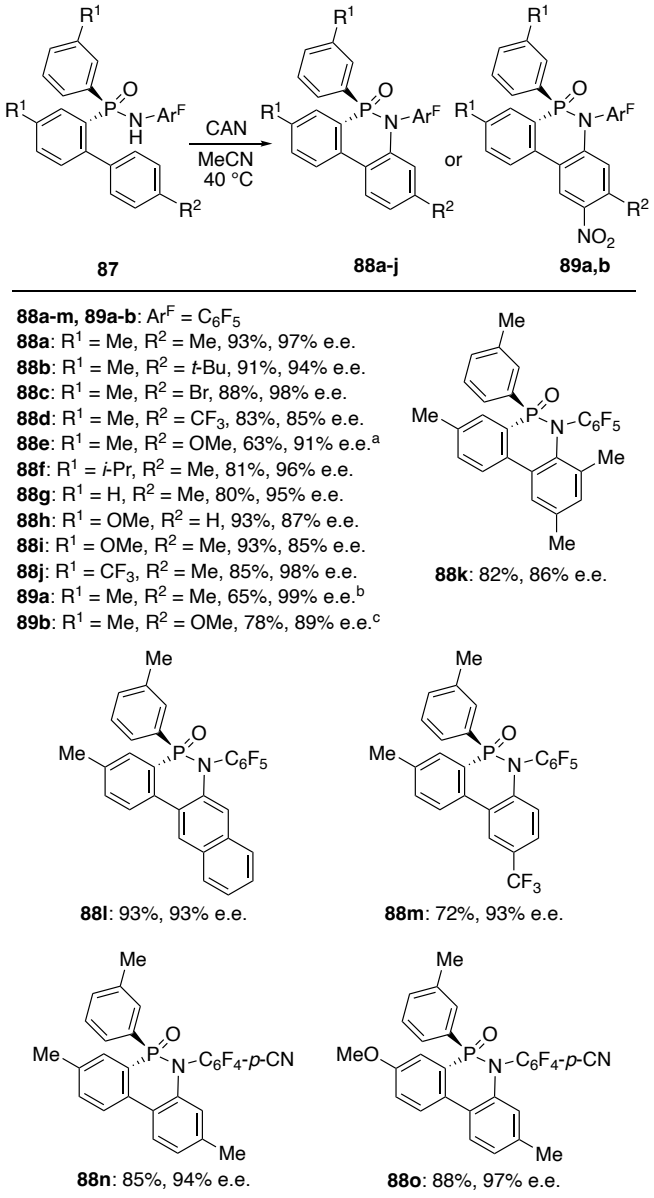

Scheme 1.36 CAN-mediated heteroannulation to afford **88**. [a]10 equiv. of water added. [b]5 equiv. of CAN added and conducted at 60 °C. [c]Run for 2 h.

Further experiments were conducted examining the post-synthetic modifications available to the azaphosphinine core. In the interest of making *P*-stereogenic bidentate ligands (**90, 91**) for asymmetric catalysis, the P–N bond of **88a** could be cleaved by either LiMe or NaOMe (Scheme 1.37). Alternatively, conversion of **88a** to the sulfide **92** followed by treatment with MeOTf and then finally $P(NMe_2)_3$ gave the

corresponding dibenzo[*c,e*]-1,2-dihydro-1,2λ^3-azaphosphinine, namely the P^{III} species **93**, in high overall yield.

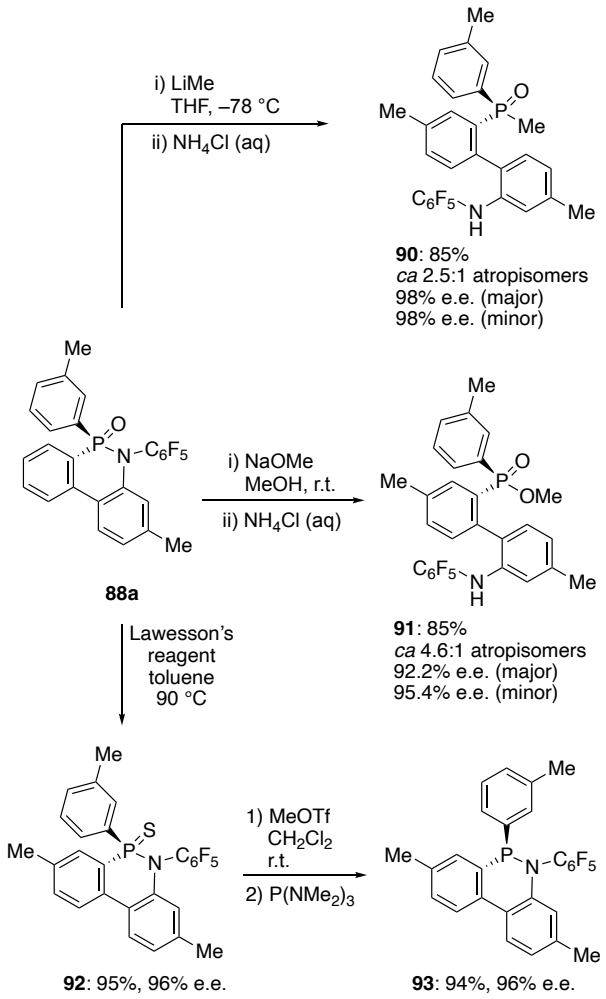

Scheme 1.37 Post-synthetic modification of **88a** to furnish chiral acyclic species **90** and **91**, and P^{III} species **93**.

Heterocycle **88a** could be used as a chiral LB catalyst in the condensation of enone **94** and benzaldehyde to furnish **95** (Scheme 1.38), similar to the reaction effected by Cramer in Scheme 16.[38] While the reaction proceeded in excellent yield, the diastereoselectivity and enantioselectivity were considerably lower than what was previously reported. Regardless, these experimental results in concert with those of

Cramer heavily suggest such *P*-stereogenic species could find excellent application in asymmetric catalysis upon proper optimization.

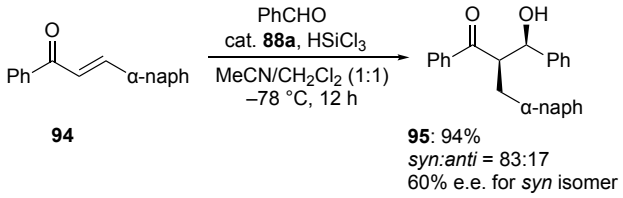

94

95: 94%
syn:anti = 83:17
60% e.e. for *syn* isomer

Scheme 1.38 Asymmetric catalyst **88a** used in condensation reaction.

In 2015, our lab published the first of over a dozen research articles on benzo[*e*]-1,2λ^5-azaphosphinines, benzo[*e*]-1,2-dihydro-1,2λ^5-azaphosphinine 2-oxides, and related fused systems. The team had been studying arylethynyl scaffolds as anion receptors when they serendipitously discovered[76] that *ortho*-ethynylanilines react with $P(OPh)_3$ in the presence of pyridine at elevated temperatures to affect a heteroannulation incorporating an equivalent of the phosphite (Table 1.5). This was an attractive discovery as it proved to be a robust and comparatively mild route to the benzo[*e*]-1,2λ^5-azaphosphinine core without the use of transition metals. The aniline starting materials **96** were also quite easy to diversify, with most being either commercially available or the products of one- or two-step Sonogashira cross-couplings. The direct result of the cyclization was the *P*-diphenoxy species **97**; however, these in general rapidly hydrolyzed to the corresponding dihydro molecules **98** either intentionally or during purification, depending on the derivative.

Table 1.5 Phosphite cyclization of *ortho*-ethynylanilines.

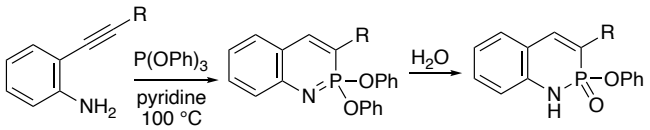

96 **97a-j** **98a-j**

R	Product	Yield **97** (%)	Yield **98** (%)
3,5-$(CF_3)_2C_6H_3$	**a**	—[a]	39
p-CNC_6H_4	**b**	54	79
p-$(CO_2Et)C_6H_4$	**c**	54	74
p-ClC_6H_4	**d**	—[a]	80
Ph	**e**	45	72
p-MeC_6H_4	**f**	63	82
p-$OMeC_6H_4$	**g**	56	66
p-$(NMe_2)C_6H_4$	**h**	68	—[a]
n-Pen	**i**	—[a]	73
2-pyridyl	**j**	71	31

[a]Not isolated.

Both azaphosphinines **97** and **98** display notable photophysical properties (Table 1.6). The authors comment that the emissive behavior is like that of the analogous carbostyril scaffold, with the key differences being an overall redder emission, stronger solvatochromism, and more acidic N–H bond. Deprotonating **98** with DBU resulted in a strong bathochromic shift in emission of 22–124 nm. Following this initial publication, several more papers were published on the benzo[*e*]-fused scaffolds,[77–83] work that was summarized in an account in 2020.[39]

Table 1.6 Fluorescence properties of selected **97**, **98**, and deprotonated **98** in $CHCl_3$.

Cmpd	**97** λ_{em} (nm), Stokes shift (nm)	**98** λ_{em} (nm), Stokes shift (nm)	**98** + DBU λ_{em} (nm), Stokes shift (nm)
b	483, 83	430, 81, 4%[a]	554, 137, 41%[a]

c	473, 90	432, 81, 5%[a]	553, 151, 31%[a]
e	453, 80	418, 76	491, 127
f	450, 81	413, 72	482, 114
g	447, 78	410, 71	473, 107
j	467, 79	442, 79	514, 102

[a] Photoluminescent quantum yield; other molecules not measured.

The emissive data in Table 6 suggested that the photophysical properties of the resultant heterocycles are highly dependent on the electronic properties of the R-group. Knowing this, we broadened the substrate scope to include species with the group R^2 located para to the aniline nitrogen **99**, in turn yielding the more substituted series **100** (Scheme 1.39).[83] This facilitated a second handle with which to tune absorption and emission. It should be noted for nearly all subsequent studies that the pre-hydrolysis diphenoxy 'imidate' form **97** was not isolated, but rather all yields reflect both the cyclization and hydrolysis steps. There is no recognizable preference between R-groups in the yields, as both electron-rich and -deficient substituents result in modest to good yields (26–61%).

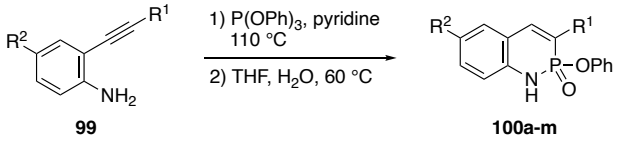

99 **100a-m**

100a: R^1 = *p*-CNC_6H_4, R^2 = CN, 26%
100b: R^1 = *p*-CNC_6H_4, R^2 = CF_3, 61%
100c: R^1 = *p*-CNC_6H_4, R^2 = Cl, 44%
100d: R^1 = *p*-CNC_6H_4, R^2 = *t*-Bu, 36%
100e: R^1 = *p*-$OMeC_6H_4$, R^2 = *t*-Bu, 44%
100f: R^1 = *p*-MeC_6H_4, R^2 = *t*-Bu, 50%
100g: R^1 = Ph, R^2 = *t*-Bu, 56%
100h: R^1 = 3,4-$(CN)_2C_6H_3$, R^2 = *t*-Bu, 34%
100i: R^1 = *p*-ClC_6H_4, R^2 = *t*-Bu, 60%
100j: R^1 = Ph, R^2 = CN, 42%
100k: R^1 = *p*-$OMeC_6H_4$, R^2 = CN, 30%
100l: R^1 = Ph, R^2 = CO_2Et, 55%
100m: R^1 = *p*-CNC_6H_4, R^2 = OEt, 54%

Scheme 1.39 Difunctionalized azaphosphinines **100**.

Compared to the series **98**, the addition of the second R-group added a new dimension to the understanding of how the electronic groups modulate the photophysics (Table 1.7), as donor and acceptor pairs typically resulted in redder absorption and emission. This effect was more prominent when the electron-withdrawing group was in the R^1-position and the electron-donating group was at R^2 (e.g., **100k** vs. **100m**).

Table 1.7 Photophysical properties of selected **100**.[a]

Cmpd	R^1	R^2	λ_{abs} (nm), ε (M^{-1} cm^{-1})	λ_{em} (nm), φ (%)[b]	Stokes shift (nm/cm^{-1})	Brightness (ε•φ)
100a	*p*-CNC_6H_4	CN	346, 12000	430, 18	84/5600	2160
100e	*p*-$OMeC_6H_4$	*t*-Bu	344, 16000	421, 6	77/5300	960
100f	*p*-MeC_6H_4	*t*-Bu	343, 14000	424, 8	81/5600	1120
100k	*p*-$OMeC_6H_4$	CN	345, 15000	471, 28	126/7800	4200
100m	*p*-CNC_6H_4	Oet	379, 25000	490, 24	111/6000	6000

[a]All values collected in $CHCl_3$ at room temperature. [b]Excited at 365 nm and collected using quinine sulfate (0.1 M H_2SO_4) standard.

Given the sensitivity of the photophysical properties to simple functional group substitutions, we next investigated the effect of arene backbone extension as well. These included heterocycles featuring pyreno[2,1-*e*]- **101**, naphtho[1,2-*e*]- **102**, naphtho[2,1-*e*]- **103**, and naphtho[2,3-*e*]- **104** fusion patterns (Scheme 1.40).[39,78–81]

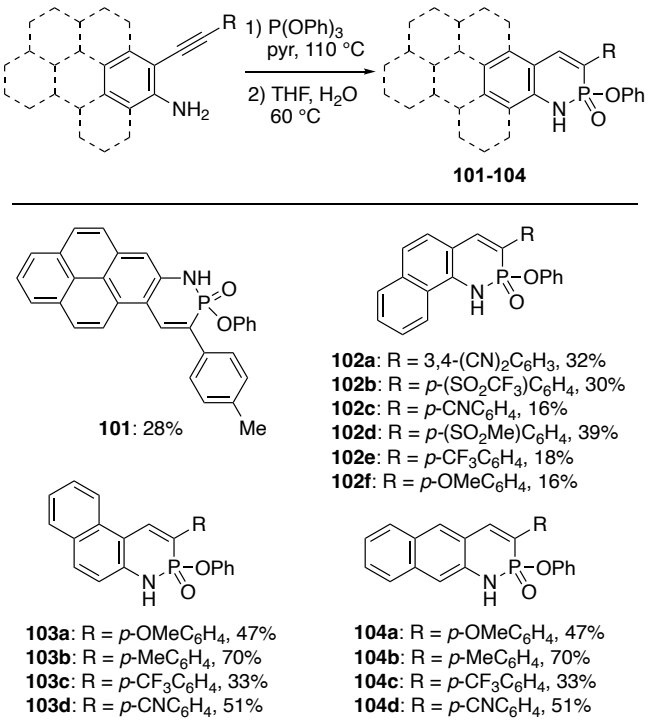

Scheme 1.40 Scope of arene-core extended azaphosphinines.

While simple modification of the aniline starting material could dramatically alter the final azaphosphinine topology, this did beg the question as to what impact, if any, would arise from alteration of the phosphorus substituent. By substituting $PhP(OPh)_2$ for $P(OPh)_3$, running the cyclization under the same conditions generated the analogous benzo[*e*]-1,2-dihydro-2-phenyl-1,2λ^5-azaphosphinine 2-oxides **105** (Scheme 1.41).[77]

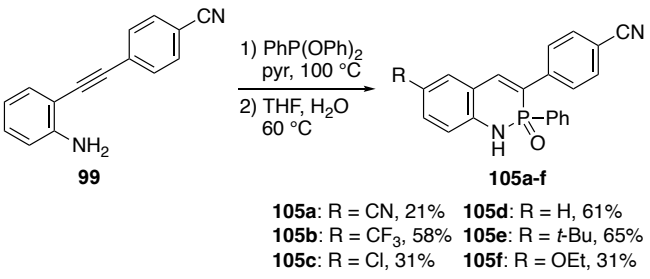

Scheme 1.41 *P*-phenyl substitution to afford azaphosphinines **105**.

In addition to P substitution, we explored the inclusion of the N atom in another ring to furnish heterocycles **106** (Scheme 1.42).[79] Ethynylpyrene **107**, the precursor of **101**, was cyclized using $PhP(OPh)_2$. The crude mixture was hydrolyzed and then iodinated under acidic conditions to give **108**, a *P*-phenyl analogue to **101**. Finally, Sonogashira cross-coupling followed by intramolecular cyclization of the alkyne with the NH group afforded π-extended and rigid **106** in good yields (63–87%).

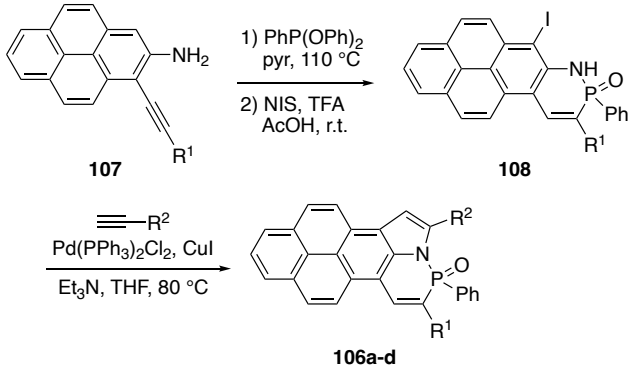

107 **108**

106a-d

106a: R^1 = *n*-Bu, R^2 = Ph, 87%
106b: R^1 = *n*-Bu, R^2 = *p*-$(NPh_2)C_6H_4$, 63%
106c: R^1 =. 3,5-$(CF_3)_2C_6H_3$, R^2 = Ph, 81%
106d: R^1 = 3,5-$(CF_3)_2C_6H_3$, R^2 = *p*-$(Ph_2N)C_6H_4$, 67%

Scheme 1.42 *P*-phenyl substituted PN-fused pyrenes **106**.

Comparison of the photophysical properties of the extended fused-arene core heterocycles (**101**–**104**) and the *P*-phenyl heterocycles **105** and **106** (Table 1.8) with those of **100** showed that the different families cover a wide range of values in all tabulated categories. As a result of the large linearly fused core, the naphtho[2,3-*e*]-fused **104** exhibit comparatively large absorption coefficients and red-shifted emissions; however, they also display quite low quantum yields, and as a result, possess consistently low brightness values. The two isomeric families of **102** and **103** display predictably similar absorption, emission, and Stokes shift values but deviate in terms of quantum yield. The 'bent-down' naphtho[1,2-*e*]-fused **102** family overall has a

comparably high quantum yield with **102a** standing out dramatically at 93%. Conversely, the 'bent-up' naphtho[2,1-*e*]-fused **103** have significantly diminished quantum yield values that are comparable to the benzo-fused analogues **100**. Lastly, the *P*-phenyl derivatives **105** across the board are improvements over their *P*-phenoxy counterparts **100**. It is proposed that the enhancement of their quantum yield and Stokes shift, as well as the overall red-shifting of emission, are all a result of the rigidification/reduced degrees of freedom of the scaffold and increased planarity of the aryl rings.

Table 1.8 Photophysical properties of selected heterocycles **101**–**106**[a]

Cmpd	λ_{abs} (nm), ε (M^{-1} cm^{-1})	λ_{em} (nm), φ (%)[b]	Stokes shift (nm/cm^{-1})	Brightness (ε•φ)
101	395, 26000	465, 70	70/3800	18000
102a	404, 12000	493, 93	89/4500	11000
102b	397, 5200	490, 80	93/4800	4100
103a	384, 13000	461, 12	77/4300	1600
103b	375, 9800	450, 10	75/4400	980
104a	339, 27000	464, 7	125/7900	1900
105a	348, 15000	447, 76	99/6400	11400
106b	431, 32000	551, 62	120/5100	20000
106d	437, 42000	622, 23	185/6800	9700

[a][Values collected in $CHCl_3$ at room temperature. [b]Excited at 365 nm and collected using a quinine sulfate (in 0.1 M H_2SO_4) standard.

The pyreno[2,1-*e*]- heterocycle **101** enjoys both a large quantum yield and absorption coefficient, resulting in one of the highest brightnesses of the data set. Despite this, the small Stokes shift value presents a potential issue with self-quenching and could be modulated with further functional group tuning, i.e., the **106** series. Among the azaphosphinines synthesized from our lab, compounds **106** stand in a league of their own for photophysical properties. While all of them exhibit comparatively high brightness and quantum yields, **106a** and **106d** exhibit the highest brightness value and most red-shifted emission tabulated, respectively. Fascinatingly, it was found that there was little-to-no charge transfer between excited pyrene units in mixtures of **106**, and the authors were able to show near-perfect solution-state white light emission in a mixture of **106a**, **106b**, and **106d**.[79]

One of the unique benefits of the heteroannulation reaction studied by our lab is the hydrogen-bond donating N–H motif resulting from the hydrolysis. Up until this point, nearly all azaphosphinine systems discussed contain either *N*-alkyl or *N*-aryl groups (e.g., **43**, **57**) or are sp^2 nitrogen centers with no possible proton (e.g., **49**, **97**). As previously noted, **98** can be deprotonated to dramatic effect in terms of heterocycle emission. However, we also performed extensive studies in using that site as a hydrogen-bond donor as generally the molecules form homodimers that are oriented in a head-to-tail fashion (Figure 1.5), as the highly polarized phosphonyl acts as hydrogen bond acceptor to complement the N–H bond donor.

With exception of the **104** and **106**, we have assessed all their azaphosphinines for homodimerization strength (K_{dim}). The experiments are conducted via variable concentration (VC) ^{1}H and ^{31}P NMR experiments in water-saturated $CDCl_3$ at room temperature (Table 1.9). From the compiled data, it is noted that electron-deficient ring systems result in a higher dimerization constant (e.g., **100j**), as the N–H bond is being

further polarized, which in turn generates a stronger hydrogen bond donor. For series **100**, the identity of the R^2 group on the fused benzene core has a greater impact than the identity of the R^1 aryl substituent, which is thought to be a result of closer proximity to the hydrogen-bonding face. Lastly, the *P*-phenyl derivatives **105** consistently show lower dimerization values compared to their *P*-phenoxy **100** counterparts due to greater steric repulsion from proximity of the Ph group at the hydrogen-bonding face. Interestingly, X-ray crystallographic analysis of several dimers in the solid state mirror the solution data—those with the largest K_{dim} values exhibit the shortest intermolecular N•••O distances (e.g., 2.768(2) Å for **100j**), and those with small K_{dim} values exhibit the longest N•••O distances (e.g., 2.856(11) Å for **98g**) (Figure 1.5).[83] In the solid state, nearly every heterocycle dimerizes as the *meso*-dimer with one *R*- and one *S*-enantiomer, although a few solid-state structures possess a polymeric zigzag ribbon structure (e.g., **100b**), likely due to steric issues within the structure.

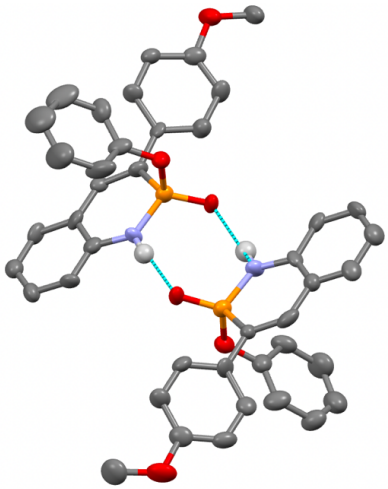

Figure 1.5 Representative *meso*-dimer of **98g**. Blue dashed lines represent hydrogen bonds between phosphonamidate moieties. Nonparticipating hydrogen atoms omitted for clarity.

Table 1.9 VC ^{1}H and ^{31}P NMR–measured dimerization constant for select azaphosphinines.

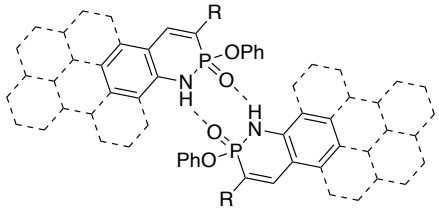

Heterocycle	K_{dim} (M^{-1}) [a]	Heterocycle	K_{dim} (M^{-1}) [a]
98e	62	**102b**	306
98g	56	**102e**	84
100b	293	**102f**	77
100j	525	**103a**	206
100l	200	**103b**	150
101	179	**105b**	82

[a]Values collected at room temperature in water saturated $CDCl_3$.

In 2020, our lab outlined a protocol for the thionation of the benzo[*e*]-fused systems using Lawesson's reagent (Scheme 1.43).[84] The reaction was conducted on both *P*-phenoxy **100** and *P*-phenyl **105**. Comparison of the photophysical properties of the thionated heterocycles **109** to the previously synthesized oxo-analogues (Table 1.10) showed that there was no apparent change to the absorption profiles upon thionation; however, it was noted that there was a substantial reduction in brightness values and a consistent ~20 nm redshift of emission, which was attributed to a lower S_1 excited state level resulting from the weaker P–S bond.

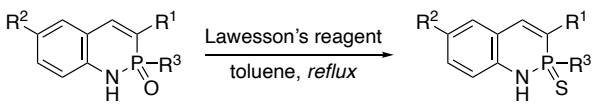

100, 105 **109a-f**

109a: R^1 = *p*-MeC_6H_4, R^2 = *t*-Bu, R^3 = OPh, 27%
109b: R^1 = *p*-CNC_6H_4, R^2 = H, R^3 = OPh, 60%
109c: R^1 = *p*-CNC_6H_4, R^2 = *t*-Bu, R^3 = OPh, 60%
109d: R^1 = *p*-CNC_6H_4, R^2 = H, R^3 = Ph, 59%
109e: R^1 = *p*-CNC_6H_4, R^2 = *t*-Bu, R^3 = Ph, 89%
109f: R^1 = *p*-CNC_6H_4, R^2 = CF_3, R^3 = Ph, 59%

Scheme 1.43 Lawesson's reagent-mediated thionation.

Table 1.10 Photophysical properties of selected **109**.[a]

Cmpd	λ_{abs} (nm), ε (M^{-1} cm^{-1})	λ_{em} (nm), φ (%)[b]	Stokes shift (nm/cm^{-1})	Brightness (ε•φ)
109a	348, 7180	444, 2	96, 6200	140
109b	352, 8600	462, 6	110, 6800	520
109e	373, 7950	492, 8	119, 6500	640
109f	357, 6840	466, 2	109, 6600	140

[a[Values collected in $CHCl_3$ at room temperature. [b]Excited at 365 nm and collected using a quinine sulfate (in 0.1 M H_2SO_4) standard.

Later entries on azaphosphinine chemistry from our lab focused primarily on the introduction of a second nitrogen atom in the fused ring. The pyrido[*e*]-1,2-dihydro-1,2λ^5-azaphosphinine 2-oxides were synthesized in a similar manner using aminopyridine substrates **110** in place of anilines (Scheme 1.44). The first of these reports focused on a family of pyrido[2,3-*e*]- fused heterocycles **111** that displayed unexpected tautomerization capabilities,[85] as X-ray crystallography revealed that **111a-d** underwent a prototropic tautomerization in the solid-state to assume the corresponding non-aromatic form **111'**. Only fluorinated **111e** did not undergo tautomerization in the solid state, which was attributed to the diminished basicity of the pyridyl nitrogen. Because of the regioselectivity of the alkylation from **111** to **112**, the quinoidal orientation of the core could be trapped, leading to stable samples that could be further analyzed in solution. A combination of photophysical, computational, and NMR experiments revealed that the tautomer only existed in the solid state, leading the authors to conclude that the heterocycles remained in their aromatic form in solution,

regardless of environment, and tautomerized as a packing effect. Greater intermolecular forces resulting from solidification promoted the tautomerization to **111'** to allow the heterocycles to arrange in long coordination polymer-like chain of head-to-tail self-association. Computed relative free energies indicated that there is a 6.3 kcal mol^{-1} stabilizing effect for the observed tautomerization when the azaphosphinines is protonated, indicating how a close-knit hydrogen-bonding network may shift the tautomeric preference.

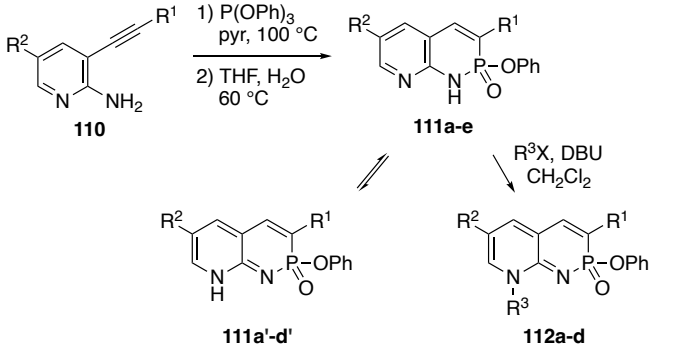

111a-d, 112a-d: R^2 = H
111a: R^1 = *p*-MeC_6H_4, 38%
111b: R^1 = *p*-$OMeC_6H_4$, 35%
111c: R^1 = *p*-$CF_3C_6H_4$, 38%
111d: R^1 = *p*-CNC_6H_4, 39%
111e: R^1 = *p*-MeC_6H_4, R^2 = F, 29%
112a: R^1 = *p*-MeC_6H_4, R^3 = Me, 20%
112b: R^1 = *p*-$CF_3C_6H_4$, R^3 = Me, 61%
112c: R^1 = *p*-CNC_6H_4, R^3 = CH_2CH_2OH, 39%
112d: R^1 = *p*-MeC_6H_4, R^2 = F, R^3 = Me, 41%

Scheme 1.44 Pyrido-fused azaphosphinines **111** and their trapped tautomeric forms **112**.

The second publication on pyrido[*e*]1,2λ^5-azaphosphinine 2-oxides focused on cyclization of 3-aminopyridines **113** to furnish pyrido[3,4-*e*]-1,2λ^5-azaphosphinine **114** and corresponding dihydro **115** (Scheme 1.45), molecules that possessed a donor-acceptor conjugated system through the azaphosphinine scaffold.[86] By orienting the pyridyl nitrogen via this fusion pattern, a linear conjugation network was established from the electron-withdrawing pyridine to the aryl substituent of the azaphosphinine ring. After preparing several derivatives of **114** and **115** with varying degrees of electron donation from group R, assessment of the optoelectronic properties (Table

1.11) showed the presence of a low energy absorption band. The absorption coefficient of this peak increased linearly with electron donation and was attributed to an internal charge transfer (ICT) band, which became the dominant transition in the strong donor-acceptor pairs **114d** and **115d**. As a result of this intense conjugation, these heterocycles became the model system for the azaphosphinine scaffold as a charge transfer system. The emission spectra of **114d** and **115d** exhibited intense solvatochromism of 63 and 52 nm, respectively, in solvents ranging from toluene to DMSO. The pair also displayed comparatively high quantum yields with **115d** reaching 90%, likely due to the rigidity of the scaffold in the quinoidal ICT state.

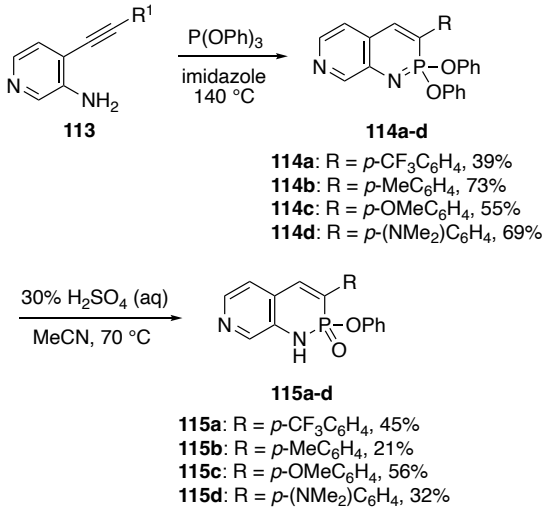

Scheme 1.45 Pyrido[3,4-*e*]-fused azaphosphinines.

Table 1.11 Photophysical properties of selected **114** and **115**.[a]

Cmpd	High-energy λ_{abs} (nm), ε (M^{-1} cm^{-1})	Low-energy λ_{abs} (nm), ε (M^{-1} cm^{-1})	λ_{em} (nm), φ (%)[b]	Stokes Shift (nm/cm^{-1})[c]
114a	295, 15800	390, 7200	475, 22	85, 4590
114b	310, 14000	385, 7700	459, 9	74, 4190
115c	331, 14000	351, 13400	415, 45	64, 4390
115d	330, 4500	405, 21000	489, 90	84, 4240

[a]Values collected in $CHCl_3$ at room temperature. [b]Excited at 365 nm and collected using standards of quinine sulfate (in 0.1 M H_2SO_4) and anthracene in EtOH. [c]Calculated from low-energy ICT band.

In 2019, our lab took advantage of the hydrogen-bond donating and accepting ability of **100** by incorporating an azaphosphinine group into a supramolecular receptor for binding hydrogen sulfate (HSO_4^-).[82] HSO_4^- is typically seen as a contaminant in agricultural and industrial fields.[87] Oxoanions in general make poor guests in anion host-guest complexes because of their mix of hydrogen-bond acceptors and donors as well as relatively oblong or tetrahedral geometries when compared to more spherical guests like halides. The nonplanar alignment of the hydrogen-bond accepting P=O and hydrogen bond donating N–H provides a unique and complementary pocket for the non-spherical HSO_4^- anion. In this instance a stronger host-guest interaction results when compared to a more planar receptor such as an analogous bis-urea species.[88–91] To prepare this new host, **100d** was iodinated to yield **100d'** (Scheme 1.43). This was attached to one of two aryl-ethynyl arms (**116**) via Sonogashira cross-coupling followed by urea formation to ultimately generate receptors **117**. This receptor class not only recognized HSO_4^- selectively over all other competing anions (Table 1.12) but could also be recycled for further use by washing the host-guest complex in aqueous media. This high level of selectivity for the HSO_4^- anion (~40:1 for **117b**) results not only from the tetrahedral phosphorus center but also the mix of hydrogen bond donors and acceptors in the azaphosphinine core that maps ideally to the mix of donors and acceptors in HSO_4^-.

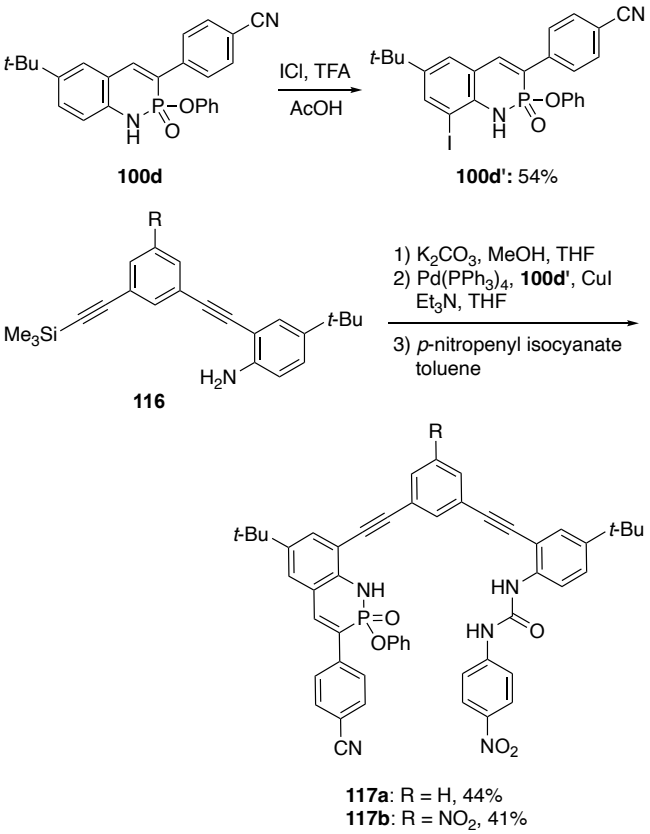

Scheme 1.46 Synthesis of azaphosphinine-based anion receptors **117**.

Table 1.12 Association constants[a] (K_a, M^{-1}) of receptors **117** with various anions in 10 vol% DMSO-d_6/$CDCl_3$ at room temperature.

Anion	**117a**	Relative Affinity[b]	**117b**	Relative Affinity[c]
HSO_4^-	1420 (1480)	1	9600 (10500)	1
NO_3^-	40 (30)	0.028	105 (100)	0.011
Cl^-	200	0.14	260	0.027
Br^-	30	0.021	75	0.008
I^-	—[d]	0	20	0.002
ClO_4^-	—[d]	0	—[d]	0

[a]1:1 binding fit. All reported association constants represent the average value from triplicate titrations. The values derived from ^{31}P NMR titrations are given in parentheses. Uncertainties less than 15%. All anions used as TBA salts. [b]Relative to the ^1H NMR titration derived K_a of **117a**•HSO_4^-. [c]Relative to the ^1H NMR titration derived K_a of **117b**•HSO_4^-. [d]No binding or too weak to be quantified.

Very recently, our lab published work describing the application of benzo[*e*]-1,2-dihydro-1,2λ^5-azaphosphinine 2-oxides for cellular imaging.[92] Use in cellular imaging is often a long-term goal for small molecule fluorophores. While this field is typically dominated by more traditional dyes (e.g., coumarins, xanthenes, cyanines etc.),[93–95] we envisioned the easily functionalized and emissive azaphosphinines our lab has developed as promising candidates as well. Initial studies proved that **118** (Figure 1.6) was not only cell permeable at 0.5% DMSO in water but also maintained its weak emission (λ_{em} = 452 nm, φ = 23%) inside HeLa cells. Encouraged by this initial result, we developed successive generations **119** and **120**. Molecule **119** introduced both *N*-methyl substitution, which decreased pH sensitivity, and an aryl ester functional handle, which redshifted the emission (λ_{em} = 499 nm, φ = 23%). Cytotoxicity measurements taken of **119** in HeLa cells suggested negligible cytotoxicity after 30 min in concentrations up to 150 μM. The next iteration of the initial cell dyes, **120**, was designed with the addition of a morpholine appendage for sub-cellular targeting, as the morpholine group is commonly used for lysosome targeting due to its basic nature.[96] While **120** had almost the exact same emission as **119**, the quantum yield was significantly higher (λ_{em} = 500 nm, φ = 50%). To test specific subcellular localization of **120**, three different concentrations (1, 3, and 5 μM) were co-incubated with 50 nM LysoTracker Deep Red in HeLa cells. The colocalization fidelity was measured using the Pearson correlation coefficient, revealing moderate colocalization for the three concentrations with Pearson coefficients of 0.49, 0.61, and 0.65 respectively. The success of this experiment was showing the cell permeability, lack of cytotoxicity, and broad pH stability range in the azaphosphinine core, suggesting future work could be done to further optimize successive generations of azaphosphinine dyes with subcellular targeting capabilities.

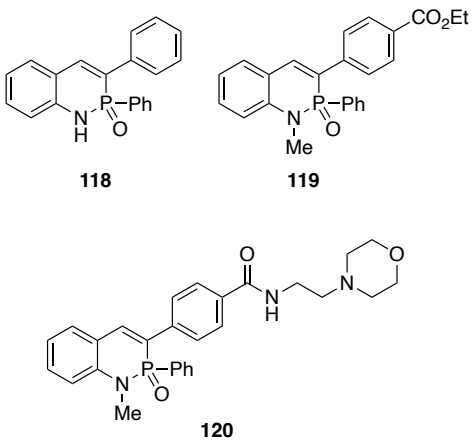

Figure 1.6 Benzo[*e*]-1,2-dihydro-1,2λ^5-azaphosphinine 2-oxide cellular imaging dyes.

In 2021 Park and coworkers disclosed the preparation of a highly substituted benzo[*e*]-1,2λ^3-azaphosphinine following a similar synthetic thread to previous publications, cyclizing *o*-(phenylethynyl)aniline **96e** with phenylphosphonyl dichloride ($PhPOCl_2$) under basic conditions at extremely high temperature (Scheme 1.47).[97] After screening a variety of bases, using 0.5 equivalents of DBU in 1,2,4-trichlorobenzene (TCB) furnished the desired product **121** good yield. Installation of two more phenyl substituents via Chan-Lam and Suzuki cross-coupling reactions gave **122** and **123**, respectively. Finally, to reduce the system from P^V to P^{III}, **123** was first thionated with Lawesson's reagent leading to **124** and then lastly methylated with MeOTf followed by $P(NMe_2)_3$ yielding **125**. Unlike its carbocyclic analogue tetraphenylnaphthalene (TPN), X-ray crystallographic analysis of **125** showed all four phenyl substituents were perpendicular to the core, indicating poor conjugation through the whole system; nonetheless, cyclic voltammetry of **125** revealed a diminished HOMO-LUMO energy gap compared to TPN (2.75 vs 3.83 eV).

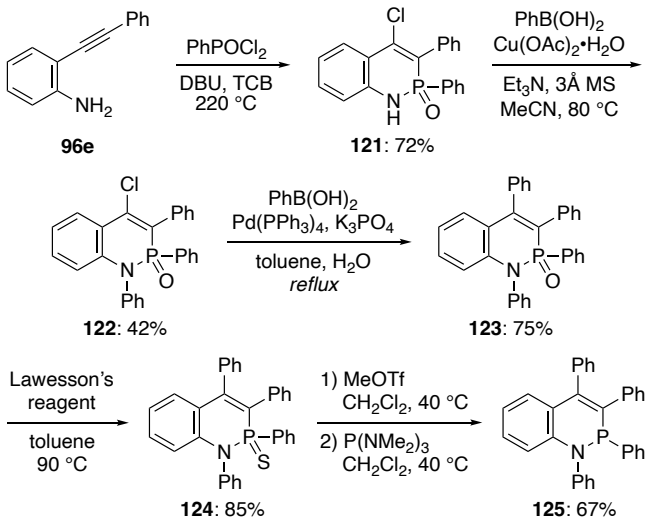

Scheme 1.47 Synthesis of azaphosphinine **125**.

A recent addition to this field comes from Deng et al. in 2022, which took a new approach to the Pd-catalyzed route to dibenzo[*c*,*e*]-1,2λ^5-azaphosphinines.[98] Instead of the typical approach, which until this point has involved P^V starting materials that are then incorporated into the final azaphosphinine, this publication used P^{III} phosphanamines **126**. Much like the similar work from Shi and coworkers[62] published in 2023, the trivalent phosphorus starting materials are oxidized to the pentavalent state during the heteroannulation. However, unlike Shi and coworkers the reaction explored in this work did not involve any intermolecular condensations or additions to furnish the final azaphosphinines. Instead, halide functional handles on the biphenyl substituent of the phosphanamines were used to close the azaphosphinine ring and generate a series of dibenzo[*c*,*e*]-1,2λ^5-azaphosphinines **127** (Scheme 1.48). In terms of substrate scope, Deng et al. first explored achiral phosphanamines with identical *P*-substituents. They synthesized a wide library of **127** containing functional groups of varying electronic character in the biphenyl backbone (**127a-w**) including alkenyl, alkynyl, heteroaromatic, and acene fusions. Despite the wide variety of biphenyl substituents, the only derivative that saw a drop in yield from the usual 68–92% range was the

binapthyl derivative **127ai**. Next, several P-substituents were tried (**127w**–**aa**). It was noted that less sterically hindered groups such as cyclohexyl or *i*-Pr resulted in diminished yields.

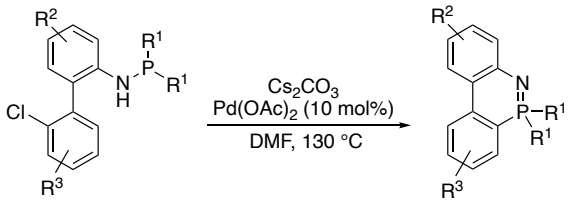

126 **127**

127a-v: R^1 = *t*-Bu
127a: R^2 = *m*-Me, R^3 = H, 79%
127b: R^2 = *p*-Me, R^3 = H, 85%
127c: R^2 = H, R^3 = *p*-Me, 86%
127d: R^2 = H, R^3 = *m*-Me, 68%
127e: R^2 = *p*-*i*-Pr, R^3 = H, 88%
127f: R^2 = *p*-*t*-Bu, R^3 = H, 79%
127g: R^2 = *p*-OMe, R^3 = H, 92%
127h: R^2 = H, R^3 = *p*-OMe, 72%
127i: R^2 = *p*-F, R^3 = H, 90%
127j: R^2 = H, R^3 = *m*-F, 81%
127k: R^2 = H, R^3 = *o*-F, 72%
127l: R^2 = 3,4-$(F)_2$, R^3 = H, 91%
127m: R^2 = *m*-Cl, R^3 = H, 86%
127n: R^2 = *p*-Cl, R^3 = H, 85%
127o: R^2 = H, R^3 = *p*-Cl, 72%
127p: R^2 = H, R^3 = *m*-Cl, 87%
127q: R^2 = *p*-OCF_3, R^3 = H, 98%
127r: R^2 = H, R^3 = *m*-CF_3, 89%
127s: R^2 = *p*-CN, R^3 = H, 82%
127t: R^2 = *p*-CO_2Et, R^3 = H, 85%
127u: R^2 = *p*-Ph, R^3 = H, 89%
127v: R^2 = *p*-$(NPh)_2$, R^3 = H, 69%
127w-aa: R^2 = R^3 = H
127w: R^1 = Cy, 25%
127x: R^1 = *i*-Pr, 56%
127y: R^1 = Ad, 70%
127z: R^1 = Ph, 64%
127aa: R^1 = 1-naphthyl, 83%

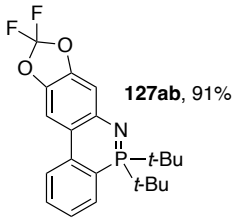

127ab, 91%

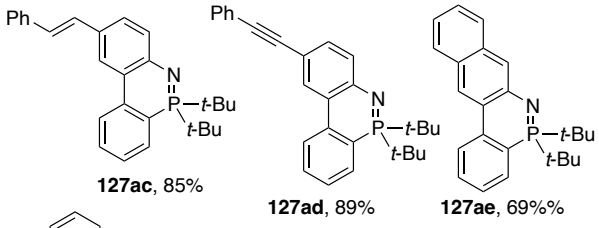

127ac, 85% **127ad**, 89% **127ae**, 69%%

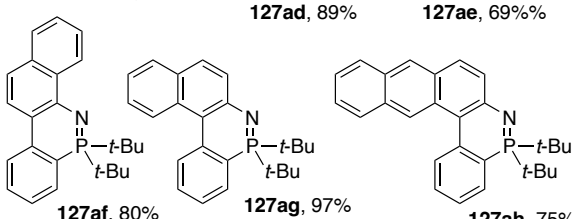

127af, 80% **127ag**, 97% **127ah**, 75%

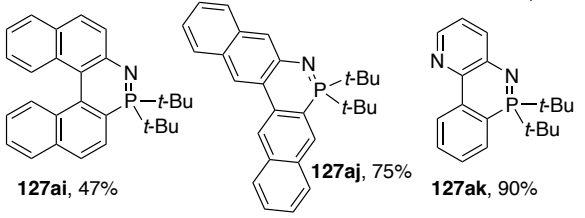

127ai, 47% **127aj**, 75% **127ak**, 90%

Scheme 1.48 Pd-catalyzed heteroannulation of achiral phosphanamines **126** to furnish dibenzo[*c*,*e*]-1,2λ^5-azaphosphinines **127**.

Next, Deng et al. decided to investigate the stereospecificity in their heteroannulation. First a library of chiral phosphanamines were isolated via HPLC, then these enantioenriched starting materials were protected by complexing with borane to furnish **128**. These chiral complexes were then subjected to the same heteroannulation conditions developed previously to ultimately yield **129** (Scheme 1.49). In almost every substrate used, the chiral heteroannulation resulted in an excellent e.e. of >99%. The extremely high and consistent stereoretention in such a comparatively simple system is very promising for future directions. Retention of stereocenters when converting directly from an acyclic to cyclic phosphorus species is a useful tool in the development of targeted phosphorus heterocycles, azaphosphinine or otherwise.

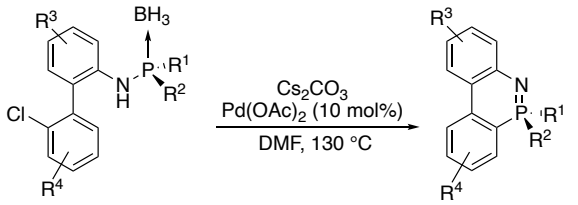

128 **129**

129a-c: R^1 = Ph, R^2 = *t*-Bu
129a: R^3 = R^4 = H, 85%, 99% e.e.
129b: R^3 = R^4 = *p*-OMe, 69%, >99% e.e.
129c: R^4 = *p*-F, R^4 = H, 58%, 99% e.e.
129d-g: R^3 = R^4 = H
129d: R^1 = Ph, R^2 = Cy, 81%, >99% e.e.
129e: R^1 = Ph, R^2 = *i*-Pr, 87%, >99% e.e.
129f: R^1 = *o*-MeC_6H_4, R^2 = *t*-Bu, 72%, >99% e.e.
129g: R^1 = Cy, R^2 = *t*-Bu, 61%, 84% e.e.

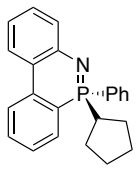

129h, 77%, >99% e.e.

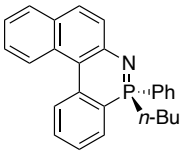

129i, 93%, >99% e.e.

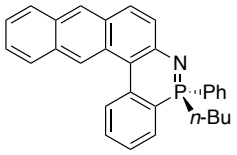

129j, 83%, >99% e.e.

Scheme 1.49 Retention of stereogenic P-center in heteroannulation of phosphanamine **128**.

Deng et al. continue to note that **127** are quite emissive and display both solution and solid-state fluorescence with high quantum yields, with **127s** especially exhibiting

77% in CH_2Cl_2. Due to the range of λ_{em} in **127**, the authors calculated the frontier molecular orbitals of their dibenzo[*c*,*e*]-1,2λ^5-azaphosphinines scaffold to determine what regions made the highest contributions to the HOMO and LUMO. Interestingly, it was found that C(2), located *para* to the nitrogen atom made the highest contribution to the HOMO and none to the LUMO. Conversely, C(9) located *para* to the phosphorus provided the opposite effect. The consequence of these contributions is represented in the photophysical properties of **127s** vs **127r**. In the former, the electron-withdrawing nitrile lowers the energy of the HOMO, blueshifting the emission (450 nm), while the energy of the LUMO is lowered in the latter due to the trifluoromethyl substituent, leading to a redder emission (505 nm).

1.4 1,3-Azaphosphinines

1.4.1 Heteroatom Exchange

1,3-Azaphosphinines are significantly less studied than their 1,2-azaphosphinine counterparts, yet there are still several papers exploring their preparation and post-synthetic modification.[99] A vast majority of the methods used to prepare the 1,3λ^3-azaphosphinine motif begin with a nitrogen-containing heterocycle to which a phosphorus atom is then added. One of the most direct and earliest examples of this was shown by Märkl and Dorfmeister in 1987.[100] Building off work forming 1,3-azaphospholes, they converted a series of triaryl-1,3-azapyrilium tetrafluoroborate salts **130** into the respective 1,3λ^3-azaphosphinine products **131** in the presence of tris(trimethysilyl)phosphane in modest yields (Scheme 1.50).[101,102]

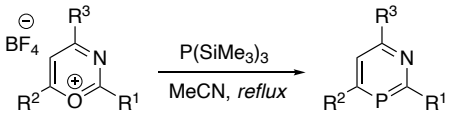

130a-f **131a-f**

131a: $R^1 = R^2 = R^3 =$ Ph, 26%
131b: $R^1 = p\text{-MeC}_6H_4$, $R^2 = R^3 =$ Ph, 21%
131c: $R^1 = R^2 =$ Ph, $R^3 = p\text{-MeC}_6H_4$, 18%
131d: $R^1 = R^3 =$ Ph, $R^2 = p\text{-MeC}_6H_4$, 20%
131e: $R^1 = p\text{-ClC}_6H_4$, $R^2 = R^3 =$ Ph, 24%
131f: $R^1 = p\text{-ClC}_6H_4$, $R^2 =$ Ph, $R^3 = p\text{-MeC}_6H_4$, 26%

Scheme 1.50 Conversion of azapyrilium tetrafluoroborate salts to 1,3λ^3-azaphosphinines **131**.

Treating the 2,4,6-triphenyl derivative **131a** with phenyl lithium added a phenyl group to the phosphorus center to afford phosphinyl anion **132**, and subsequent protonation by water gave non-aromatic 2,3-dihydro-1,3λ^3-azaphosphinine **133** (Scheme 1.51). Alternatively, **131a** could react as a diene in a [4 + 2] cycloaddition with either DMAD or methyl propiolate followed by cycloreversion to extrude benzonitrile, forming phosphinines **134a** or **134b**, respectively, in good yields.

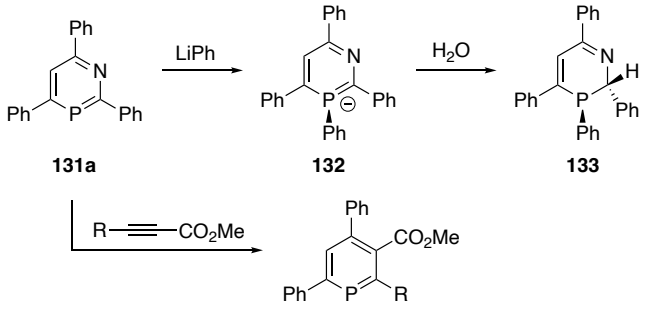

131a **132** **133**

134
134a: R = CO_2Me, 64%
134b: R = H, 76%

Scheme 1.51 Probing the reactivity of azaphosphinine **131a**.

1.4.2 Pericyclic / Cycloadditions

About the same time as Märkl's study, Appel et al. showed, also in 1987, that reaction of *α*-pyrone analogue **135** with two different phosphaalkynes resulted in

formation of 1,3λ^3-azaphosphinines **136** (Scheme 1.52)[103] via Diels-Alder reaction and subsequent evolution of CO_2 gas. Yields were not reported for this reaction. While a brief study, it laid the groundwork for many future works by proving that the 1,3λ^3-azaphosphinine moiety can be synthesized, isolated, and spectroscopically characterized. Specifically, several examples follow the cycloaddition/cycloreversion method instead of the above-mentioned heteroatom exchange, likely owing to synthetic flexibility.

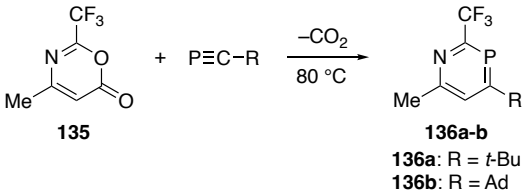

135 **136a-b**
136a: R = *t*-Bu
136b: R = Ad

Scheme 1.52 Diels-Alder route to 1,3λ^3-azaphosphinines **136**.

In 1988, Regitz and coworkers explored the reactivity of tri-*tert*-butylazete **137** and showed the molecule could undergo [4+2] cyclization with (2,2-dimethylpropylidyne)phosphane to generate Dewar benzene-like **138** in very good yield (Scheme 1.53).[104] The authors then explored the reactivity of **138** upon exposure to heat and light, which isomerized to form prismane **139** and 1,3λ^3-azaphosphinine **140**, respectively. Interestingly, prismane **139** slowly rearranged to 1,4λ^3-azaphosphinine **141** at room temperature, which could then be irradiated to form azaphosphabenzvalene **142** that also aromatizes to **140** upon heating.[105] These unusual transformations all resemble those observed for the purely hydrocarbon benzene valence isomers $(CH)_6$.[106]

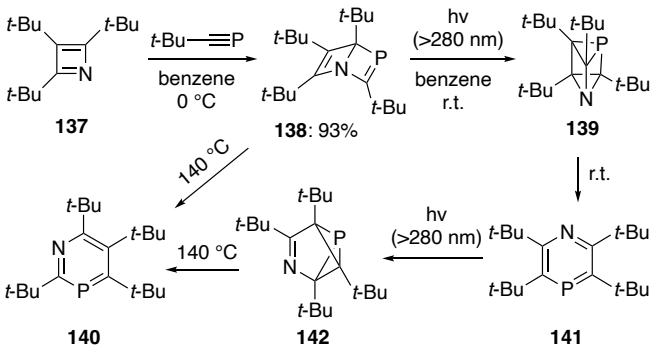

Scheme 1.53 Complex synthetic pathway leading to either 1,3λ^3- or 1,4λ^3-azaphosphinines.

The next entry into the family of 1,3-azaphosphinines came in 1989, where Appel and Poppe expanded upon their initial work with oxazinone **135** by performing a cycloaddition with an *N*-silyl-phosphaalkyne to produce intermediate **143**, which then extruded CO_2 gas to afford 4-silylamino-1,3λ^3-azaphosphinine **144** (Scheme 1.54).[107] Subsequent hydrolysis afforded the final heterocycle **145** in moderate yield.

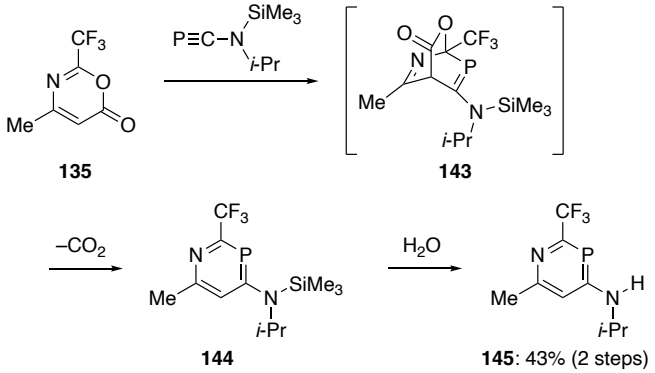

Scheme 1.54 Diels-Alder mediated synthesis of amine-bearing 1,3λ^3-azaphosphinine **145**.

Next, in 1991, Märkl and Dörges showed that 1,5,3-diazaphosphinines **146** undergo [4 + 2] cycloaddition with internal alkynes to first form bicyclic structures **147** before undergoing cycloreversion to extrude benzonitrile and form 1,3λ^3-azaphosphinines **148** (Scheme 1.55).[108]

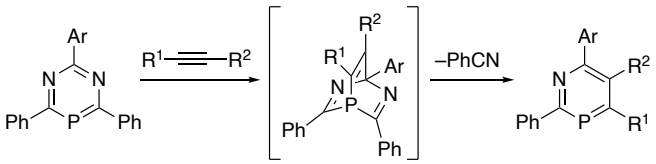

146 **147** **148**

148a: R^1 = H, R^2 = Ph
148b: R^1 = $SiMe_3$, R^2 = Ph
148c: R^1 = R^2 = CO_2Et

Scheme 1.55 Consecutive cycloaddition / cycloreversion pathway to furnish heavily substituted 1,3λ^3-azaphosphinines **148**. No yields reported for **148**.

This reaction can be repeated with another equivalent of internal alkyne to extrude another equivalent of benzonitrile to afford phosphinine **149** (Scheme 1.56), for which no yields were reported.[53,109–110] Interestingly, when treated instead with a phosphalkyne, 1,3λ^3-azaphosphinines instead form an azaphosphabarrelene **150**.

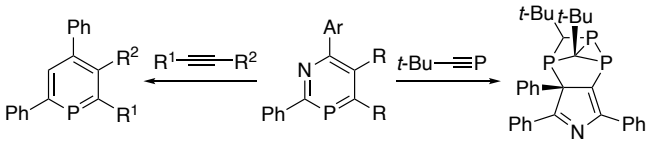

149a-c **148** **150**: 15%

149a: R^1 = H, R^2 = Ph
149b: R^1 = $SiMe_3$, R^2 = Ph
149c: R^1 = R^2 = CO_2Et

Scheme 1.56 Post-synthetic modification of **148** to either phosphinine **149** (left) or azaphosphabarrelene **150** (right).

In 1986, the first example of a 1,3λ^5-azaphosphinine was prepared by Galishev et al.[111] They first reacted imidoyl chloride **151** with diethyl(phenylethynyl)phosphonite to give zwitterion **152**, which then intramolecularly cyclized to form **153** (Scheme 1.57).

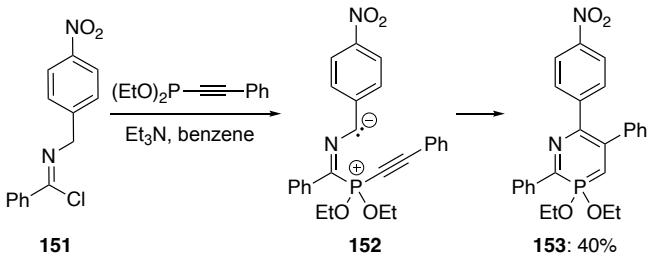

Scheme 1.57 Generation of heavily substituted **153** via zwitterionic intermediate.

While studying the synthesis of similar 1,3λ^5-azaphosphinines, the Märkl team reported that 1,3λ^3-azaphosphinine **131a** can be oxidized to the corresponding 1,3λ^5-azaphosphinine **154** upon treatment with diazoalkanes in alcohol solutions, adding both an alkyl group and a methoxy group in the process (Scheme 1.58). When run in ether rather than alcohol, however, the "dimeric" polycycle **155** was formed.[112]

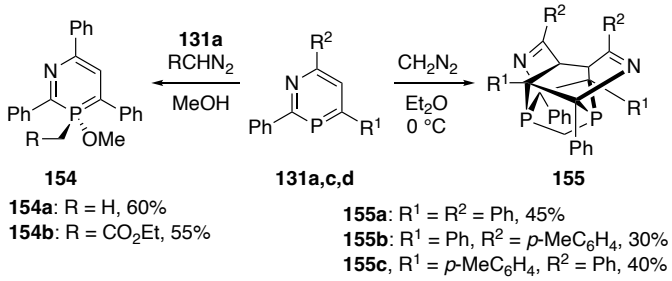

Scheme 1.58 Oxidation of **131** to P^V heterocycle **154** (left) or conversion to polycyclic **155** (right).

In 1999, Le Floch and co-workers performed a computational study exploring a series of nitrogen and phosphorus heterocycles to better understand their structure and reactivity.[113] This paper was a follow-up to previously published results that showed the 1,3,2-diazaphosphinine and 1,2-azaphosphinines reacted much more quickly with alkynes than their 1,3,5-diazaphophinine and 1,3-azaphosphinine counterparts, respectively, due to increased dipolar characteristics.[53,114] In this computational study,

they concluded that the 1,3λ^3-azaphosphinine scaffold was both planar and weakly aromatic, showing decreased shortening of the P–N double bond on average compared to the double bonds in pyridine or the double bond in phosphinine. They also determined the internal bond angles for the C–P–C, P–C–N, and C–N–C bond angles were 98.0°, 129.3°, and 120.1°, respectively. This C–P–C angle is significantly smaller than the C–N–C bond angle in pyridine (117.1°), which is likely the result of the longer P–C bonds. Also, increased s-character in the P lone pair that leads to more p-character in the P–C bonds since P is a higher Z (and more electropositive) element than N.

In 2018, Hansmann developed a novel inverse electron demand hetero-Diels-Alder reaction to form 1,3λ^3- and 1,4λ^3-azaphosphinines from several 1,2,4-triazine starting materials **156** (Scheme 1.59).[115] This was achieved at 90 °C through the use of sodium phosphaethynolate (NaOCP) and subsequent loss of N_2 gas to drive the reaction. The substituent groups on the starting triazine led to a dramatic difference in the ratio of formation of the 1,3λ^3-azaphosphinine **157** compared to the competing 1,4λ^3-derivative **158**. For instance, placement of phenyl rings in the 5- and 6-positions as well as either a phenyl or *p*-trifluoromethylphenyl group in the 3-position leads to formation of the 1,3λ^3-azaphosphinine derivative **157** in a 1:4 ratio to the 1,4λ^3-azaphosphinine **158** (Scheme 1.59). This ratio was determined through examination of the ^{31}P NMR spectrum and comparison to predicted values determined through DFT; however, the computed thermodynamic stabilities of the two scaffolds were very close, with the 1,3λ^3-derivative favored by 1.7 kcal mol^{-1}, suggesting that the mechanism of formation likely leads to this discrepancy.

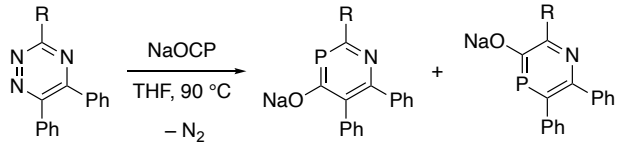

Scheme 1.59 Conversion of triazine **149** to mixture of corresponding 1,3λ^{3-} and 1,4λ^{3}-azaphosphinines.

To further examine the directing effects of the substituent groups, 2-pyridyl groups were introduced as ion tethers in multiple positions on triazene **156c-e**, resulting in dramatic shifts in the ratios of **157c-e** to **158c-e** (Scheme 1.60). In the 3-position, the 2-pyridyl on triazene **156** leads to a 1:15 ratio of 1,3λ^{3}-azaphosphinine **157c-d** to 1,4-azaphosphinine **158c-d** upon treatment with NaOCP at 60 °C. This was true when starting with either diphenyltriazene **156c** or with dimethyltriazene **156d**. When starting with triazene **156e** at room temperature, however, only 1,4λ^{3}-azaphosphinine **158e** was formed.

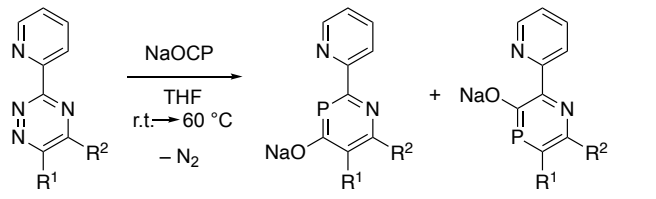

Scheme 1.60 Use of 2-pyridyl directing group to dramatically favor 1,4λ^{3} product **158**.

With the 2-pyridyl group on both the 5- and 6-positions and a phenyl group in the 2-position on triazene **156f**, treatment with NaOCP at 60 °C gave a 4:1 ratio of 1,3λ^{3}-azaphosphonine **157f** to 1,4λ^{3}-azaphosphinine **158f** (Scheme 1.61), likely due to the directing nature of the pyridyl groups. Interestingly, when running the same reaction in

the presence of 15-crown-5, a reversed trend of 1:2.5 **157f:158f** was observed, supporting the idea that the Na^+ ion plays a large directing role in the product ratio. To further favor the 1,3λ^3-azaphosphinine product **157g**, the reaction was run with a hydrogen in place of the phenyl group, which led to a 15:1 **157g**:**158g** ratio in good yields.

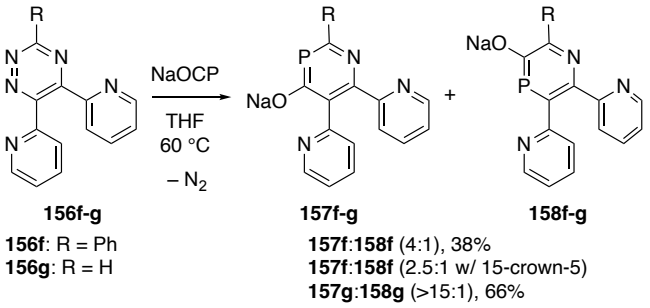

Scheme 1.61 Reversed trend in selectivity for azaphosphinine isomer based on substitution pattern of starting triazine **156**.

Lastly, when starting from 1,2,3-triazene **159** and treating it with NaOCP at –78 °C in THF, the sodium salt of 1,3λ^3-azaphosphinine 2-oxide **160** was solely formed (Scheme 62), confirming the versatility of this synthetic route.

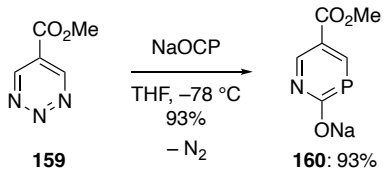

Scheme 1.62 Use of 1,2,3-triazine **159** to give exclusively 1,3λ^3 product **160**.

1.4.3 Intramolecular cyclization reactions

In 2018, Mathey and coworkers explored a more conjugated system containing the 1,3-azaphosphinine moiety.[116] Bromination of **161** with *N*-bromosuccinimide (NBS) afforded indole **162**, which was then protected as the dimethoxy acetal **163** (Scheme 1.63). Lithiation and subsequent addition to *P*-cyano-3,4-dimethylphosphole gave phosphorus- and nitrogen-containing structure **164**. The phosphole ring then underwent a [4 + 2] cycloaddition with N-phenylsuccinimide to first furnish **165**, which upon treatment with $AlCl_3$ gave *P*-chloro intermediate **166**. Elimination of HCl with 1,4-diazabicyclo[2.2.2]octane (DABCO) afforded 1,3λ^3-azaphosphinine **167** in a good yield. Alternatively, reaction of **166** with Et_2NH and then S_8 gave thionated 1,3λ^3-azaphosphinine 3-sulfide **168** in excellent yield.

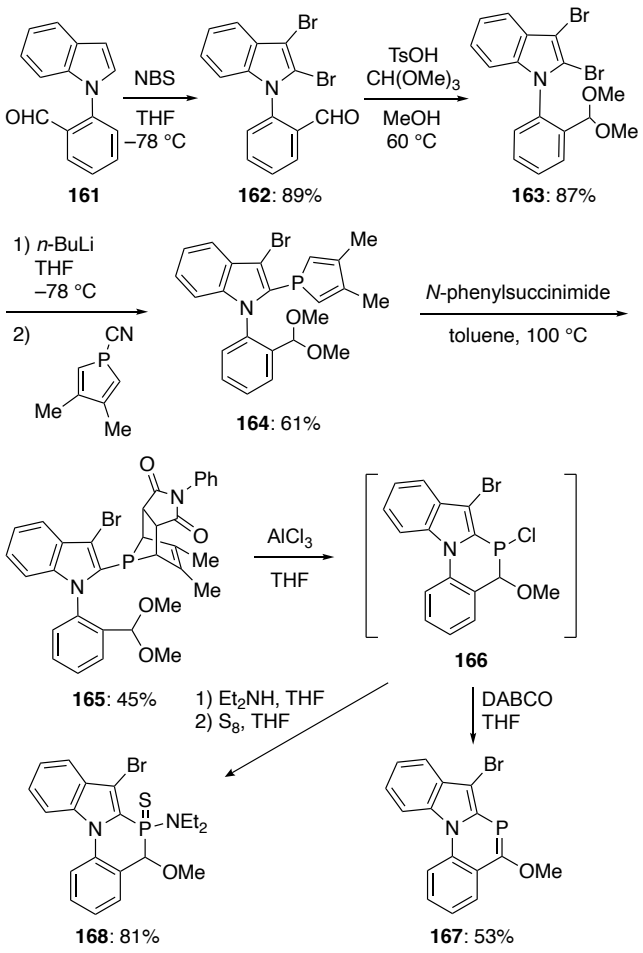

Scheme 1.63 Synthetic pathway to π-extended 1,3λ^3 azaphosphinine **167** and corresponding 1,3λ^5 azaphosphinine sulfide **168**.

To explore the reactivity of π-extended **167**, heating in MeOH at 60 °C gave dimethoxy product **169** in very good yield (Scheme 1.64). Additionally, the phosphorus-containing double bond could undergo a Diels-Alder reaction with 2,3-dimethyl-1,3-butadiene in toluene at 100 °C to furnish heterocycle **170**, which could be oxidized with H_2O_2 to afford the respective 1,3λ^5-heterocycle **171** in excellent yield.

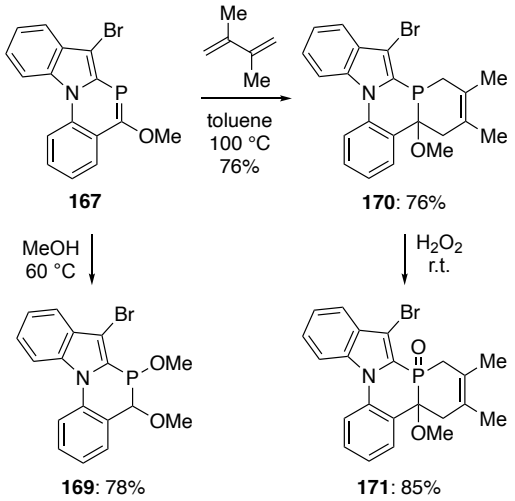

Scheme 1.64 Synthesis of dimethoxy **169** (left) and consecutive Diels-Alder / oxidation to give product **171** (right).

1.5 1,4-Azaphosphinines

1.5.1 Bis-β-ketophosphane oxide cyclization

One of the earliest examples of a 1,4-dihydro-1,4λ^5-azaphosphinine 4-oxide comes from Aguiar and coworkers in 1971.[36] Unlike most early publications in this review, their synthesis was not primarily concerned with just pushing the bounds of novel heteroaromatics, but rather, designing new bioactive species. Starting from (diethynyl)phenylphosphane oxides **172**, conjugate addition of butylamine followed by

hydrolysis afforded the corresponding bis-β-keto-phosphane oxides **173** (Scheme 1.65). Lastly, **173** were cyclized with ammonium carbonate to furnish the desired dihydro product **174**. As apparent from the next few entries in this review, this particular technique of synthesizing an azaphosphinine scaffold was extremely influential and facilitates much of the early work performed on the 1,4-isomer.

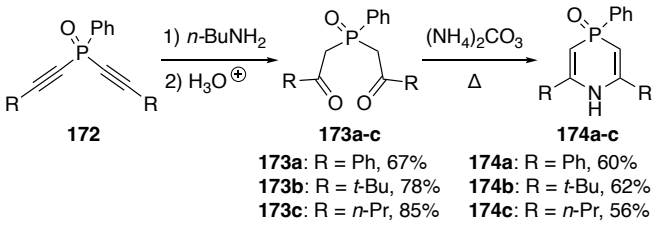

Scheme 1.65 Synthesis of 1,4-dihydro-1,4λ^5-azaphosphinine 4-oxide **174**.

The earliest published example of any non-fused, aromatic λ^3-azaphosphinine came from Märkl and Matthes in 1972.[32] The initial interest for this system arose from curiosity surrounding previously synthesized azaarsine heterocycles. Their synthetic approach involved thermolyzing a dihydro precursor to the fully aromatized system (Scheme 1.66). The success of this technique led to it being used later in some of the other early syntheses of 1,4λ^3-azaphosphinines.[66,68] The first four steps of their syntheses are directly analogous to that of Aguiar et al. but use a suitable 'leaving group' (*t*-Bu) instead of a Ph ring. Bis(phenylethynyl)-*t*-butylphosphane **175** was oxidized and the water formally added to the alkynes to give bis-β-keto-phosphane oxide **176**. This was cyclized with ammonium carbonate and reduced to P^{III} with phenylsilane to afford **177**, which lastly was thermolyzed to furnish the desired 2,6-diphenyl-1,4λ^3-azaphosphinine **178**.

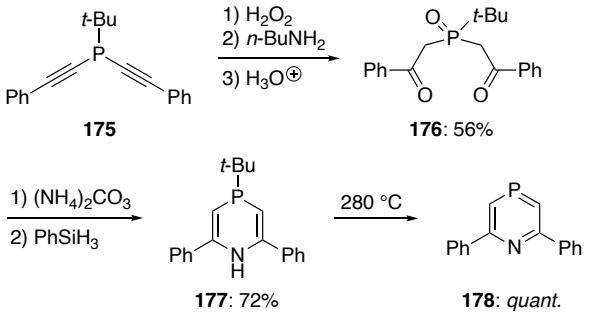

Scheme 1.66 Synthesis of 2,6-diphenyl-1,4λ^3-azaphosphinine **178**.

Like prior azaphosphinine examples, the differences in the heteroatom electronegativity meant that **178** was quite electrophilic (Scheme 1.67). Several dihydro products (**177**, **179, 180**) could be synthesized through the attack of various nucleophiles at the phosphorus center, followed by either protonation or methylation to afford the secondary or tertiary amino species, respectively.

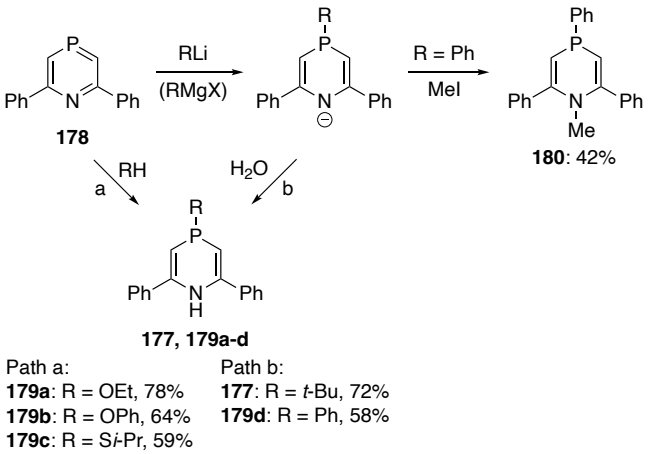

Scheme 1.67 Dihydro-products resulting from attack of various nucleophiles.

Also in 1972, Mebazaa and Simalty were developing their synthesis of the first non-fused 1,4λ^5-azaphosphinine, a pathway that would become standard for nearly a decade in the development of such species (Scheme 1.68).[117] Starting from phosphonium pyran salt **181**, hydrolysis furnished bis-β-keto-phosphane oxide **182**. Analogous to the

previous two 1,4-azaphosphinine syntheses, **182** was cyclized with ammonium acetate to yield **183**.[32,36] Anion exchange gave the perchlorate salt **183'**, which was subsequently deprotonated with NaH to furnish 2,4,4,6-tetraphenyl-1,4λ^5-azaphosphinine **184**. While the exact method of anion exchange was not reported in the paper, a similar publication from the same authors used sodium perchlorate;[118] no product yields were reported for either. The authors make the case for the aromaticity of their target **184** through the UV-Vis spectra and its dramatic change upon protonation. However, through the modern perspective noted at the beginning of this review, while there may be a degree of delocalization via the ylidic nature of **184**, there is no "aromaticity" as one would typically define it.

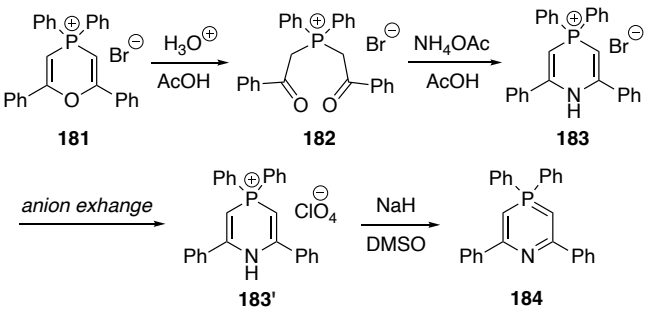

Scheme 1.68 Synthesis of 2,4,4,6-tetraphenyl-1,4λ^5-azaphosphinine **184**.

In 1984, Quin et al. expanded upon the synthetic pathway initially developed by Aguiar.[36,119] They had been examining methods of converting phospholene oxides **185** into bis-β-ketophosphane oxides **173a** and **186** via ozonolysis (Scheme 1.69).[120] Their alternative approach to generating the acyclic starting material of the 1,4-dihydro-1,4λ^5-azaphosphinine 4-oxide scaffold **174a** and **187** facilitated novel functional groups and substitution patterns. While their substrate scope was primarily limited to phenyl and methyl groups, they were able to furnish heterocycles with only one substituent α to the nitrogen atom, which was not achievable with previous symmetric bis-β-keto-

phosphane oxides. While there was limited analytical data provided for the compounds, the ^{13}C NMR spectra showed a strong upfield shift (91–93 ppm) of the olefinic carbon β to the nitrogen atom, suggesting a transfer of electron density from the nitrogen atom to this carbon similar to enamines.

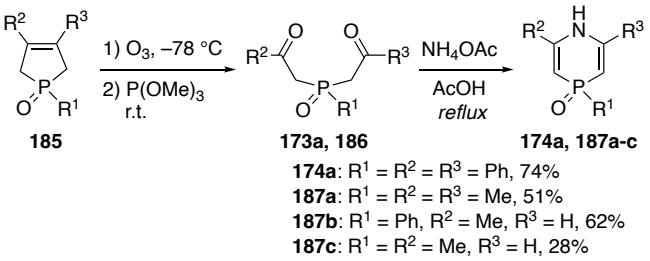

Scheme 1.69 Ozonolysis-based approach to 1,4-dihydro-1,4λ^5-azaphosphinine 4-oxides **174a** and **187**.

By 1990, Quin and Marsi published a more comprehensive work on phosphorus heterocycles derived from more exotic bis-β-keto-phosphane oxides **188** and **189** (Scheme 1.70).[121] While many of these species do not fit the scope of this review, there were a few interesting examples that explore the possibilities of extension via saturated ring fusion such as **190** and **191**.

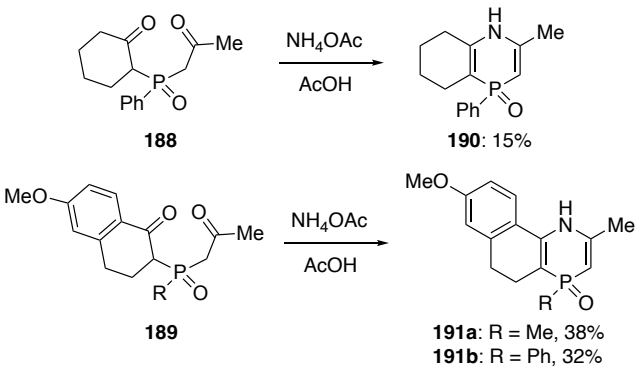

Scheme 1.70 Additional examples of ring-fused 1,4-dihydro-1,4λ^5-azaphosphinine 4-oxides.

1.5.2 Pericyclic/Cycloaddition Reactions

Work from Barluenga et al. began to emerge around this time that was focused on developing alternative pathways to 1,4-azaphosphinines. Some of the limitations of the aforementioned bis-β-keto-phosphane oxides were i) a lack of functionalization at the 3- and 5-positions and ii) the harsh conditions required to reduce the phosphorus atom from P^V to P^{III}.[122] A popular technique in the early days of 1,2-azaphosphinine chemistry, Barluenga used cycloaddition/electrocyclization reactions to his advantage. Starting from previously described phosphazene **192** (Scheme 1.71),[35] reaction with DMAD proceeded through a [2+2] cycloaddition/4π-electron ring-opening to furnish acyclic intermediate **193** (where R^1 = H), which upon further heating yielded azaphosphinine **194** after loss of an equivalent of aniline. If R^1 was an alkyl substituent, the reaction furnished **194** directly, likely proceeding via the same mechanism with the corresponding derivatives of **193** being too reactive to isolate.

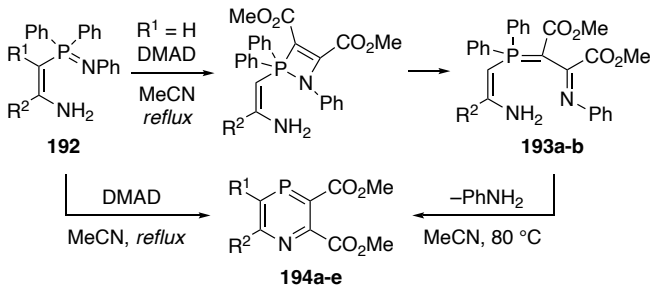

193a-b, 194a-b: R^1 = H
193a: R^2 = *p*-MeC_6H_4, 86%
193b: R^2 = Cy, 82%
194a: R^2 = *p*-MeC_6H_4, 80%
194b: R^2 = Cy, 77%
194c: R^1 = Me, R^2 = *p*-MeC_6H_4, 76%
194d: R^1 = $CH_2CH{=}CH_2$, R^2 = *p*-MeC_6H_4, 79%
194e: R^1 = Bn, R^2 = Cy, 78%

Scheme 1.71 Synthesis of azaphosphinines **194**.

Barluenga et al. soon departed from the cycloadditions route and instead examined the reactivity of 2-aza-1,3-dienes, which were gaining popularity in Diels-Alder type

reactions.[123] The authors hypothesized that these 2-aza-1,3-dienes could also be employed as nucleophiles in cyclization reactions using suitable electrophiles. Reacting several 2-aza-1,3-dienes **195** with dichlorophenylphosphane led to a mild, one-pot synthesis of the corresponding tetrasubstituted 1,4-dihydro-1,4λ^5-azaphosphinine 4-oxides **196** (Scheme 1.72). The authors could trap trivalent **197** by removing *in situ*-generated HCl with Et_3N, and subsequently showed that **197** could be oxidized to either oxide **196** or sulfide **198** with H_2O_2 or S_8, respectively.

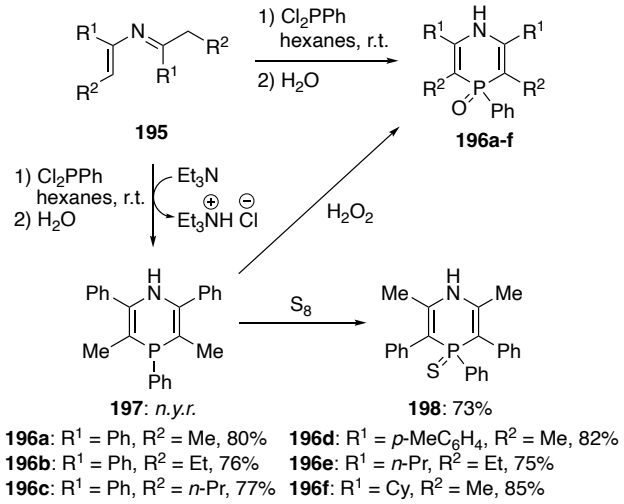

Scheme 1.72 One-pot cyclization to form 1,4-dihydro-1,4λ^5-azaphosphinines **196**.

Barluenga et al. also showed that substituting phosphorus trichloride for dichlorophenylphosphane in the cyclization could furnish **196'** (Scheme 1.73).

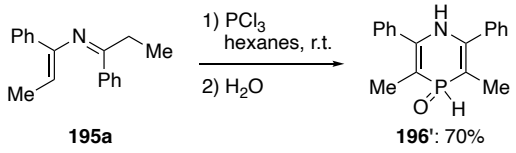

Scheme 1.73 Synthesis of secondary 1,4λ^5-azaphosphinine 4-oxide **196'**.

Barluenga et al. returned to the cycloaddition route in a 1990 publication concerning the synthesis of 2-oxo-1,4λ^5-azaphosphinines.[124] Just prior to this report, the same authors had described a method for formation of conjugated phosphonium ylides using phosphazenes and DMAD, then subsequently converting them to phosphole derivatives.[125] The reaction between one of the two alkyne diesters, DMAD or diethyl acetylenedicarboxylate (DEAD), and the *N*-alkoxycarbonylphosphazene **199** is proposed to proceed via [2 + 2] cycloaddition and subsequent electrocyclic ring opening to yield the conjugated phosphonium ylides **200** (Scheme 1.74). This is a similar process to the group's earlier work on formally conjugated 1,4λ^3-azaphosphinines.[122] However, for these derivatives the *N*-alkoxycarbonyl functionality served as an electrophile, in which deprotonation of the CH_2 unit next to P and cyclocondensation ultimately furnished azaphosphinines **201** in excellent yields.

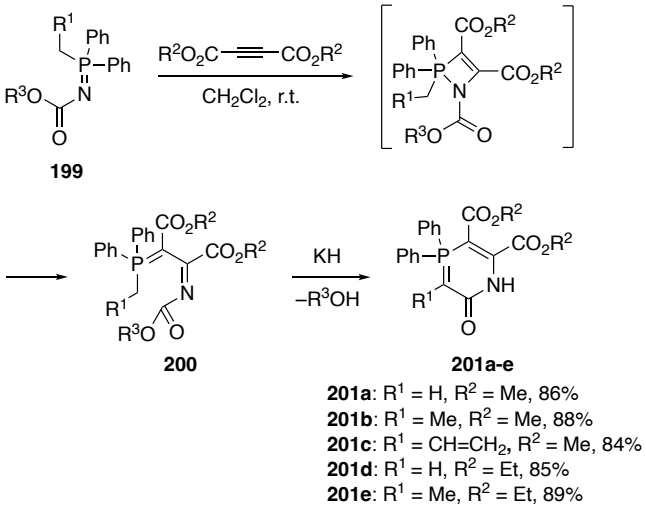

Scheme 1.74 Cycloaddition/intramolecular cyclization route to 2-oxo-1,4λ^5-azaphosphinines **201**. R^3 is either Me or Et.

In 2011, Alajarin et al. reinvestigated generating azaphosphinine scaffolds from phosphazene-alkyne cycloaddition.[126] Unlike previous works that used diester-functionalized alkynes, this study involved *in situ*-generated benzyne derivatives. The

reaction of phosphazenes **202** with various *o*-trimethylsilylphenyl triflates **203** furnished the saturated benzo[*b*]-tetrahydro-1,4-azaphosphonium triflate **204** via the cycloaddition/electrocyclization mechanism proposed in Scheme 1.75. While the authors do generate several derivatives of this species, the saturated nature of the azaphosphinine ring puts it beyond the scope of this review aside from this single mention.

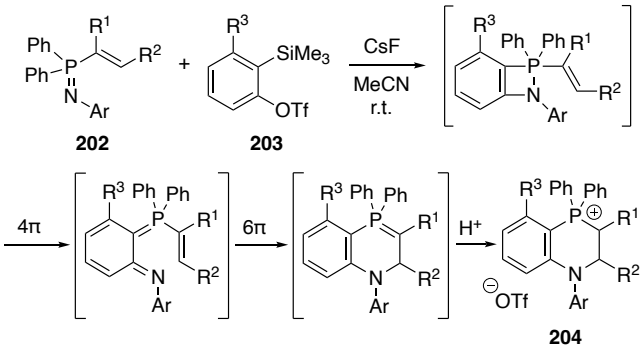

Scheme 1.75 Proposed general mechanism to generate tetrahydro species **204**.

Importantly, Alajarin et al. applied the reaction strategy outlined in Scheme 1.75 to several *P*-alkynyl-λ^5-phosphazenes **205** and produced the corresponding benzo[*b*]-1,4-dihydro-1,4-azaphosphininium triflates **206** (Scheme 1.76). The proposed mechanism is believed to be the same for both **204** and **206**. One could imagine if an unprotected nitrogen atom could survive this synthesis, the whole ring system could be deprotonated with strong base like the synthesis by Mebazaa and Simalty.[117]

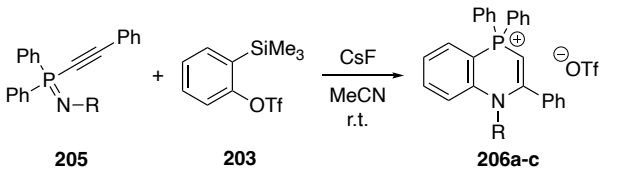

206a: R = *p*-MeC_6H_4, 69%
206b: R = *p*-BrC_6H_4, 65%
206c: R = 2,3-$(NO_2)_2C_6H_3$, 59%

Scheme 1.76 Phosphazene **205** heteroannulation with benzyne to give azaphosphinines **206**.

A very unusual contribution came from Bertrand and coworkers describing the use of a benzo-λ^5-phosphete for the synthesis of a benzo[*b*]-1,4λ^5-azaphosphinine **207** (Scheme 1.77).[127] Fused 1,4-azaphosphinines of any valence are extremely rare in the literature, and this novel approach took advantage of an even less-common substrate. This work hinges on the unusual stability of phosphetes. When fused to a benzene ring, phosphete ring **208** becomes highly reactive and sensitive to oxygen and moisture, likely due to the lengthened P–C bonds. This high reactivity gave rise to the unexpected formation of the benzo[*b*]-1,4λ^5-azaphosphinine **207** in excellent yield when reacted with acetonitrile, the structure of which was supported by spectroscopic analysis. This substitution pattern is unexpected because it must arise from cycloaddition of the C–C bond of the 4-membered ring in **208** with acetonitrile, rather than the expected cycloaddition with the P–C bond.

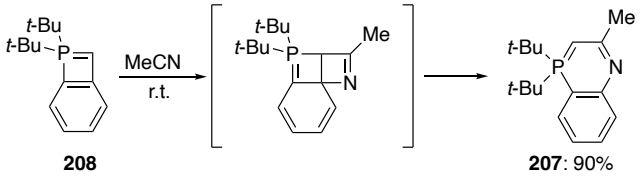

208 **207**: 90%

Scheme 1.77 Phosphete route to benzo[*b*]-1,4λ^5-azaphosphinine **207**.

As is the case with the other azaphosphinine isomers, more modern research gravitates toward transition-metal catalyzed reactions. Accordingly, in 2002 Leung and coworkers published their work on the Pd-catalyzed synthesis of 1,2,4,6-tetraphenyl-1,4-dihydro-1,4λ^3-azaphosphinine **209** (Scheme 1.78).[128] The primary benefit of this approach is the simplicity and one-pot nature of the reaction. Whereas no reactivity

occurred between bis(phenylethynyl)phenyl phosphane **210** and aniline alone, addition of $PdCl_2(MeCN)_2$ allowed the reaction to proceed forming stable monomeric **211** and dimeric **212** azaphosphinine complexes with Pd that were confirmed via X-ray crystallography. This is an interesting and more modern take on the 1,4-dihydro-1,4λ^3-azaphosphinines synthesized by Märkl and Matthes where the multistep oxidation and heteroannulation is replaced by a single catalytic step.[32] The azaphosphinine ring could subsequently be liberated with the addition of KCN, affording **209**. The authors note that the geometry and bond lengths of the nitrogen atom in both cases are that of sp^2 hybridization, indicating delocalization around the azaphosphinine ring. The low-field NMR shift of the azaphosphinine proton signal (δ 7.73) suggests the presence of aromaticity within the λ^3-azaphosphinine ring.

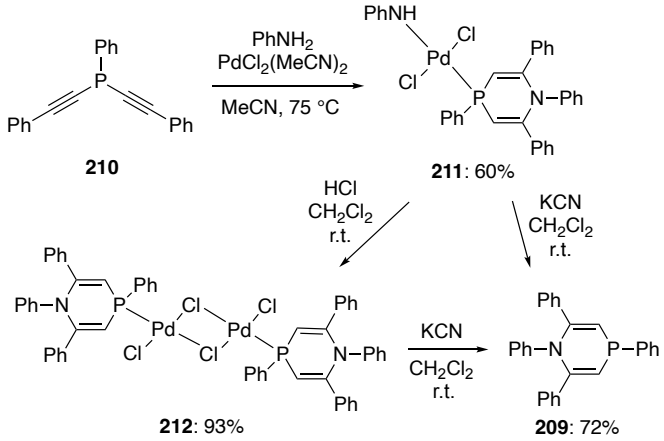

Scheme 1.78 Pd-catalyzed heteroannulation to give 1,2,4,6-tetraphenyl-1,4-dihydro-1,4λ^3-azaphosphinine **209**.

In 2015, Duan, Mathey and coworkers followed up on the efforts of both Alajarin and Leung to develop new routes to both benzo[*b*]-1,4-dihydro-1,4-azaphosphonium triflates and a transition metal catalyzed dimeric azaphosphonium species.[126,128,129] *o*-Diarylphosphinoaryl isocyanides **213** are first methylated with MeOTf to give **214**, which are then treated with *t*-BuOK base and then triflic acid to yield azaphosphonium

triflates **215** (Scheme 1.79). The proposed mechanism of this latter transformation involves deprotonation to form an ylidic species that undergoes [2 + 2] cycloadditon with the *o*-isocyanide moiety; a hydrogen shift, cycloreversion, and protonation complete the transformation. These salts are directly analogous to those prepared by Leung and coworkers but without a *N*-atom substituent, as well as less substitution on the azaphosphininium ring itself.

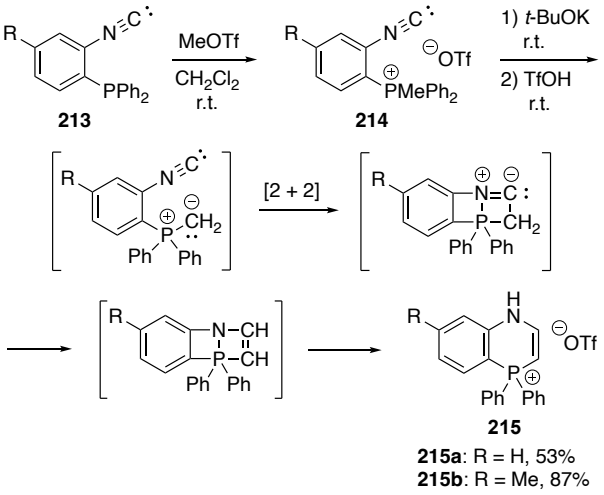

Scheme 1.79 Intramolecular cyclization of *o*-diarylphosphinoaryl isocyanide ylides.

Conversely, when **213a** is subjected to room temperature conditions in the presence of $NiCl_2$ an entirely different process occurs. Stable dicationic species **216** is the only isolable product of the reaction (Scheme 1.80). The authors note the mechanism of formation is not clear, and only provide NMR and X-ray crystallographic data in terms of analysis. Although the yield is omitted, this fused azaphosphininium species is quite novel in its chemistry and again begs the question if a strong base is used, would the heterocycle convert to the neutral 1,4λ^5-azaphosphinine like those of Mebazaa and Simalty?[117]

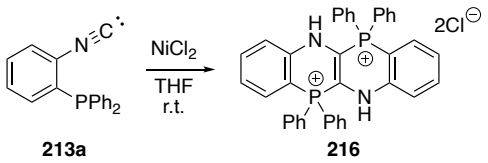

213a **216**

Scheme 1.80 Cyclization of isocyanide **213a** into dicationic **216**.

1.6 Comparing electronic properties of the azaphosphinine isomers

With such varied examples of azaphosphinines across several isomers and valences, it becomes easy to lose track of the exhibited properties, namely aromaticity, of each heterocycle. Only azaphosphinine compounds with an endocyclic P^{III}=X double bond are formally aromatic. In this state the rings are analogous to both pyridine and phosphinine, the single heteroatom-containing nitrogen and phosphorus analogues. As noted earlier, the computational work from Le Floch and co-workers in 1999 sought to compare the aromaticities of 1,2λ^3- and 1,3λ^3-azaphosphinines not only to each other but also to pyridine and phosphinine.[113] This work compared Nucleus Independent Chemical Shift (NICS) values (Table 1.13, left), computed bond lengths, and computed bond angles. In the NICS calculations, negative values denote aromaticity. From these data there is a clear distinction between the aromaticities of the 1,2λ^3- and 1,3λ^3-isomers, with both being less aromatic than the single heteroatom species. The authors ascribe this difference to the dramatically different electronegativities of the nitrogen and phosphorus atoms, which cause more π-electron localization when the two are directly bonded. Interestingly, it is also noted that even though the 1,3λ^3-isomer is more aromatic, it is also less stable. While it is typically thought that increased aromaticity should lead to higher stabilities, this suggests that the opposite is true for these molecules. Upon further study of the molecular orbitals through NBO analysis, it was found that the placement of heteroatoms within the 1,3-azaphosphinine and 1,3,2-

diazaphosphinine leads to electron distribution which limits electronic delocalization within the ring. This is rationalized computationally by calculating the [1,4] P–C_4 dipole in the 1,2λ^3-isomer as well as qualified by experimental observations made in a previous publication from this group.[53]

In 2018, Elguero et al. published a computational study that calculated the NICS values for a large number of P–N heterocycles including several theoretical species such as the parent 1,2λ^3, 1,3λ^3, and 1,4λ^3-azaphosphinines (Table 1.13, right).[131] The small differences in NICS values between the two studies are likely due to different levels of theory and different scanning distances used above the theoretical ring (0.5 vs. 1.0 Å). Regardless, both data sets follow the same basic trend of aromaticity in the azaphosphinine derivatives, with the later work by Elguero et al. suggesting that 1,4λ^3-azaphosphinine would be the most aromatic, rivaling that of phosphinine. Both studies include the benzene, pyridine, and phosphinine as reference values to their computations.

Table 1.13 Computed NICS values of relevant heterocycles computed by Le Floch (left) and Elguero (right).

Compound	NICS(0.5) (ppm)[a]	NICS(1) (ppm)[b]
benzene	–11.5	–10.2
pyridine	–10.6	–10.2
phosphinine	–10.2	–9.7
1,2λ^3-azaphosphinine	–8.9	–9.2
1,3λ^3-azaphosphinine	–9.3	–9.6
1,4λ^3-azaphosphinine	—	–9.7
1,3,2λ^3-diazaphosphinine	–7.5	–8.5

[a]Computed 0.5 Å above ring centers at GIAO-SCF/6-31+G*//B3LYP/6-31G* level.
[b]Computed 1 Å above ring center at B3LYP 6-311++G/d,p level.

By comparison, pentavalent azaphosphinine rings cannot be described as aromatic. Modern computational and experimental work into the nature of pentavalent phosphorus indicate that the bonds are almost entirely ionic in nature. Due to the readily available electron density that is transferred to electronegative substituents (e.g., N, O), a considerable amount of donation then occurs in the form of negative hyperconjugation. While this effect is in essence the distribution of electron density to adjacent bonds, it does not constitute aromaticity as the delocalization is not global and cannot pass through the phosphorus atom. Despite the P^V azaphosphinine rings themselves failing to meet the criteria of aromaticity, most compounds discussed in this review still exhibit some local aromaticity. This is due to fusion of the azaphosphinine ring to aromatic species such as benzene, naphthalene, or pyridine.

There is no published computational work that assesses the electronics and localized charge in P^V azaphosphinines. However, using ^1H and ^{31}P NMR we can speculate on the effect of different azaphosphinine characteristics. Properties such as endo- vs. exocyclic double bonds and the relative position of the two pnictogen atoms on the ring will of course result in changes to the electronic character of the complex system. ^1H and ^{31}P NMR data for selected azaphosphinines are described in Table 1.14. **61**, **131b**, and **178** represent the 1,2λ^3, 1,3λ^3, and 1,4λ^3 isomers respectively. As expected, all the proton signals for the three P^{III} azaphosphinines are at an appropriately deshielded chemical shift for aromatic species. Comparison of **178** to its P^V counterparts **174a** and **184** directly demonstrates this loss of aromaticity in the same proton signal. H(3/5) of **178** undergoes a dramatic upfield shift to 5.62 and 5.10 ppm in **174a** and **184**, respectively.

The notably different ^1H NMR chemical shifts of **16b** does well to illustrate the ylidic nature of the P^V azaphosphinine ring, in which the 2, 4, and 6 positions of the

ring will distribute a negative charge. One could imagine much of this electron density would rest on the electronegative nitrogen atom,; however, H(5) of this ring still experiences a shielding effect causing the ^{1}H NMR signal to appear at 6.06 ppm. Comparison of compounds **97f** and hydrolysis product **98f** leads to a commonly observed change in the ^{31}P NMR spectra. As a greater number of electronegative substituents are bonded to the pentavalent phosphorus, the chemical shift becomes more like that of phosphonium compounds, emphasizing the lack of electron density on the phosphorus. This effect is also directly observed in the analogous example of **174a** and **184**.

Table 1.14 Comparison of selected ^{1}H and ^{31}P NMR chemical shifts across selected azaphosphinine systems.

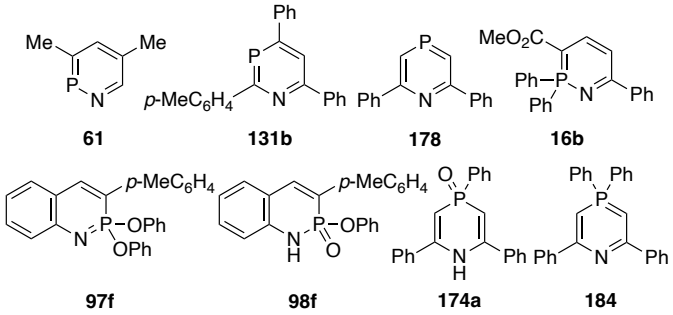

Cmpd	^{1}H NMR δ [ppm] (m, Hz)[a]	^{31}P NMR δ [ppm] (m, Hz)[a,b]
61	9.11 (H6), 7.58 (H4)	263.3
131b	8.10 (H5, d, 5.23)	161.3
178	8.66 (H3/5, d, 18)	–245.5 (t, 18)
16b	8.04 (H4), 6.06 (H5)	23.6
97f	8.07 (H4, d, 41.2)	25.68 (d, 41.2)
98f	7.57 (H4, d, 40.5)	11.15 (d, 40.5)
174a	5.62 (H3, d, 6)	–8.7
184	5.10 (H3, d, 12)	–1.5

[a]Values collected in $CDCl_3$ at room temperature. [b]Measured against H_3PO_4 standard.

1.7 Conclusions

As detailed in this review, azaphosphinines can assume three regioisomeric geometries (1,2- vs. 1,3- vs. 1,4-) with two different valences of the phosphorus center (P^{III} vs. P^{V}). Because of the disparity in stabilities of the isomers, there is a notable difference in the amount of research published on each. The 1,2-isomers of both valences are by far the most studied, and an abundance of reaction pathways can be used to prepare them. A vast majority of the known azaphosphinine structures were prepared simply as experimental curiosities, i.e., can they be made? Recent efforts over the last decade by several groups have nonetheless demonstrated that these unique heterocycles can be used in a wide variety of applications, such as a chiral catalyst for stereospecific transformations, as a hydrogen bond donor and acceptor motif in anion receptors, as a fluorophore in cellular imaging, and as a potential pharmacophore in medical chemistry. Azaphosphinines also serve as an interesting model in how we define heteroaromatic structures. While λ^3-azaphosphinines are aromatic, λ^5-azaphosphinines most certainly are not. Nonetheless, the unique properties specific to systems containing both phosphorus and nitrogen atoms combine regions of local aromaticity with regions of unique electronic complexity. These recent studies only scratch the surface of the vast future potential uses of azaphosphinines. We for one are excited to see how this field continues to blossom over the next 10-20 years.

CHAPTER II

CONTROLLING TAUTOMERIZATION IN PYRIDINE-FUSED PHOSPHORUS-NITROGEN HETEROCYCLES

This chapter includes previously published and co-authored materials from McNeill, J. N.; Karas, L. J.; Bard, J. P.; Fabrizio, K.; Zakharov, L. N.; MacMillan, S. N.; Brozek, C. K.; Wu, J. I.; Johnson, D. W.; Haley, M. M. Controlling Tautomerization in Pyiridine-Fused Phosphorus-Nitrogen Heterocycles. *Chem. Eur. J.*, **2022**, *28*, e202200472. This manuscript was written by J. Nolan McNeill with assistance from Dr. Jeremy P. Bard, Prof. Darren W. Johnson, and Prof. Michael M. Haley. The project in this chapter was conceived by Prof. Michael M. Haley, Prof. Darren W. Johnson, and J. Nolan McNeill. The experimental work in this chapter was performed by J. Nolan McNeill. The computational work in this chapter was performed by Kevin Fabrizio with the help of Prof. Carl K. Brozek and Dr. Lucas Karas with the help of Prof. Judy I. Wu. X-ray crystallographic measurements were performed by Lev N. Zakharov and Samantha N. MacMillan.

2.1 Introduction

Exploration of phosphorus-nitrogen-containing heterocycles has been of interest to chemists since the 1960s.[1,2] Several heterocyclic species featuring the P-N bond have been reported; however, their preparation often involved difficult synthetic techniques and/or suffered from low yields. Within the last few years there have been several reports on the novel cyclization of 2-arylethynylaniline species into the phosphaquinolinone scaffold (Figure 2.1).[3–7] Because of the modular synthesis and

variety of commercially available anilines, these PN-heterocycles are easily derivatized to explore various structure-property effects. Applications related to the fluorescence and hydrogen-bond directed self-association of the phosphaquinolinone scaffold have been the primary focus of research.

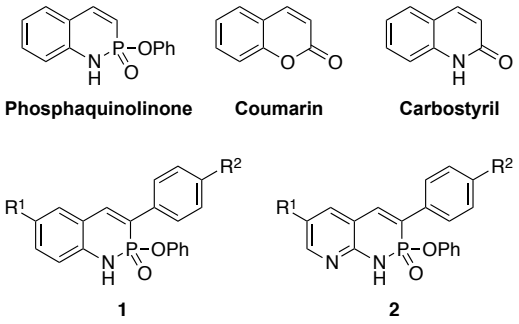

Figure 2.1 Phosphaquinolinone and analogous heterocycles (top), as well as previously derivatized PN-motif **1** and new pyridine-PN scaffold **2** (bottom).

Structurally analogous to the popular fluorophores coumarin and carbostyril (Figure 2.1), the phosphaquinolinone motif exhibits notable photophysical properties. Both the quantum yield and wavelength of emission can be tuned by alteration of the pendant functional groups as well as by fundamental changes to the acene backbone.[8–11] Use of strong electron-withdrawing groups as pendant moieties on derivatized scaffold **1** also resulted in dramatic enhancement of the heterocycle's dimerization in solution, affording dimerization constants that are one to two orders of magnitude stronger than the analogous lactam carbostyril.[3,4,12] Because of the phosphorus atom's decreased electronegativity compared to carbon, the phosphonyl motif has increased electron density on the oxygen and acts as superior hydrogen-bond acceptor.[3,7,13–16] Simultaneously, strong withdrawing groups facilitate stronger hydrogen-bond donation by pulling electron density away from the phosphonamide hydrogen, resulting in increased polarization and H-bond acidity.[17,18]

Interested in exploring the effect that an electron-withdrawing group built into the core of the heterocycle itself would have on the dimer strength, we set out to prepare a series of pyridine-bearing PN-heterocycles **2**. With the phosphonamide unit *ortho* to the pyridyl nitrogen atom, we could achieve a similar withdrawing effect, independent of the pendant groups on the backbone. Inclusion of this second N, however, does open up the potential that the aromatic form of **2a** could tautomerize into the non-aromatic quinoidal form (Figure 2.2a). While at first glance the non-aromatic quinoidal form would appear to be much less stable, we wondered if it was possible (a) to induce such a shift away from the aromatic form, and (b) to determine what factors could control the tautomer equilibrium via functional group placement, in a similar vein to the aforementioned photophysical and dimerization properties.

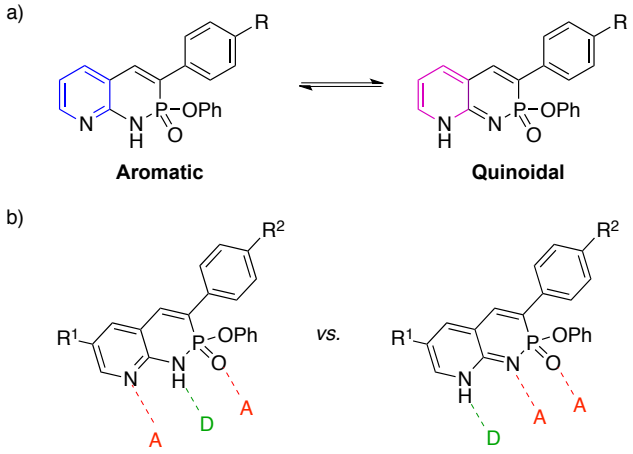

Figure 2.2 (a) The two tautomeric forms of heterocycle **2a**; colors represent aromatic (blue) core vs nonaromatic (pink) core. (b) Hydrogen-bonding nature of the aromatic (left) and quinoidal (right) tautomers.

Access to nonaromatic tautomers of heterocycles has been studied in detail but has been mainly focused on nitrogen-containing species.[19–22] The aromatic form of the pyridine-PN series has an ADA hydrogen-bonding base pair array, but this switches to DAA upon tautomerization (Figure 2.2b). Research into switchable hydrogen-bonding faces has been gaining interest due to the ubiquitous nature of hydrogen-bonding in

both biological and supramolecular processes.[23-25] Access to a strongly hydrogen-bonding heterocyclic core featuring switchable hydrogen-bonding arrays suggests practical applications in sensors or molecular recognition.

Herein we describe our initial investigations into the tautomerization of pyridine-fused PN-heterocycles, which are required to enable longer term applications in developing switchable, complementary hydrogen-bonding arrays. While ^{1}H NMR spectroscopy facilitates comparison between molecules, it cannot give direct evidence on the whether the quinoidal or aromatic form predominates; rather, strong evidence of the former is achieved in the solid state through X-ray diffraction and in solution by alkylating the heterocycle, locking the system into the quinoidal form. Interestingly, placement of a fluorine atom *meta* to the pyridyl-nitrogen reduces its basicity, resulting in a solid-state structure that does not exhibit this tautomerization. Comparing the general pyridine-PN species to their quinoidal alkylated analogues by ^{1}H NMR spectroscopy reveals consistent chemical shifts, suggesting a uniform transformation of the aromatic to quinoidal form upon going from the solution phase to the solid state.

2.2 Results and Discussion

2.2.1 Synthesis of PN-pyridines 2a-e

Inclusion of a second N-atom as part of the aromatic core to yield **2a-d** (Scheme 2.1a) begins by Sonogashira cross-coupling aminopyridine **3a** using excess trimethylsilylacetylene (TMSA) to afford alkyne **4**. Conversely, use of 4-ethynyltoluene allows one to proceed directly to tolane **5a**. Base-induced protiodesilylation of **4** followed by a second Sonogashira cross-coupling with various aryl halides gives arylethynyl aminopyridines **5b-d**.

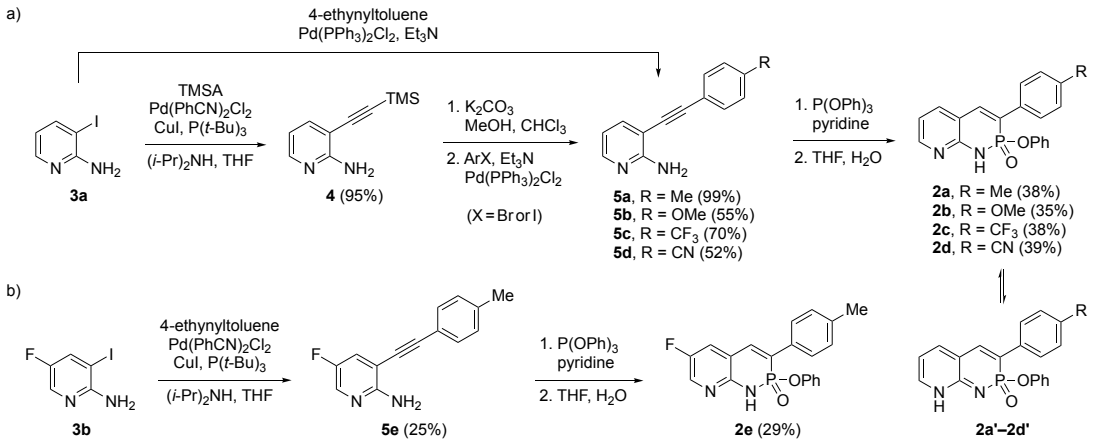

Scheme 2.1 Synthetic pathway for the preparation of pyridine-containing PN heterocycles (a) **2a-d** and (b) **2e**.

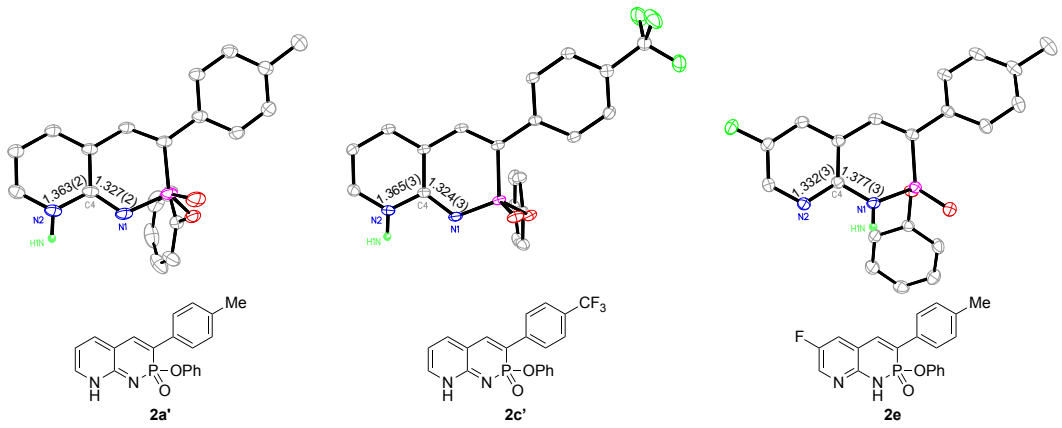

Figure 2.3 X-ray crystal structures (173 K; ellipsoids at 30% probability) and corresponding ChemDraw representations of the pyridine-fused PN-heterocycles. Heterocycles **2a'** and **2c'** display quinoidal tautomerization in the solid state whereas **2e** remains as the aromatic form. N1-C4 and N2-C4 bond lengths (Å) are shown inside the rings.

These are then reacted with $P(OPh)_3$ and pyridine for 48 h at 110 °C and subsequently hydrolyzed to afford pyridine-PNs **2a-d** in moderate yields. ^{1}H NMR spectroscopy indicates the pyridine-PN series share the wide splitting doublet (~40 Hz) of the hydrogen attached to the alkene, a result of coupling to the phosphonamide motif. The pyridyl-nitrogen being protonated in the observed tautomer also suggested the transformation may be stabilized by the pyridine's basicity. To test this hypothesis,

fluorinated pyridine-PN **2e** (Scheme 2.1b) was synthesized similarly as an electron deficient analogue to **2a**.

2.2.2 X-ray Crystallography

X-ray diffraction provided key insights into the form the different derivatives of the pyridine-PNs assume in the solid state. The bond lengths between the two nitrogen atoms and the quaternary carbon between them, N1-C4 and N2-C4, could be used to identify which nitrogen was protonated as it would have a longer C–N bond length. To determine if tautomerization is caused by the electronic nature of the pendant aryl group, crystals of both methyl- (**2a**) and trifluoromethyl-bearing (**2c**) heterocycles were obtained. Placement of the fluorine in the *meta* position relative to the pyridyl-nitrogen as in **2e** was chosen because of fluorine's Hammett σ_{meta} and σ_{para} values of 0.34 and 0.06, respectively. Due to the far weaker withdrawing effect felt by the *para* position, the phosphonamide nitrogen should experience a relatively similar electronic environment to the H-substituted derivative **2a**, allowing for an assessment of the electron withdrawing effect on only the pyridyl nitrogen.

Suitable crystals for diffraction studies were grown by slow diffusion of hexanes into a CH_2Cl_2 solution of each molecule, and the resultant X-ray structures are shown in Figure 2.3. Comparison of the N1-C4 and N2-C4 bond lengths in heterocycles **2a** (1.327(2) and 1.363(2) Å, respectively) and **2c** (1.324(3) and 1.365(3) Å, respectively) suggests both molecules assume the quinoidal forms **2a'** and **2c'** in the solid state. The lack of significant differences in the X-ray structures, combined with the similarities of the proton NMR shifts, leads to the conclusion that the aryl substituent plays little or no effect determining which tautomer is formed. Conversely, these bond lengths are reversed in heterocycle **2e**: N1-C4 is significantly longer (1.377(3) Å) and N2-C4

significantly shorter (1.332(3) Å). This latter structure supports the theory that the observed tautomerization can be inhibited by reducing the electron density in the pyridyl nitrogen, ultimately making it less basic. Interestingly, none of the molecules exhibit the P=O•••H–N homodimerization normally observed in the crystal lattice;[3] rather, molecules **2a** and **2c** arrange as zigzag 1D hydrogen-bonded "polymers" (Figures A2 and A4) with O•••N distances of ca. 2.69 Å. Heterocycle **2e** however does form a homodimer (Figure A6), but through complementary N•••H–N bonds (N•••N distance of 2.876(3) Å).

2.2.3 Heterocycle Alkylation

With the crystal structure of **2e,** we now had an example of a pyridine-PN molecule where it was no longer favorable thermodynamically to tautomerize as a solid, and to that extent in solution. Until this point, there was no way of determining the tautomer from the NMR spectra alone; however, the proton shifts of **2e** now provide evidence for characterizing this tautomer in solution. To directly contrast the aromatic proton shifts to quinoidal ones, the heterocycles were alkylated. The N-alkylation of the phosphonamide in the phosphaquinolinone scaffold is achieved by adding 1,6-diazabicyclo[5.4.0]undec-6-ene (DBU) dropwise to a stirred solution of heterocycle and alkylating reagent. Interestingly, the reaction under the same conditions with the pyridine-PN substrate results in regioselective alkylation of the pyridyl nitrogen atom rather than the phosphonamide (Scheme 2.2).

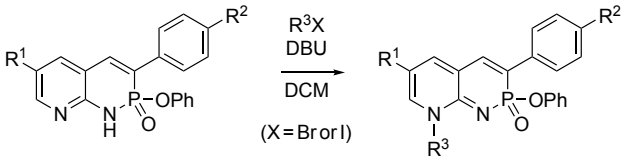

6a, R^1 = H, R^2 = Me, R^3 = Me (20%)
6b, R^1 = H, R^2 = CF_3, R^3 = Me (61%)
6c, R^1 = H, R^2 = CN, R^3 = $(CH_2)_2OH$ (39%)
6d, R^1 = F, R^2 = Me, R^3 = Me (41%)

Scheme 2.2 Synthesis of alkylated pyridine-PNs **6a-d**.

The regioselectivity of the alkylation was initially confirmed across several alkylating reagents and heterocycles by 2D HMBC NMR spectroscopy, and subsequently by X-ray crystallography for compound **6a** (Figure 2.4). Substitution at the pyridyl-nitrogen has the benefit of locking the heterocycle as the quinoidal tautomer, allowing analysis of the resulting proton shifts by ^{1}H NMR spectroscopy. When comparing the nitrogen-carbon bond lengths of all four X-ray structures to assess tautomer preference, the N1-C4 values (1.317(2)-1.327(2) Å) are consistently shorter than N2-C4 (1.363(2)-1.380(2) Å) in the quinoidal structures **2a'**, **2c'**, and **6a**, whereas the values/trend is reversed for the aromatized pyridine structure of **2e** (1.377(3) and 1.332(3) Å, respectively). In addition, the observed N1-C4 bond length in **2e** (1.377(3) Å) is on par with the bond lengths of N1-C4 (1.38-1.40 Å) in the many X-ray structures determined for derivatives of **1**.[3]

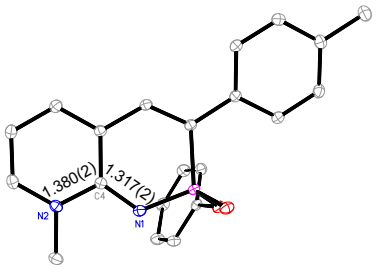

Figure 2.4 X-ray crystal structure (100 K; ellipsoids at 30% probability) of **6a**, displaying the pyridyl-nitrogen N-alkylation. N1-C4 and N2-C4 bond lengths (Å) are

shown inside the rings and are the average of the values from two independent molecules.

2.2.4 NMR Chemical Shift Comparison

The difference in proton NMR shifts from heterocycle **2e** as it is transformed into **6d** illustrates the spectroscopic changes upon molecule tautomerization. All the protons on the heterocyclic core shift upfield, which would be expected with a loss of aromaticity. The shift is most pronounced in proton H1 *ortho* to the pyridyl nitrogen. This shift is due to the increased localization of electron density *ortho* to this proton. Comparing the shifts of the analogous ring protons upon alkylation for the other heterocycles (Table 2.1), it becomes clear that all these protons are experiencing the same change in chemical environment experienced by heterocycle **2e**. Upon alkylation all the heterocycles in solution change from aromatic to quinoidal. Proton H2 is absent in heterocycle **2e**, but in the other alkylated species we observe a large and consistent

Table 2.1 Changes in the ^{1}H NMR chemical shifts (ppm) before and after the alkylation reaction to give **6a-d**.

Alkylated PN	ΔH1[a]	ΔH2[a]	ΔH3[a]	ΔH5[a]
6a	–0.75	–0.46	–0.04	–0.15
6b	–0.73	–0.56	–0.15	–0.16
6c	–0.73	–0.53	–0.13	–0.18
6d	–0.69	N/A	+0.07	–0.12
Std. Dev.	0.02 ± 0.01	0.04 ± 0.02	0.09 ± 0.06	0.02 ± 0.01

[a] Data collected in DMSO-d_6 solution. Proton assignments correspond to the atom labeling scheme shown in Figure S12.

Upfield shift that reflects the increase in electron density now that the lone pair of the tertiary amine can donate into that carbon. Conversely, protons H3 and H5, which are less influenced by the amine lone pair and thus undergo a smaller yet noticeable upfield shift due to the general loss of aromaticity. The higher standard deviation of the proton H3 shift is likely due to the proximity of the fluorine to the outlier, as the inductive withdrawing effect of fluorine will shift proton H3 on heterocycle **6d** significantly more downfield than the other non-fluorinated species. We calculated the proton NMR chemical shifts for aromatic **2a** and for its quinoidal counterpart **2a'** (as the analogue of **6a**, Figure A10) and found that computational numbers showed good agreement with the experimental trends described above. Finally, variable temperature ^{1}H NMR experiments were conducted on **2a** to explore the possibility of inducing tautomerization at higher temperatures in both polar (protic and aprotic) and less polar solvents; however, in all cases no new peaks were observed at cooled or elevated temperatures (Figures A14-A16).

In conjunction with the ^{1}H NMR analysis, the carbon NMR chemical shifts of both **2a** and **2a'** were also calculated (PCM, $CHCl_3$). Interestingly, a significant upfield shift for the signal of the carbon atom beta to N2 upon tautomerization occurs, from 116.1 to 106.7 ppm, respectively. For **2a** and **6a**, the experimental values ($CDCl_3$) for this same carbon resonance show good agreement at 116.8 and 108.3 ppm, respectively. This shifted resonance, which is a result of the quinoidal core taking on enamine-like character, should also be present in solid samples of **2a** upon tautomerization to **2a'**. To test this theory, a solid-state ^{13}C NMR spectrum was obtained for **2a**/**2a'** (Figure A16). When referenced to the remote toluene methyl groups of the solution spectra of **2a** and **6a** (21.3 and 21.4 ppm, respectively), there is a clear peak at 109.0 ppm, correlating to

said upfield-shifted carbon signal, further corroborating the quinoidal nature of **2a** as tautomer **2a'** in the solid state.

2.2.5 UV-Vis Spectroscopy Comparison

To support the evidence that PN series **2** and **6** are not the same tautomer in solution, UV-Vis spectroscopy was employed to compare the λ_{abs} of heterocycles **2a**, **2e**, **6a** and **6d** (Table 2.2). Structurally all four heterocycles are similar, with **2e** and **6d** being the fluorinated counterparts to **2a** and **6a**, respectively. Such minor differences should result in relatively small changes in absorbance unless a significant difference in conjugation is present (i.e., different tautomers). When comparing the λ_{abs} of the heterocycles, there is a large redshift in the λ_{max} as a result of alkylation (Figure 2.5). The series **2** heterocycles have similar absorbance values of 333 and 345 nm (12 nm difference), indicating similar conjugation. Likewise, the two quinoidal heterocycles have similar absorbances (15 nm difference) despite being significantly more redshifted; however, when we compare the λ_{max} as a direct result of alkylation (**2a** to **6a** and **2e** to **6d**), we observe much larger redshifts in absorbance values indicative of different conjugation patterns. In conjunction with the consistent ^{1}H NMR chemical shifts seen upon alkylation, we conclude that the solution-state heterocycles are not in the same tautomeric form as their quinoidal alkylated analogues.

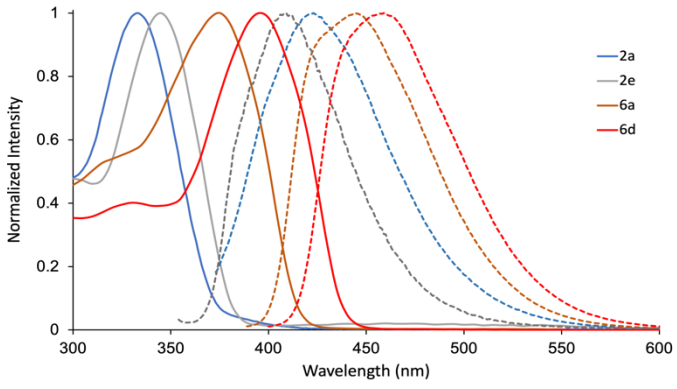

Figure 2.5 Comparison of heterocycle absorbance (solid line) and emission (dashed line) data of pre- (**2**) and post-alkylation (**6**) of PN-heterocycles.

Table 2.2 Photophysical properties of heterocycles **2a**, **2e**, **6a**, and **6d**.

PN	λ_{abs} (nm)[a]	λ_{abs} (nm)[b]	λ_{em} (nm)[a]	Stokes Shift (nm)[a]	ε (M^{-1} cm^{-1})[a]
2a	333	351	423	90	10,000
2e	345	348	409	64	17,300
6a	380	378	444	64	13,900
6d	395	—	563	68	10,900

[a] Data collected in $CHCl_3$ as ca. 10^{-5} M solutions. [b] Samples were diluted with ground $BaSO_4$ before measurement; pseudo-Lambda max were determined by peak maxima in Kubelka-Munk vs. wavelength units.

2.2.6 Solid-state UV-Vis Comparison

Because of the notably redshifted absorbance of **6a** compared to its aromatic counterpart **2a**, we were interested if this difference was visible by analyzing the photophysical properties of the heterocycles in the solid-state. Diffuse reflectance spectra were collected for compounds **2a**, **2e**, and **6a** (Figure A9) and the data are plotted in Kubelka-Munk units (Table 2.2). It is apparent from the data that compound **2a** is undergoing a change in conjugation in the solid state, as there is a ca. 20 nm redshift, indicating that the structure is becoming more like that of quinoidal form **6a**. As controls, **2e** and **6a** were assessed on the same basis and highlight the lack of bathochromic shift since no tautomerization occurs. The crystal data suggested fluorinated compound **2e** retains its aromaticity in the solid state, this is also reflected in the solid-state absorbance data. Moving from solution to solid there is a negligible change in the absorbance of **2e**. In a similar vein, heterocycle **6e** is already locked into the quinoidal tautomer in solution, and as a result, there is no redshift in the solid-state

either. These findings serve to further confirm our conclusions on the tautomeric forms these three types of pyridine-PN assume in both solution and the solid-state.

2.2.7 Calculations

To understand how solid-state packing affects the tautomeric preference of the PN-heterocycles, relative free energies at B3LYP-D3/6-311+G(d,p) and nucleus independent chemical shifts at PW91/IGLOIII were computed for **2a** (aromatic form) and **2a'** (quinoidal form), as well as the protonated analogues of the two tautomers (see Figure 2.6). Protonated tautomers were considered as models for the effects of hydrogen-bonding on monomers in the solid state of the PN-heterocycle. As shown in Figure 6, **2a** is 8.3 kcal mol^{-1} lower in energy than **2a'** (top); however, this trend reverses for the protonated set, and the quinoidal form is 6.3 kcal mol^{-1} lower in energy than the aromatic form (bottom). These results suggest that hydrogen-bonding may shift the tautomeric preference of the PN-heterocycle towards **2a**.

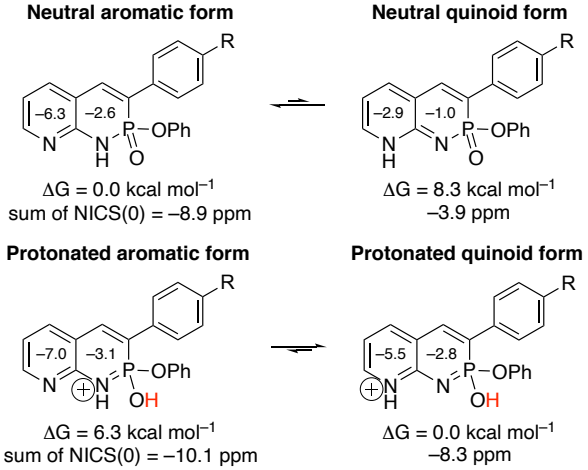

Figure 2.6 Computed relative free energies (ΔG, kcal mol^{-1}) and NICS(0) (ppm) values for **2a** vs. **2a'** (top) and their protonated analogues (bottom).

Computed nucleus independent chemical shifts (NICS)[26.27] suggest that, in the solid state, the hydrogen bonded PN-heterocycles adopt a dominant quinoidal form as

a result of aromaticity gain. Similar effects of hydrogen bonding assembly on aromaticity gain are known and have been reported.[28-32] Isotropic NICS(0) values were computed at each of the six-membered ring centers of the PN-heterocycles, and the sum of NICS(0) values were compared to quantify the aromatic character of the tautomers. Here, we applied the NICS(0) index so that computed data for **2a** and **2a'** could be compared directly to isotropic NICS(0) data computed for a tetramer assembly of PN-heterocycles (Figure A12). In the tetramer assembly, placing NICS probes at the ring centers (i.e., 0 Å) of a PN-heterocycle (rather than at 1 Å or other distances) avoids spurious magnetic shielding effects that can arise from stacking arrangements of the monomers.

As shown in Figure 2.6, the computed sum of NICS(0) value for **2a** is large and negative (–8.9 ppm), and that of the protonated form is close in value (–10.1 ppm). In sharp contrast, the computed sum of NICS(0) value for **2a'** is modestly negative (–3.9 ppm) but the protonated form becomes considerably more so (–8.3 ppm), indicating aromaticity gain. NICS computed for a tetramer assembly of PN-heterocycles also support a dominant quinoidal form and illustrates the effects of aromaticity gain of the hydrogen bonded monomers (see Figures A11 and A12). Even in the absence of hydrogen bonding, computed Hirshfeld charges for **2a'** suggest that there is a tendency for the nonaromatic quinoidal form to aromatize (i.e., through a zwitterionic resonance form; see Figure A13 and discussion in the Supporting Information). Hydrogen bonding helps aromatize the π-system of **2a'** even more. Importantly, these results suggest that solid state packing and the opportunity for hydrogen-bonding can shift the tautomeric preference of self-assembling heterocycles.

2.3 Conclusion

In summary, this work reports on the synthesis of novel pyridine-bearing PN-heterocycles. By X-ray diffraction, we observed that the heterocycles exhibit an unexpected change to a nonaromatic tautomer in the solid state. In the interest of controlling this transformation, it was necessary to understand the environmental and chemical factors that induce this change. Computational analysis concluded that the pyridine-PN scaffold becomes more thermodynamically stable as the intermolecular forces between heterocycles increases. While the identity of the pendant aryl substituent seemingly had no effect on the tautomerization, we found that reducing the basicity of the pyridyl nitrogen preserved the aromatic form in the solid state, e.g., **2e**. Alkylation of this persistently aromatic heterocycle locked it into the quinoidal form. Comparison of the shifts in both the proton and carbon NMR spectra to other similarly alkylated heterocycles indicated extremely consistent trends as a result of this tautomeric change. Taken as a whole (solution and solid-state NMR, solution and solid-state UV-Vis, X-ray, calculations), this study suggests every heterocycle assessed starts aromatic in solution and only shifts to the quinoidal form upon solidification (**2a**-**d**) or alkylation (**6a**-**d**). This work will assist future efforts to develop novel and switchable, complementary hydrogen-bonding base pairs for use in selective molecular recognition and sensors.

CHAPTER III

IMPACT OF INTERNAL CHARGE TRANSFER ON THE PHOTOPHYSICAL PROPERTIES OF PYRIDINE-FUSED PHOSPHORUS-NITROGEN HETEROCYCLES

This chapter includes previously published and co-authored material from McNeill, J. N.; Kascoutas, M. A.; Karas, L. J.; Zakharov, L. N.; Wu, J. I.; Johnson, D. W.; Haley, M. M. Impact of Internal Charge Transfer on the Photophysical Properties of Pyridine-Fused Phosphorus-Nitrogen Heterocycles. *Chem. Eur. J.* **2023**, *29*, e202203918. This manuscript was written by J. Nolan McNeill and Prof. Michael M. Haley with editorial assistance from Melanie A. Kascoutas and Prof. Darren W. Johnson. The project in this chapter was conceived by Prof. Michael M. Haley and J. Nolan McNeill. The experimental work in this chapter was performed by J. Nolan McNeill and Melanie A. Kascoutas. The computational work in this chapter was performed by Dr. Lucas J. Karas with assistance from Prof. Judy I. Wu. The X-ray crystallography work in this chapter was performed by Lev N. Zakharov.

3.1 Introduction

Small molecule fluorescent probes have been of great interest in recent years due to their myriad applications. In many cases, small molecules are preferable to larger oligomeric or polymeric materials because of their highly defined nature, as well as their ease of structural modification to fit a specific use.[1-4] Among small molecule fluorophores, coumarin (2*H*-1-benzopyran-2-one, Figure 3.1) stands out as a privileged

scaffold that has garnered significant attention. Coumarin and its derivatives have been applied to a wide variety of sensing applications including detection of anions, pH, metals, reactive oxygen species (ROS), and more.[5-9]

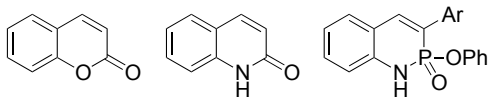

Figure 3.1 Coumarin, carbostyril, and phosphaquinolinone scaffolds.

Since 2015, we have been studying the properties of the rarely-accessed phosphaquinolinone scaffold.[10–14] The heterocyclic core is structurally similar to both coumarin and carbostyril—coumarin's aza-counterpart—the difference being that the carbonyl has been replaced with an isolobal phosphonyl group (Figure 3.1). The structural similarities of the phosphaquinolinone scaffold to coumarin and carbostyril also extend to other features, including the highly tunable and substitution-dependent photophysical properties as well as the homodimerization seen in lactams.[15] Beyond this, these phosphorus-nitrogen (PN) heterocycles boast the benefit of containing a chiral center on the phosphorus atom and stronger homodimerization due to the highly polarized P=O bond. The tetrahedral center has been shown to facilitate the selective binding of hydrogen sulfate, a typically difficult anion to host due to its geometry and combination of both hydrogen-bond donor and acceptors.[16]

More recently, we have reported a small family of phosphaquinolinone analogues containing a pyridine ring in the backbone (**1**, Figure 3.2). This nitrogen atom, when located "*ortho*" to the phosphonamide face, undergoes an interesting tautomerization, in which a quinoidal, nonaromatic isomer **1'** is preferred in the solid state.[12] In this current

work, we have moved the location of the nitrogen to be "*meta*" to the phosphonamide face. Doing so means that the "3-pyridine PN" (**2**) is no longer capable of this tautomerization. Instead, we are now left with a species that has a linear conjugation pathway from its aryl-substituent down through the electron-withdrawing pyridyl nitrogen. As observed in fluorescent coumarin derivatives, internal charge transfer (ICT, **2'**) occurs when an electron donating unit is conjugated through a variety of possible linkers to an electron accepting unit.[17–22] This phenomenon has been widely studied in several systems, and the impact upon photophysical properties depends on several factors including molecule rigidity, linker distance, and steric hindrance of the electronic groups.

The initial product of the PN cyclization reaction is the phosphaquinoline (imidate, **I**) counterpart to the phospha-quinolinone form (amidate, **A**). X-ray data of both forms suggested that the imidates possess more uniform bond lengths across the heterocyclic core, implying superior conjugation (Figure 3.2).[10] In prior studies, we have generally omitted data concerning the imidate form because of its facile hydrolysis into the amidate, and its inability to engender the hydrogen bond dimerization observed in the amidates. However, the inclusion of the 3-pyridine motif in the core of the PN-heterocycle dramatically increases imidate stability, affording a good opportunity to explore this species. In the interest of maximizing conjugation in the system and promoting ICT effects, we report the synthesis of several 3-pyridine PN-heterocycles as both their imidate and amidate forms, documenting and comparing the observed photophysical properties. The aryl substituents chosen vary in electron-donating and -withdrawing capabilities to illustrate the scaffold's capacity for ICT. There is also a notable positive solvatochromism

observed as a result of the quinoidal excited charge transfer state responsible for the ICT emission.[23–25]

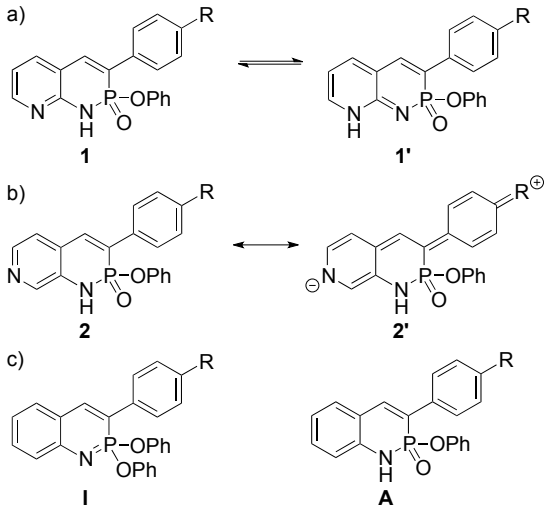

Figure 3.2. a) 2-Pyridine PN (**1**) and its key tautomeric form **1'**.[12] b) 3-Pyridine PN (**2**) and the highly-polarized quinoidal resonance form **2'**. c) Comparison between imidate (**I**) and amidate (**A**) forms of the PN-heterocycle scaffold.

3.2 Results and Discussion

3.2.1 Synthesis of 3-pyridine PNs

We selected four functional groups (R–) that cover a range of Hammett σ_{para} values, from trifluoromethyl (0.54) to *N,N*-dimethylamino (–0.83).[26] The cyclization precursors **5** were prepared by Sonogashira cross-coupling of aminopyridine **3** with either the corresponding 4-ethynylarene (**a-c**) or first with trimethylsilylacetylene to give **4** followed by protiodesilylation and a second Sonogashira reaction with 4-iodo-*N,N*-dimethylaniline (**d**). A range of different Sonogashira conditions was applied across the various substitutions (see Appendix B) All 3-amino-4-(4-arylethynyl)pyridines (**5**) were then cyclized using $P(OPh)_3$ in imidazole at 150 °C. Our lab has traditionally performed this

cyclization with pyridine as the solvent at 110 °C for 1-2 days;[11] however, we recently found that use of imidazole, which boils significantly higher (256 °C), reduces reaction times from days to hours with no apparent decrease in yield. The purification of these modified cyclizations is also considerably simpler as imidazole is a solid at room temperature and thus is easier to remove from the reaction compared to pyridine. The product of this cyclization is the imidate form (**6**) of the PN-heterocycles. As noted earlier, X-ray crystallography has shown that the bond length of the isolated alkene in the PN-ring is noticeably longer in this form, suggesting better conjugation across the PN-core. Imidates **6** can be converted into the amidate PN-heterocycles **2** via mild hydrolysis; however, imidate **6d** required slightly more rigorous conditions (30% aq. H_2SO_4, 70 °C) to hydrolyze.

Scheme 3.1. Synthesis of 3-Pyridine PNs.

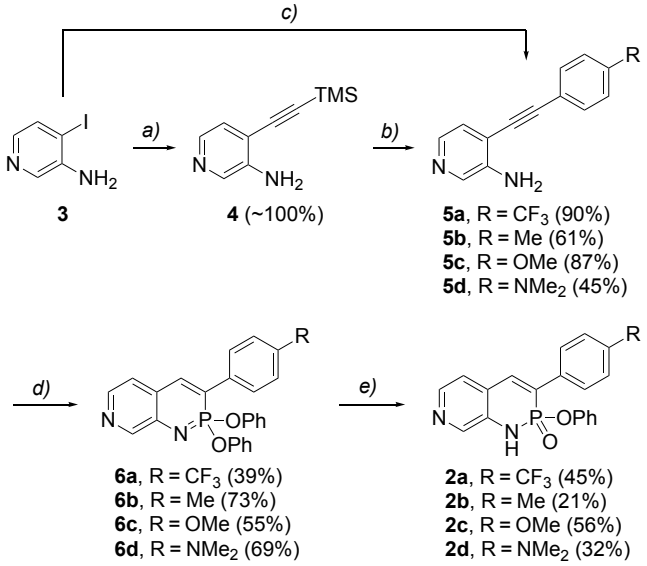

a) Trimethylsilylacetylene, $[Pd(PPh_3)_2Cl_2]$, CuI, Et_3N, THF. *b)* i) K_2CO_3, MeOH, $CHCl_3$; ii) 4-iodo-*N,N*-dimethylaniline, $[Pd(PPh_3)_2Cl_2]$, CuI, Et_3N, THF. *c)* for **5a:** 4-ethynyl(trifluoromethyl)benzene, $[Pd(PhCN)_2Cl_2]$, CuI, *10% wt/v* P(*t*-Bu)$_3$, (*i*-Pr)$_2$NH, THF; for **5b**: 4-ethynyltoluene, $[Pd(PPh_3)_2Cl_2]$, CuI, Et_3N, THF; for **5c**: 4-ethynylanisole,

[$Pd(PhCN)_2Cl_2$], CuI, *10% wt/v* P(*t*-Bu)$_3$, (*i*-Pr)$_2$NH, THF. *d)* P(OPh)$_3$, imidazole, 150 °C. *e)* for **2a-2c**: H_2O, THF; for **2d**: 30% aq. H_2SO_4, MeCN, 70 °C.

3.2.2 Absorption and Emission Data

Comparison of the absorption spectra of the 3-pyridine PNs as both imidates (**6**) and amidates (**2**) makes the effect of the aryl substituent easily visible. Every heterocycle in both forms displays two absorption bands, where the higher energy band corresponds to the π-π* transition while the lower energy band is that of the internal charge transfer. As would be expected, the intensity of the ICT band relative to the π-π* band is proportional to the electron donating capabilities of the aryl substituent (Figure 3.3).[27] A summary of the absorption data between both the higher and lower energy bands and the emissions are given in Table 3.1.

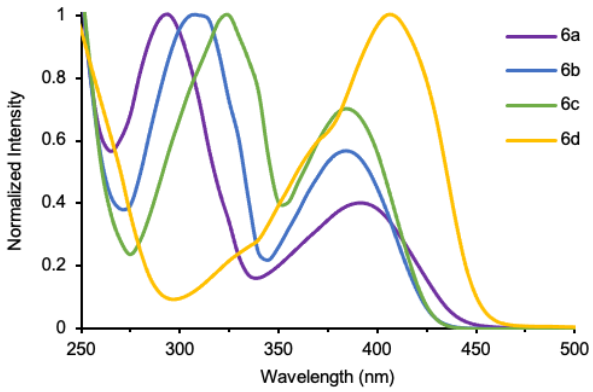

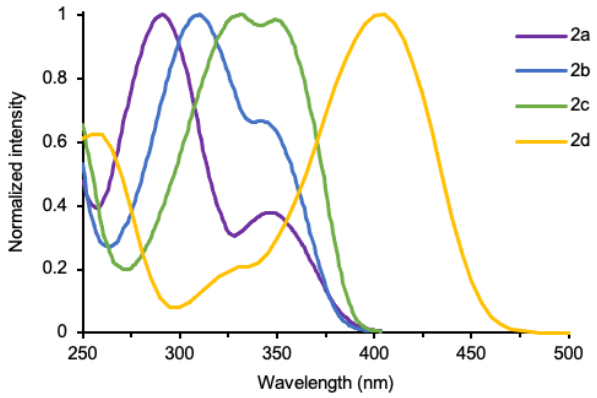

Figure 3.3 Electronic absorption spectra of imidates **6** (top) and amidates **2** (bottom) in $CHCl_3$ (~10^{-5} M) at room temperature.

As the electron-donating ability of the substituent increases, the extinction coefficient ε of the lower energy absorption band grows closer to that of the higher energy band. Finally in heterocycles **2d** and **6d**, the donor strength of the *N,N*-dimethylamine substituent flips the relative ratios of the extinction coefficients to where the ICT band is now stronger than that of the π-π*. The ~20 and ~60 nm range of bathochromic shifts observed in the ICT bands of heterocycles **6d** and **2d**, respectively, compared to the relatively constant absorption values of the other ICT bands, suggests a higher degree of linear conjugation. The stokes shift is consistently smaller in the imidate forms of each heterocycle. This data is corroborated by previous observations in crystal structures of imidates that suggest a higher degree of conjugation based on more uniform bond lengths.[11] Within the two series of heterocycles, the more electron-rich aryl substituents lead to a smaller stokes shifts as a result of better conjugation. For both the amidate and imidate heterocycles, there is no clear trend in the λ_{max} of the lower energy band, with the inductively donated **2b** absorbing bluer or at the same wavelength as the inductively withdrawn **2a**.

The dominant absorption of the ICT bands in **6d** and **2d** made these compounds interesting candidates for solvatochromic studies. The emissive species resulting from the

excited state charge transfer is the highly polar quinoidal resonance form (Figure 3.2b). As such, the stability of this more polar structure should be highly dependent on solvent. Both *N,N*-dimethylamine bearing species had their absorption and emissions compared in toluene, $CHCl_3$, and DMSO to observe the photophysical effects resulting from different solvent polarities (Figure 3.4; summarized in Table 3.2). It is interesting to note that across both forms, the λ_{abs} remains relatively consistent. This suggests that the ground states of **6d** and **2d** are similar, independent not only of the solvent but also of whether being in the amidate or imidate form. It is instead the linear conjugation from donor to acceptor unit that drives this absorption. Despite this, there is a notable positive solvatochromic trend in the emission spectra. A bathochromic shift of emission is observed with increasing solvent polarity while the absorption stays relatively constant. This is due to the highly polarized excited state being significantly more stabilized by polar media. This then leads to lower energy, redder emission and corroborates the hypothesis that the ICT emission is the predominant band and is excited from a neutral ground state molecule. Interestingly, when

Table 3.1 Experimental and computational photophysical properties of amidates **2** and imidates **6**.

	experimental							calculated[c]	
Cmpd	Higher energy λ_{abs} (nm)[a]	ε_{high} (cm^{-1} M^{-1})[a]	Lower energy λ_{abs} (nm)[a]	ε_{low} (cm^{-1} M^{-1})[a]	λ_{em} (nm)[a]	Stokes shift (cm^{-1})[a]	Φ (%)[b]	S_1 (nm)	S_2 (nm)
6a	295	15,800	390	7,200	475	4,590	22	—	—
6b	310	14,000	385	7,700	459	4,190	9	—	—
6c	325	19,500	385	13,400	456	4,040	11	—	—
6d	375	13,700	405	21,500	468	3,320	72	—	—
2a	291	14,300	346	5,100	434	5,860	32	353	315
2b	310	23,200	341	15,400	420	5,520	18	351	313
2c	331	14,000	351	13,400	415	4,390	45	366	317
2d	330	4,500	405	21,000	489	4,240	90	428	322

[a] Data collected in $CHCl_3$ as ~10^{-5} M solutions at room temperature. Stokes shifts calculated from lower energy band. [b] Data collected in $CHCl_3$ and measured against

standards of quinine in 0.1 M H_2SO_4 (aq.) (λ_{ex} = 365 nm, Φ = 0.54) and anthracene in EtOH (λ_{ex} = 365 nm, Φ = 0.27).[28] [c] Calculated excitation energies at PCM-B3LYP-D3/6-311+G(d,p) with $CHCl_3$ solvent.

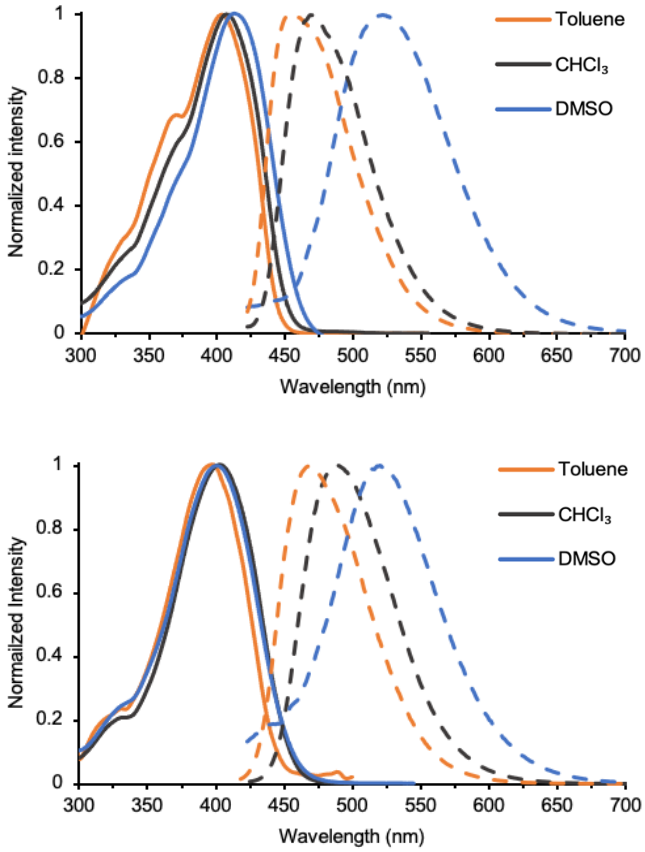

Figure 3.4 Absorption (solid) and emission (dashed) spectra of a solvatochromic study on **6d** (top) and **2d** (bottom) taken at room temperature.

Table 3.2 Solvatochromic photophysical measurements of **6d** and **2d**.

[a] Data collected in $CHCl_3$ at room temperature.

Compound	Solvent	λ_{abs} (nm)[a]	λ_{em} (nm)[a]	Stokes shift (cm^{-1})[a]
	toluene	405	458	2,860
6d	$CHCl_3$	405	469	3,370
	DMSO	415	521	4,900
	toluene	395	468	3,950
2d	$CHCl_3$	405	489	4,240
	DMSO	400	520	5,770

considering the fluorescence of **6** and **2**, there is a dramatic hypsochromic shift in the emission of amidates **2a-c** (Figure 3.5). This shift is not present in the corresponding imidates, where the emissions are all within 20 nm of one another. This is likely another example of how hydrolyzing the heterocycles into the amidate form begins to interrupt the conjugation of the system. Only the heterocycle with the strongest electron donor **2d** can force the aryl substituent into planarity and as a result, retain the lower emission observed in all the imidates.

There are an extremely limited number of molecules in the literature that resemble heterocycles **6** and **2**. While the coumarin analogues of **2b** and **2c** are known,[29] no photophysical data were reported, and the other coumarins as well as the carbostyril

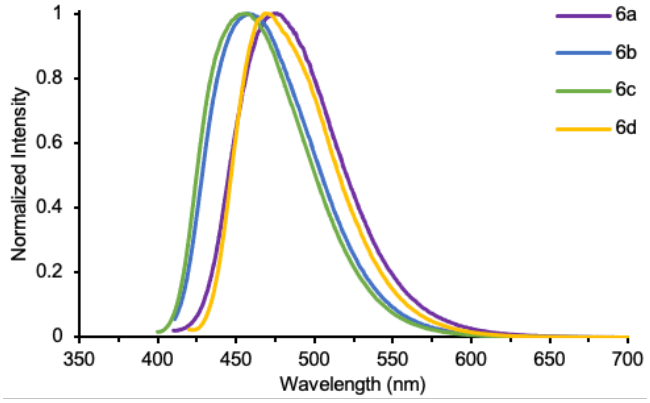

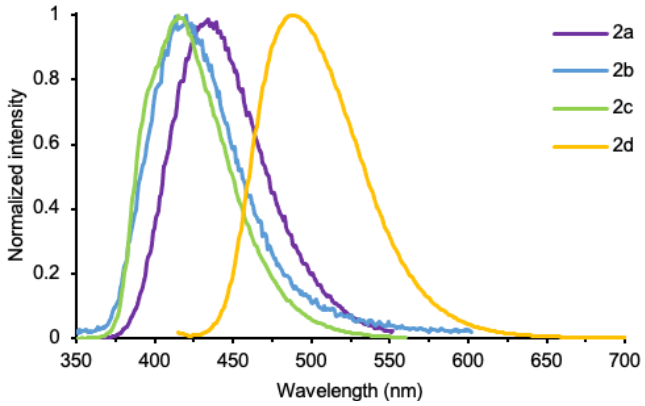

Figure 3.5 Emission spectra of **6** (top) and **2** (bottom) in $CHCl_3$ at room temperature.

analogues are unknown; thus, drawing conclusions to assess the effect that inclusion of the PN moiety has on the photophysical data is difficult. A recent publication from Cao and co-workers, however, performed an extensive investigation into the photophysical properties of stilbazoles.[30] In particular, the authors analyzed *para*-substituted species that bare a marked similarity to the 3-pyridine PNs, excluding the PN moiety (Figure 3.6). Comparison of the λ_{abs} for the *para*-substituted stilbazoles to those of heterocycles **6** and **2** would indicate how attaching the PN motifs directly impact the observed absorption, versus what effect is simply a result of the donor-acceptor (D-A) system. Three of the molecules Cao studied were direct counterparts to PNs **a-c** (R = CF_3, Me, OMe), while the NMe_2-bearing stilbazole corresponding to **6d**/**2d** was prepared following a procedure from Pepitone et al.[31]

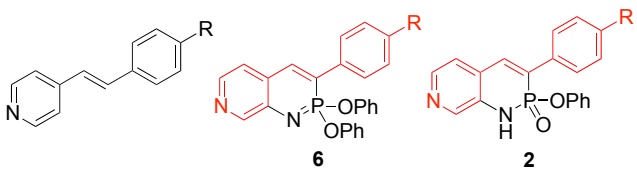

Figure 3.6 Example of *para*-substituted stilbazole (left) and the motif superimposed on imidate PN **6** and amidate PN **2**.

Table 3.3 Selected bond lengths (Å) and dihedral angle (°) of **2a-d**, **2d'**, and **6d**.

	2a	**2b**	**2c**	**2d**	**2d'**	**6d**[a]
C1–C2	1.351(2)	1.352(2)	1.346(2)	1.360(3)	1.354(4)	1.372(8)/1.375(8)
C2–C3	1.444(2)	1.446(2)	1.448(2)	1.439(3)	1.446(4)	1.443(8)/1.441(8)
C3–C7	1.401(2)	1.400(2)	1.400(2)	1.397(3)	1.400(4)	1.407(9)/1.404(8)
C6–C7	1.374(2)	1.371(2)	1.372(2)	1.376(4)	1.370(4)	1.359(9)/1.369(9)
N2–C6	1.347(2)	1.342(2)	1.345(2)	1.352(4)	1.343(4)	1.350(10)/1.343(9)
C1–C8	1.488(2)	1.490(2)	1.479(2)	1.473(3)	1.466(4)	1.473(7)/1.475(7)
C8–C9	1.394(2)	1.400(2)	1.401(2)	1.393(3)	1.401(4)	1.397(9)/1.396(9)
C9–C10	1.381(2)	1.383(2)	1.379(2)	1.378(3)	1.374(4)	1.375(9)/1.374(8)
C10–C11	1.386(2)	1.393(2)	1.393(2)	1.401(4)	1.418(4)	1.407(10)/1.408(9)
dihedral ∠ C2-C1-C8-C9	38.7(2)	23.3(2)	39.2(2)	0.4(4)	27.4(4)	20.6(8)/20.0(8)

[a] Crystal structure contains two nonequivalent molecules. Both sets of bond lengths and dihedral angles listed

The UV-Vis spectra of series **6** and **2** were collected in anhydrous EtOH (Figure B15) to give a direct comparison to the absorption values found by Cao. In each case, inclusion of the PN ring facilitated the development of the low energy ICT band that was not present in any stilbazole. While the π-π* band seems relatively unaffected by the presence of the PN, the ICT band is 60–30 nm red shifted for series **6** and 40–18 nm red shifted for series **2** (Tables B1 and B2). It is interesting that the higher energy band is nearly identical from stilbazole to PN, suggesting that the presence of the PN moiety has little-to-no effect on that transition. Despite this, said moiety is crucial to facilitating the ICT band, even in the presence of a strong D-A pair such as the NMe_2-bearing stilbazole.

3.2.3 X-ray Crystallography

Crystals suitable for X-ray diffraction were grown of via slow vapor diffusion of hexanes into CH_2Cl_2 (**2a**-**d**) or Et_2O into MeOH (**2d'** and **6d**). Structures for imidate **6d** and amidate **2d** are shown in Figure 3.7 with the relevant atoms labeled (see also Figures B1-B14). As discussed previously, the primary difference between the six structures is the dihedral angle between carbons C2-C1-C8-C9 (Table 3.3). In heterocycles **2a**-**c**, and in nearly every PN structure previously analyzed by X-ray diffraction, there is an appreciable 30-40° angle between the planes of the aryl substituent and the PN core. This out of plane twisting disrupts the conjugation throughout the π-network; however, **2d** has a dihedral angle of almost 0°, likely due to the strong donor-acceptor behavior present even in the ground state. The superior conjugation of **2d** not only leads to a lower energy absorption but also keeps the emission from undergoing the hypsochromic shift the other amidates experience as a result of hydrolysis. Interestingly, this is the most co-planar example of

any PN-structure we have observed by X-ray crystallography.[11] Indeed, the other heterocycles in the series (**2a-c**) have considerably larger dihedral angles ranging from 23-39°.

The bond lengths of the different heterocycles shows that there is a clear development of more quinoidal characteristics increasing with the electron donating capabilities of functional group. In a more quinoidal system there should be an alternation of bond lengths with more single-bond character in C11–C10 and C9–C8. This indicates the emerging stability of the charge-transfer resonance form even in the ground state. This follows the expected trend of $–CF_3$ < –Me < –OMe < $–NMe_2$. Interestingly, despite being only inductively donating, the methyl substituent of **2b** is still capable of causing slightly stronger bond-length alternation than **2a**. Comparison of the structure of imidate **6d** with amidate **2d** suggests that the former possesses even stronger bond-length alternation, though the larger uncertainty in the data does not permit meaningful analysis. Molecules **2a**, **2b**, and **2d** pack as a *meso*-dimeric pair, which is typical of a majority of PN-heterocycles.[11,14] On the other hand, **2c** forms a staggered, repeating hydrogen bonding "polymer", where the N–H and P=O moiety of each monomer coordinates with a different heterocycle, forming a continuous zigzag chain, a pattern we have also observed in some PN-heterocycles.[14]

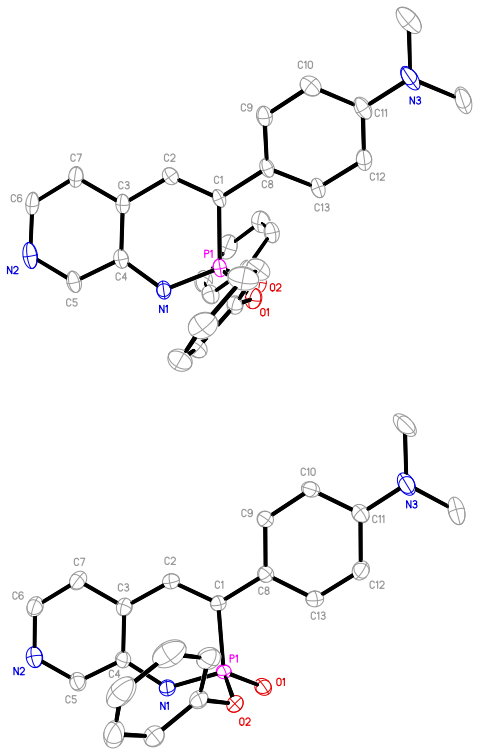

Figure 3.7 Crystal structures of imidate **6d** (top) and amidate **2d** (bottom) with labeled atoms; ellipsoids drawn at the 30% probability level.

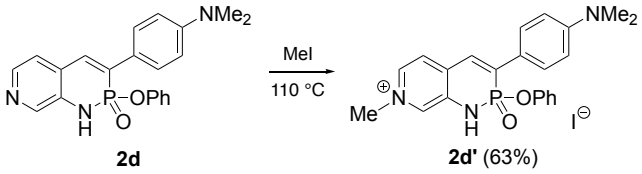

Scheme 3.2 Synthesis of *N*-methyl pyridinium PN heterocycle **2d'**.

To probe the possible enhancement of this bond-length alternation and coplanarity, **2d** was methylated to make an even stronger donor-acceptor pair in **2d'** (Scheme 3.2). Interestingly, only the pyridine nitrogen was methylated; no evidence of reactivity at the –

NMe_2 group was observed, again supporting the contribution of resonance form **2'**. This reactivity parallels that found in 4-(*N,N*-dimethylamino)pyridine,[32,33] of which **2d** could be considered an expanded DMAP analogue. Compared to the data of the non-methylated heterocycles, the NMe_2-aryl substituent exhibits the greatest degree of bond-length alternation within the stilbazole motif (Table 3.3), suggesting higher contribution of the quinoidal resonance structure in that ring. Interestingly though, the high degree of coplanarity seen in **2d** is no longer observed and the bond-length alternation in the core of the heterocycle itself is not notable in comparison to the others. This departure from coplanarity may be due to the bulky iodide anion that causes the aryl ring to rotate slightly so it may be closer in space as seen in the crystal packing (Figure B11). The packing of pyridinium **2d'** reveals a dimeric pair to minimize dipole-dipole interactions with a close contact of 3.057(3) Å where O1 of one molecule points into C6 of its neighbor (Figure S12). The PN dimers are linked throughout the lattice by additional P=O•••CH interactions with the pyridinium N–Me (3.078(3) Å / 165(3)°) and Ar–H (3.362(4) Å / 155°) motifs. Finally, the amidate N–H shows a close interaction (3.549(2) Å / 167(3)°) with the iodide anion.

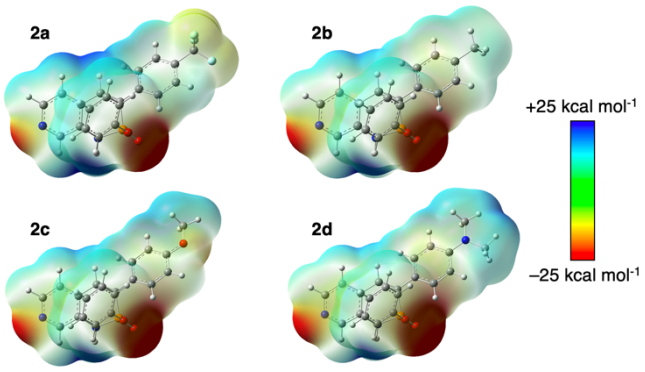

Figure 3.8. Computed molecular electrostatic potential maps for **2a-2d** at B3LYP-D3/6-311+G(d,p); the pyridine N atom is on the left.

3.2.4 DFT Calculations

Computed molecular electrostatic potential (MEP) maps for the series of 3-pyridine PN heterocycles, **2a-2d**, document increased internal charge transfer (ICT) in **2d**, resulting from a more electron donating aryl R group (R = NMe_2). Figure 3.8 shows an increasingly electron-rich N3 position in **2d** (note the larger red colored region at N3 on the left side of the MEP plot). Computed natural bond orbital (NBO) charges at the N3 atom for **2a** (–0.425), **2b** (–0.431), **2c** (–0.432), **2d** (–0.436) agree and show more negative charges for **2d**. These results suggest that the high intensity ICT absorption band observed for **2d** (Figure 3, right) may arise from charge accumulation at the N3 position Excitation energies to the S_1 (ICT) and S_2 ($\pi\pi^*$) states for **2a**–**2d** (Table 3.1) were computed with implicit solvation (PCM, solvent = $CHCl_3$) and match well with the experimental absorption data. All computations were performed at the B3LYP-D3/6-311+G(d,p) level employing Gaussian16.[34]

3.3 Conclusions

Herein we have reported the synthesis and characterization of a small family of pyridine-containing derivatives of the phosphaquinolinone (amidate **2**) scaffold. Through selective placement of the pyridyl nitrogen atom, linear conjugation through the aryl substituent is facilitated. Substitution of the aryl ring with increasingly electron donating groups leads to a red-shifted internal charge transfer band. In the case of the strongest donor **2d** this charge transfer band becomes the predominant absorption band. The wavelength of

emission from this highly polarized excited state is dependent on solvent polarity. A positive solvatochromic trend is observed due to the stabilization of the excited state in more polar media. Comparison of the UV-Vis spectra of the PN-heterocycles to analogous stilbazoles showed that the PN moiety is necessary for the ICT band, even in the presence of a strong D-A system.

CHAPTER IV

THIONATION OF THE 2-λ^5-PHOSPHAQUINOLIN-2-ONE SCAFFOLD WITH LAWESSON'S REAGENT

This chapter includes previously published and co-authored material from Bard, J. P.; McNeill, J. N.; Warren, G. I.; Zakharov, L. N.; Johnson, D. W.; Haley M. M. Thionation of the 2-λ^5-Phosphaquinolin-2-one Scaffold with Lawesson's Reagent. *Isr. J. Chem.* **2021**, *61*, 217–221. This manuscript was written by Prof. Jeremy P. Bard and J. Nolan McNeill with editorial assistance from Profs. Darren W. Johnson and Michael M. Haley. The project in this chapter was conceived by Profs. Jeremy P. Bard, Darren W. Johnson, and Michael M. Haley. The experimental work in this chapter was performed by Jeremy P. Bard and J. Nolan McNeill. The computational work in this chapter was performed by Gabrielle I. Warren. The X-ray crystallographic work in this chapter was performed by Lev N. Zakharov.

4.1 Introduction

Lawesson's reagent (LR, Figure 4.1) is a widely-used thionating reagent that converts carbonyl groups into their respective thiocarbonyls, with several authoritative reviews highlighting its utility.[1,2] This reagent reacts with a wide variety of carbonyl-containing scaffolds, including, but not limited to, ketones, amides, imides, and aldehydes. These transformations, beyond being structurally interesting, often lead to changes in the physicochemical properties of the scaffolds between the oxo and thio forms.

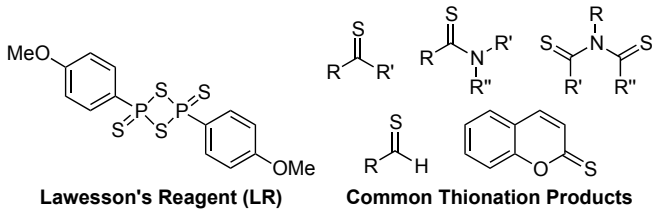

Figure 4.1 Lawesson's Reagent and a sampling of commonly prepared thiocarbonyl compounds.

One framework of particular interest that has served as a substrate for LR is the well-studied fluorescent lactone coumarin.[3–6] Coumarin, as well as other related fluorescent carbonyl-containing systems, exhibit red-shifted emissions and decreased quantum yields upon thionation with LR. Additionally, in many cases the thio form can be converted back to the respective oxo form through various means, a transformation which often shows a turn-on fluorescence response.[5,7–9] Additionally, similar non-aromatic aminophosphonic esters have been converted to their respective thio forms as well.[10-12] The utility of LR and the physicochemical changes it imparts upon the substrates pose the question: what other carbonyl-like systems can be similarly modified?

In recent years, we have reported the synthesis and physicochemical studies of the coumarin-like 2-λ^5-phosphaquinolin-2-one scaffold.[13] In addition to their well-defined self-specific meso-dimerization, these phosphorus- and nitrogen-containing (PN) heterocycles have tunable emissive properties. Similar to the aforementioned analyses of coumarin derivatives, we have reported a series of studies to modify and improve the physicochemical properties of the 2-λ^5-phosphaquinolin-2-ones through substituent group alteration, phosphorus center modification, and acene backbone elongation.[13–15] To further explore the versatility and modularity of the phosphaquinolinone scaffold, we

report herein the conversion of the phosphine oxide into the corresponding thionate form using Lawesson's reagent and discuss in detail the resultant structural and photophysical changes.

4.2 Results and Discussion

To accomplish this study, oxo-heterocycles **1a-1f** were prepared as previously reported.[14,15] These were treated with LR in dry toluene under N_2 at reflux until only trace starting material was observed via TLC (ca. 24 h), affording thio-heterocycles **2a-2f** in modest to very good isolated yield (Scheme 4.1). The purification of heterocycles **2** nonetheless presented some challenges, as the reaction biproducts of LR are structurally similar to the attained products and/or may coordinate with the donor-acceptor face of the PN product. In the case of **2a**, this meant multiple rounds of silica gel chromatography and recrystallization, resulting in material likely being lost in purification and thus the diminished isolated yield.

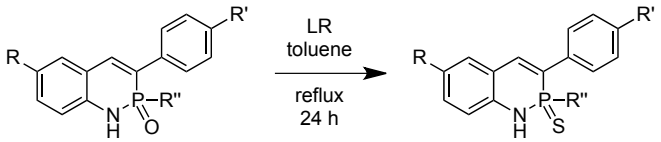

1a	R = *t*-Bu, R' = Me, R'' = OPh	**2a** (27%)
1b	R = H, R' = CN, R'' = OPh	**2b** (60%)
1c	R = *t*-Bu, R' = CN, R'' = OPh	**2c** (60%)
1d	R = H, R' = CN, R'' = Ph	**2d** (59%)
1e	R = *t*-Bu, R' = CN, R'' = Ph	**2e** (89%)
1f	R = CF_3, R' = CN, R'' = Ph	**2f** (59%)

Scheme 4.1 Conversion of oxo-heterocycles **1** to thio-heterocycles **2** with Lawesson's Reagent (LR).

Heterocycles **2** were examined by NMR spectroscopy (Figures C7-C25). First, the ^{31}P NMR signals shift significantly downfield (~ 30-35 ppm) from their respective oxo

analogs **1**, appearing around 40-50 ppm, which can be explained by the larger deshielding effect that the sulfur has upon the P center as seen for other examples in the literature.[2] Furthermore, the proton NMR spectra show the characteristic $^{3}J_{\{31P,1H\}}$ coupling between the P center and the carbon in the isolated C=C bond along the backbone. The coupling constants range from 30.5-37.7 Hz, and correlate to the standard splitting seen in these systems; however, the N–H proton signal appears solely as a doublet ($J \approx$ 6-7 Hz), which before in heterocycles **1** has been observed only as a broad singlet. While slightly confusing, examination of the ^{31}P NMR spectra indicated that the phosphorus center was likely coupling to the adjacent nitrogen, as the phosphorus peaks appear as doublet of doublets for **2a**-**2c**, and doublet of triplets for **2d**-**2f**. It should be noted, however, that the coupling between the phosphorus center and the attached phenyl ring may mask this interaction. This coupling between the phosphorus center and the N–H proton could potentially be explained due to a more partially-positively charged P atom resulting from the more polarized P–S bond. Furthermore, none of the characteristic shifting in any of the N–H signals was seen as a function of concentration, suggesting little to no meso-dimerization as is observed for heterocycles **1** in solution. This is likely due to the relatively large thiophosphonyl S acting as a "soft" Lewis base because of its more diffuse charge and the concurrent larger polarizability.[16] This phenomenon is also observed for sulfur-containing H-bonds in proteins.[17,18]

Slow diffusion of pentane into CH_2Cl_2 solutions of heterocycles **2d** and **2e** furnished single crystals suitable for X-ray diffraction. In the heterocyclic core of these structures, the P–N bond distances are 1.665(1) and 1.668(1) Å, the P–C bond distances are 1.794(2) and 1.802(1) Å, the N–C bond distances are 1.394(2) and 1.395(1) Å, and the isolated C=C

double bond distances are both 1.355(2) Å, respectively. All of these bond lengths are within the ranges determined for previous PN-heterocycles,[13] suggesting that thionation has no significant structural effect on the conjugated backbone. The only differences in bond lengths are observed for the P–N bond distances, which are about 0.02 Å longer than those in **1**,[13] and, unsurprisingly, the P=S bond distances of **2d** and **2e** (1.959(1) and 1.958(1) Å) are ~0.5 Å longer than the respective P=O bonds in heterocycles **1** because of the larger sulfur atom.

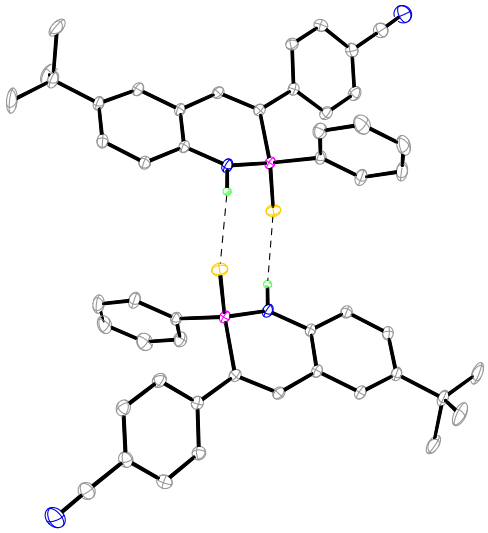

Figure 4.2 ORTEP drawing of the thioheterocycle **2e** mesodimer; thermal ellipsoids drawn at 30% probability level.

The solid-state structures of the meso-dimers of **2d** and **2e** also provide some interesting observations (Figures 4.2 and C1-C4). The N···S intermolecular distance is 3.406(1) Å for **2d** and 3.404(1) Å for **2e**, which are significantly longer than any previously measured N···O bond distances (~2.77-2.82 Å).[13] The P–N···S, N···S–P, and the S–P–N angles are 118.2°, 102.5°, and 115.7(1)° for **2d** and 114.6°, 107.4°, and 116.2(1)° for **2e**,

respectively. These all deviate to varying degrees from the ideal 120° for the pseudo six-membered chair conformation, like their P=O analogues. Also, the S–P–N–H torsional angles for **2d** and **2e** are 56.5° and 60.7°, respectively. These characteristics further support the lack of solution-state dimerization since we have shown previously a correlation between solid-state distances/angles and solution-state dimerization strengths.[15] Finally, the dihedral angle between the heterocyclic cores and the pendant 4-NCC_6H_4 groups is ca. 28-38°, illustrating good conjugation between the two π-units in the solid state.

Table 4.1 Photophysical properties of heterocycles **2.**[a]

cmpd	λ_{abs} (nm)	λ_{em} (nm)	Stokes Shift (nm / cm^{-1})	ε ($M^{-1}cm^{-1}$)	ϕ (%)[b]	τ (ns)
2a	348	444	96/6213	7180	2	0.10[c]
2b	352	462	110 / 6764	8600	6	0.24[c]
2c	350	470	120 / 7294	6520	3	0.19[c]
2d	365	479	114 / 6520	6380	8	0.75 (76%), 4.6 (24%)[d]
2e	373	492	119 / 6484	7950	8	0.82 (85%), 4.8 (15%)[d]
2f	357	466	109/6552	6840	2	0.17 (84%), 3.0 (16%) [d]

[a]All values collected in $CHCl_3$ with ca. 10^{-5} M solutions. [b]Collected using a quinine sulfate in 0.1 M H_2SO_4 solution. [c]Decay curves fitted with a monoexponential model. [d]Decay curves fitted with a biexponential model

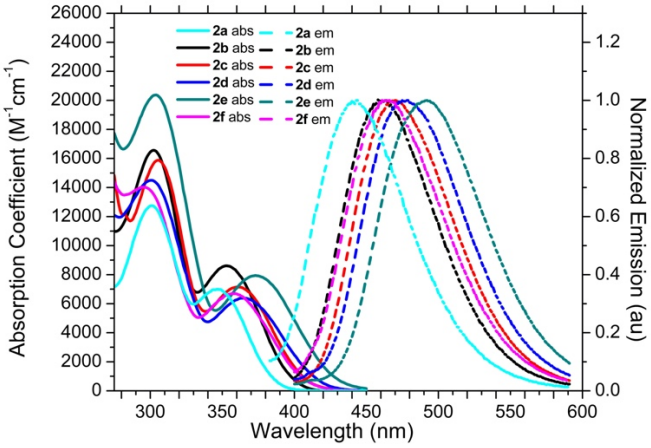

Figure 4.3 Stacked absorption and emission spectra of heterocycles **2**.

We next examined the effects of thionation upon the photophysical properties of **2** (Table 4.1, Figure 4.3). First, the lowest energy absorption peaks of thio-heterocycles **2** range from 348 to 372 nm. These fall in line with the typical PN heterocycle absorbance peaks, albeit they are slightly lower energy likely due to the lowered LUMO energies and subsequently lower π to π* transitions upon introduction of the sulfur atoms in **2**.[19] Furthermore, the absorption coefficients for **2** range from 20,800 to 12,700 $M^{-1}cm^{-1}$for the $\lambda_{abs,max}$ peaks around 300 nm (see Appendix C) and from 6380 to 8600 $M^{-1}cm^{-1}$ for the lowest energy absorbances. This are within the range of those seen for oxo-heterocycles **1**, suggesting that there is no significant effect of the thionation upon the conjugation or absorptivity of the scaffold.

When examining the emissive properties of **2**, however, a few interesting, yet predictable changes were observed. For P–OPh containing heterocycles **2a-2c**, ca. 20 nm redshifts in the emission are observed when compared to their respective oxo-heterocycle **1** derivatives. Similarly, the P–Ph containing heterocycles **2d-2f** exhibit 12, 27, and 17 nm redshifts compared to **1d-1f**, respectively. This is likely due to the weaker P–S bond in **2**

compared to the P–O bond in **1** and the concurrent lower energy of the excited state (S_1). With this lower energy S_1 state, the S_1 to S_0 transition is lower in energy, as cited for thiocarbonyls vs. their parent carbonyls.[20] Furthermore, all derivatives of **2** exhibited decreased quantum yields (3-8%) compared to their **1** counterparts (11-52%). This is a common phenomenon as sulfur promotes the "heavy atom effect" which acts to quench fluorescence through several electronic transitions in the excited state.[21,22] This effect is most pronounced in **2d-2f**, which show a dramatic reduction in quantum yield, though this is likely just due to their respective **1** counterparts having higher quantum yields as previously described.[14] An additional interesting difference between the P–OPh containing heterocycles **2a-2c** and the P–Ph containing congeners **2d-2f** is seen when determining the fluorescence lifetimes of the heterocycles. For the P–OPh heterocycles, the decays are monoexponential, and range from 0.10 to 0.24 ns, whereas the P–Ph heterocycles show biexponential lifetimes with a predominant shorter component (0.17 to 0.82 ns) as well as a longer-lived component (4.8 to 3.0 ns). This is likely due to the increased potential for charge transfer in the excited state of the P–Ph heterocycles as we have seen before.[13] Examination of the absorption and emission of **2c** and **2e** in the more polar acetonitrile (Figure C5 and Table C1) indicate that this charge transfer is likely observed in this system as well, as **2e** shows a higher energy Stokes shift in the more polar solvent, yet **2c** shows a lower one. The frontier orbital geometries of the ground- and excited-state geometries were also examined by DFT and TD-DFT calculations, respectively (Figure C6 and Table C2). A larger separation between frontier orbitals is observed in the HOMO and LUMO for the S0 state of the P–Ph containing **2e** when compared to the respective P–OPh containing **2c**. When looking at the respective S1 state

geometries, a slightly larger orbital separation can be seen for **2e** as well, though it is not as dramatic as that of the ground state. This, paired with the increased Stokes shift of **2e** in a more polar solvent imply that a more prominent charge transfer event can be taking place for the P–Ph containing **2d**-**2f**. thus leading to the biexponential decay curves. This conjecture also is corroborated by the longer lifetime components observed with the P–Ph heterocycles since charge-transfer has longer lifetime than the dominant π^* to π transitions.

4.3 Conclusions

In summary, the utility and versatility of Lawesson's reagent has permitted the transformation of oxo-heterocycles **1a-1f** into their respective thiocarbonyl derivatives **2a-2f**, affording interesting changes in physicochemical properties as well as new functionality of the compounds. With LR working well to convert the phosphaquinolinone scaffolds in the same way, and the inherent diversity of performing the transformation upon this fluorescent phosphonyl center, it opens the door for the potential utilization of these P=O(S) heterocycles as turn-on fluorescent sensors, markers, or chemodosimeters for oxidizing/reducing species. These studies will be disclosed in due course.

APPENDIX A

SUPPLEMENTARY INFORMATION FOR CHAPTER II

Appendix A is the supplementary information for Chapter II of this dissertation. It includes experimental details, experimental data, spectra, and computational details relevant to the content of Chapter II.

Experimental Details

General. All oxygen- and water-free reactions were performed under an N_2 atmosphere using Schlenk technique. Column chromatography was performed using silica gel (240–300 mesh), with solvent systems being referenced to the most abundant solvent. NMR spectra were acquired at room temperature on a Varian Inova 500 (^{1}H: 500 MHz, ^{13}C: 126 MHz, ^{19}F: 471 MHz, ^{31}P: 202 MHz), a Bruker Avance III HD 500 equipped with a Prodigy multinuclear cryoprobe (^{1}H: 500 MHz, ^{13}C: 126 MHz, ^{31}P: 202 MHz), or a Bruker Avance-III-HD 600 MHz (^{1}H: 599.98 MHz, ^{13}C: 150.87 MHz, ^{19}F: 565 MHz) spectrometer. ^{1}H and ^{13}C chemical shifts (δ) are expressed in ppm relative to residual $CHCl_3$ shifts (^{1}H: 7.26 ppm, ^{13}C: 77.16 ppm), DMSO shifts (^{1}H: 2.50 ppm, ^{13}C: 39.52 ppm), or CH_2Cl_2 (^{1}H: 5.32, ^{13}C: 53.84). ^{31}P NMR are referenced to 85% H_3PO_4 (δ 0 ppm) as an external reference, and ^{19}F NMR are referenced to $CFCl_3$ (δ 0 ppm) as an external standard. UV-vis spectra were recorded using an Agilent Technologies Cary 60 UV-vis spectrophotometer in $CHCl_3$. Fluorescence emission spectra were recorded using a Horiba Jobin Yvon FluoroMax-4 fluorimeter. High-resolution mass spectra (HRMS) were recorded on a Waters XEVO G2-XS mass spectrometer. Diffuse reflectance UV-vis spectroscopy (DRUV-vis) was

performed on a Perkin Elmer Lambda 1050 UV/Vis/NIR spectrometer, with a 150 mm InGaAs integrating sphere in the range of 2000-200 nm paired with a Harrick Scientific Praying Mantis Diffuse Reflection (DRP) accessory. To ensure adequate absorbance, all samples were diluted with ground $BaSO_4$ before measurement. Pseudo-Lambda max were determined by peak maxima in Kubelka-Munk vs. wavelength units.

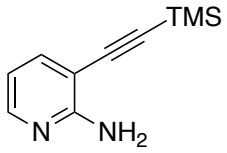

2-Amino-3-(2-trimethylsilyl)ethynylpyridine (4). 2-Amino-3-iodopyridine (500 mg, 2.27 mmol, 1 equiv), $Pd(PhCN)_2Cl_2$ (26 mg, 0.07 mmol, 0.03 equiv.), and CuI (9 mg, 0.05 mmol, 0.02 equiv.) were combined in a round bottom flask and dissolved in THF (2.5 mL). The flask was evacuated and backfilled with N_2 a total of three times. While stirring under N_2 flow, $(i\text{-Pr})_2NH$ (0.38 mL, 2.72 mmol, 1.2 equiv.) and $P(t\text{-Bu})_3$ (10 wt% in hexanes, 0.4 mL, 0.136 mmol, 0.06 equiv.) were added via syringe. Trimethylsilylacetylene (1.62 mL, 11.36 mmol, 5 equiv.) was then added dropwise and the reaction stirred at room temperature for 1.5 h. The reaction was then quenched with EtOAc (5 mL) and transferred to a separatory funnel. The crude mixture was extracted with EtOAc (3x), dried (Na_2SO_4), filtered and concentrated. The residue was then dry-loaded onto a silica plug and flushed with hexanes to remove nonpolar impurities. The product was then eluted with a 1:10 mixture of acetone:CH_2Cl_2 and concentrated *in vacuo* to afford **4** (400 mg, 95% yield) as a brown solid. ^{1}H NMR (500 MHz, DMSO-d_6) δ 7.95 (dd, J = 4.9, 1.9 Hz, 1H), 7.50 (dd, J = 7.5, 1.9 Hz, 1H), 6.52 (dd, J = 7.5, 4.9 Hz, 1H), 6.07 (br s, 2H), 0.24 (s, 9H). ^{13}C NMR

(126 MHz, $CDCl_3$) δ 158.91, 147.30, 140.48, 113.34, 103.44, 101.62, 99.91, –0.04. HRMS (ASAP) $[M+H]^+$ calcd for $C_{10}H_{15}N_2Si$ 191.1004, found 191.1019.

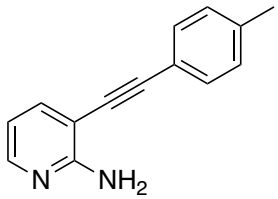

2-Amino-3-(2-(4-methylphenyl)ethynyl)pyridine (5a). 2-Amino-3-iodopyridine (**3a**, 500 mg, 2.27 mmol, 1 equiv.), 4-ethynyltoluene (0.4 mL, 3.40 mmol, 1.5 equiv.), and $Pd(PPh_3)_2Cl_2$ (64 mg, 0.09 mmol, 0.04 equiv.) were combined in a scintillation vial. The solid reagents were suspended in Et_3N (2 mL) and three drops of MeCN. The resulting slurry was placed in a preheated sand bath at 70 °C and stirred for 20 min. The mixture was extracted into EtOAc (3 x 20 mL), dried (Na_2SO_4), filtered, and condensed *in vacuo*. The residue was purified by silica plug by removing impurities with hexanes before eluting the product in CH_2Cl_2, which afforded aminopyridine **5a** (468 mg, 99% yield) as brown solid. ^1H NMR (500 MHz, DMSO-d_6) δ 7.96 (br s, 1H), 7.57 (dd, J = 7.5, 1.8 Hz, 1H), 7.52 (d, J = 8.1 Hz, 2H), 7.23 (d, J = 7.8 Hz, 2H), 6.56 (dd, J = 7.5, 4.9 Hz, 1H), 6.25 (br s, 2H), 2.33 (s, 3H). ^{13}C NMR (126 MHz, DMSO-d_6) δ 159.87, 148.57, 140.13, 138.78, 131.80, 129.64, 120.01, 112.51, 101.76, 95.16, 85.23, 21.52. HRMS (ASAP) $[M+H]^+$ calcd for $C_{14}H_{13}N_2$ 209.1079, found 209.1074.

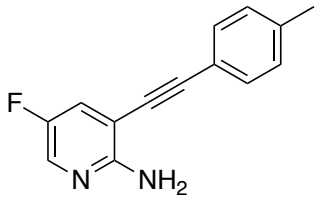

2-Amino-5-fluoro-3-(2-(4-methylphenyl)ethynyl)pyridine (5e). 2-Amino-5-fluoro-3-iodopyridine (**3b**, 800 mg, 3.36 mmol, 1 equiv.), $Pd(PhCN)_2Cl_2$ (38 mg, 0.100 mmol, 0.03 equiv.), and CuI (13 mg, 0.067 mmol, 0.02 equiv.) were suspended in THF (4 mL) and the flask was evacuated and backfilled with N_2 (3x). While stirring, $(i\text{-Pr})_2NH$ (0.57 mL, 4.03 mmol, 1.2 equiv.) and $P(t\text{-Bu})_3$ (10 wt% in hexanes, 0.60 mL, 0.202 mmol, 0.06 equiv.) were added by syringe. 4-Ethynyltoluene (0.60 mL, 5.04 mmol, 1.5 equiv.) was then added dropwise and the mixture was stirred under N_2 for 3 d. The reaction was quenched with Et_2O (10 mL) and filtered through celite. The filtrate was transferred to a separatory funnel and washed with water (3x) before being dried (Na_2SO_4) and filtered. The crude mixture was then condensed *in vacuo* before being dry loaded on to silica and flushed with hexanes. The crude product was then eluted (1:5 acetone:CH_2Cl_2). The organic residue was then dry loaded on to silica again and purified by column chromatography (gradient of hexanes to CH_2Cl_2 to 1:5 acetone:CH_2Cl_2) to afford **5e** (190 mg, 25%) as a brown solid. ^{1}H NMR (500 MHz, DMSO-d_6) δ 7.96 (d, J = 3.1 Hz, 1H), 7.58 (dd, J = 8.9, 3.0 Hz, 1H), 7.54 (d, J = 8.2 Hz, 2H), 7.24 (d, J = 7.9 Hz, 2H), 6.24 (br s, 2H), 2.34 (s, 3H). ^{13}C NMR (151 MHz, DMSO-d_6) δ 156.61, 151.53 (d, J = 238.9 Hz), 138.75, 135.02 (d, J = 23.8 Hz), 131.50, 129.23, 126.54 (d, J = 21.0 Hz), 119.08, 101.67 (d, J = 5.5 Hz), 95.44, 83.76, 21.09. ^{19}F NMR (565 MHz, DMSO-d_6) δ –144.60. HRMS (ASAP) $[M+H]^+$ calcd for $C_{14}H_{12}N_2F$ 227.0985, found 227.0964.

General Synthesis of 2-Amino-3-arylethynylpyridines. Pyridine **4** (1 equiv.) and K_2CO_3 (4 equiv.) were suspended in a 1:1 mixture of $CHCl_3$:MeOH (7.6 M) and stirred at room temperature for 2 h. The reaction mixture was then condensed *in vacuo*, dissolved in

EtOAc, and transferred to a separatory funnel. The organic layer was then washed with DI water (3x), dried (Na_2SO_4), and filtered. The filtrate was condensed *in vacuo* to give 2-amino-3-ethynylpyridine which was used directly for the aryl halide coupling.

2-Amino-3-ethynylpyridine (1 equiv.), aryl halide (1.2 equiv.) and $Pd(PPh_3)_2Cl_2$ (0.04 equiv.) were combined in a scintillation vial. The solid reagents were suspended in Et_3N (6.00 equiv.) and the resulting slurry was stirred for 30 min in a preheated sand bath at 70 °C. The mixture was extracted into EtOAc (3 x 20mL), dried (Na_2SO_4), filtered, and condensed *in vacuo*. The crude mixture was then purified by silica plug.

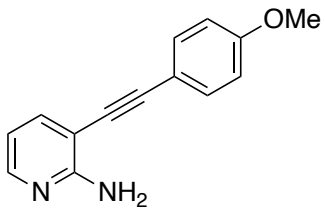

2-Amino-3-(2-(4-methoxyphenyl)ethynyl)pyridine (5b). Crude 2-amino-3-ethynylpyridine (600 mg, 3.15 mmol, 1 equiv.), 4-iodoanisole (600 mg, 3.78 mmol, 1.2 equiv.), and $Pd(PPh_3)_2Cl_2$ (88 mg, 0.126 mmol, 0.04 equiv.) were reacted in Et_3N (1.32 mL) and MeCN (1.5 mL) following the general procedure described above. Recrystallization from CH_2Cl_2 with hexanes afforded aminopyridine **5b** (390 mg, 55%) as a yellow solid. ^1H NMR (500 MHz, $CDCl_3$) δ 8.02 (dd, J = 5.1, 1.8 Hz, 1H), 7.57 (dd, J = 7.5, 1.8 Hz, 1H), 7.45 (d, J = 8.7 Hz, 2H), 6.88 (d, J = 8.8 Hz, 2H), 6.63 (dd, J = 7.5, 5.0 Hz, 1H), 5.10 (br s, 2H), 3.83 (s, 3H). ^{13}C NMR (126 MHz, $CDCl_3$) δ 160.14, 158.64, 147.20, 140.09, 133.18, 114.81, 114.29, 113.73, 104.00, 95.91, 83.01, 55.50. HRMS (ASAP) $[M+H]^+$ calcd for $C_{14}H_{13}N_2O$ 225.1028, found 225.1050.

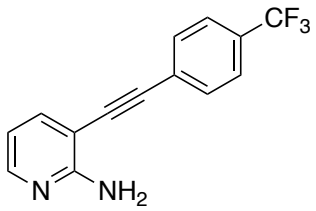

2-Amino-3-(2-(4-trifluoromethylphenyl)ethynyl)pyridine (5c). Crude 2-amino-3-ethynylpyridine (600 mg, 3.15 mmol, 1 equiv.), 4-iodobenzotrifluoride (555 mL, 3.78 mmol, 1.2 equiv.), and $Pd(PPh_3)_2Cl_2$ (88 mg, 0.126 mmol, 0.04 equiv.) were reacted in Et_3N (2.75 mL) with MeCN (1.5 mL) following the general procedure described above. The residue was purified by silica plug first with CH_2Cl_2 to remove impurities and then eluting the product (1:5 acetone:CH_2Cl_2) to afford aminopyridine **5c** (500 mg, 70%) as light-yellow solid. ^{1}H NMR (500 MHz, DMSO-d_6) δ 8.00 (dd, J = 4.9, 1.9 Hz, 1H), 7.87 (d, J = 8.0 Hz, 2H), 7.78 (d, J = 8.1 Hz, 2H), 7.63 (dd, J = 7.5, 1.9 Hz, 1H), 6.58 (dd, J = 7.5, 4.9 Hz, 1H), 6.44 (s, 2H). ^{13}C NMR (126 MHz, $CDCl_3$) δ 158.97, 148.77, 140.43, 131.82, 130.41 (q, J = 32.6 Hz), 126.64, 125.54 (q, J = 3.8 Hz), 122.89 (q, J = 272.5 Hz), 113.77, 102.45, 94.10, 87.02. ^{19}F NMR (471 MHz, DMSO-d_6) δ 61.19. HRMS (ASAP) $[M+H]^+$ calcd for $C_{14}H_{10}N_2F_3$ 263.0796, found 263.0812.

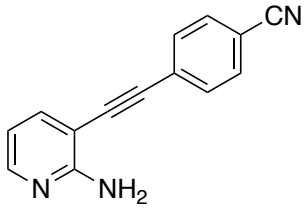

2-Amino-3-(2-(4-cyanophenyl)ethynyl)pyridine (5d). Crude 3-ethynyl-2-aminopyridine (600 mg, 3.15 mmol, 1 equiv.), 4-bromobenzonitrile (688 mg, 3.78 mmol, 1.2 equiv.), and $Pd(PPh_3)_2Cl_2$ (88 mg, 0.126 mmol, 0.04 equiv.) were reacted in Et_3N (2.75

mL) with MeCN (1 mL) following the general procedure described above. The residue was purified by silica plug first with CH_2Cl_2 to remove impurities and then eluting product (1:5 acetone:CH_2Cl_2) to afford aminopyridine **5d** (359 mg, 52%) as brown solid. ^{1}H NMR (500 MHz, DMSO-d_6) δ 8.01 (dd, J = 4.9, 1.8 Hz, 1H), 7.87 (d, J = 8.1 Hz, 2H), 7.83 (d, J = 8.1 Hz, 2H), 7.63 (dd, J = 7.5, 1.8 Hz, 1H), 6.58 (dd, J = 7.5, 4.9 Hz, 1H), 6.47 (br s, 2H). ^{13}C NMR (126 MHz, $CDCl_3$) δ 158.95, 149.10, 140.53, 132.25, 132.02, 127.69, 118.47, 113.79, 111.95, 102.07, 93.82, 89.03. HRMS (ASAP) $[M+H]^+$ calcd for $C_{14}H_{10}N_3$ 220.0875, found 220.0874.

General Cyclization Procedure. 2-Amino-3-arylethynylpyridine (1 equiv.) and $P(OPh)_3$ (4 equiv.) in a scintillation vial were dissolved into a minimal amount of pyridine. The vial was sealed and heated in a sand bath at 110 °C for 48-72 h. The mixture was diluted with toluene, and the solvent was removed *in vacuo*. The crude material was redissolved in MeCN and 5-10 drops of water were added. The solution was heated in a sand bath at 80 °C for 1-2 h before being dried (Na_2SO_4), filtered, and concentrated *in vacuo*. The crude mixture was either purified by recrystallization or column chromatography.

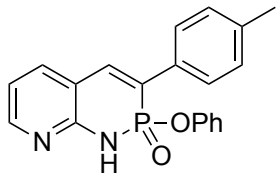

Heterocycle 2a. Following the general cyclization procedure, aminopyridine **5a** (200 mg, 0.96 mmol, 1 equiv.) and $P(OPh)_3$ (1 mL, 3.81 mmol, 4 equiv.) were reacted in pyridine

(2.5 mL) for 48 h. The crude material was purified by column chromatography (gradient of CH_2Cl_2 to acetone) to afford **2a** (120 mg, 38%) as yellow solid. ^{1}H NMR (500 MHz, DMSO-d_6) δ 10.80 (br s, 1H), 8.14 (s, 1H), 7.86 (d, J = 5.7 Hz, 1H), 7.83 (d, J = 40.3 Hz, 1H), 7.78 (d, J = 7.5 Hz, 2H), 7.30 (d, J = 7.9 Hz, 2H), 7.19 (t, J = 7.8 Hz, 2H), 7.03 (t, J = 7.4 Hz, 1H), 6.95 (t, J = 6.4 Hz, 1H), 6.86 (d, J = 8.0 Hz, 2H), 2.36 (s, 3H). ^{13}C NMR (126 MHz, DMSO-d_6) δ 151.30 (d, J = 4.2 Hz), 150.70 (d, J = 8.9 Hz), 146.71, 139.10, 138.06, 137.39 (d, J = 7.0 Hz), 132.43 (d, J = 8.7 Hz), 129.44, 127.41 (d, J = 6.2 Hz), 126.36, 125.17, 124.62, 120.91 (d, J = 4.1 Hz), 115.53, 115.21, 20.81. ^{13}C NMR (126 MHz, $CDCl_3$) δ 151.29 (d, J = 3.2 Hz), 150.34 (d, J = 9.1 Hz), 147.50, 139.03, 138.67, 137.39 (d, J = 7.8 Hz), 132.14 (d, J = 8.9 Hz), 129.76, 129.42 (d, J = 1.6 Hz), 127.84 (d, J = 6.4 Hz), 126.58, 125.00 (d, J = 1.9 Hz), 121.33 (d, J = 3.9 Hz), 116.81, 115.92 (d, J = 12.4 Hz), 21.33. ^{31}P NMR (202 MHz, DMSO-d_6) δ 10.54 (d, J = 40.8 Hz). HRMS (ASAP) $[M+H]^+$ calcd for $C_{20}H_{18}N_2O_2P$ 349.1106, found 349.1116.

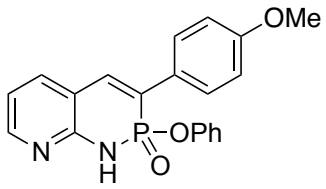

Heterocycle 2b. Following the general cyclization procedure, aminopyridine **5b** (350 mg, 1.56 mmol, 1 equiv.) and $P(OPh)_3$ (2.04 mL, 7.80 mmol, 5 equiv.) were reacted in pyridine (2 mL) for 48 h. The crude material was purified by column chromatography (gradient of 4:1 CH_2Cl_2:acetone to acetone) and then recrystallization from EtOAc to afford **2b** (200 mg, 35%) as yellow solid. ^{1}H NMR (500 MHz, DMSO-d_6) δ 10.83 (br s, 1H), 8.12 (s, 1H), 7.84 (d, J = 8.8 Hz, 2H), 7.77 (d, J = 41.6 Hz, 1H), 7.19 (t, J = 7.8 Hz,

3H), 7.09–6.99 (m, 3H), 6.97–6.90 (m, 1H), 6.86 (d, J = 8.0 Hz, 2H), 3.82 (s, 3H). ^{13}C NMR (126 MHz, DMSO-d_6) δ 159.57 (d, J = 5.1 Hz), 151.19, 150.73 (d, J = 7.9 Hz), 146.36 (br), 138.84, 136.35, 129.43, 128.85, 127.54 (t, J = 7.4 Hz), 126.08, 124.91, 124.58 (d, J = 5.2 Hz), 120.89, 115.45 (br), 114.31 (d, J = 5.3 Hz), 55.26. ^{31}P NMR (202 MHz, DMSO-d_6) δ 10.65 (d, J = 41.5 Hz). HRMS (ASAP) $[M+H]^+$ calcd for $C_{20}H_{18}N_2O_3P$ 365.1055, found 365.1048.

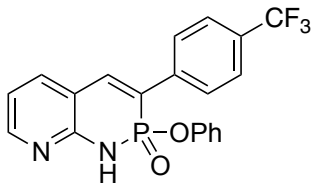

Heterocycle 2c. Following the general cyclization procedure, aminopyridine **5c** (350 mg, 1.33 mmol, 1 equiv.) and $P(OPh)_3$ (1.75 mL, 6.67 mmol, 5 equiv.) were reacted in pyridine (2 mL) for 48 h. The product precipitated when the crude oil was triturated in EtOAc, which was collected by filtration to afford **2c** (203 mg, 38%) as yellow solid. ^{1}H NMR (500 MHz, DMSO-d_6) δ 11.40 (br s, 1H), 8.16 (s, 1H), 8.10 (d, J = 8.1 Hz, 2H), 8.00 (d, J = 39.7 Hz, 1H), 7.93 (d, J = 7.4 Hz, 1H), 7.86 (d, J = 8.2 Hz, 2H), 7.19 (t, J = 7.7 Hz, 2H), 7.04 (t, J = 7.4 Hz, 1H), 6.96 (t, J = 6.4 Hz, 1H), 6.86 (d, J = 8.0 Hz, 2H). ^{13}C NMR (151 MHz, DMSO-d_6) δ 152.15 (d, J = 5.1 Hz), 150.96 (d, J = 8.5 Hz), 141.04, 140.26 (d, J = 6.3 Hz), 140.03 (d, J = 8.6 Hz), 129.91, 128.92 (q, J = 31.3 Hz), 128.64 (d, J = 5.9 Hz), 127.95, 126.19 (q, J = 3.8 Hz), 125.55, 125.13, 124.58, 124.66 (q, J = 272.0 Hz), 121.18 (d, J = 4.4 Hz), 116.40, 115.59. ^{31}P NMR (202 MHz, DMSO-d_6) δ 9.96 (d, J = 39.1 Hz). ^{19}F NMR (471 MHz, DMSO-d_6) δ –60.99. HRMS (ASAP) $[M+H]^+$ calcd for $C_{20}H_{15}N_2O_2PF_3$ 403.0823, found 403.0860.

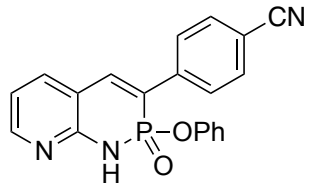

Heterocycle 2d. Following the general cyclization procedure, aminopyridine **5d** (300 mg, 1.37 mmol, 1 equiv.), and $P(OPh)_3$ (1.79 mL, 6.84 mmol, 5 equiv.) were reacted in pyridine (2 mL) for 48 h. The product precipitated when the crude oil was triturated in EtOAc, which was collected by filtration to afford **2d** (203 mg, 39%) as a yellow solid. ^{1}H NMR (600 MHz, $CDCl_3$) δ 11.35 (br s, 1H), 8.28 (d, *J* = 5.3 Hz, 1H), 7.95 (d, *J* = 8.0 Hz, 2H), 7.82 (d, *J* = 7.5 Hz, 1H), 7.74 (d, *J* = 8.0 Hz, 2H), 7.58 (d, *J* = 40.5 Hz, 1H), 7.17 (t, *J* = 7.6 Hz, 2H), 7.09 (d, *J* = 5.3 Hz, 1H), 7.06 (d, *J* = 7.1 Hz, 1H), 6.91 (d, *J* = 7.9 Hz, 2H). ^{13}C NMR (126 MHz, DMSO-d_6) δ 151.77 (d, *J* = 4.7 Hz), 150.63 (d, *J* = 8.9 Hz), 146.22, 140.42 (d, *J* = 20.0 Hz), 140.29, 132.73, 129.51, 129.35, 128.22 (d, *J* = 6.0 Hz), 124.66, 124.36 (d, *J* = 148.3 Hz), 120.85 (d, *J* = 4.2 Hz), 118.73, 115.40 (d, *J* = 157.4 Hz), 115.21, 110.67. ^{31}P NMR (202 MHz, DMSO-d_6) δ 9.83 (d, *J* = 39.6 Hz). HRMS (ASAP) $[M+H]^+$ calcd for $C_{20}H_{15}N_3O_2P$ 360.0902, found 360.0932.

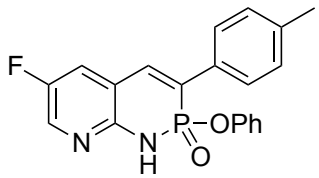

Heterocycle 2e. Following the general cyclization procedure, aminopyridine **5e** (180 mg, 0.80 mmol, 1 equiv.) and $P(OPh)_3$ (0.837 mL, 3.18 mmol, 4 equiv.) were reacted in

pyridine (2 mL) for 72 h. The crude product was purified by column chromatography (gradient of CH_2Cl_2 to EtOAc), and then solid was recrystallized from CH_2Cl_2 with hexanes to afford **2e** (86 mg, 29%) as pale-yellow solid. ^{1}H NMR (600 MHz, DMSO-d_6) δ 10.71 (br s, 1H), 8.26 (d, J = 2.9 Hz, 1H), 7.86 (d, J = 40.3 Hz, 1H), 7.83 (s, 1H), 7.77 (d, J = 7.8 Hz, 2H), 7.32 (d, J = 7.7 Hz, 2H), 7.21 (t, J = 8.0 Hz, 2H), 7.06 (t, J = 7.4 Hz, 1H), 6.87 (d, J = 8.0 Hz, 2H), 2.37 (s, 3H). ^{13}C NMR (126 MHz, DMSO-d_6) δ 155.58, 153.64, 150.80 (d, J = 9.0 Hz), 148.00, 139.05, 137.25, 137.01 (d, J = 26.3 Hz), 132.32 (d, J = 9.4 Hz), 130.04 (d, J = 4.2 Hz), 127.93 (d, J = 6.4 Hz), 127.02 (d, J = 119.1 Hz), 125.41, 124.86 (d, J = 20.4 Hz), 121.40 (d, J = 4.0 Hz), 115.35, 21.31. ^{31}P NMR (202 MHz, DMSO-d_6) δ 10.32 (d, J = 41.8 Hz). ^{19}F NMR (565 MHz, DMSO-d_6) δ –137.81. HRMS (ASAP) $[M+H]^+$ calcd for $C_{20}H_{17}N_2O_2PF$ 367.1012, found 367.1022.

General Heterocycle Alkylation Procedure. Pyridine-PN (1 equiv.) and alkylating reagent (10 equiv.) were suspended in CH_2Cl_2 (0.7M) in a scintillation vial. DBU (5 equiv.) was added dropwise to the vial and the capped solution stirred at room temperature for 3-24 h. The crude mixture was then transferred to a separatory funnel where it was washed with DI water (3x), 3M HCl (aq) (1x), and 1M KOH (aq) (1x). The organic layer was then dried (Na_2SO_4), filtered, and condensed *in vacuo*. The crude oil was purified by silica plug.

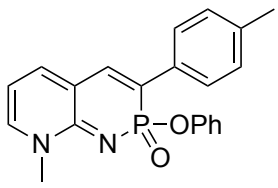

Heterocycle 6a. Following general alkylation procedure, pyridine-PN **2a** (150 mg, 0.430 mmol, 1 equiv.), iodomethane (0.267 mL, 4.30 mmol, 10 equiv.), and DBU (0.327 mL, 2.15 mmol, 5 equiv.) were reacted in CH_2Cl_2 (2 mL) for 24 h. The crude material was purified by silica plug, initially flushing with EtOAc to remove impurities, and then eluting the product with acetone. Recrystallization from CH_2Cl_2 with hexanes afforded **6a** (31 mg, 20%) as a yellow solid. ^{1}H NMR (500 MHz, CD_2Cl_2) δ 7.81 (d, *J* = 7.9 Hz, 2H), 7.53 (d, *J* = 6.9 Hz, 2H), 7.39 (d, *J* = 36.2 Hz, 1H), 7.24 (d, *J* = 7.9 Hz, 2H), 7.12 (t, *J* = 7.7 Hz, 2H), 6.97 (t, *J* = 7.4 Hz, 1H), 6.88 (d, *J* = 8.6 Hz, 2H), 6.48 (t, *J* = 6.9 Hz, 1H), 3.81 (s, 3H), 2.38 (s, 3H). ^{13}C NMR (126 MHz, CD_2Cl_2) δ 153.62 (d, *J* = 10.6 Hz), 152.35 (d, *J* = 8.6 Hz), 139.78, 139.05 (d, *J* = 2.0 Hz), 139.00, 135.40 (d, *J* = 8.6 Hz), 134.08 (d, *J* = 5.9 Hz), 131.33, 130.27, 129.85, 129.40, 128.22 (d, *J* = 5.6 Hz), 124.25 (d, *J* = 1.7 Hz), 122.38 (d, *J* = 23.5 Hz), 121.84 (d, *J* = 4.1 Hz), 108.67, 40.82, 21.38. ^{13}C NMR (126 MHz, $CDCl_3$) δ 153.32 (d, *J* = 10.8 Hz), 152.02 (d, *J* = 8.6 Hz), 139.08, 138.61, 138.31 (d, *J* = 2.1 Hz), 134.90 (d, *J* = 8.8 Hz), 133.64 (d, *J* = 5.8 Hz), 131.73, 130.66, 129.62, 129.10 (d, *J* = 1.4 Hz), 128.12 (d, *J* = 5.7 Hz), 123.98 (d, *J* = 1.7 Hz), 121.66 (d, *J* = 4.1 Hz), 108.30, 40.75, 21.42. ^{31}P NMR (202 MHz, CD_2Cl_2) δ 10.84 (d, *J* = 36.3 Hz). HRMS (ASAP) $[M+H]^+$ calcd for $C_{21}H_{20}N_2O_2P$ 363.1262, found 363.1227.

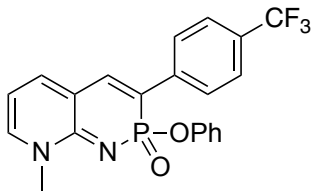

Heterocycle 6b. Following general alkylation procedure, pyridine-PN **2c** (200 mg, 0.500 mmol, 1 equiv.), iodomethane (0.31 mL, 5.00 mmol, 10 equiv.), and DBU (0.37 mL,

2.50 mmol, 5 equiv.) were reacted in CH_2Cl_2 (2 mL) for 24 h. The crude material was purified by silica plug, initially flushing with EtOAc to remove impurities, and then eluting the product with acetone. Recrystallization from CH_2Cl_2 with hexanes afforded **6b** (127 mg, 61%) as a pale-yellow solid. ^{1}H NMR (600 MHz, DMSO-d_6) δ 8.18 (s, 1H), 8.16 (d, J = 8.3 Hz, 2H), 7.95 (s, 1H), 7.90 (d, J = 35.9 Hz, 1H), 7.83 (d, J = 8.1 Hz, 2H), 7.16 (t, J = 7.7 Hz, 2H), 7.00 (t, J = 7.4 Hz, 1H), 6.80 (d, J = 8.0 Hz, 2H), 6.74 (t, J = 6.9 Hz, 1H), 3.81 (s, 3H). ^{13}C NMR (151 MHz, DMSO-d_6) δ 152.59 (d, J = 10.1 Hz), 151.35 (d, J = 8.5 Hz), 141.77, 141.65, 140.75 (d, J = 6.1 Hz), 138.38 (d, J = 7.3 Hz), 129.29, 128.26 (d, J = 5.5 Hz), 128.18 (q, J = 31.7 Hz), 127.01, 125.54 (q, J = 3.8 Hz), 124.33 (q, J = 271.1 Hz), 124.05, 121.03 (d, J = 3.8 Hz), 120.22 (d, J = 23.1 Hz), 108.86, 39.80. ^{31}P NMR (202 MHz, DMSO-d_6) δ 9.93 (d, J = 36.5 Hz). ^{19}F NMR (471 MHz, DMSO-d_6) δ –60.91. HRMS (ASAP) $[M+H]^+$ calcd for $C_{21}H_{17}N_2O_2PF_3$ 417.0980, found 417.0942.

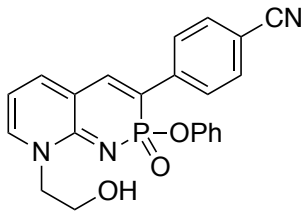

Heterocycle 6c. Following the general alkylation procedure, pyridine-PN **2d** (100 mg, 0.278 mmol, 1 equiv.), 2-bromoethanol (0.10 mL, 1.39 mmol, 5 equiv.), and DBU (0.20 mL, 1.39 mmol, 5 equiv.) were reacted in CH_2Cl_2 (1 mL) for 24 h. The crude material was purified by silica plug, initially flushing with EtOAc to remove impurities, and then eluting the product with acetone. Recrystallization from CH_2Cl_2 with hexanes afforded **6c** (43 mg, 39%) as a yellow solid ^{1}H NMR (500 MHz, DMSO-d_6) δ 8.13 (d, J = 8.2 Hz, 2H), 8.03 (d, J = 6.8 Hz, 1H), 7.95 (d, J = 7.4 Hz, 1H), 7.93 (d, J = 34.9 Hz, 1H), 7.91 (d, J = 8.5 Hz,

2H), 7.15 (t, J = 7.8 Hz, 2H), 6.99 (t, J = 7.4 Hz, 1H), 6.77 (d, J = 8.0 Hz, 2H), 6.73 (t, J = 6.9 Hz, 1H), 4.97 (t, J = 5.3 Hz, 1H), 4.45-4.31 (m, 2H), 3.83-3.65 (m, 2H). ^{13}C NMR (126 MHz, DMSO-d_6) δ 151.97 (d, J = 9.8 Hz), 142.36 (d, J = 23.4 Hz), 141.36 (d, J = 6.2 Hz), 138.92, 132.57, 129.33, 128.22, 125.65, 124.03, 120.90 (d, J = 4.1 Hz), 120.37, 120.19, 118.87, 110.31, 108.53, 57.77, 53.96. ^{31}P NMR (202 MHz, DMSO-d_6) δ 9.67 (d, J = 35.8 Hz). HRMS (ASAP) $[M+H]^+$ calcd for $C_{22}H_{19}N_3O_3P$ 404.1164, found 404.1141.

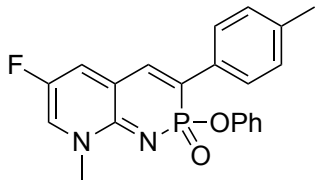

Heterocycle 6d. Following general alkylation procedure, pyridine-PN **5e** (80 mg, 0.22 mmol, 1 equiv.), iodomethane (0.137 mL, 2.20 mmol, 10 equiv.), and DBU (0.164 mL, 1.1 mmol, 5 equiv.) were reacted in CH_2Cl_2 (1 mL) for 3 h. The crude material was purified by silica plug, initially flushing with acetone to remove impurities, and then eluting the product with MeOH to afford **6d** (34 mg, 41%) as a yellow solid. ^{1}H NMR (600 MHz, DMSO-d_6) δ 8.40 (s, 1H), 8.00 (d, J = 8.3, 2.9 Hz, 1H), 7.84 (d, J = 7.8 Hz, 2H), 7.71 (d, J = 36.1 Hz, 1H), 7.28 (d, J = 7.8 Hz, 2H), 7.15 (t, J = 7.7 Hz, 2H), 6.99 (t, J = 7.4 Hz, 1H), 6.77 (d, J = 8.0 Hz, 2H), 3.76 (s, 3H), 2.35 (s, 3H). ^{13}C NMR (151 MHz, DMSO-d_6) δ 151.40 (d, J = 8.6 Hz), 150.64 (d, J = 10.1 Hz), 148.27 (d, J = 233.7 Hz), 138.15, 134.56, 133.26 (d, J = 6.2 Hz), 130.34, 129.46, 129.35, 129.25, 127.66, 127.56 (d, J = 5.5 Hz), 127.40, 123.97, 121.03 (d, J = 3.8 Hz), 20.86 (one –CH_3 under DMSO peak). ^{31}P NMR (202 MHz, $CDCl_3$) δ 10.25 (d, J = 36.0 Hz). ^{19}F NMR (565 MHz, DMSO-d_6) δ –145.25. HRMS (ASAP) $[M+H]^+$ calcd for $C_{21}H_{19}N_2O_2PF$ 381.1168, found 381.1155.

Crystallographic Data

General. Diffraction intensities for **2a**, **2c** and **2e** were collected at 173 K on a Bruker Apex2 CCD (**2c**, **2e**) and Rigaku XtaLAB SynergyS (**2a**) diffractometers using CuKα radiation, λ= 1.54178 and 1.54184 Å, respectively. Space groups were determined based on systematic absences. Absorption corrections were applied by SADABS.[1] Structures were solved by direct methods and Fourier techniques and refined on F^2 using full matrix least-squares procedures. All non-H atoms were refined with anisotropic thermal parameters. H atoms in all structures were found from the residual maps and refined with isotropic thermal parameters, except those in the terminal Me groups, C(14), in **2e** which were refined in calculated positions without restrictions on rotation around the Me-C bond (AFIX 138). All calculations were performed by the Bruker SHELXL-2014 package.[2]

Low-temperature X-ray diffraction data for **6a** were collected on a Rigaku XtaLAB Synergy diffractometer coupled to a Rigaku Hypix detector with Cu Kα radiation (λ = 1.54184 Å), from a PhotonJet micro-focus X-ray source at 100 K. The diffraction images were processed and scaled using the CrysAlisPro software.[3] The structures were solved through intrinsic phasing using SHELXT[4] and refined against F^2 on all data by full-matrix least squares with SHELXL[5] following established refinement strategies.[6] All non-hydrogen atoms were refined anisotropically. All hydrogen atoms bound to carbon were included in the model at geometrically calculated positions and refined using a riding model. Hydrogen atoms bound to oxygen were located in the difference Fourier synthesis and subsequently refined semi-freely with the help of distance restraints. The isotropic displacement parameters of all hydrogen atoms were fixed to 1.2 times the Ueq value of the atoms they are linked to (1.5 times for methyl groups).

Crystallographic Data for **2a**: $C_{20}H_{17}N_2O_2P$, M = 348.32, 0.18 x 0.15 x 0.02 mm, T = 173(2) K, Monoclinic, space group $P2_1/n$, a = 13.4719(4) Å, b = 10.3157(2) Å, c = 12.7474(3) Å, β = 110.559(3)°, V = 1658.71(8) Å^3, Z = 4, D_c = 1.395 Mg/m^3, μ(Cu) = 1.602 mm^{-1}, F(000) = 728, $2\theta_{max}$ = 151.76°, 11472 reflections, 3275 independent reflections [R_{int} = 0.0402], R1 = 0.0424, wR2 = 0.1184 and GOF = 1.042 for 3275 reflections (294 parameters) with I>2σ(I), R1 = 0.0498, wR2 = 0.1267 and GOF = 1.042 for all reflections, max/min residual electron density +0.340/–0.426 eÅ^{-3}. CCDC 2118126.

Crystallographic Data for **2c**: $C_{20}H_{14}F_3N_2O_2P$, M = 402.30, 0.19 x 0.14 x 0.02 mm, T = 173(2) K, Monoclinic, space group $P2_1/c$, a = 13.7037(5) Å, b = 10.5058(4) Å, c = 12.7309(4) Å, β = 110.056(2)°, V = 1721.70(11) Å^3, Z = 4, D_c = 1.552 Mg/m^3, μ(Cu) = 1.890 mm^{-1}, F(000) = 824, $2\theta_{max}$ = 137.00°, 14957 reflections, 3136 independent reflections [R_{int} = 0.0490], R1 = 0.0398, wR2 = 0.1049 and GOF = 1.088 for 3136 reflections (309 parameters) with I>2σ(I), R1 = 0.0463, wR2 = 0.1093 and GOF = 1.088 for all reflections, max/min residual electron density +0.356/–0.274 eÅ^{-3}. CCDC 2118125.

Crystallographic Data for **2e**: $C_{20}H_{16}FN_2O_2P$, M = 366.32, 0.18 x 0.15 x 0.09 mm, T = 173(2) K, Monoclinic, space group $P2_1/c$, a = 6.0725(3) Å, b = 23.4215(13) Å, c = 12.1311(6) Å, β = 96.794(3)°, V = 1713.26(15) Å^3, Z = 4, D_c = 1.420 Mg/m^3, μ(Cu) = 1.667 mm^{-1}, F(000) = 760, $2\theta_{max}$ = 133.53°, 9027 reflections, 3027 independent reflections [R_{int} = 0.0455], R1 = 0.0602, wR2 = 0.1774 and GOF = 1.064 for 3027 reflections (289

parameters) with I>2σ(I), R1 = 0.0626, wR2 = 0.1803 and GOF = 1.064 for all reflections, max/min residual electron density +0.438/–0.695 eÅ^{-3}. CCDC 2118124.

Crystallographic Data for **6a**: $C_{42}H_{44}N_4O_7P_2$, 2($C_{21}H_{19}N_2O_2P$)•3(H_2O), M = 778.75, 0.256 x 0.233 x 0.199 mm^3, T = 99.9(6) K, Triclinic, space group P-1, a = 9.70580(10) Å, b = 14.5759(2) Å, c = 15.5433(3) Å, α = 115.291(2)°, β = 103.9340(10)°, γ = 93.4780(10)°, V = 1895.84(6) Å^3, Z = 2, D_c = 1.364 Mg/m^3, μ(Cu) = 1.517 mm^{-1}, F(000) = 820, $2\theta_{max}$ = 77.999°, 44672 reflections, 8085 independent reflections [R(int) = 0.0356], R1 = 0.0360, wR2 = 0.0960 and GOF = 1.059 for all reflections, max/min residual electron density +1.048/–0.434 eÅ^{-3}. CCDC 2118046.

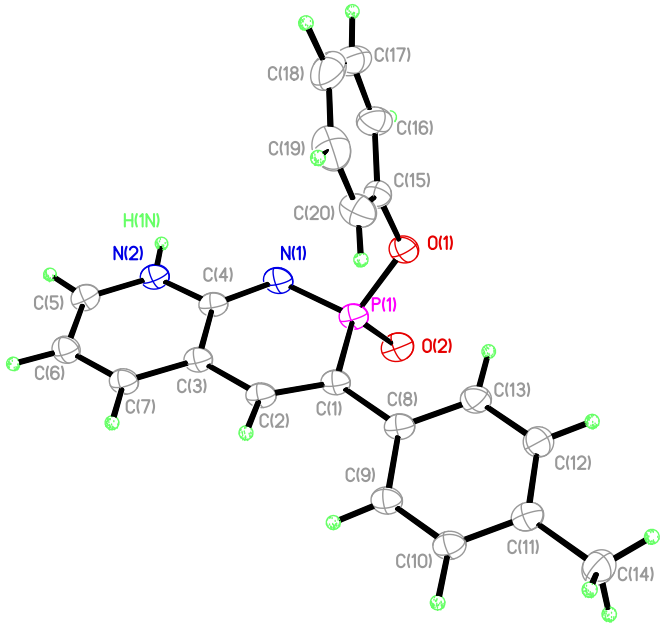

Figure A1. ORTEP drawing of pyridine-PN **2a'**; thermal ellipsoids drawn at 30% probability.

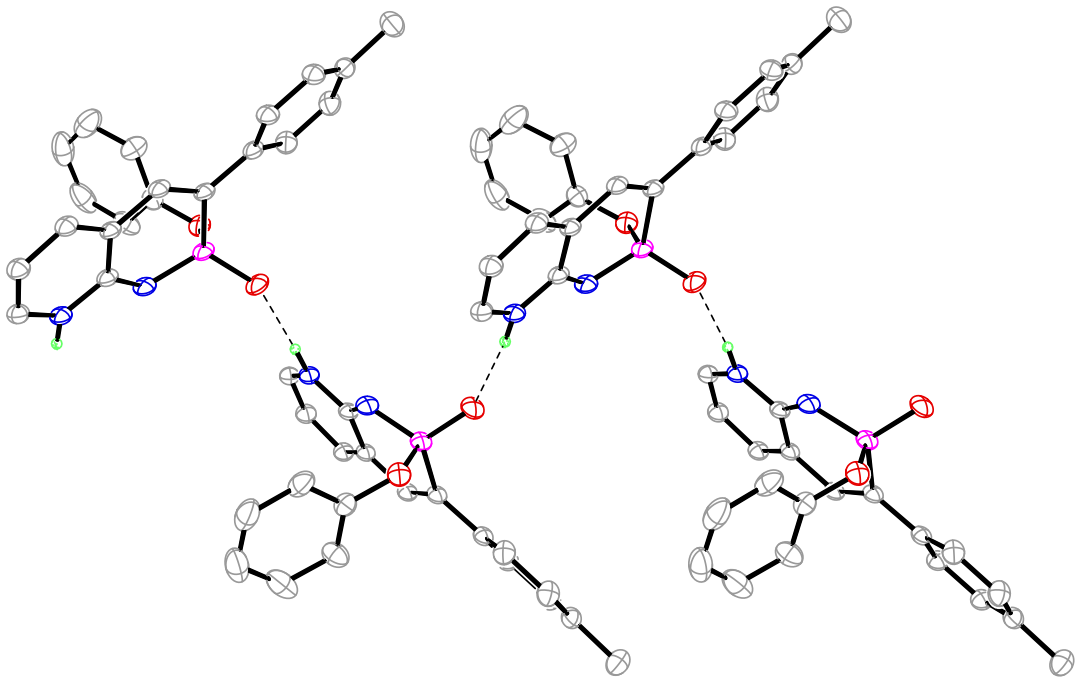

Figure A2. ORTEP drawing of the crystal packing of **2a'**; thermal ellipsoids drawn at 30% probability. Homodimers are not formed in quinoidal tautomer due to lack of complementarity to DAA hydrogen-bonding array; rather, zigzag H-bonded "polymer" strips are formed.

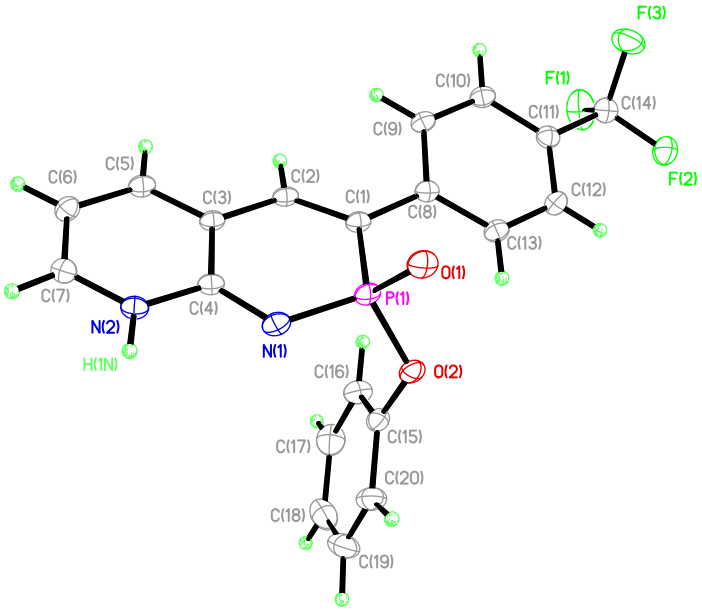

Figure A3. ORTEP drawing of pyridine-PN **2c'**; thermal ellipsoids drawn at 30% probability.

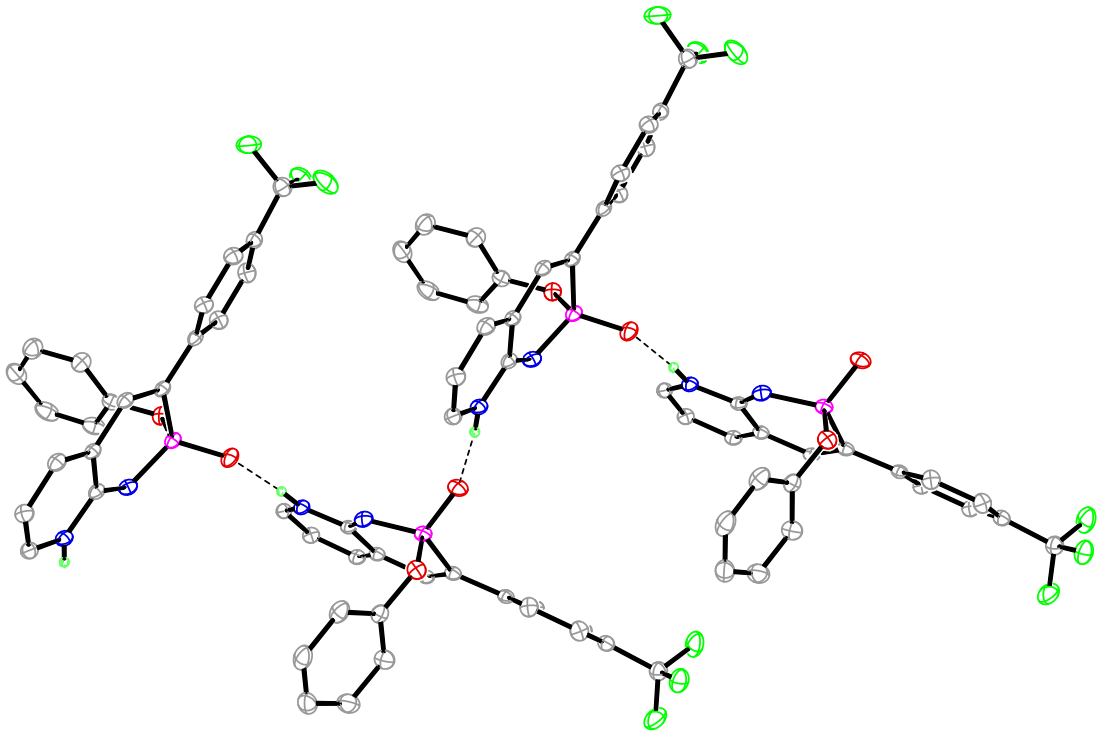

Figure A4. ORTEP drawing of the crystal packing of **2c'**; thermal ellipsoids drawn at 30% probability. Homodimers are not formed in quinoidal tautomer due to lack of

complementarity to DAA hydrogen-bonding array; rather, zigzag H-bonded "polymer" strips are formed.

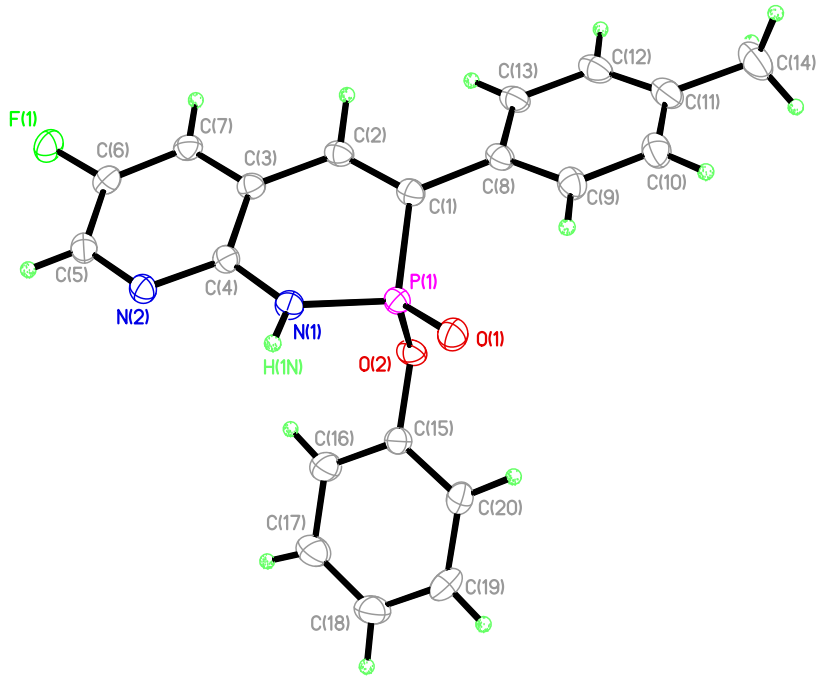

Figure A5. ORTEP drawing of pyridine-PN **2e**; thermal ellipsoids drawn at 30% probability.

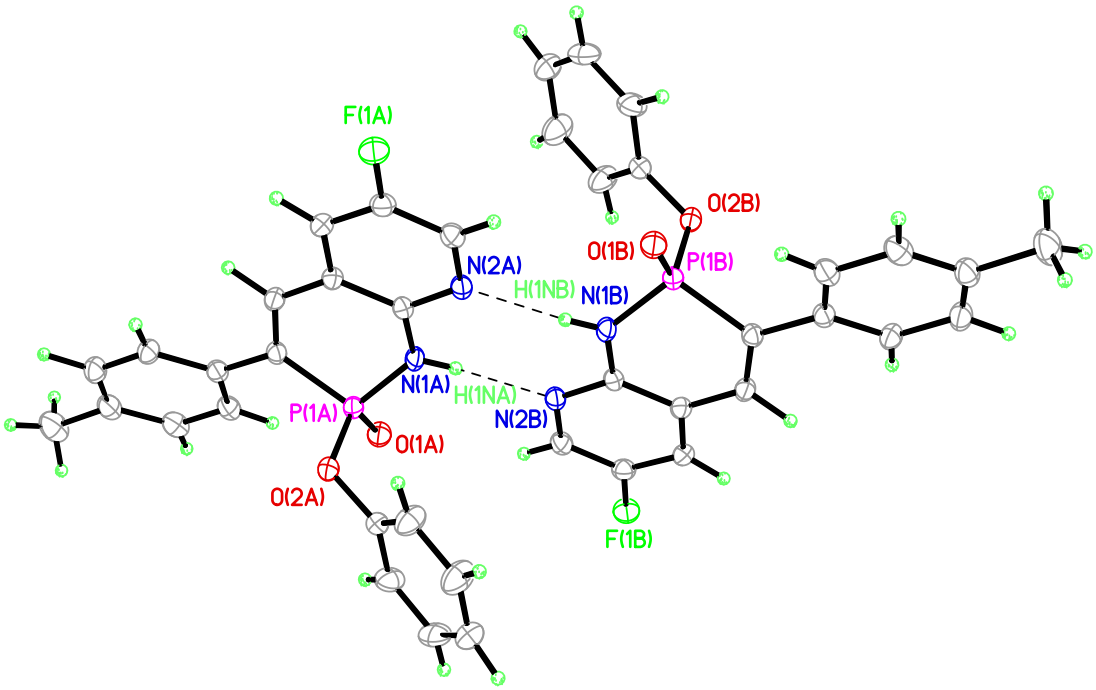

Figure A6. ORTEP drawing of the crystal packing of **2e**; thermal ellipsoids drawn at 30% probability. Homodimers form between the pairs of nitrogen atoms when aromaticity is retained.

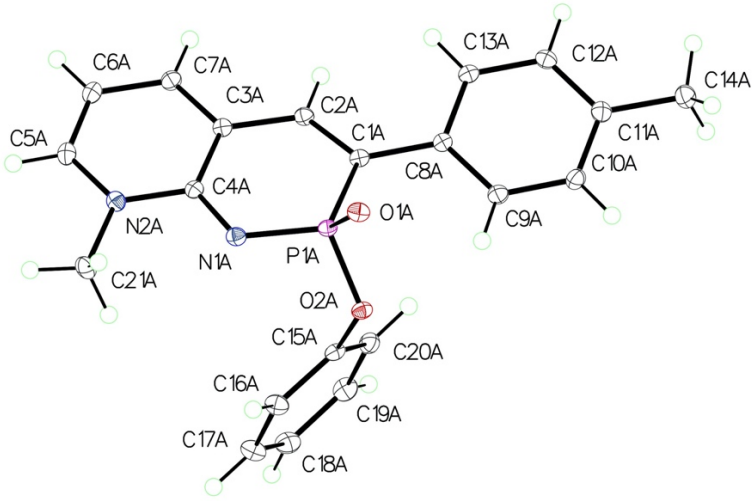

Figure A7. ORTEP drawing of pyridine-PN **6a**; thermal ellipsoids drawn at 30% probability.

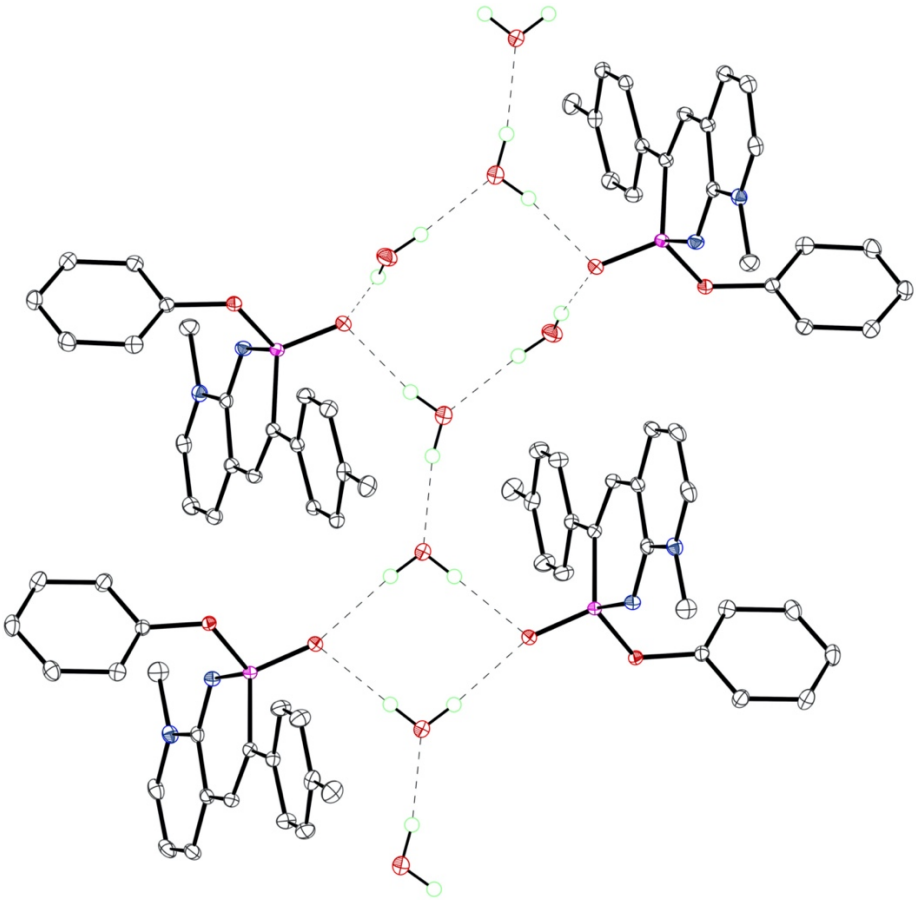

Figure A8. ORTEP drawing of the crystal packing of **6a**; thermal ellipsoids drawn at 30% probability. No homodimer is formed on the phosphonamide face; rather, there are three water molecules for every two molecules of **6a**, which stich up the structure as shown above. O•••O distances are 2.844(1), 2.874(1) and 2.953(1) Å.

Solid State UV-Vis Data

General. Diffuse reflectance UV-vis spectroscopy (DRUV-vis) was performed on a Perkin Elmer Lambda 1050 UV/Vis/NIR spectrometer, with a 150 mm InGaAs integrating sphere in the range of 1200/2000-200 nm paired with a Harrick Scientific Praying Mantis Diffuse Reflection (DRP) accessory. All samples were diluted with ground $BaSO_4$ before measurement to ensure proper percent reflectance, and to maximize pseudo-absorbance. The pseudo-λ_{abs} values were determined by peak maxima in Kubelka-Munk vs. wavelength units. All Gaussian fits were performed in Igor Pro v.6.3.7 and fit to minimize residual contribution.

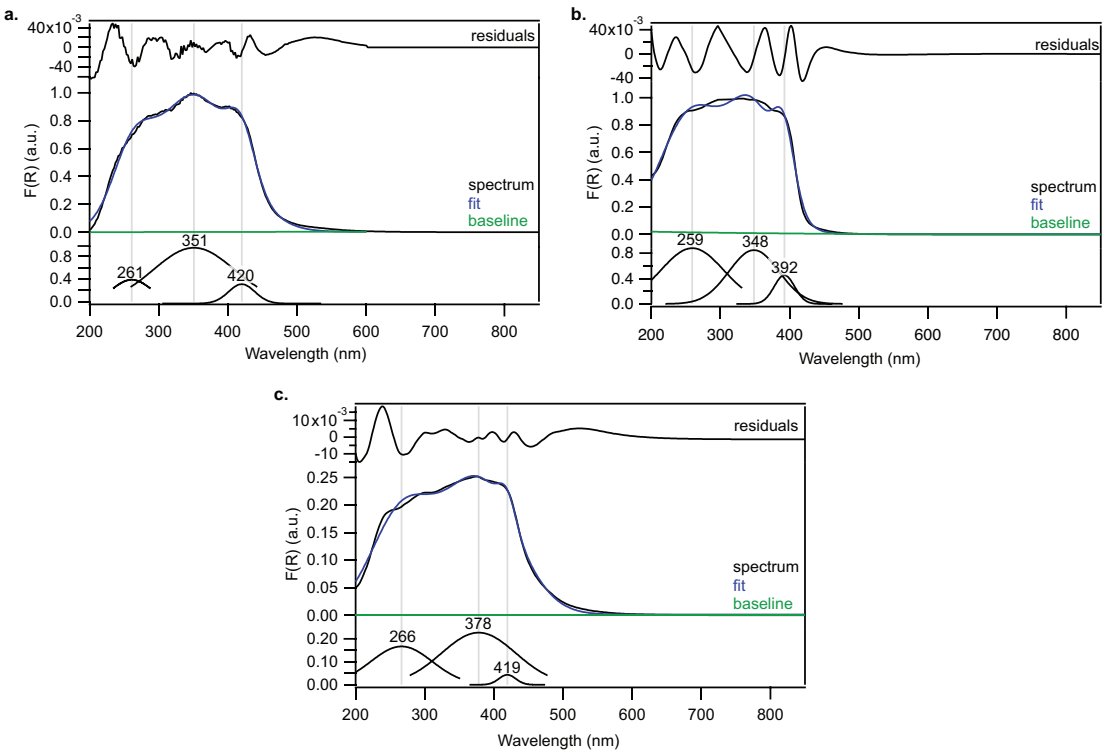

Figure A9. Diffuse reflectance UV-vis spectra reported in K-M (F(R)) units and corresponding Gaussian fits on **2a** (a), **2e** (b), and **6a** (c).

Computational Data

Calculated NMR Data.

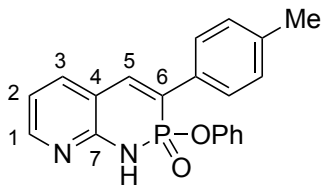

2a

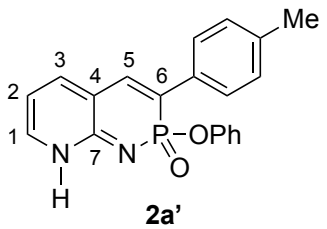

2a'

H1 = 8.0 ppm	C1 = 150.0 ppm
H2 = 6.5 ppm	C2 = 116.1 ppm
H3 = 7.0 ppm	C3 = 138.2 ppm
H5 = 7.0 ppm	C4 = 115.8 ppm
	C5 = 138.6 ppm
	C6 = 127.0 ppm
	C7 = 152.9 ppm

H1 = 7.0 ppm	C1 = 133.6 ppm
H2 = 6.0 ppm	C2 = 106.7 ppm
H3 = 6.9 ppm	C3 = 139.5 ppm
H5 = 6.9 ppm	C4 = 123.0 ppm
	C5 = 134.4 ppm
	C6 = 132.7 ppm
	C7 = 152.4 ppm

Figure A10. Computed NMR shifts for **2a** (aromatic form) and **2a'** (quinoid form) at PCM($CHCl_3$)/B3LYP-D3/6-311+G(d,p). All shifts were calculated by comparing the computed H or C chemical shieldings of **2a** and **2a'** to the computed H or C chemical shieldings of benzene ($\delta_i = \sigma_{benzene} - \sigma_i + \delta_{benzene}$).

Computed NICS for a tetramer assembly of PN-heterocycles. Geometry optimization of a tetramer assembly of PN-heterocycles identified a dominant quinoidal form (see Figure S11, starting geometry based on X-ray structure). Even though hydrogen bonding can occur both at the P=O site and at the N–H site, in the tetramer geometry, the "inner" monomers only have P=O hydrogen bonding and the "outer" monomers only have N–H hydrogen bonding. Nonetheless, both assembled monomers exhibit more negative sum of NICS(0) values compared to that of the unassembled **2a'**, suggesting aromaticity gain upon hydrogen bonding. The effects of aromaticity gain are expected to be even stronger in the solid state since all of the monomers are hydrogen bonded at both the P=O and N–H sites.

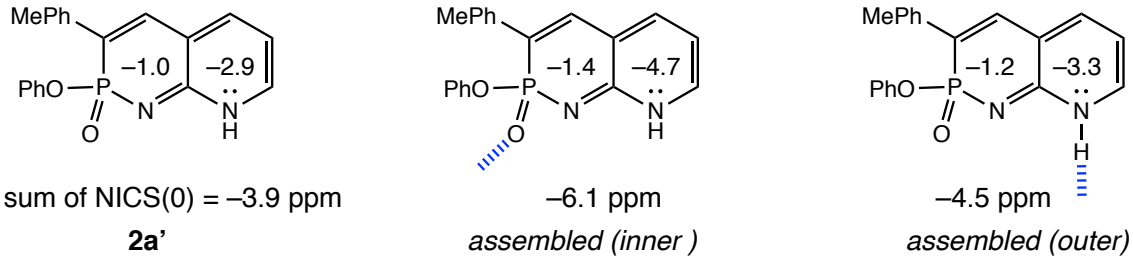

Figure A11. Computed sum of NICS(0) for **2a'** and for the assembled (inner and outer) monomers of the tetramer structure shown in Figure S12.

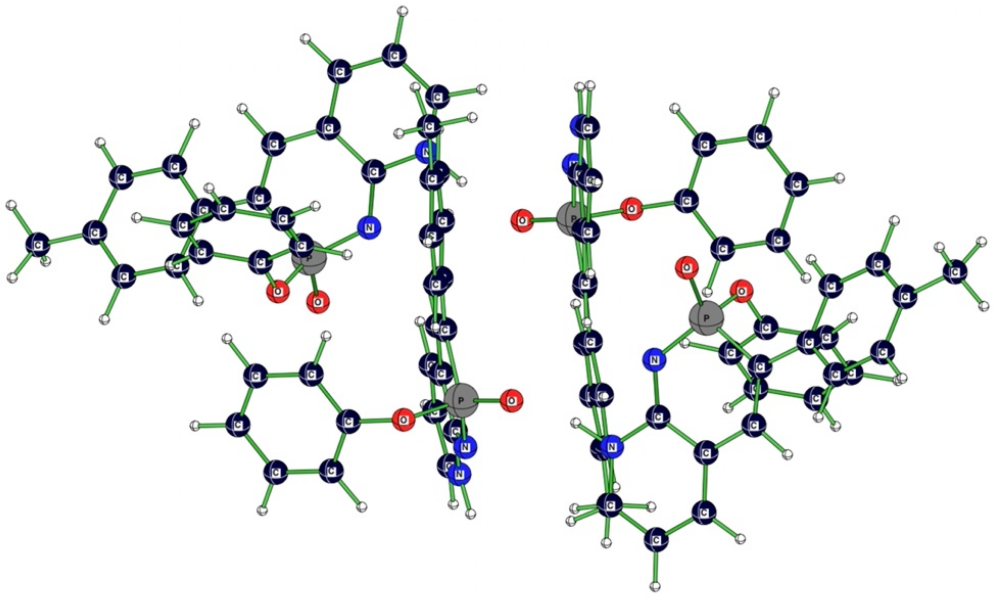

Figure A12. Based on structure obtained from X-ray determination, geometry optimization of a tetramer assembly of the PN-heterocycles suggest a dominant **2a'** form in the solid state.

Calculated charges.

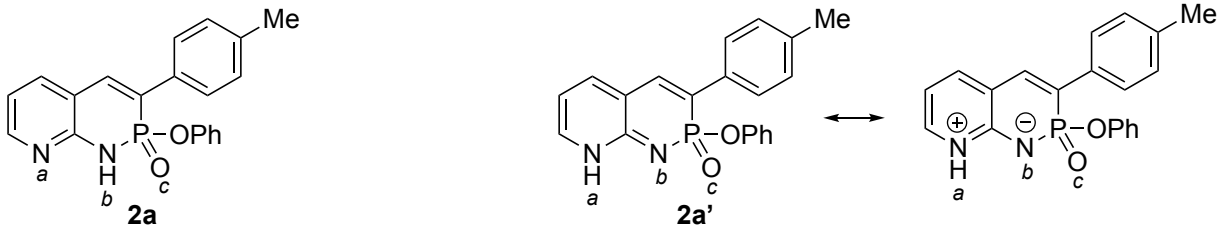

Na = –0.174
Nb = –0.125
Hb = +0.138
Oc = –0.394

Na = –0.022
Nb = –0.257
Ha = +0.149
Oc = –0.404

Figure A13. Calculated Hirshfeld charges for **2a** (aromatic form) and **2a'** (quinoid form) at B3LYP-D3/6-311+G(d,p) in the gas phase. In **2a'**, the charges on N (–0.022 for N_a and –0.257 for N_b) suggest aromatization of the π-system (see zwitterionic resonance form, note the positive charge on N_a and negative charge on N_b).

Cartesian coordinates for the optimized tetramer geometry based on the X-ray crystal structure of heterocycle **2a.**

P	1.46659	-0.69098	2.21433
O	2.97673	-0.79535	2.85652
O	0.78949	0.45539	2.91546
N	0.77213	-2.16348	2.43613
N	-0.08842	-4.16627	1.71264
C	1.66259	-0.41678	0.43873
C	1.11722	-1.34960	-0.39252
C	0.52451	-2.60101	0.01487
C	0.43190	-2.92429	1.41801
C	-0.50033	-5.07950	0.78547
C	-0.43935	-4.77390	-0.54594
C	0.06169	-3.50998	-0.92300
C	2.34696	0.80609	-0.04327
C	2.57547	1.03483	-1.41296
C	3.23064	2.17741	-1.86097
C	3.69325	3.14836	-0.96610
C	3.47076	2.92808	0.39931
C	2.81428	1.78968	0.85413

C	4.40221	4.39196	-1.44412
C	3.83162	-1.83351	2.48510
C	3.78799	-3.04026	3.18454
C	4.66349	-4.06495	2.82469
C	5.56865	-3.88337	1.77538
C	5.60117	-2.67034	1.08570
C	4.73091	-1.63735	1.43929
H	-0.13065	-4.38287	2.70176
H	1.10512	-1.18417	-1.46450
H	-0.85273	-6.02620	1.17737
H	-0.71822	-5.49674	-1.30089
H	0.12299	-3.25435	-1.97380
H	2.21509	0.33310	-2.15126
H	3.36760	2.31758	-2.93096
H	3.80041	3.67017	1.12255
H	2.63713	1.68300	1.91722
H	3.06651	-3.15605	3.98561
H	4.63481	-5.00881	3.36307
H	6.24199	-4.68718	1.49120
H	6.28918	-2.52717	0.25868
H	4.73118	-0.69199	0.90806
H	4.02462	5.28520	-0.93089
H	4.27709	4.53861	-2.52266
H	5.48034	4.34276	-1.24307
P	-2.84347	4.02022	3.71348
O	-3.82814	3.97891	2.37137
O	-2.02340	5.25751	3.62625
N	-1.99450	2.60696	3.70371
N	-1.46315	0.48484	4.39697
C	-4.03004	3.89310	5.08476
C	-4.17022	2.68126	5.69296
C	-3.36787	1.50724	5.43753
C	-2.27925	1.59250	4.48339

C	-1.68384	-0.68254	5.03949
C	-2.75909	-0.81928	5.88690
C	-3.58596	0.30395	6.09360
C	-4.83420	5.07069	5.46912
C	-5.34519	5.21310	6.77236
C	-6.13505	6.30370	7.12243
C	-6.43771	7.30847	6.19415
C	-5.91364	7.17975	4.90168
C	-5.12323	6.09195	4.54325
C	-7.26156	8.51132	6.58624
C	-4.78247	2.99293	2.17492
C	-4.40658	1.72378	1.73652
C	-5.38263	0.76219	1.47834
C	-6.73421	1.06989	1.65350
C	-7.10226	2.34395	2.09731
C	-6.12923	3.30870	2.36460
H	-0.60975	0.56188	3.80171
H	-4.94249	2.56120	6.45198
H	-0.96166	-1.46413	4.82599
H	-2.94162	-1.75625	6.39892
H	-4.41732	0.23431	6.79187
H	-5.10180	4.47298	7.52931
H	-6.51282	6.38398	8.13959
H	-6.12541	7.94740	4.16058
H	-4.73009	6.03190	3.53467
H	-3.36111	1.51231	1.57683
H	-5.07593	-0.22042	1.13027
H	-7.49648	0.32406	1.44500
H	-8.15151	2.58984	2.23908
H	-6.39603	4.29990	2.71532
H	-6.62139	9.32878	6.94472
H	-7.96500	8.27246	7.39139
H	-7.83548	8.89842	5.73715

P	-0.91896	1.45184	-2.22505
O	-2.35411	1.72909	-2.98929
O	-0.26552	0.33033	-2.97902
N	-0.11541	2.88263	-2.22519
N	0.76670	4.75920	-1.24126
C	-1.32995	1.04688	-0.51351
C	-0.96488	1.94073	0.44861
C	-0.28804	3.19327	0.22360
C	0.09551	3.55894	-1.12000
C	1.04704	5.60226	-0.20884
C	0.66662	5.27447	1.06498
C	0.00161	4.04846	1.27611
C	-2.01150	-0.22915	-0.20400
C	-2.06385	-0.72696	1.11042
C	-2.72904	-1.90947	1.41396
C	-3.35877	-2.66545	0.41764
C	-3.29854	-2.18161	-0.89599
C	-2.64310	-0.99316	-1.20524
C	-4.03338	-3.97691	0.73367
C	-3.23934	2.69055	-2.49892
C	-3.06567	4.03300	-2.83822
C	-3.96996	4.97764	-2.35081
C	-5.03475	4.58228	-1.53708
C	-5.19965	3.23451	-1.21278
C	-4.29957	2.28223	-1.69195
H	1.05597	4.98648	-2.18562
H	-1.17356	1.74096	1.49379
H	1.56622	6.51639	-0.47164
H	0.85678	5.94779	1.89108
H	-0.29919	3.77011	2.27990
H	-1.55728	-0.19960	1.90611
H	-2.74543	-2.25263	2.44622
H	-3.77193	-2.74707	-1.69543

H	-2.62256	-0.66100	-2.23629
H	-2.22526	4.31272	-3.46360
H	-3.83793	6.02629	-2.60437
H	-5.72882	5.32267	-1.14962
H	-6.01303	2.91976	-0.56677
H	-4.39828	1.23466	-1.43064
H	-3.36937	-4.81948	0.49812
H	-4.29782	-4.04884	1.79424
H	-4.94789	-4.11216	0.14547
P	2.46583	-4.20389	-3.44530
O	3.57812	-4.08245	-2.20880
O	1.48978	-5.26221	-3.07000
N	1.84610	-2.68779	-3.63702
N	1.64201	-0.62806	-4.63303
C	3.50477	-4.52313	-4.89975
C	3.75484	-3.48272	-5.74286
C	3.18504	-2.15879	-5.64616
C	2.22057	-1.87927	-4.59932
C	1.97184	0.34742	-5.50765
C	2.92545	0.12798	-6.47370
C	3.51740	-1.14910	-6.53820
C	4.07732	-5.86803	-5.11106
C	4.37128	-6.34025	-6.40316
C	4.94757	-7.59151	-6.59927
C	5.24256	-8.43209	-5.51793
C	4.93409	-7.97139	-4.23165
C	4.35758	-6.72148	-4.02663
C	5.83111	-9.80544	-5.73471
C	4.63350	-3.18454	-2.27440
C	4.42667	-1.83733	-1.97817
C	5.49869	-0.94679	-2.02437
C	6.77822	-1.40420	-2.35009
C	6.97821	-2.75872	-2.63353

C	5.90663	-3.65313	-2.60377
H	0.90042	-0.41189	-3.94059
H	4.44172	-3.63560	-6.57467
H	1.43104	1.27833	-5.37805
H	3.19264	0.91155	-7.17207
H	4.25353	-1.35878	-7.31127
H	4.12327	-5.73017	-7.26716
H	5.16032	-7.92808	-7.61178
H	5.14727	-8.60377	-3.37257
H	4.12948	-6.40074	-3.01625
H	3.43660	-1.51358	-1.69419
H	5.32499	0.10071	-1.79396
H	7.61512	-0.71178	-2.37942
H	7.97085	-3.12211	-2.88641
H	6.03956	-4.70438	-2.83666
H	5.04134	-10.56192	-5.83734
H	6.43835	-9.84409	-6.64568
H	6.46238	-10.10884	-4.89233

Variable Temperature NMR Data

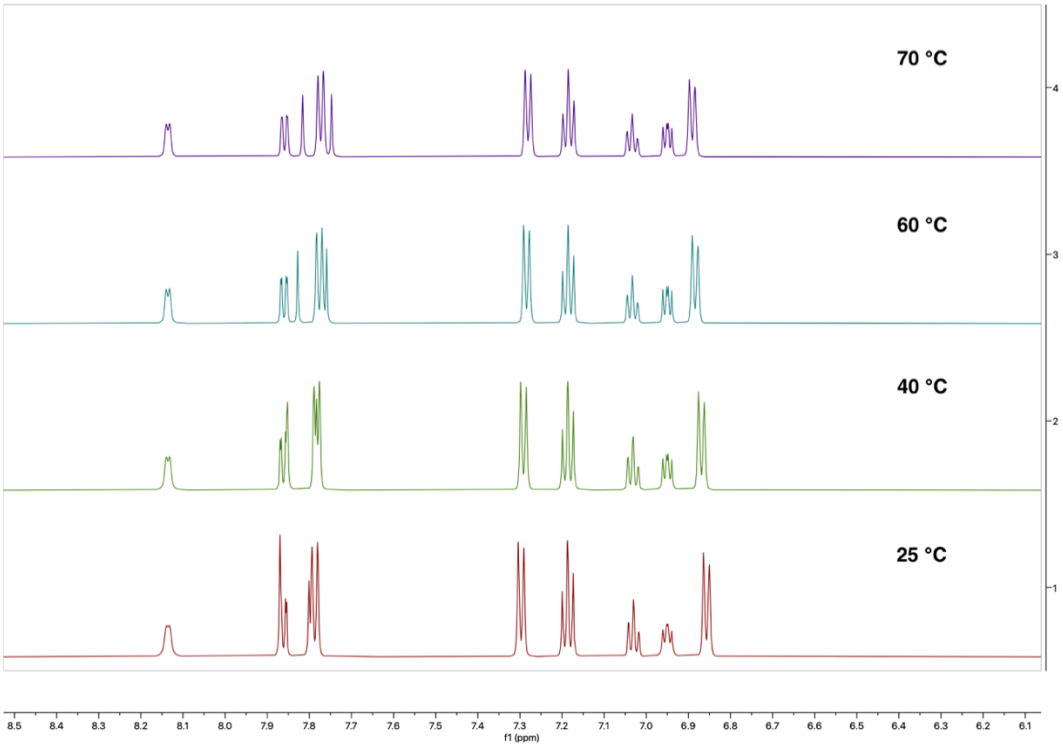

Figure A14. Stacked ^{1}H NMR spectra of the aromatic region of **2a** in DMSO-d_6 ranging from 25 to 70 °C.

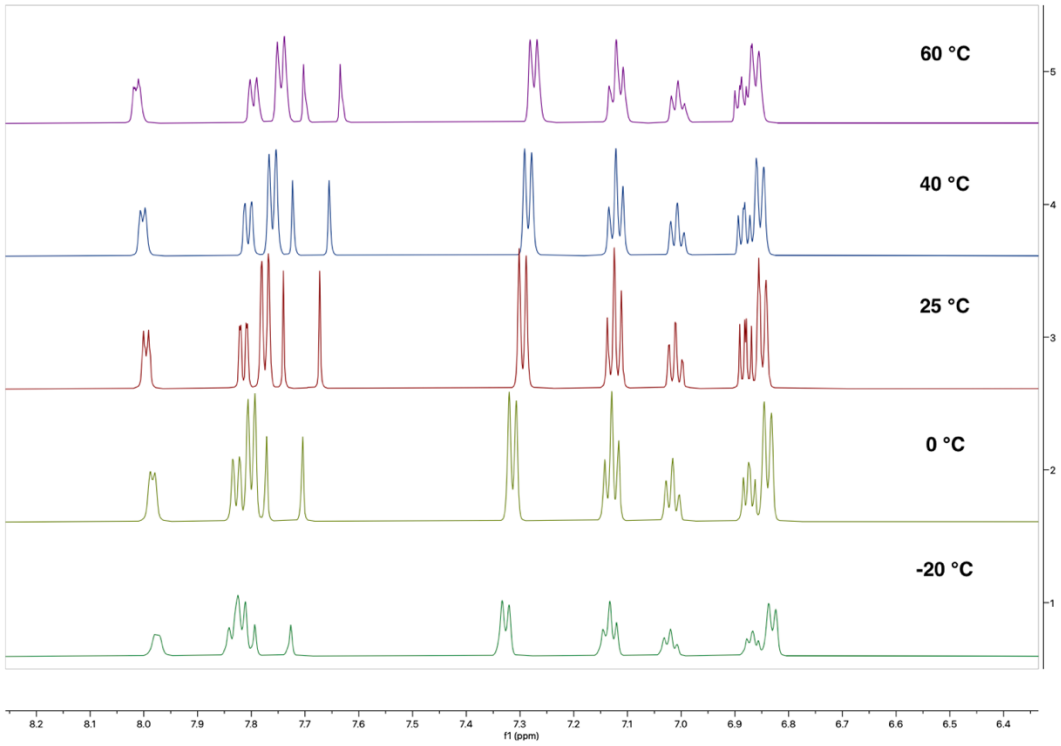

Figure A15. Stacked ^{1}H NMR spectra of the aromatic region of **2a** in CD_3OD ranging from –20 to 60 °C.

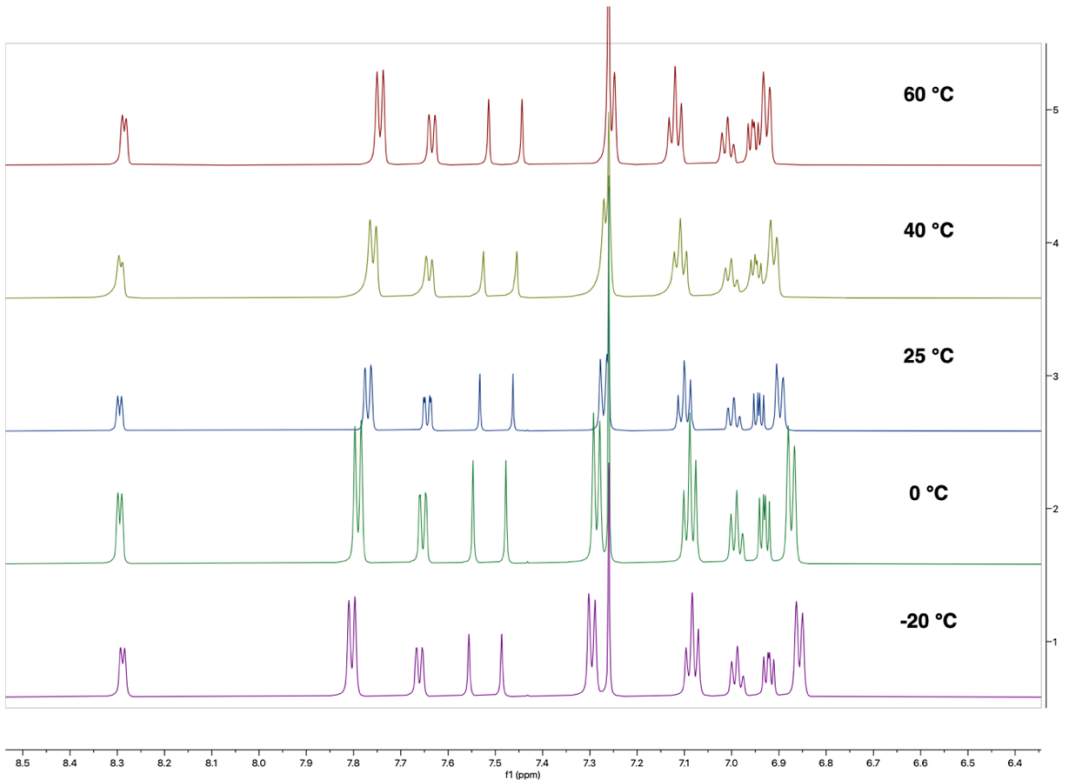

Figure A16. Stacked ^{1}H NMR spectra of the aromatic region of **2a** in $CDCl_3$ ranging from –20 to 60 °C.

Solid State ^{13}C NMR Data

General. Solid state NMR spectra were collected on a Varian VNMRS system equipped with a Phoenix HXY Premium Probe (1.6 mm rotor) operating at rotation speed of 40 kHz. ^{13}C spectra were collected at an operation frequency of 125.70 MHz using a linear ramp cross polarization pulse sequence with spinal decoupling (Varian TANCPX), 2048 scans, a relaxation delay of 2 seconds, and a 90° pulse width of 2.2 usec. Processing was performed in Mestrelab v 12.0.0 with a line broadening factor of 50 Hz.

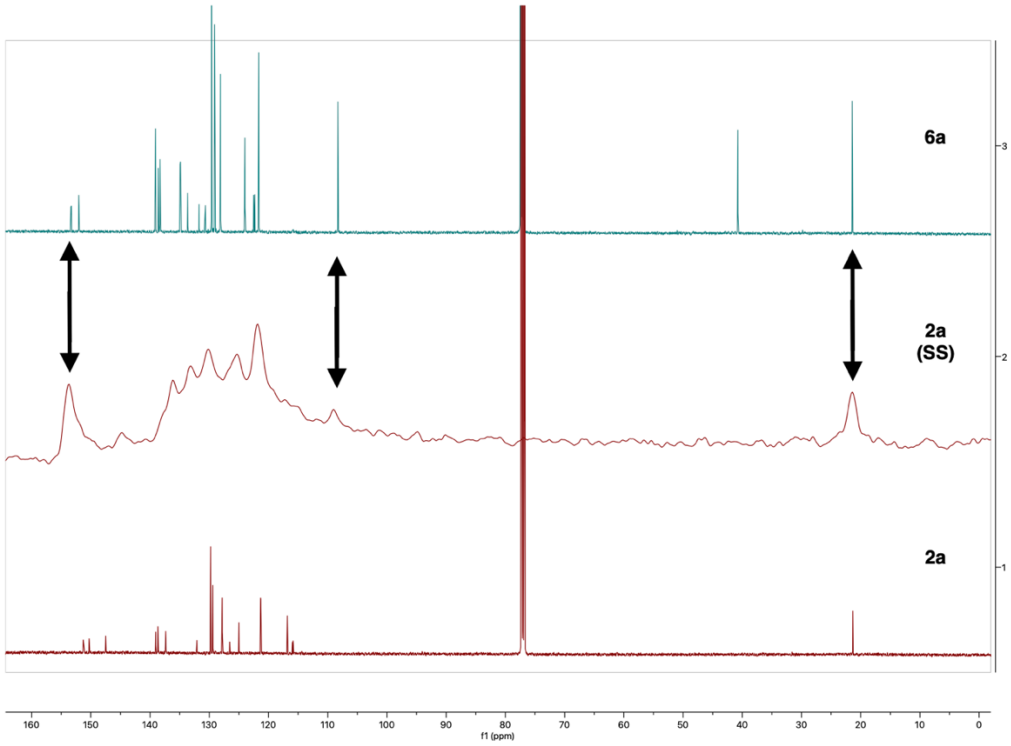

Figure A17. Stacked ^{13}C NMR spectra of heterocycles **6a** (top) and **2a** (bottom) in $CDCl_3$ compared against the solid state ^{13}C NMR spectrum of **2a**. Double headed arrows denote the quinoidal peaks mirrored in both quinoidal compounds **6a** and tautomer **2a'**.

References

1. Sheldrick, G. M. *Bruker/Siemens Area Detector Absorption Correction Program*, Bruker AXS, Madison, WI, 1998.

2. Sheldrick, G. M. Crystal structure refinement with SHELXL. *Acta Cryst.* **2015**, *C71*, 3–8.

3. CrysAlisPro; Rigaku OD, The Woodlands, TX, 2015.

4. Sheldrick, G. M. SHELXT – Integrated space-group and crystal-structure determination. *Acta Cryst.* **2015**, *A71*, 3–8.

5**.** Sheldrick, G. M. A short history of SHELX. *Acta Cryst.* **2008**, *A64*, 112–122.

6. Müller, P. Practical suggestions for better crystal structures. *Crystallogr.* **2009**, *15*, 57–83.

8. Copies of NMR Spectra

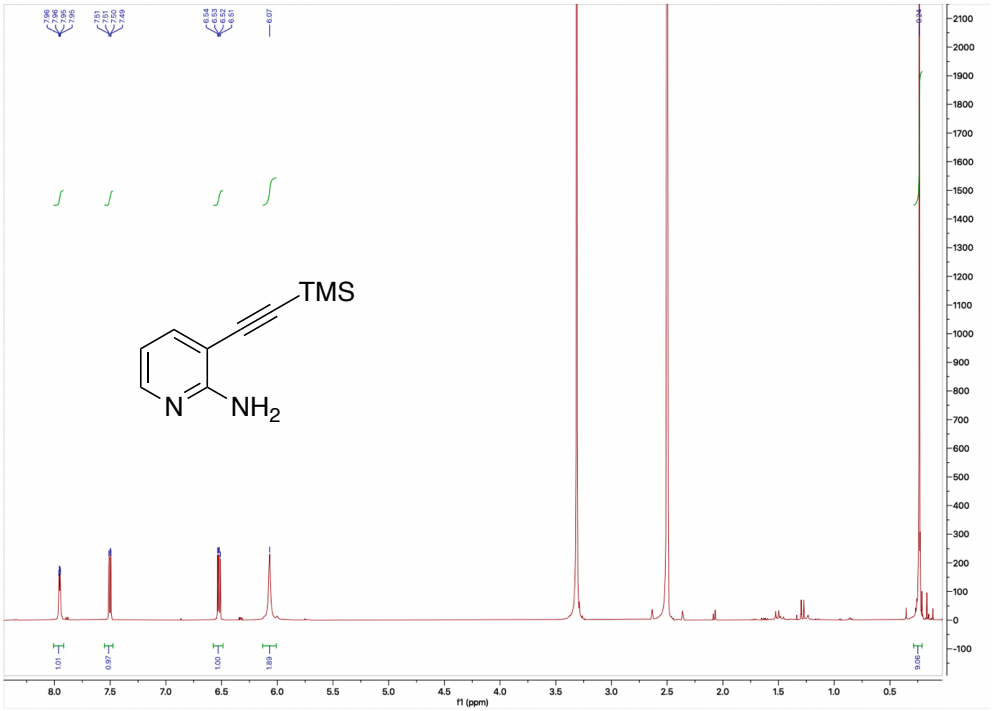

Figure A18 ^{1}H NMR Spectrum of **4** in DMSO-d_6

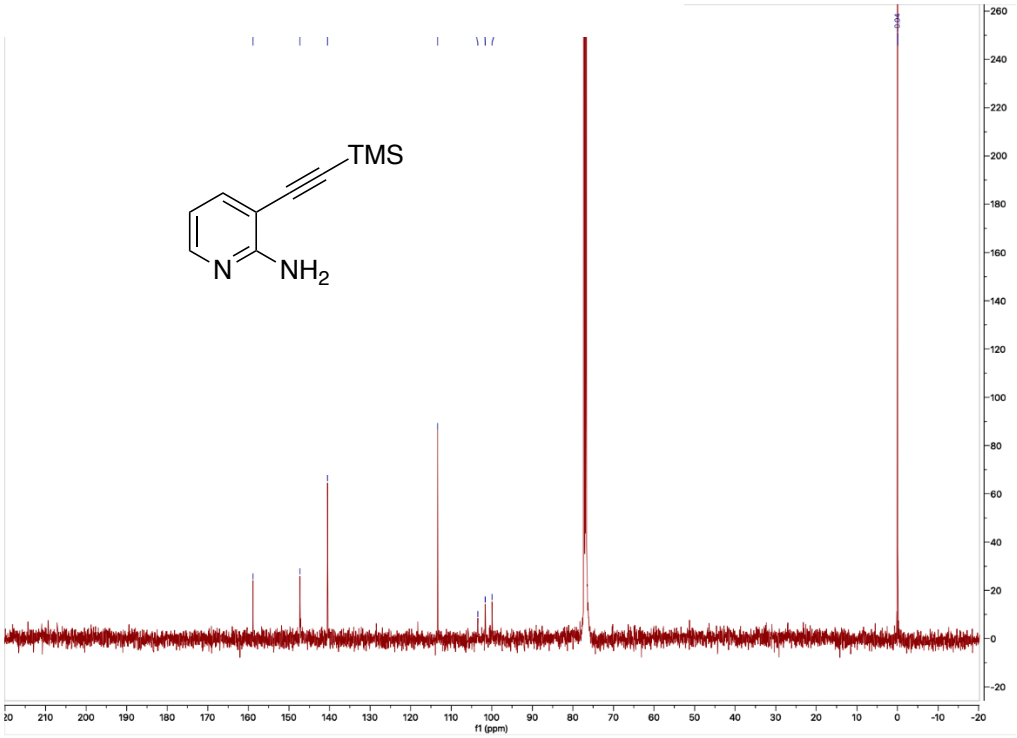

Figure A19 ^{13}C NMR Spectrum of **4** in $CDCl_3$

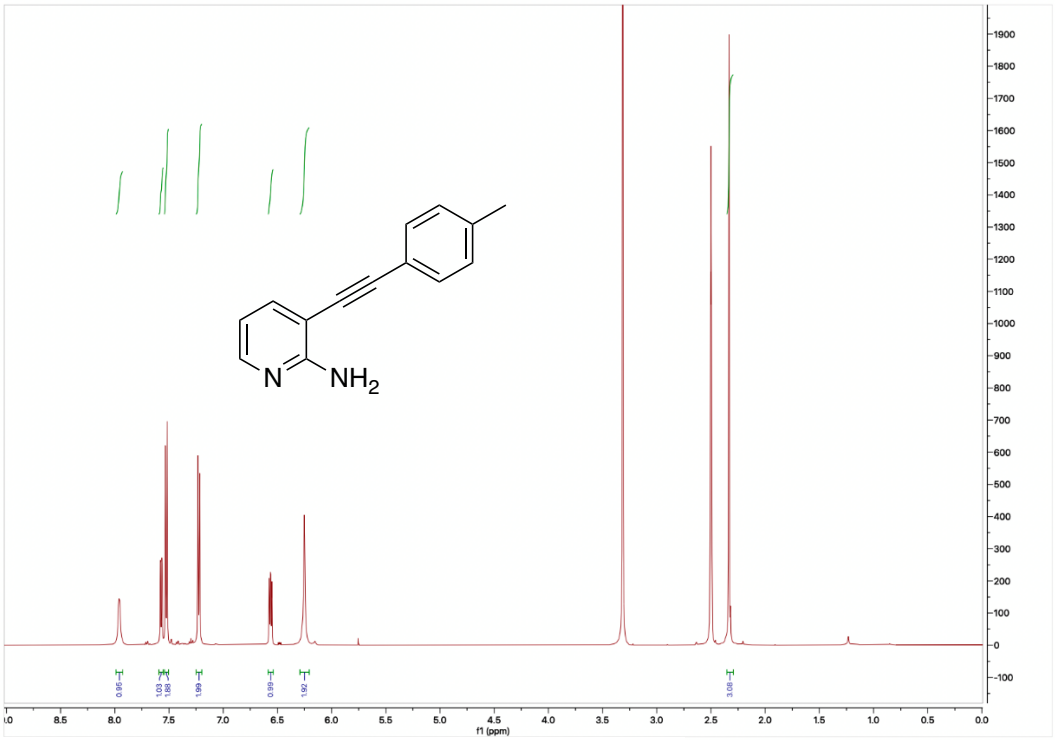

Figure A20 ^{1}H NMR Spectrum of **5a** in DMSO-d_6

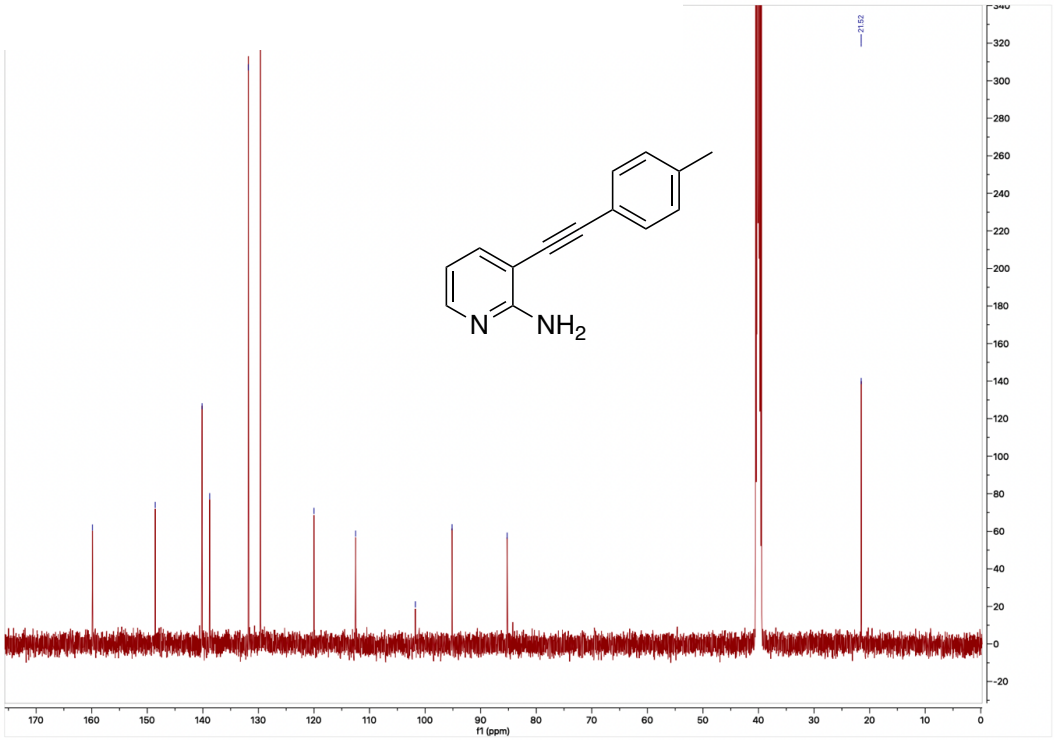

Figure A21 ^{13}C NMR Spectrum of **5a** in DMSO-d_6

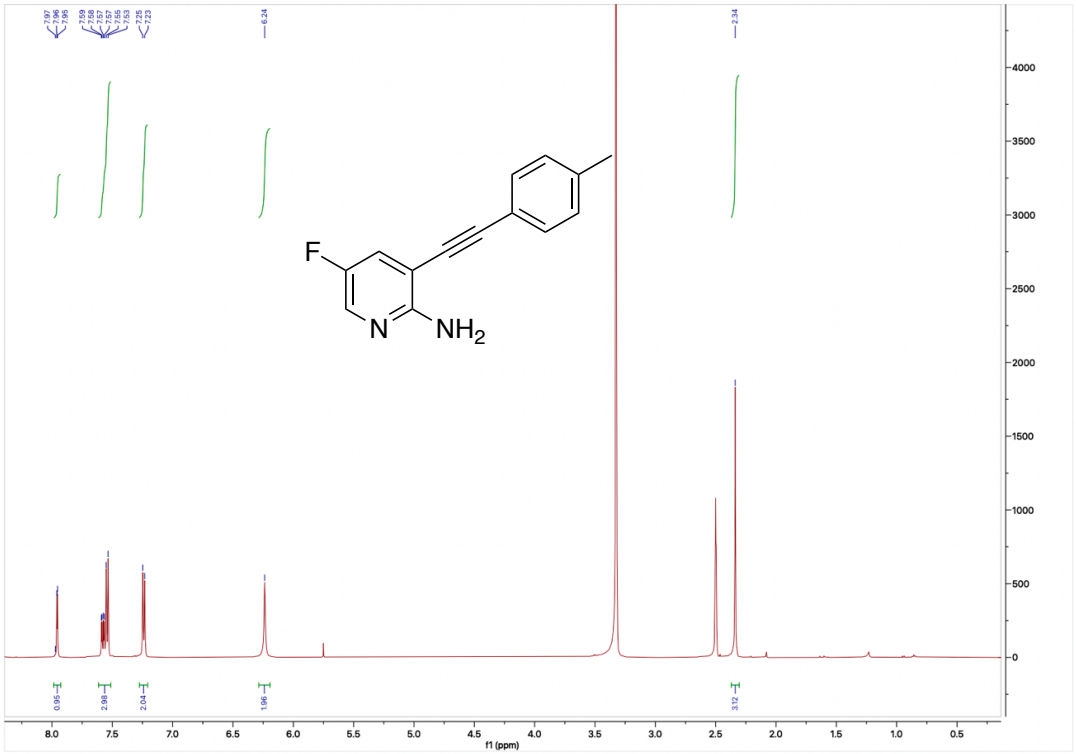

Figure A22 ^{1}H NMR Spectrum of **5e** in DMSO-d_6

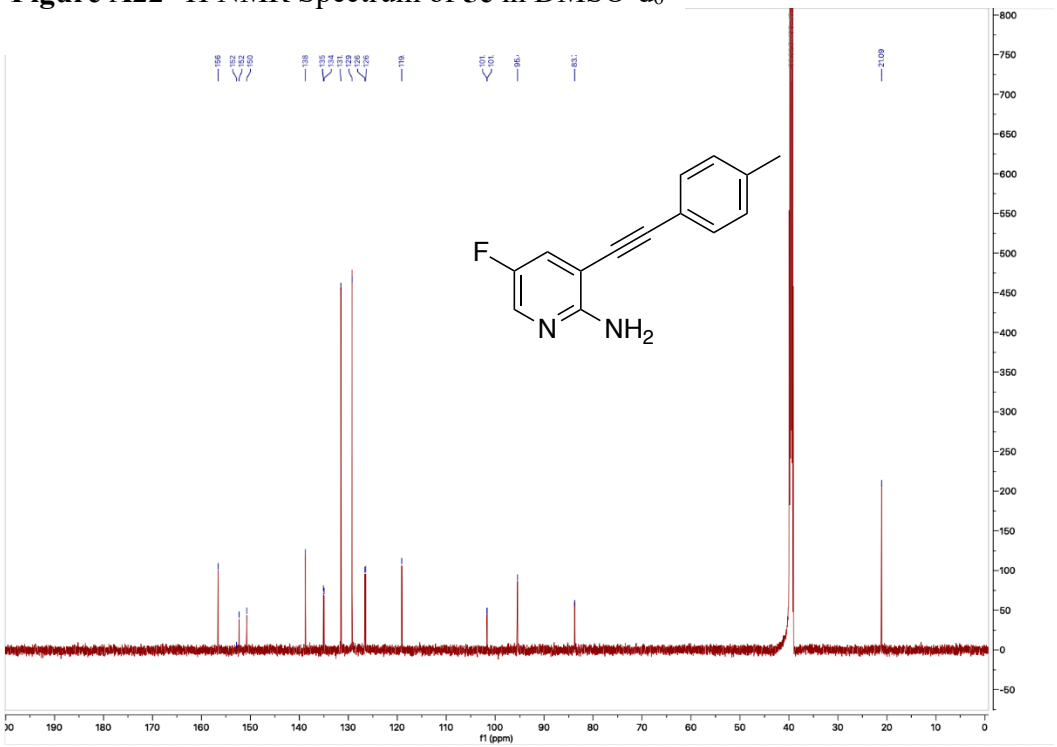

Figure A23 ^{13}C NMR Spectrum of **5e** in DMSO-d_6

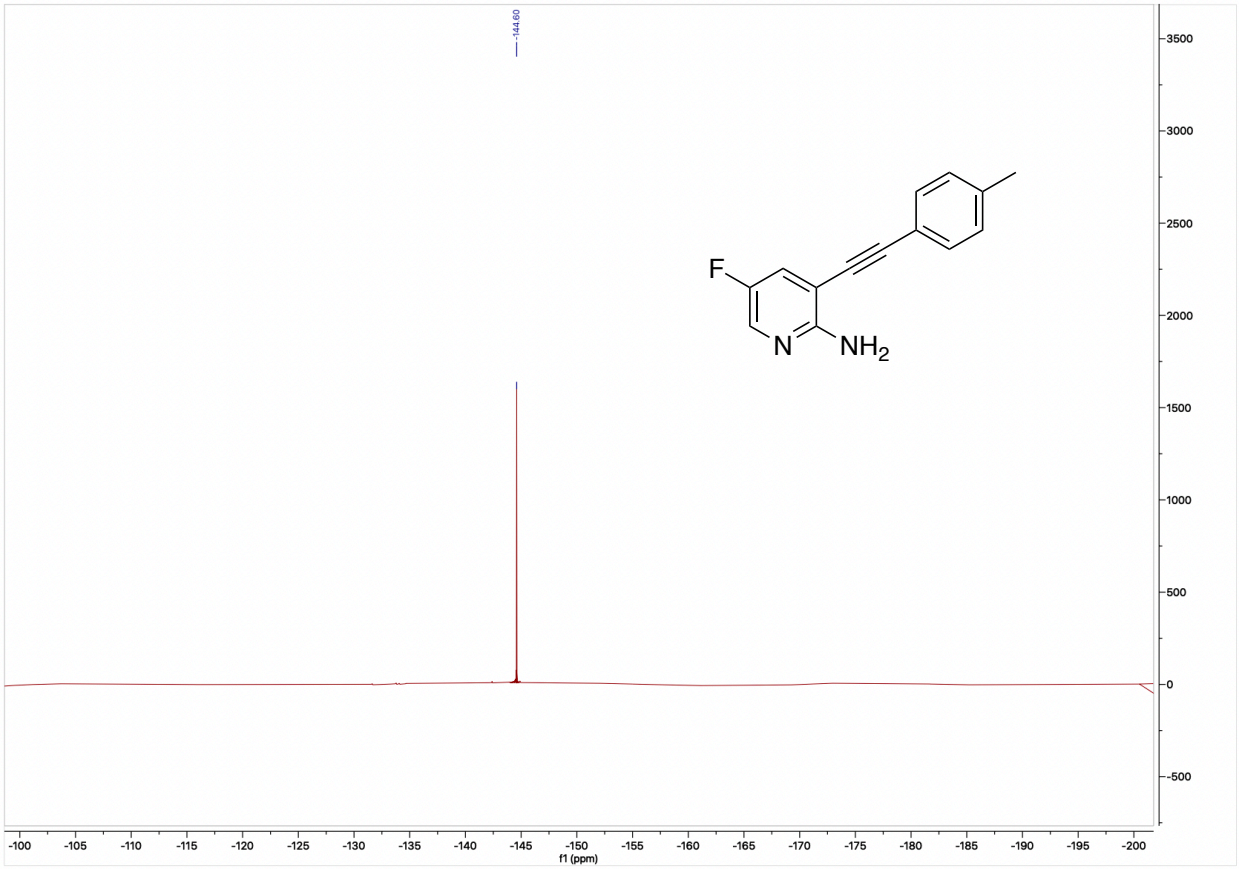

Figure A24 ^{19}F NMR Spectrum of **5e** in DMSO-d_6

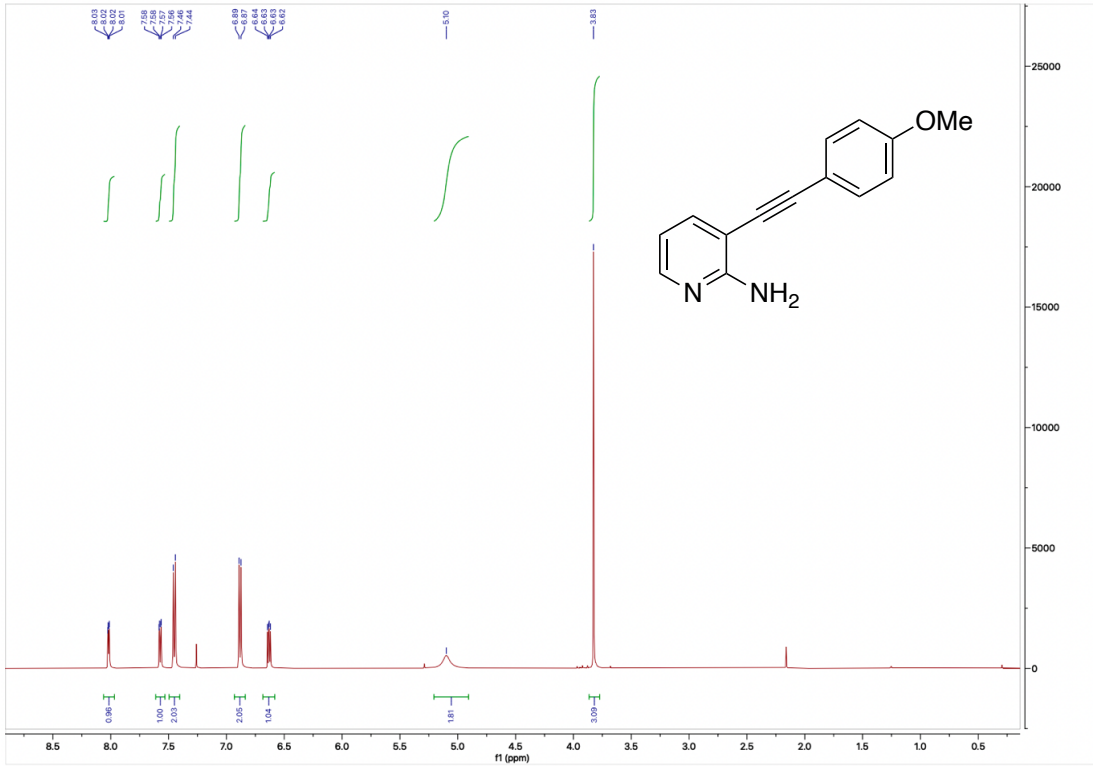

Figure A25 ^{1}H NMR Spectrum of **5b** in $CDCl_3$

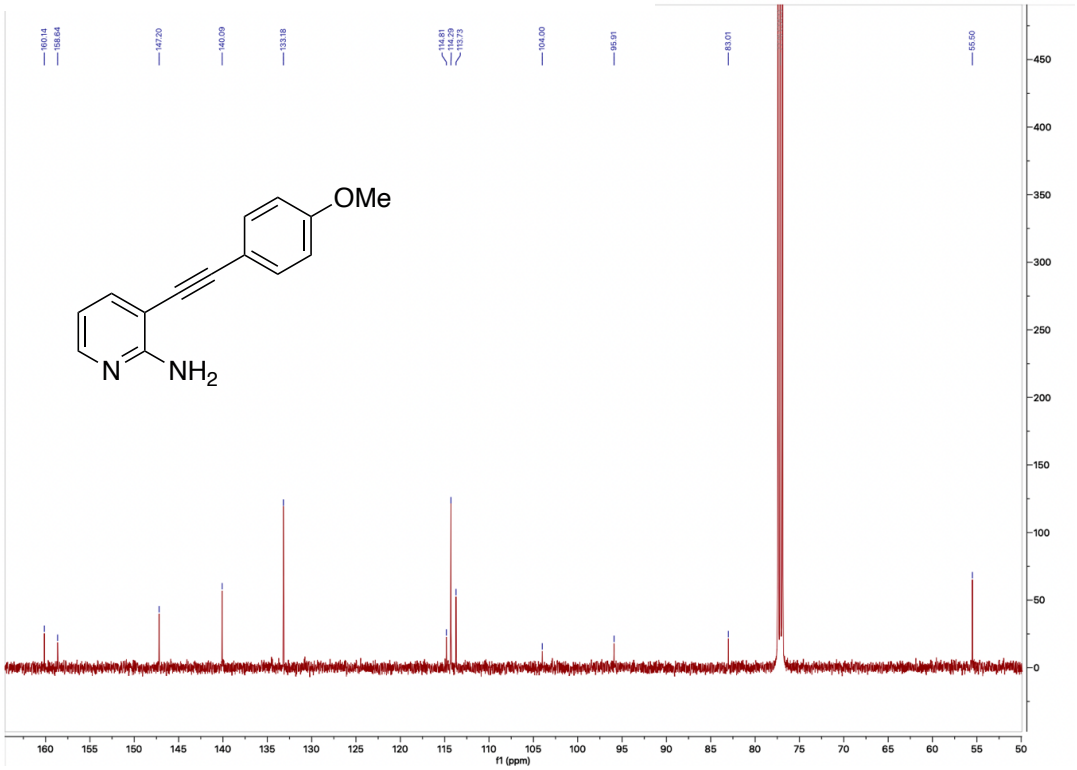

Figure A26 ^{13}C NMR Spectrum of **5b** in $CDCl_3$

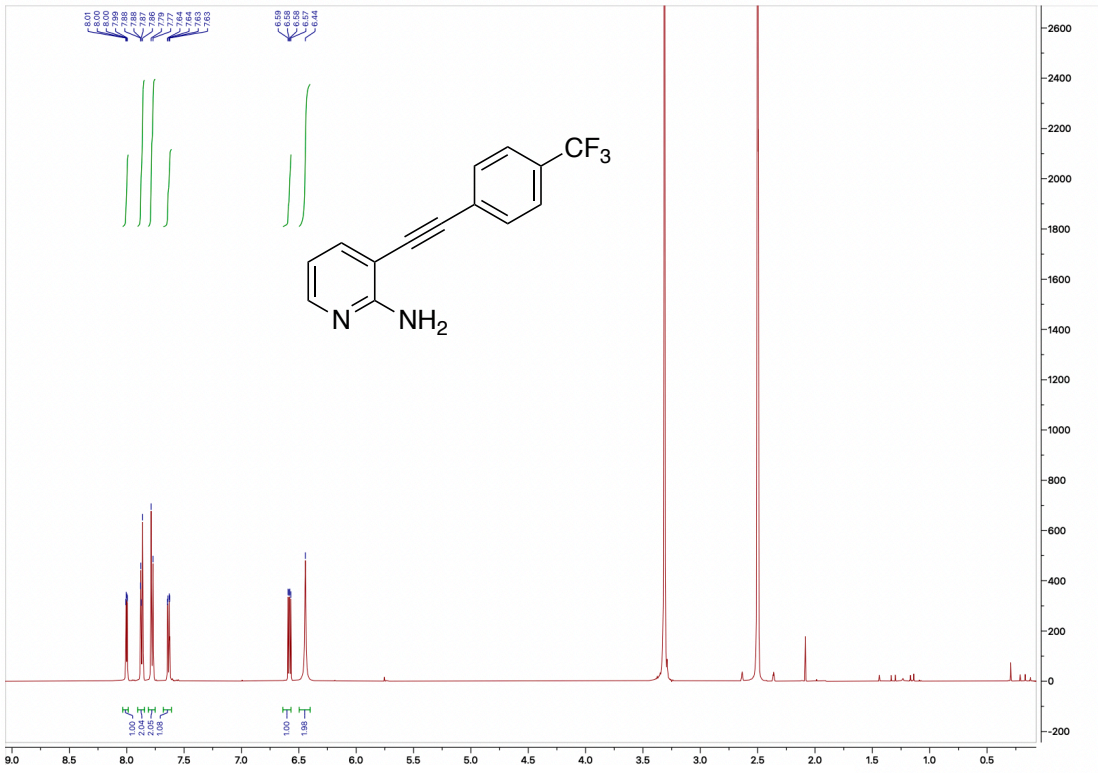

Figure A27 ^{1}H NMR Spectrum of **5c** in $CDCl_3$

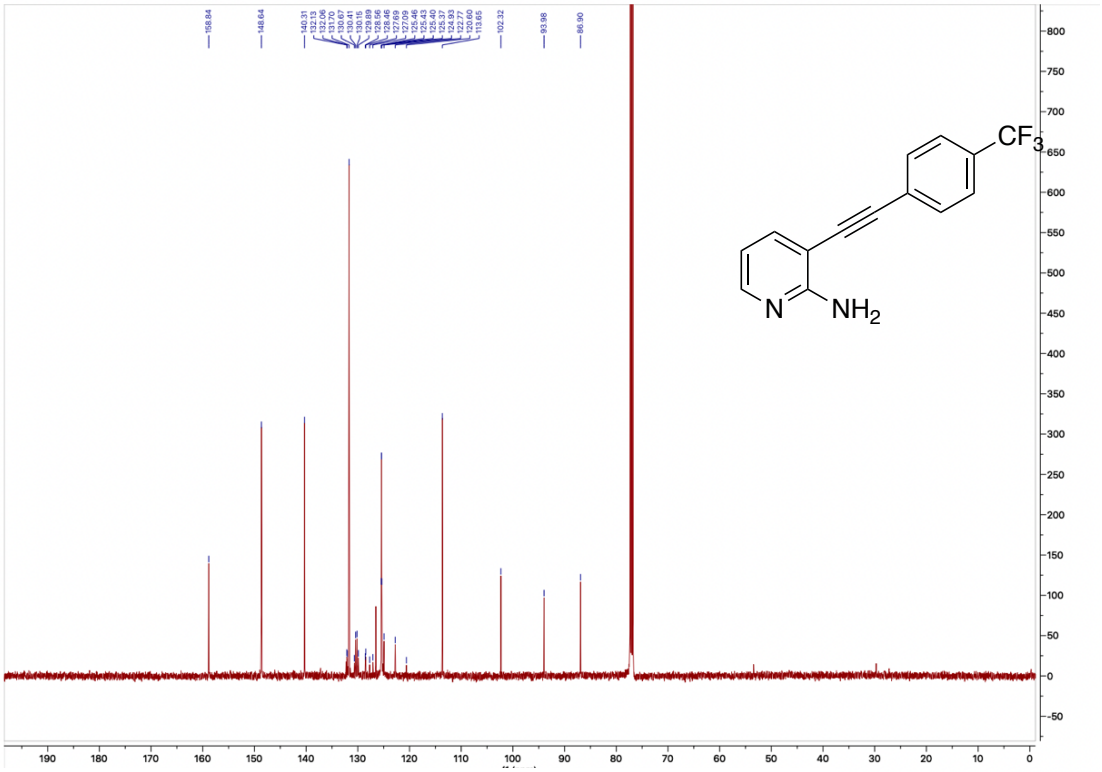

Figure A28 ^{13}C NMR Spectrum of **5c** in $CDCl_3$

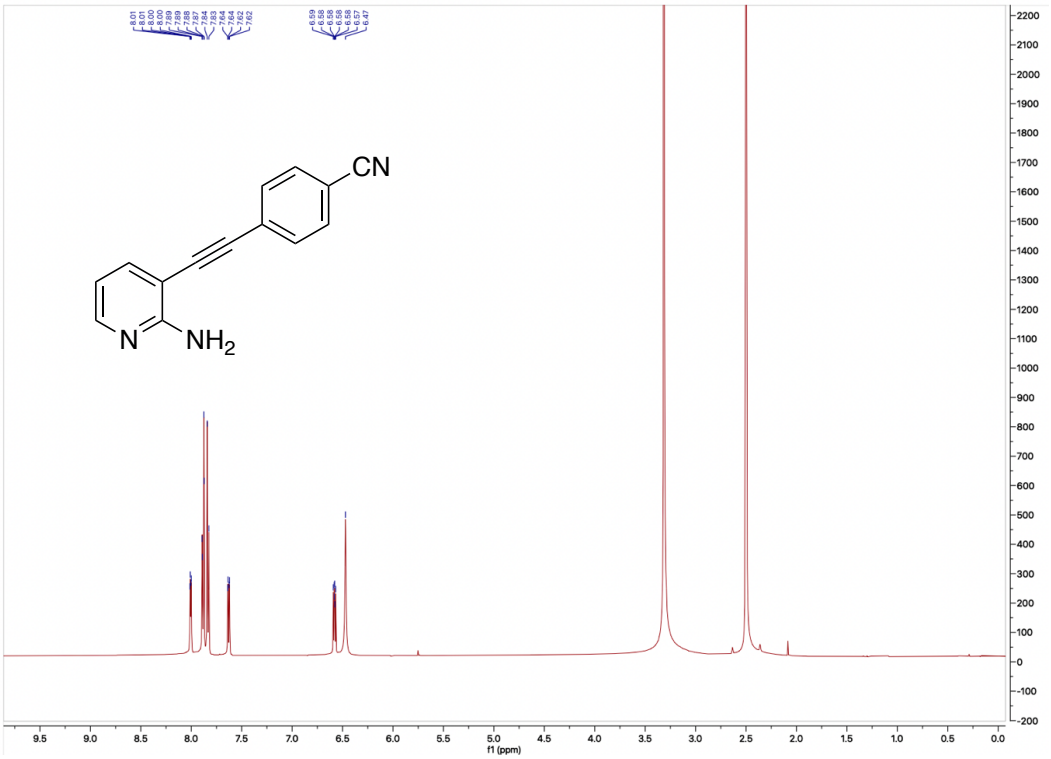

Figure A29 ^{1}H NMR Spectrum of **5d** in DMSO-d_6

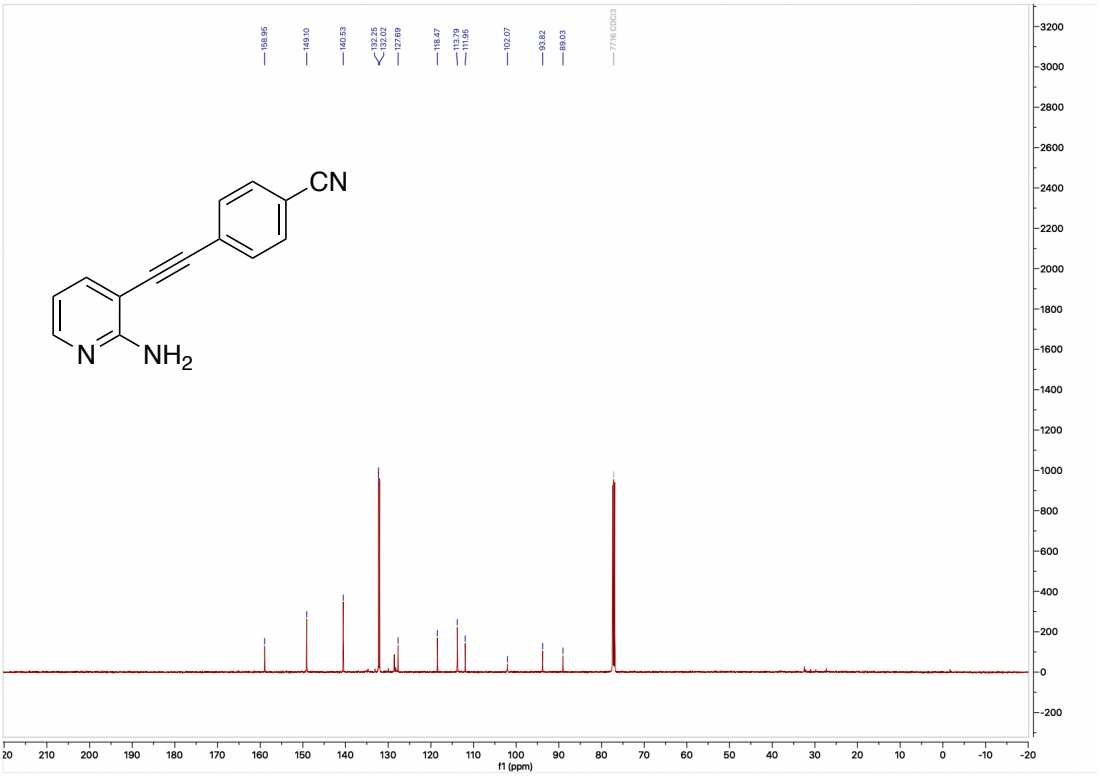

Figure A30 ^{13}C NMR Spectrum of **5d** in $CDCl_3$

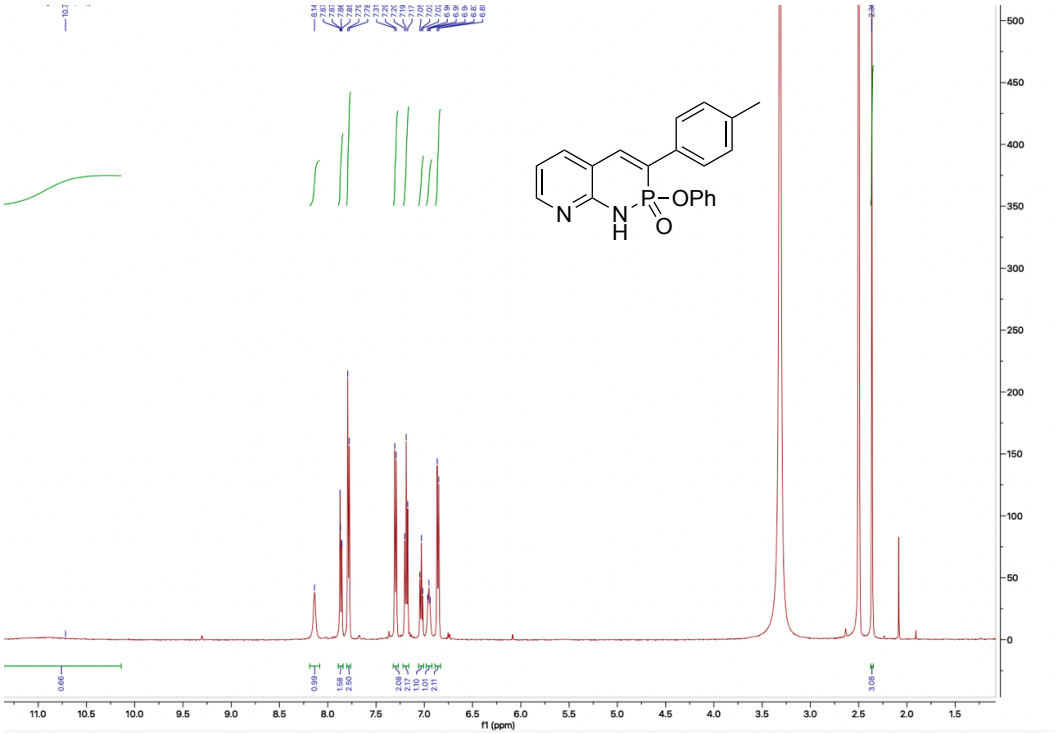

Figure A31 ^{1}H NMR Spectrum of Heterocycle **2a** in DMSO-d$_6$

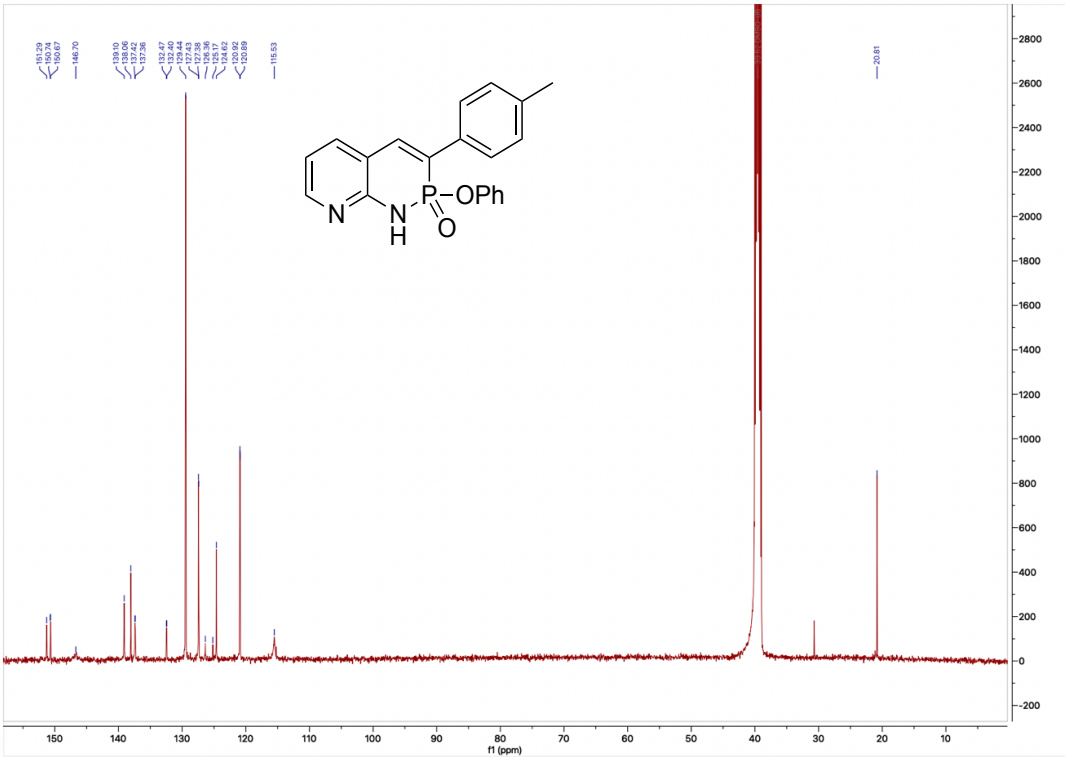

Figure A32 ^{13}C NMR Spectrum of Heterocycle **2a** in DMSO-d$_6$

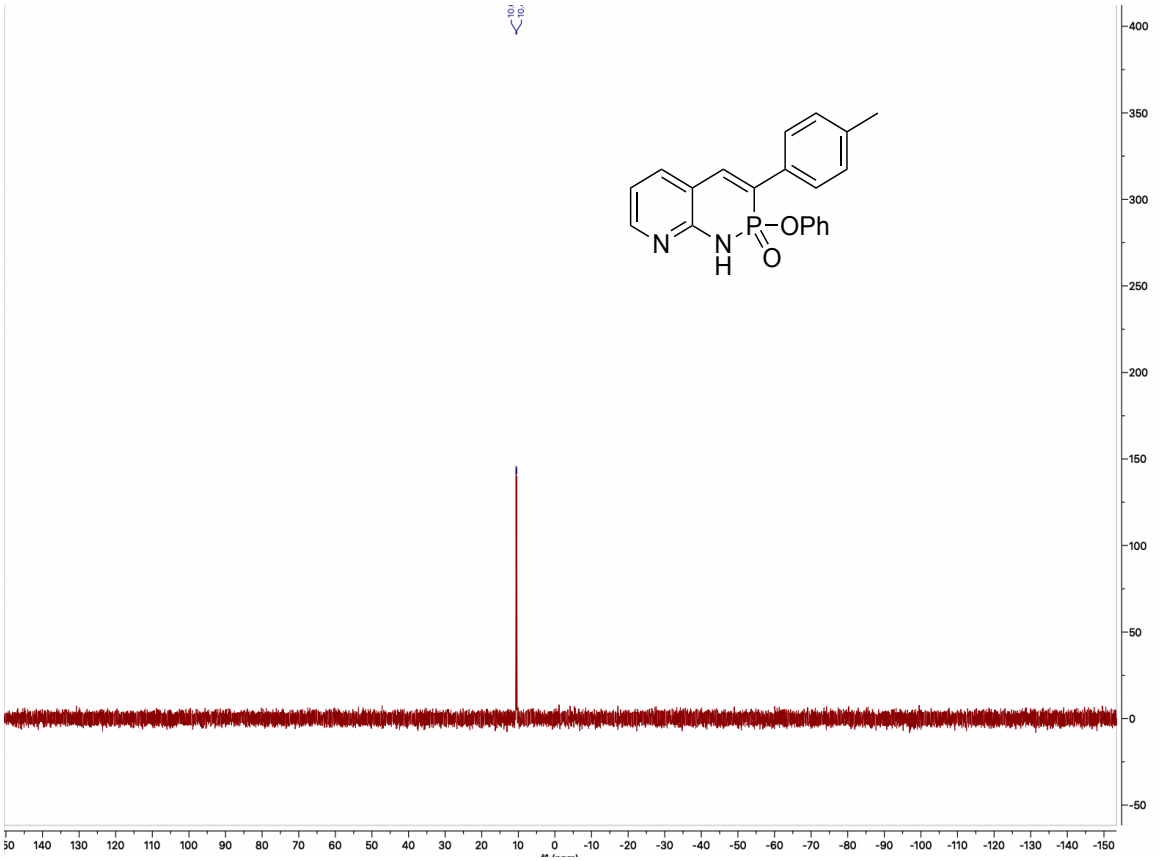

Figure A33 ^{31}P NMR Spectrum of Heterocycle **2a** in DMSO-d_6

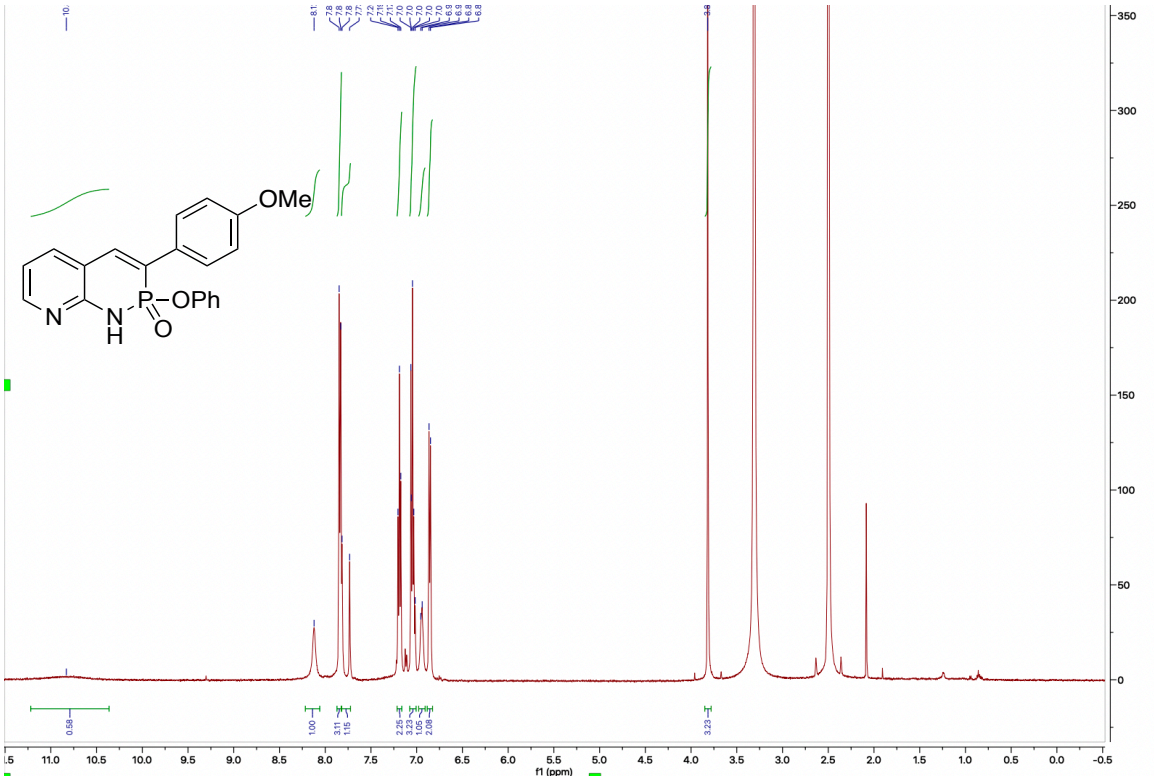

Figure A34 ^{1}H NMR Spectrum of Heterocycle **2b** in DMSO-d$_6$

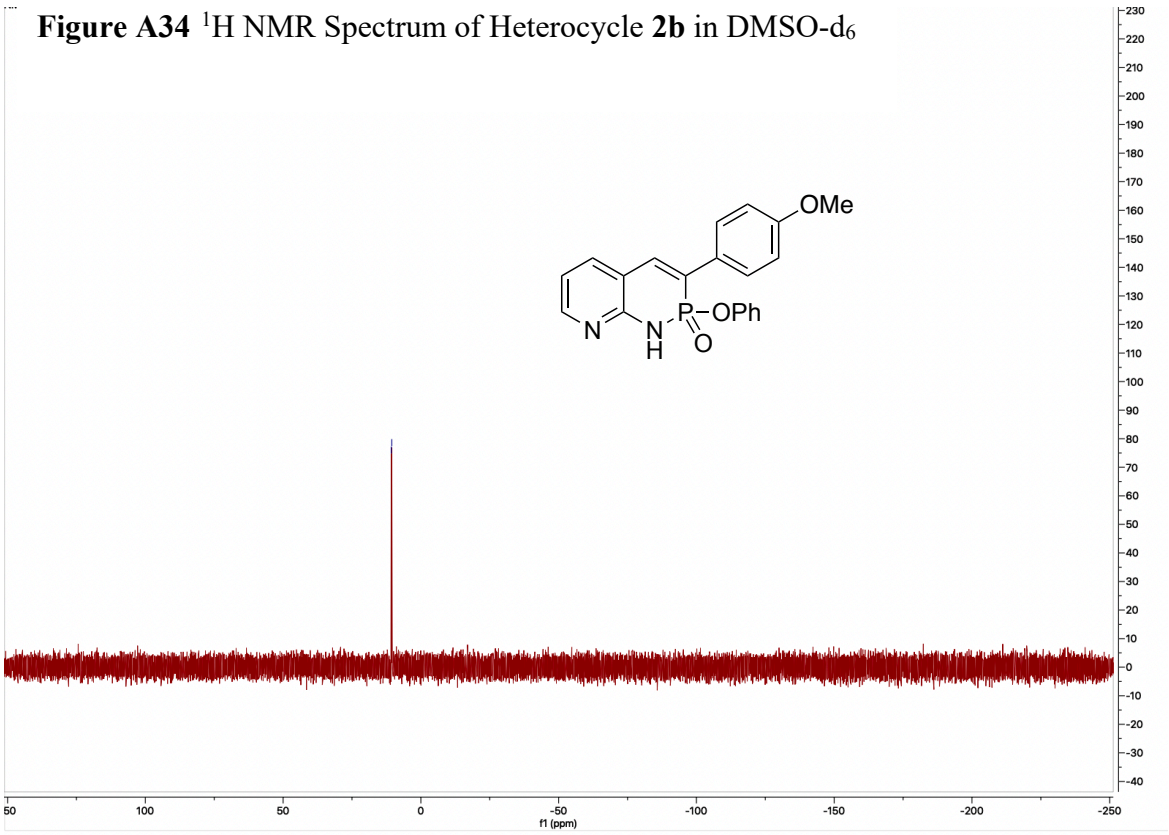

Figure A35 ^{31}P NMR Spectrum of Heterocycle **2b** in DMSO-d$_6$

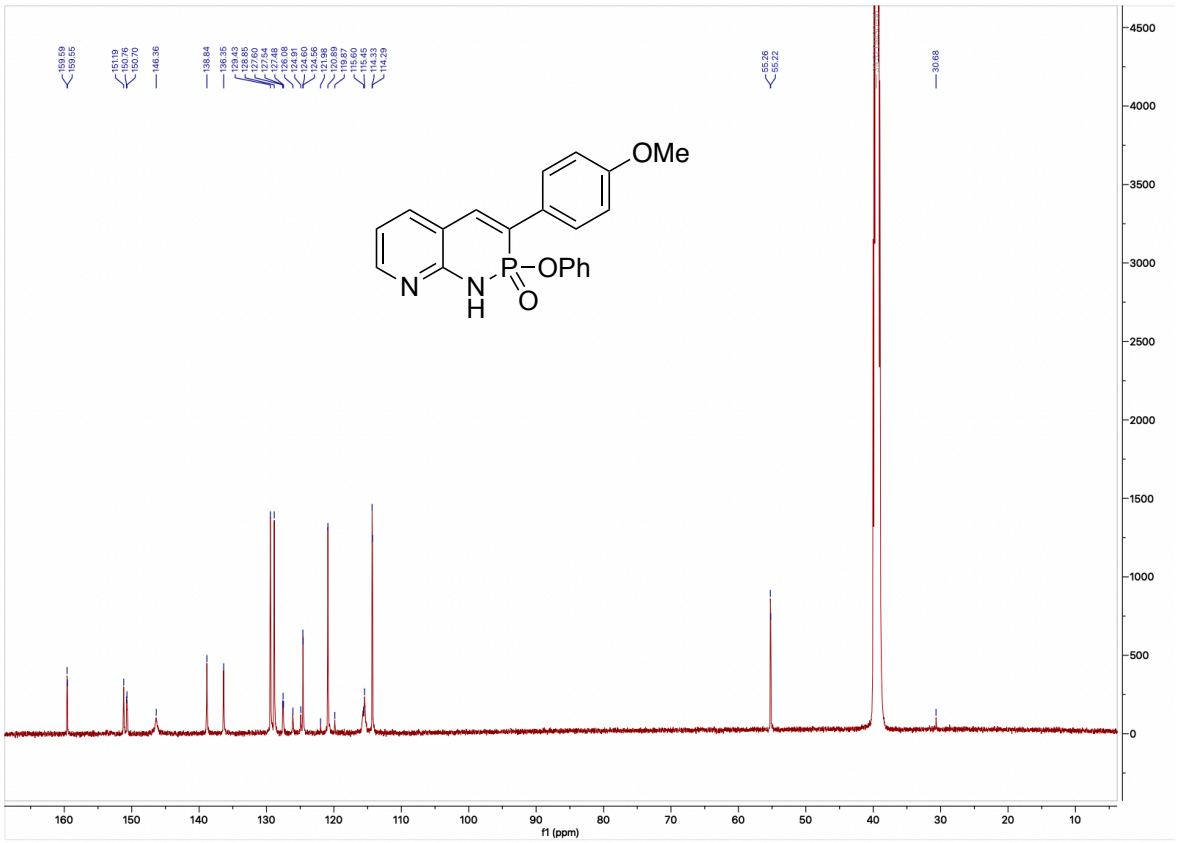

Figure A36 ^{13}C NMR Spectrum of Heterocycle **2b** in DMSO-d_6

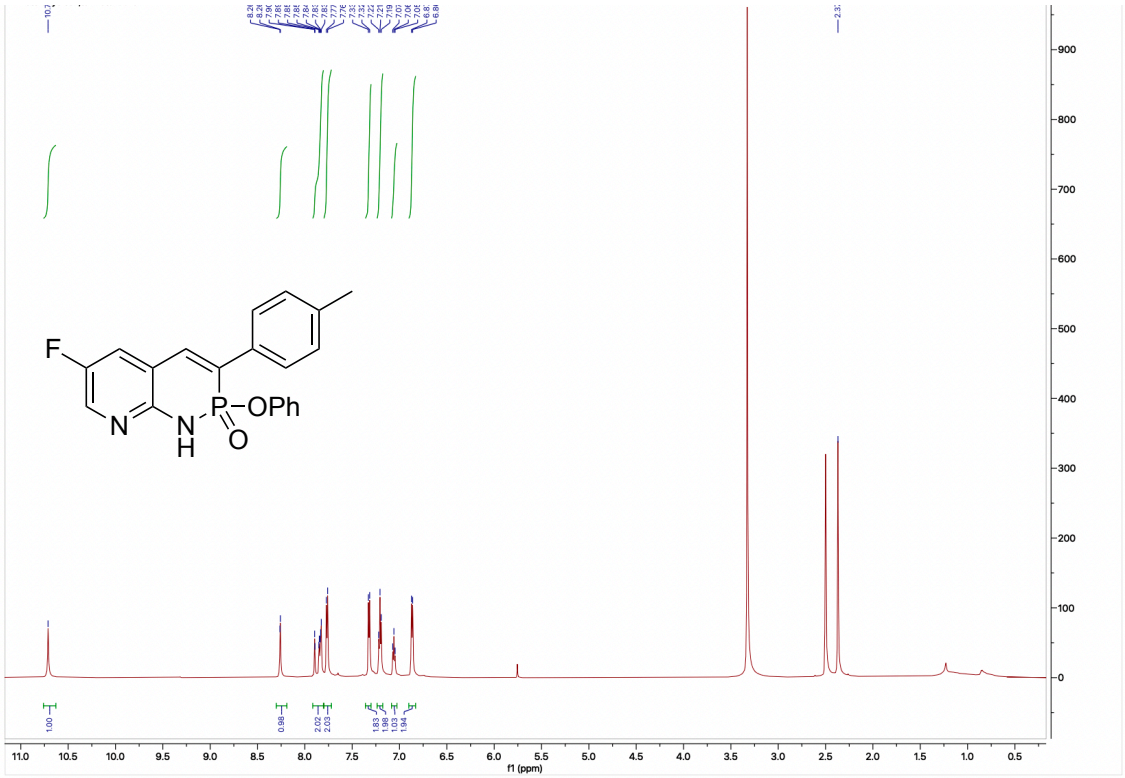

Figure A37 ^{1}H NMR Spectrum of Heterocycle **2e** in DMSO-d$_6$

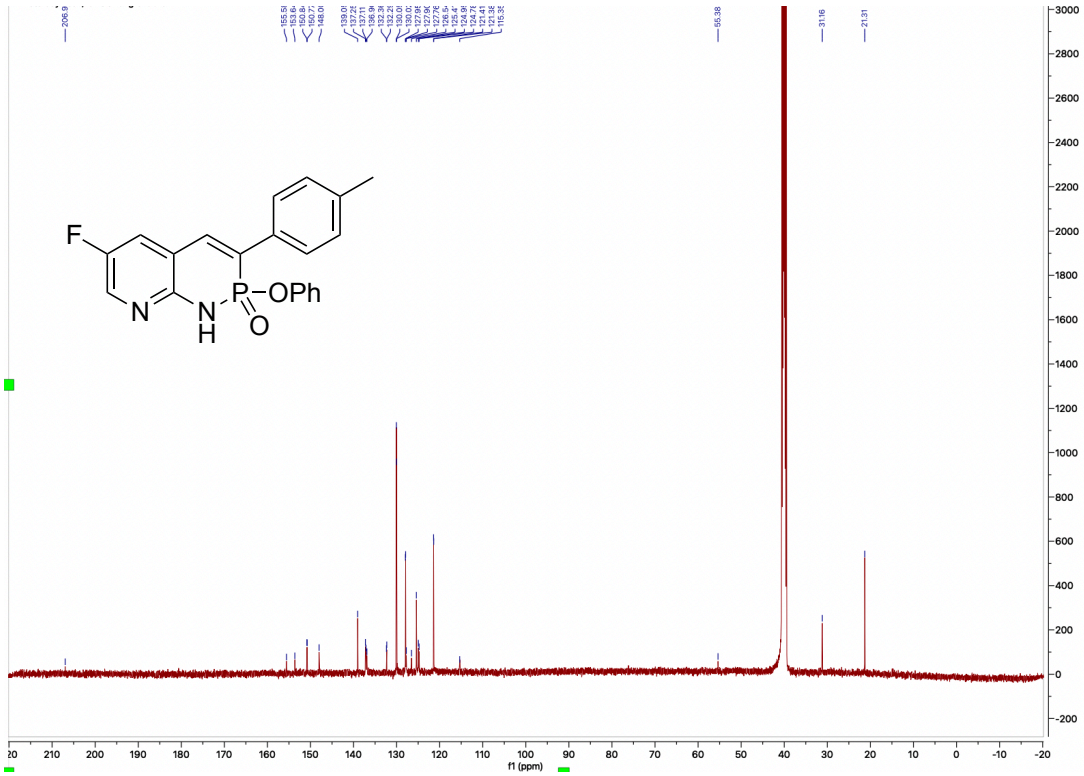

Figure A38 ^{13}C NMR Spectrum of Heterocycle **2e** in DMSO-d$_6$

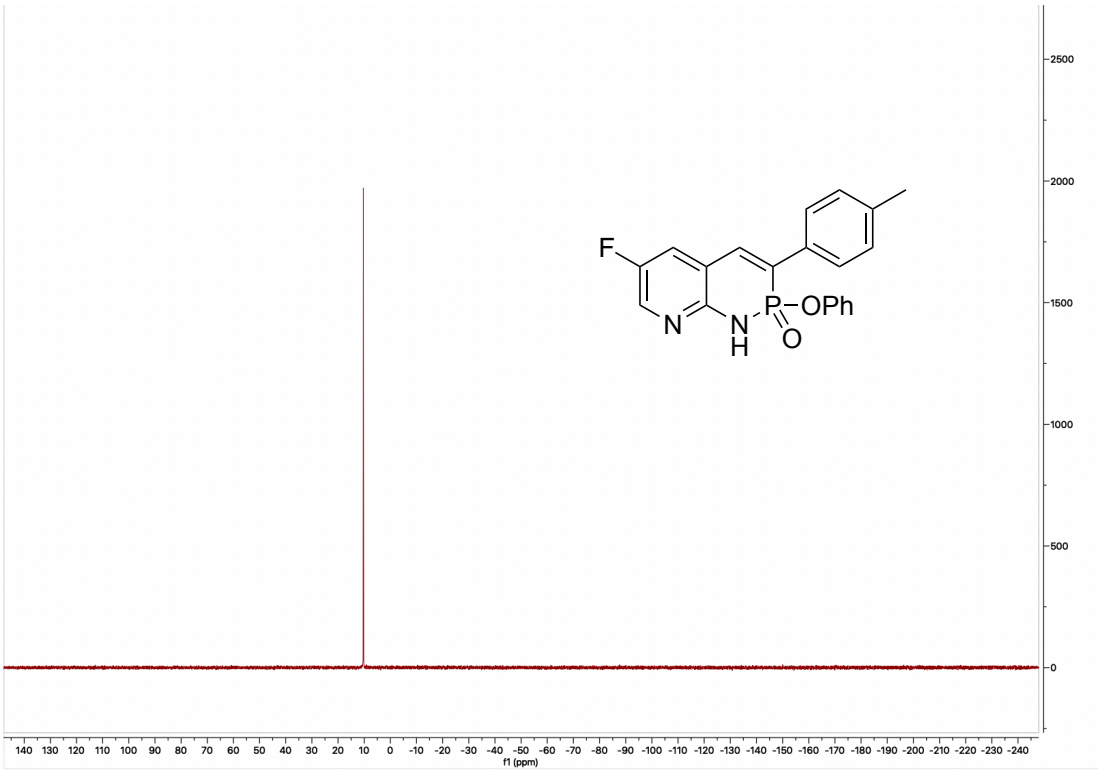

Figure A39 ^{31}P NMR Spectrum of Heterocycle **2e** in DMSO-d_6

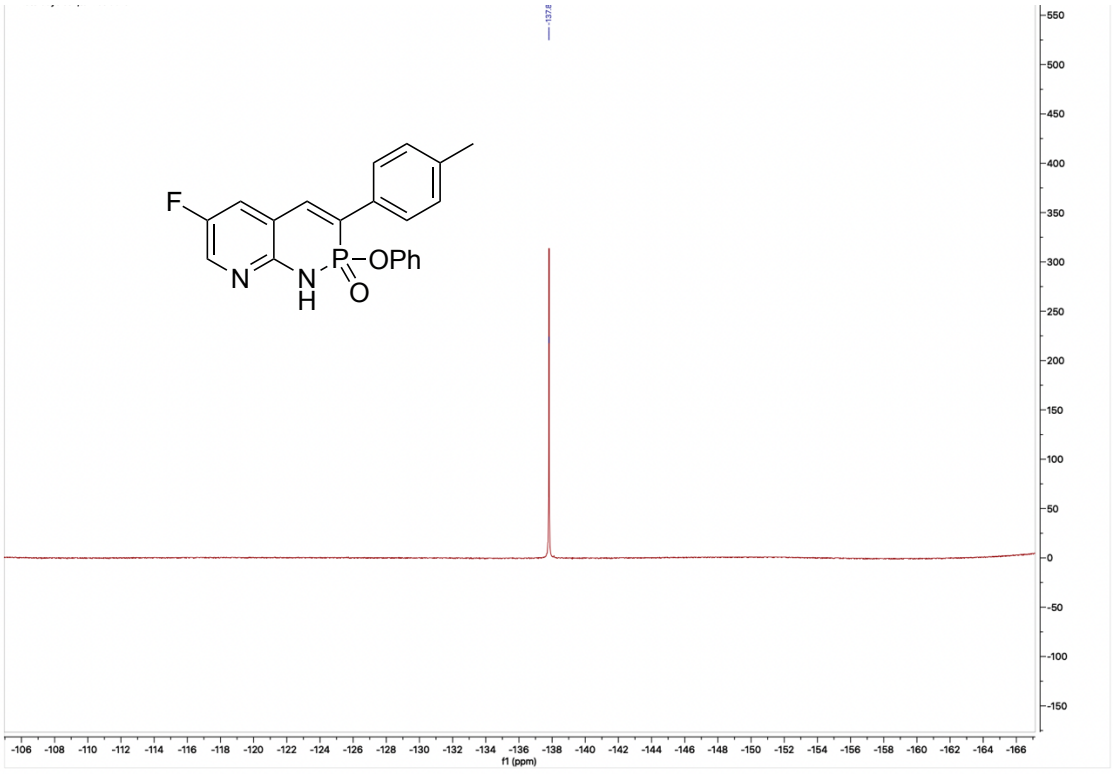

Figure A40 ^{19}F NMR Spectrum of Heterocycle **2e** in DMSO-d_6

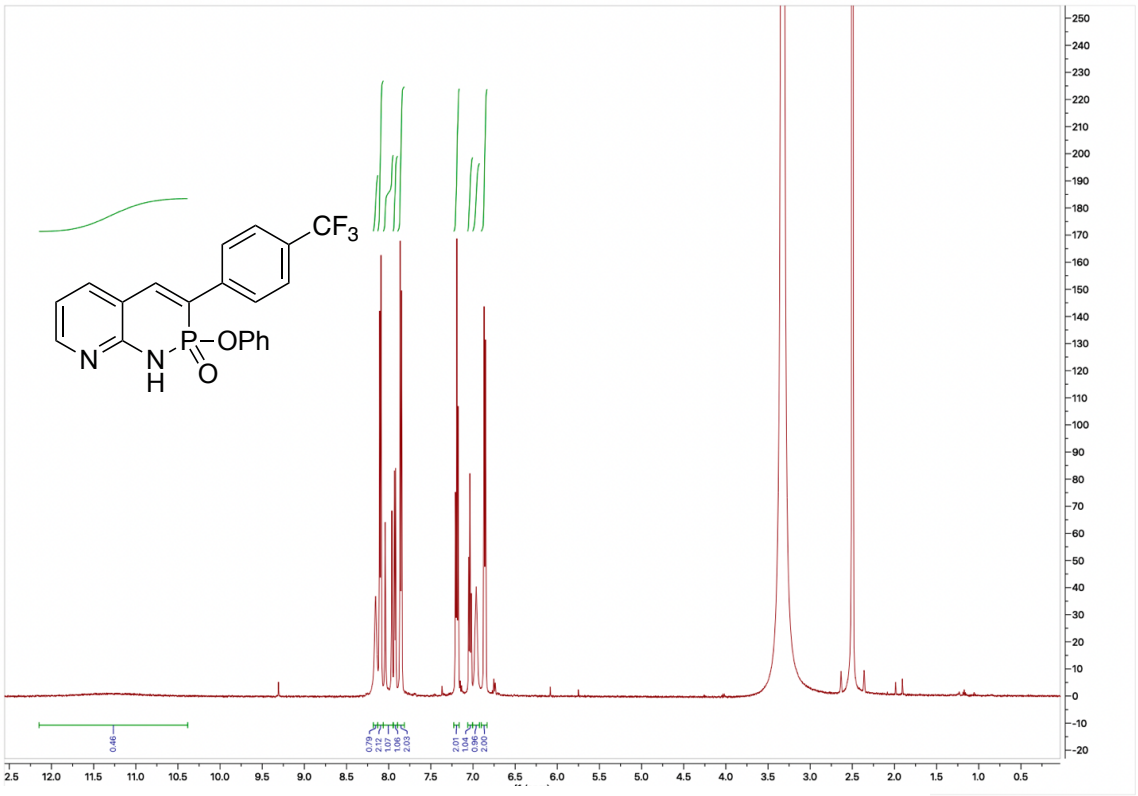

Figure A41 ^{1}H NMR Spectrum of Heterocycle **2c** in DMSO-d$_6$

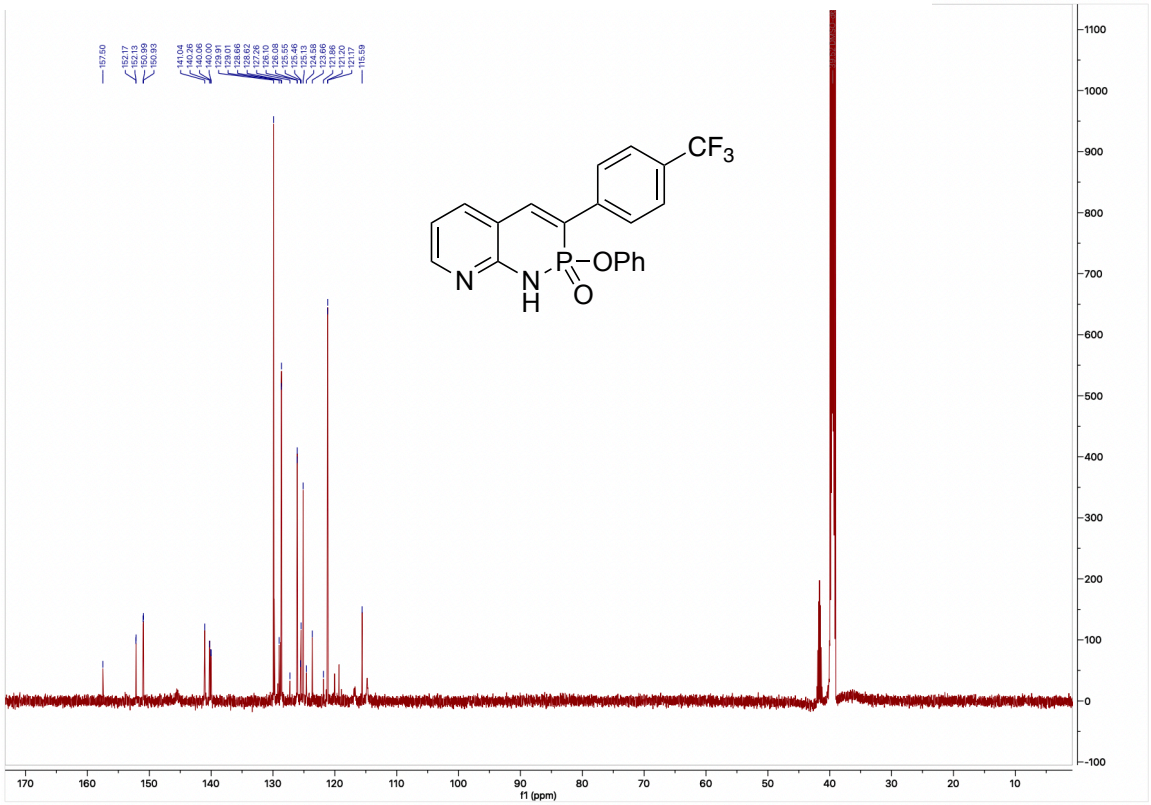

Figure A42 ^{13}C NMR Spectrum of Heterocycle **2c** in DMSO-d$_6$

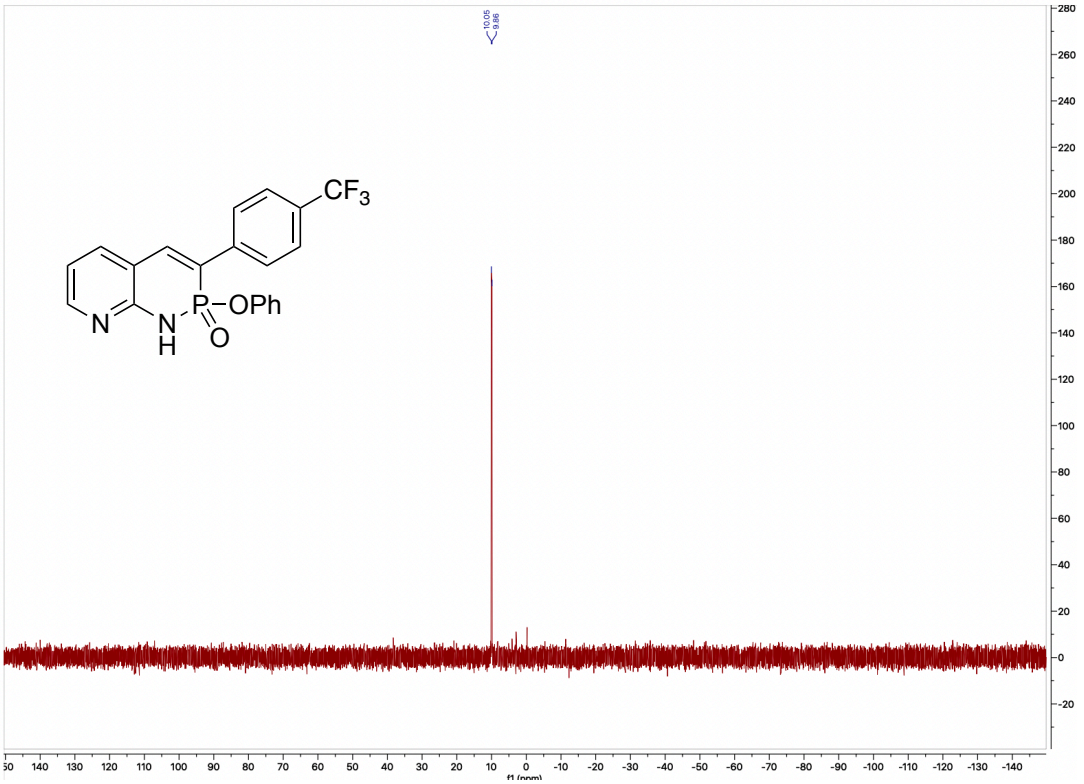

Figure A43 ^{31}P NMR Spectrum of Heterocycle **2c** in DMSO-d$_6$

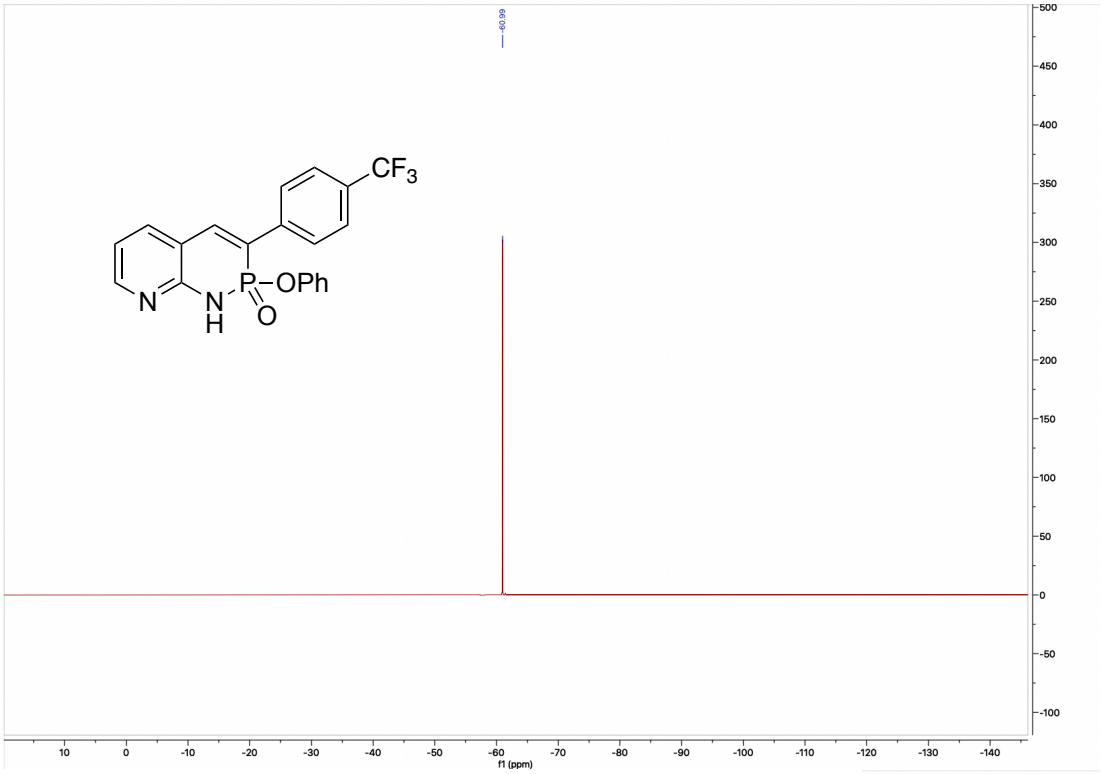

Figure A44 ^{19}F NMR Spectrum of Heterocycle **2c** in DMSO-d$_6$

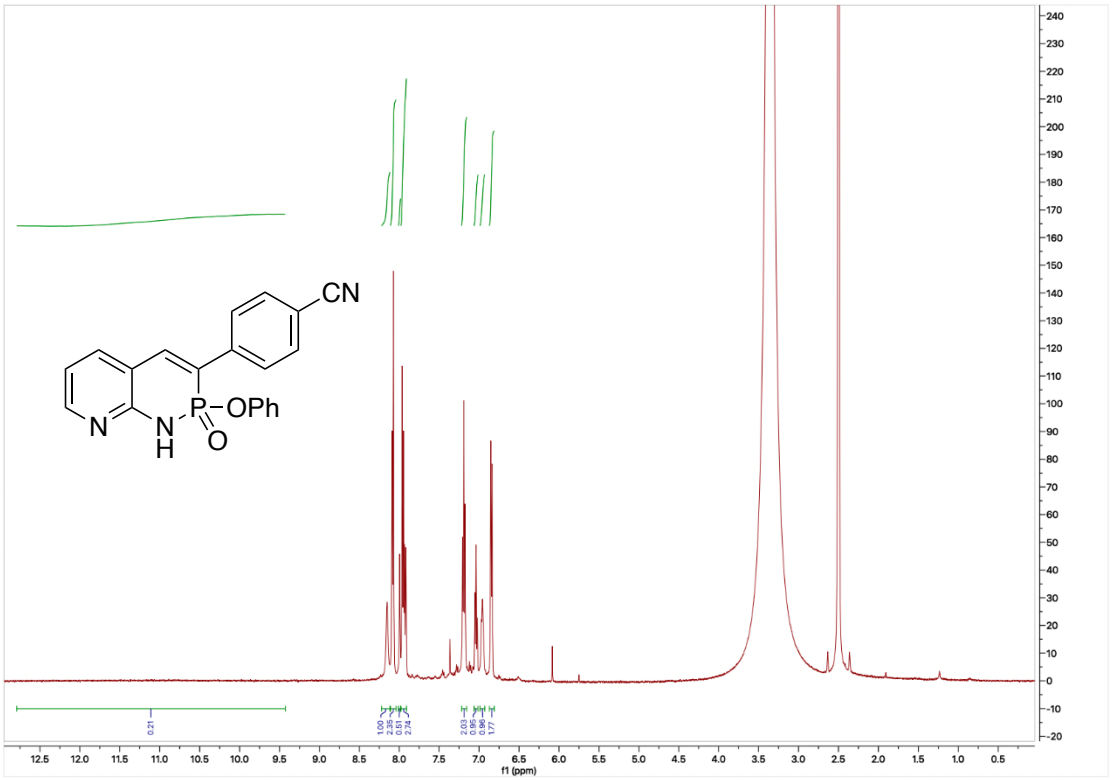

Figure A45 ^{1}H NMR Spectrum of Heterocycle **2d** in $CDCl_3$

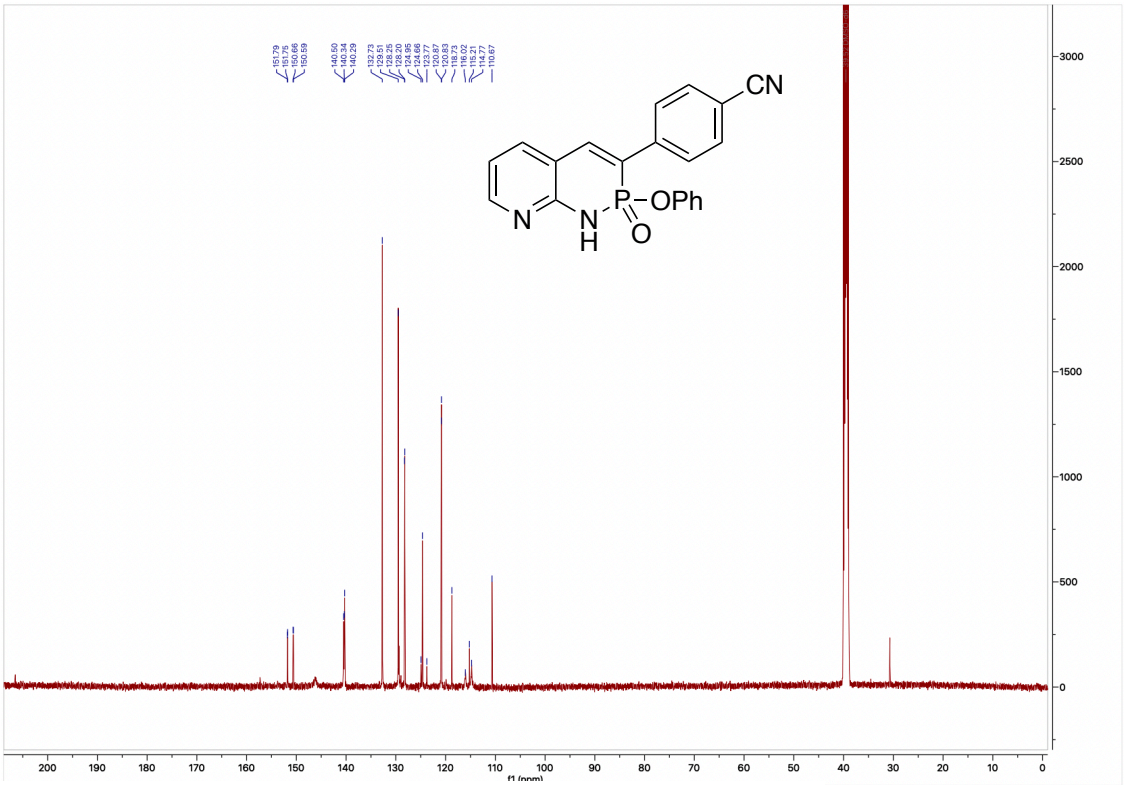

Figure A46 ^{13}C NMR Spectrum of Heterocycle **2d** in $CDCl_3$

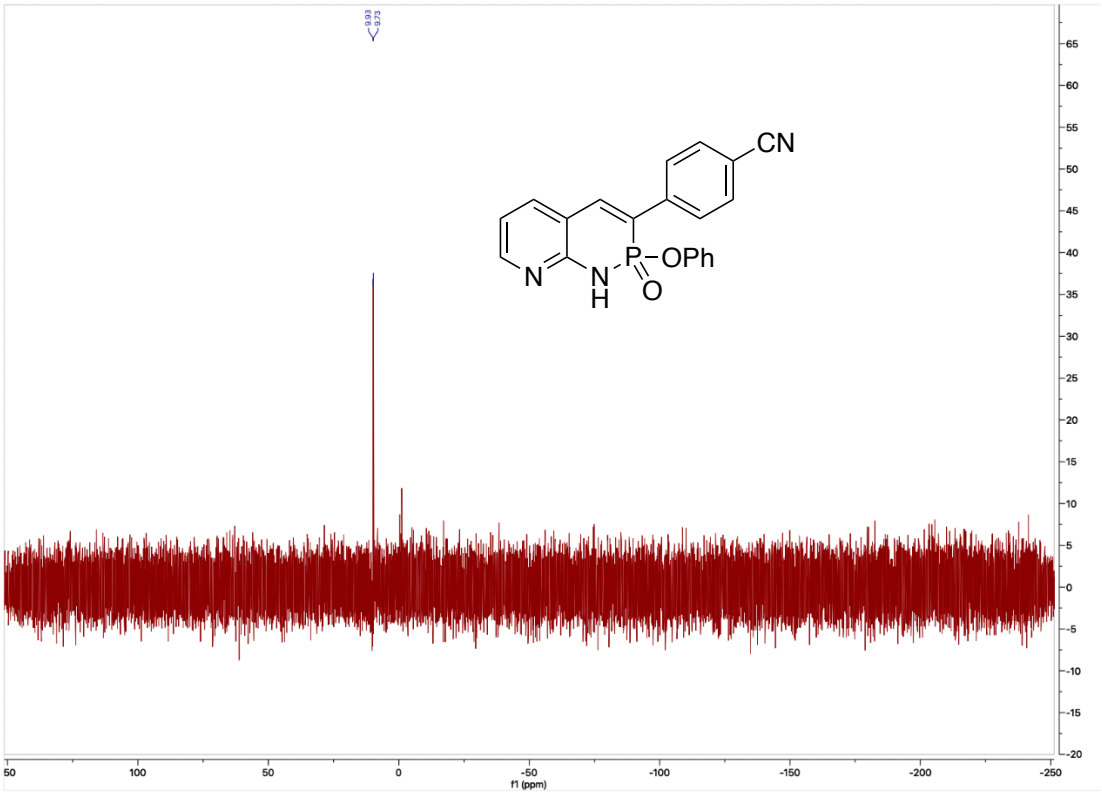

Figure A47 ^{31}P NMR Spectrum of Heterocycle **2d** in $CDCl_3$

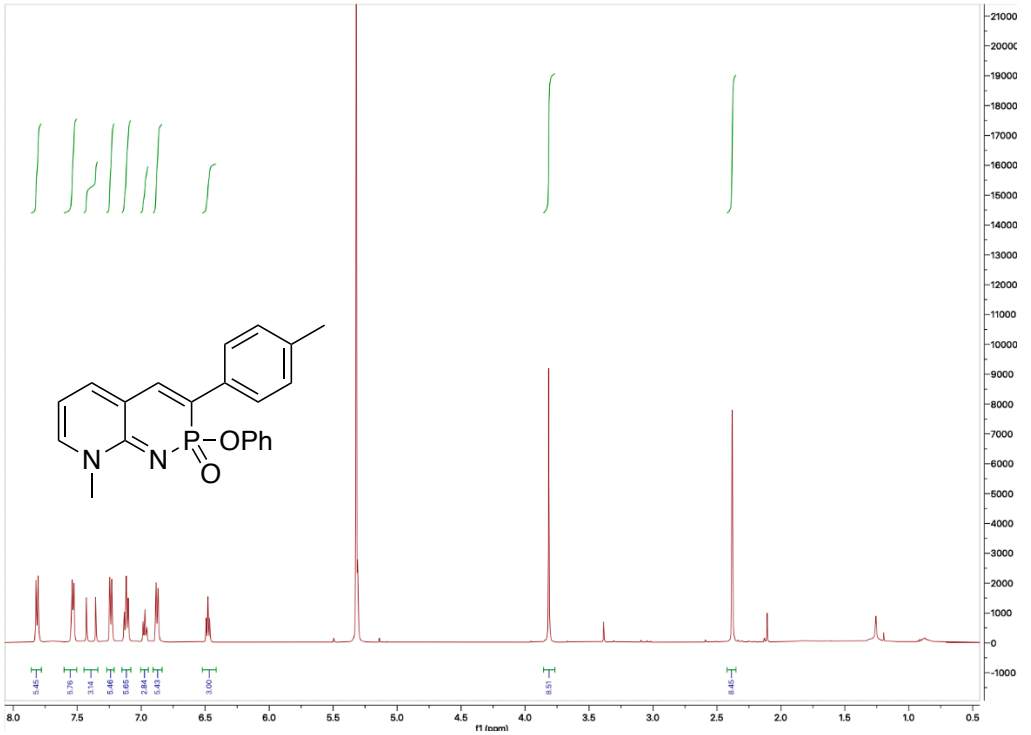

Figure A48 ^{1}H NMR Spectrum of Heterocycle **6a** in CD_2Cl_2

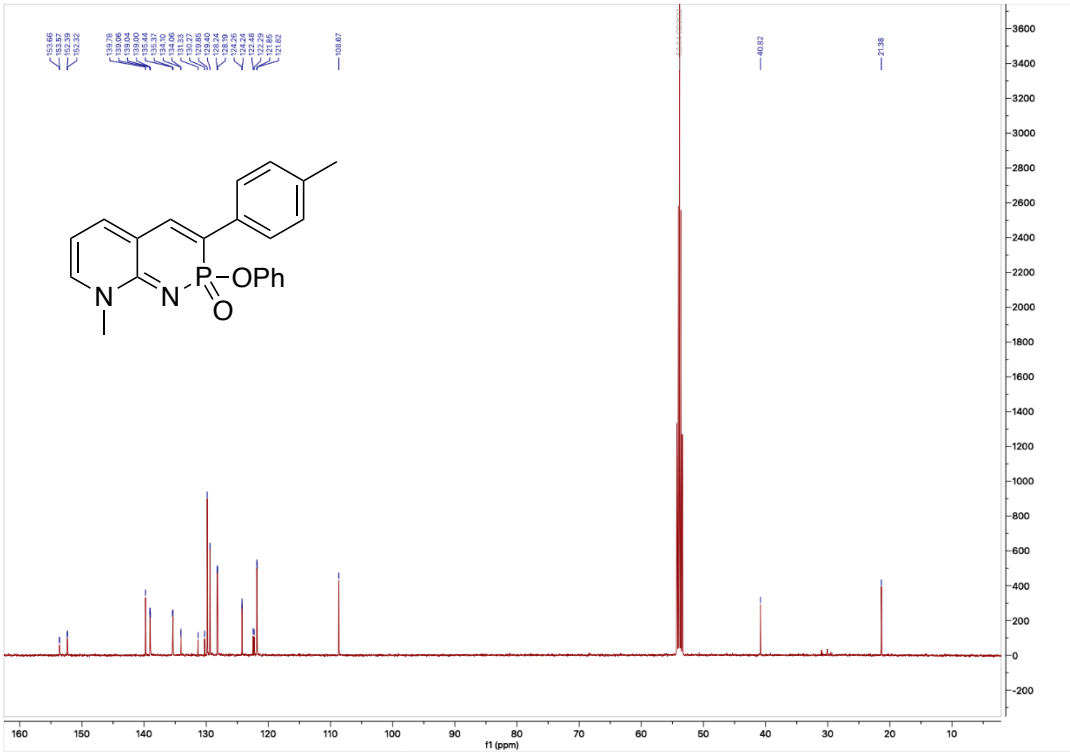

Figure A49 ^{13}C NMR Spectrum of Heterocycle **6a** in CD_2Cl_2

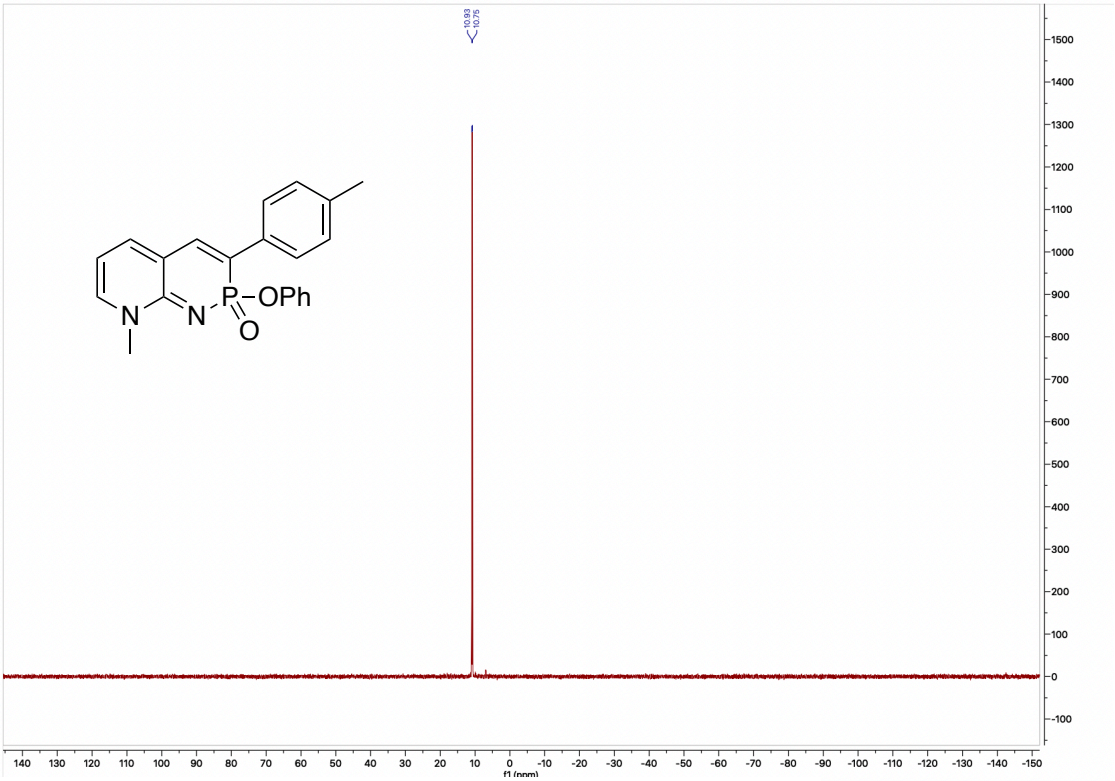

Figure A50 ^{31}P NMR Spectrum of Heterocycle **6a** in CD_2Cl_2

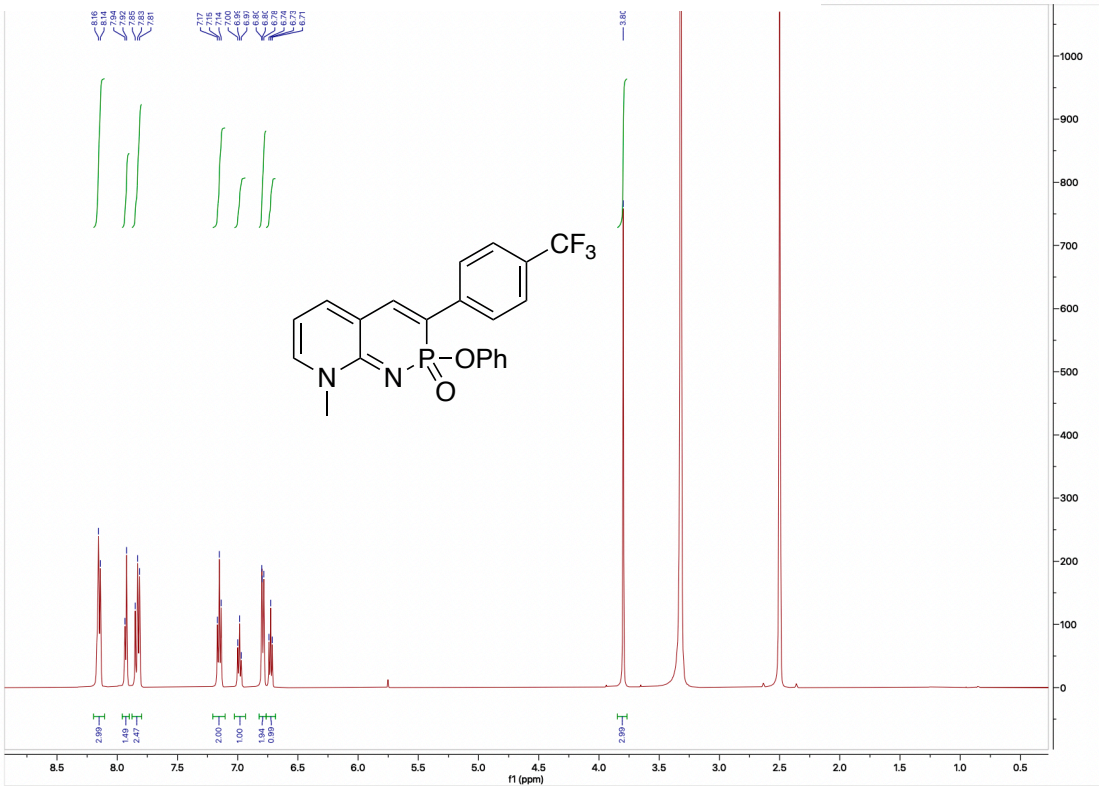

Figure A51 ^{1}H NMR Spectrum of Heterocycle **6b** in DMSO-d_6

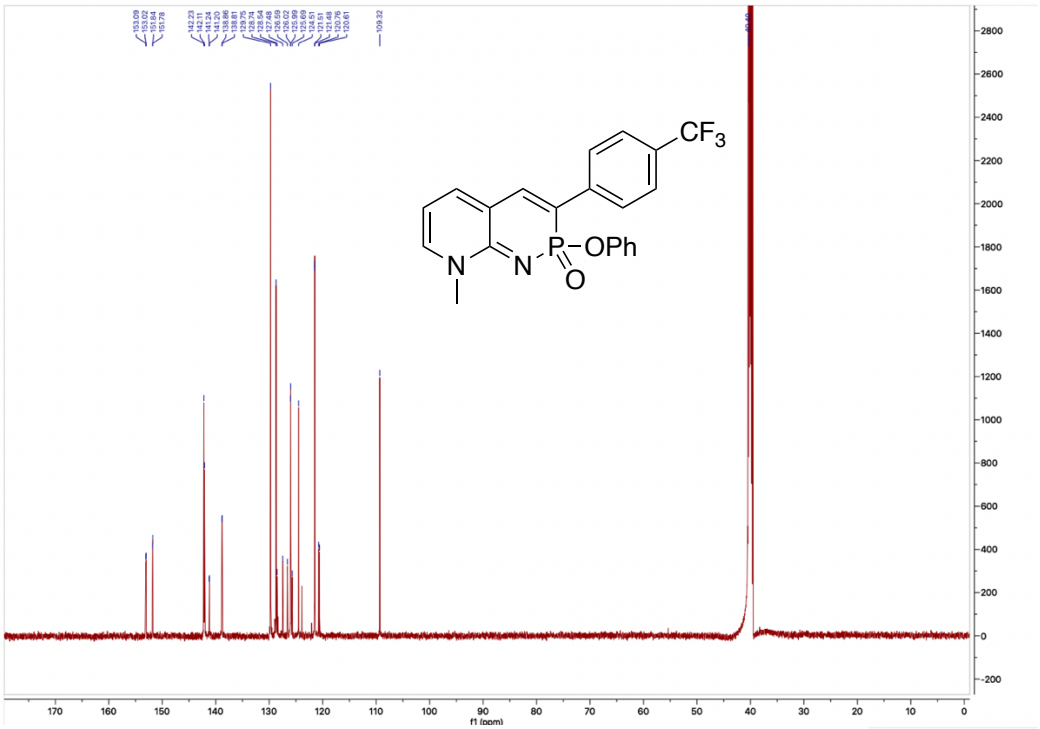

Figure A52 ^{13}C NMR Spectrum of Heterocycle **6b** in DMSO-d$_6$

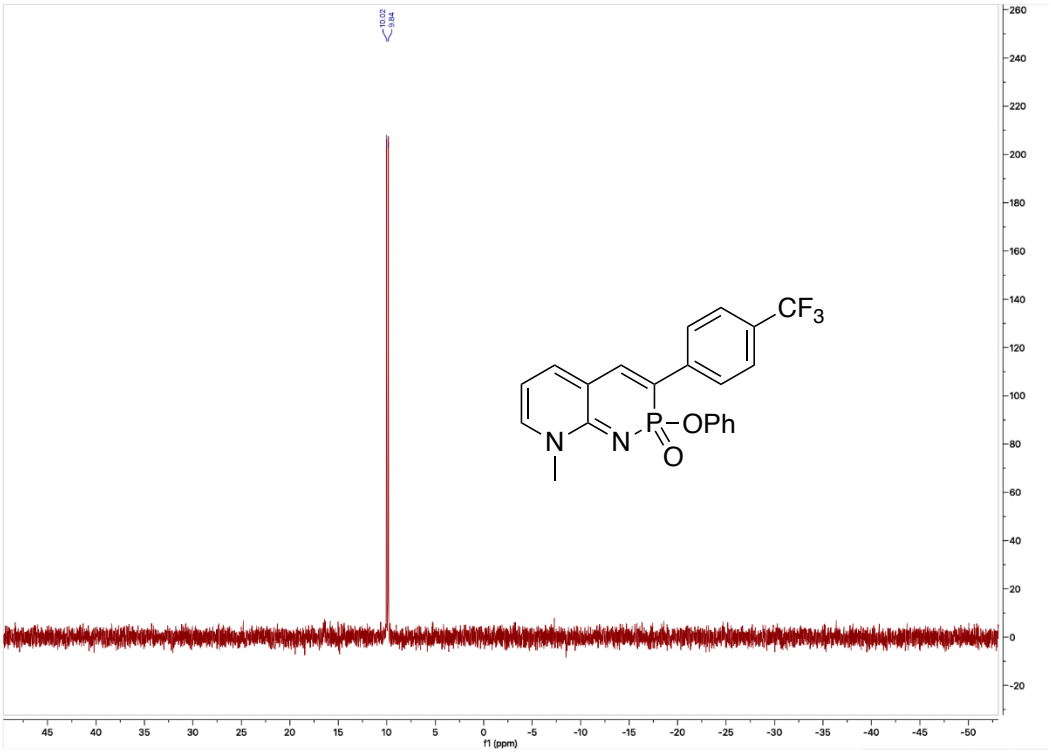

Figure A53 ^{31}P NMR Spectrum of Heterocycle **6b** in DMSO-d$_6$

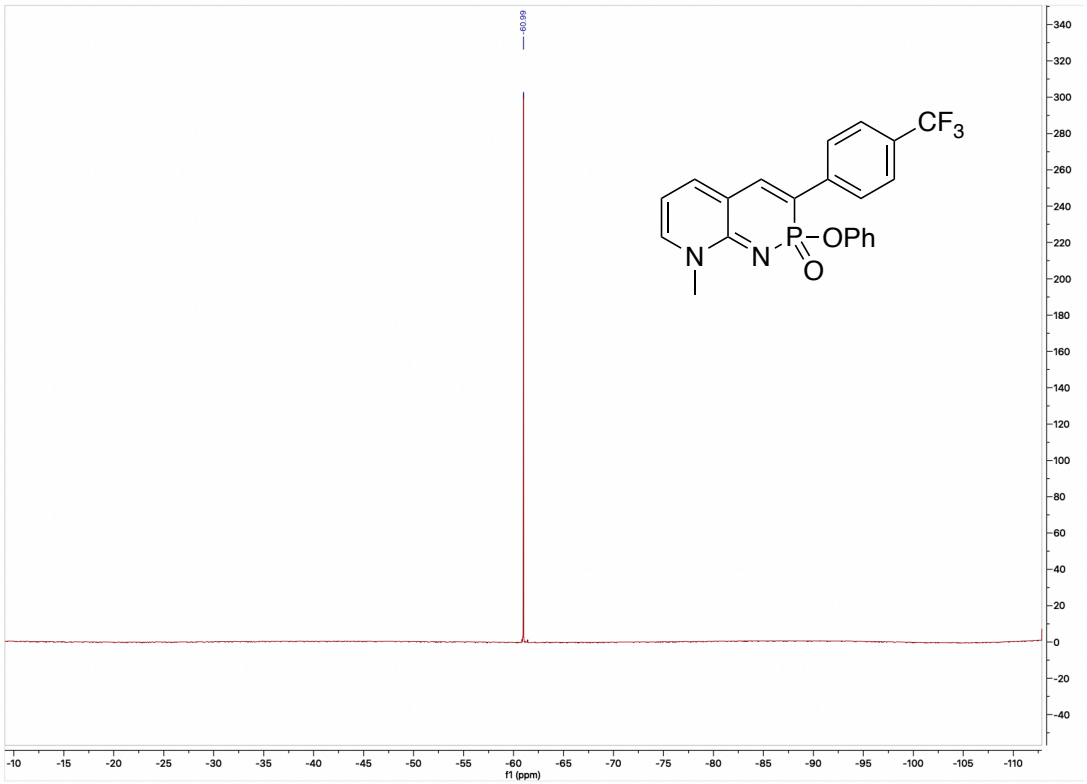

Figure A54 ^{19}F NMR Spectrum of Heterocycle **6b** in DMSO-d$_6$

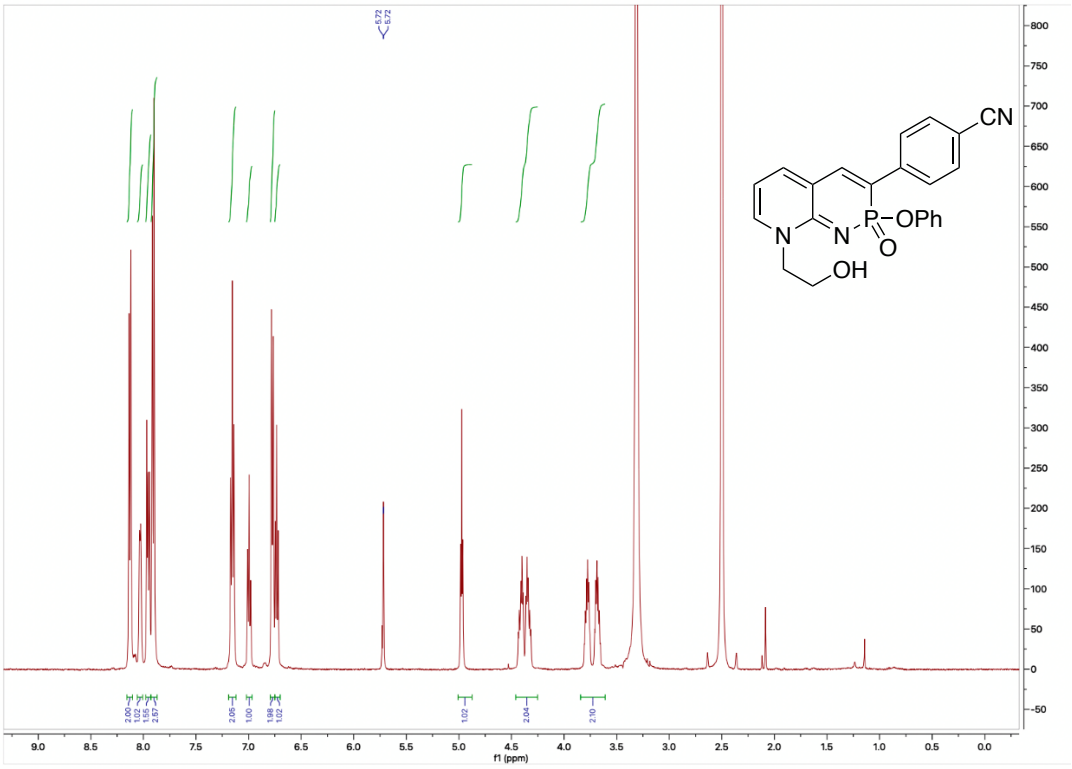

Figure A55 ^{1}H NMR Spectrum of Heterocycle **6c** in DMSO-d$_6$

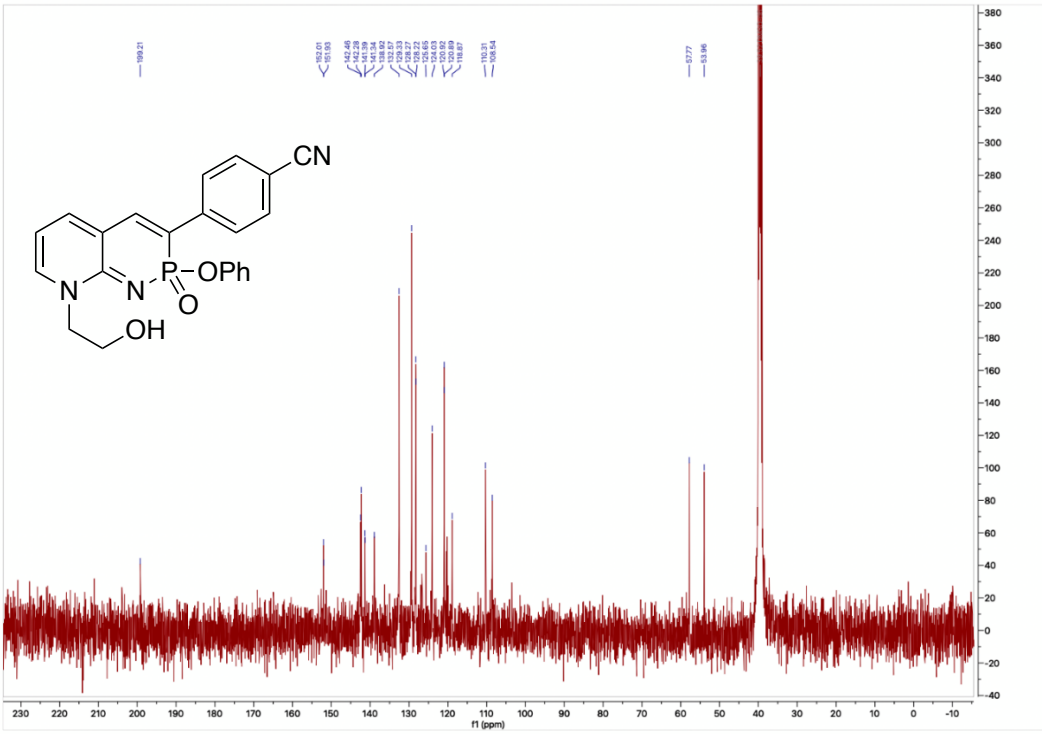

Figure A56 ^{13}C NMR Spectrum of Heterocycle **6c** in DMSO-d_6

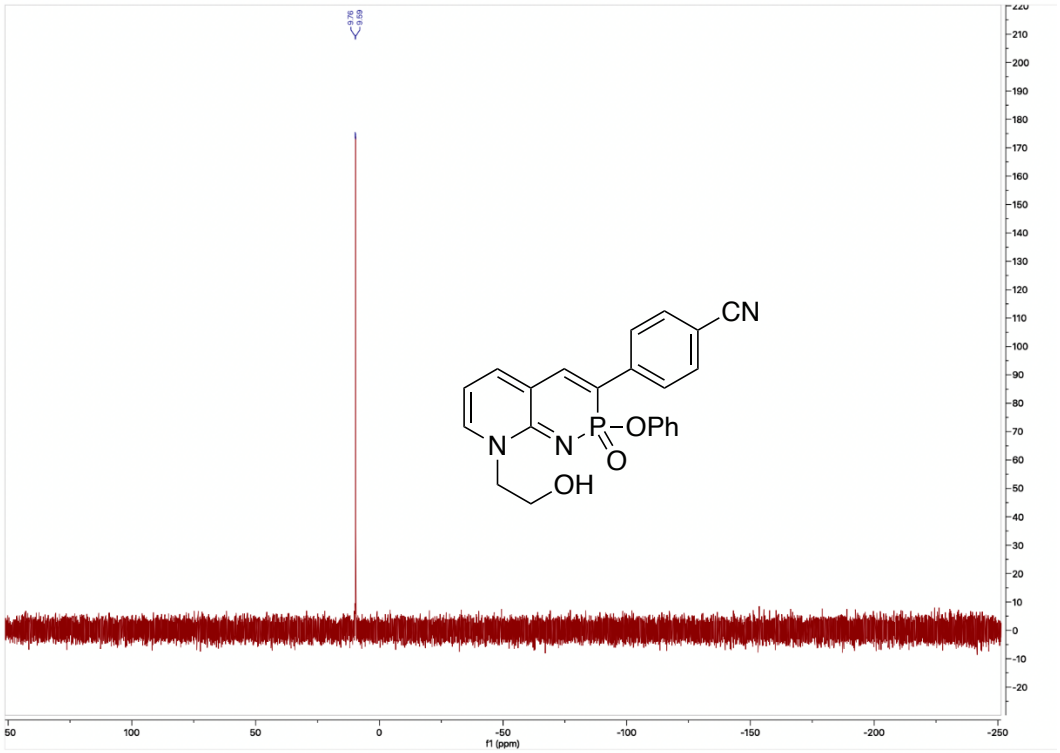

Figure A57 ^{31}P NMR Spectrum of Heterocycle **6c** in DMSO-d_6

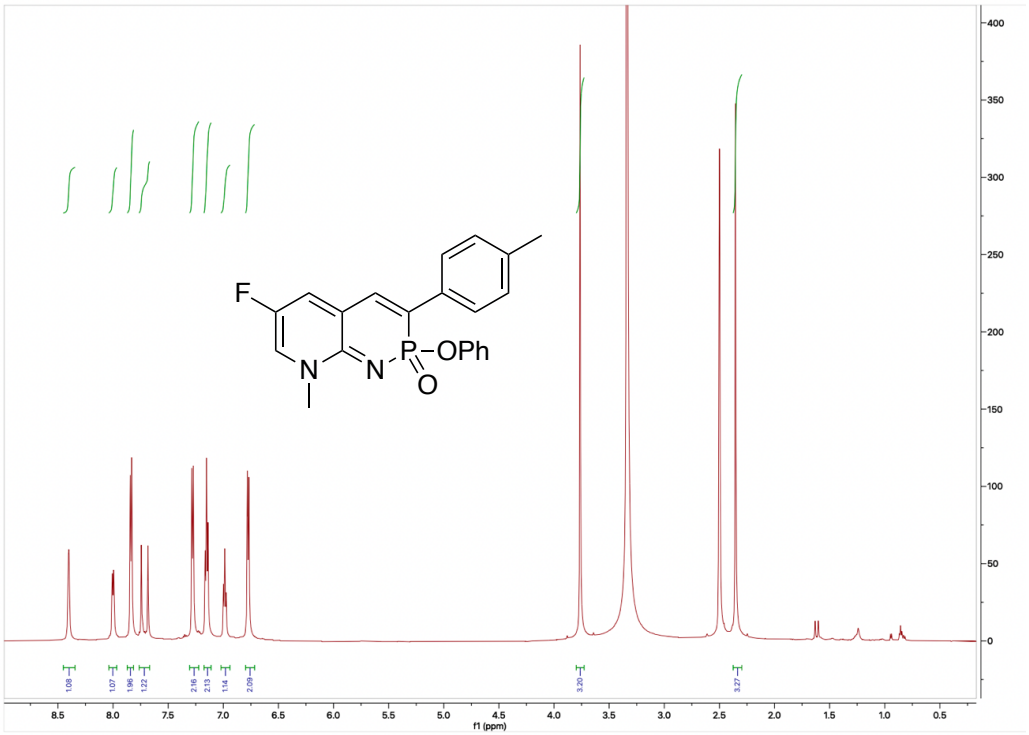

Figure A58 ^{1}H NMR Spectrum of Heterocycle **6e** in DMSO-d$_6$

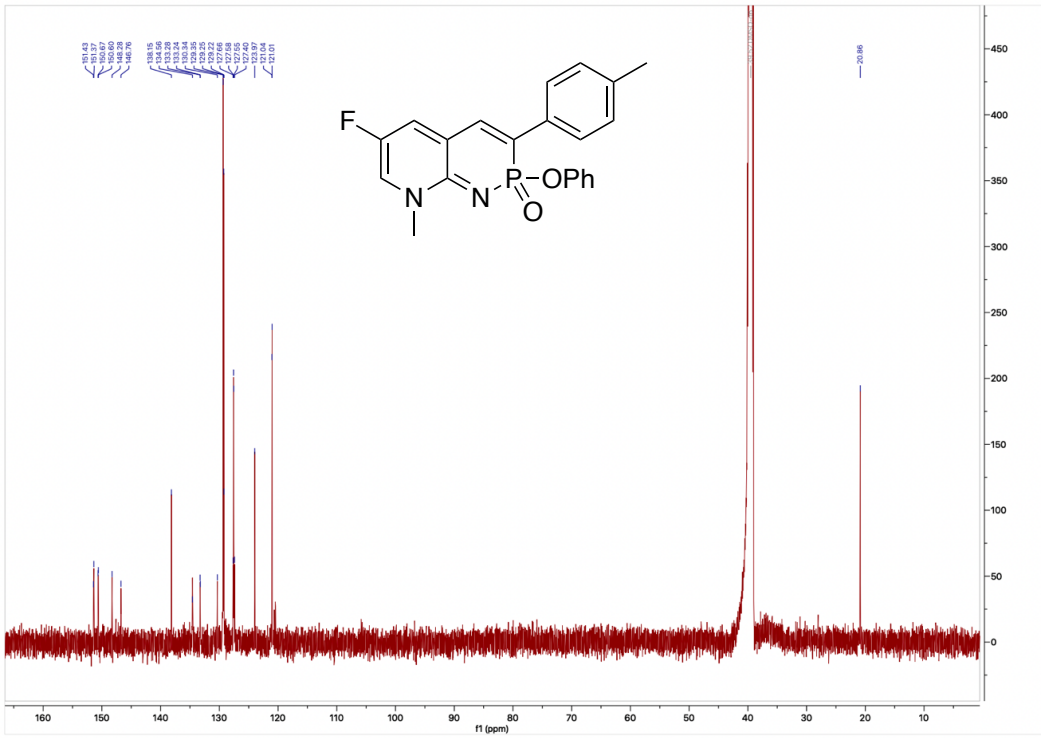

Figure A59 ^{13}C NMR Spectrum of Heterocycle **6e** in DMSO-d$_6$

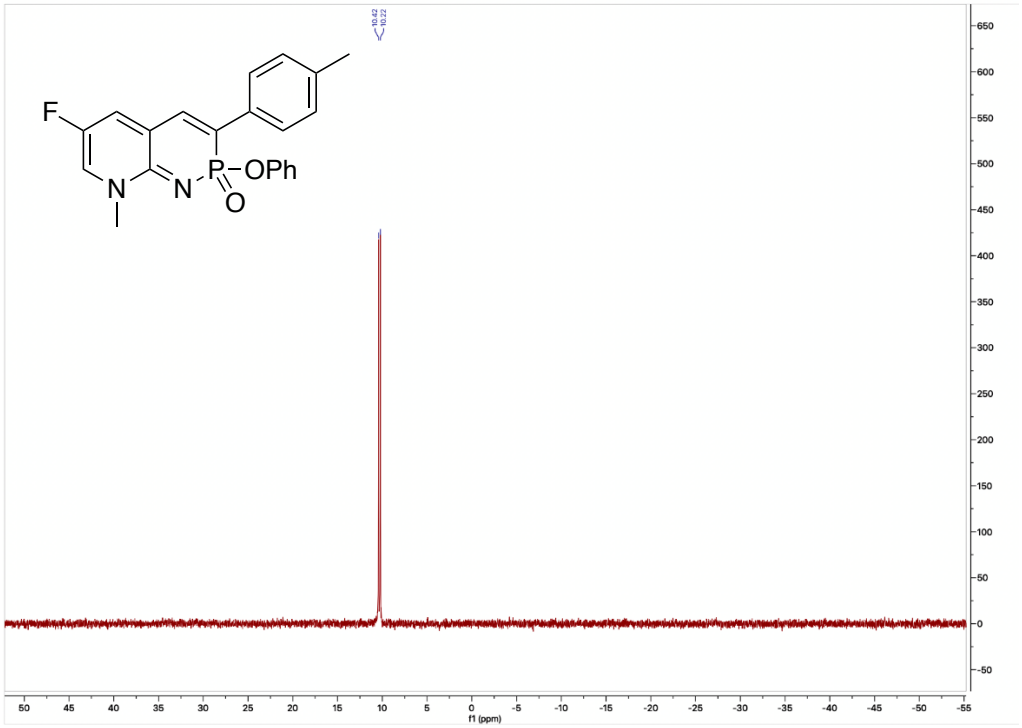

Figure A60 ^{31}P NMR Spectrum of Heterocycle **6e** in DMSO-d_6

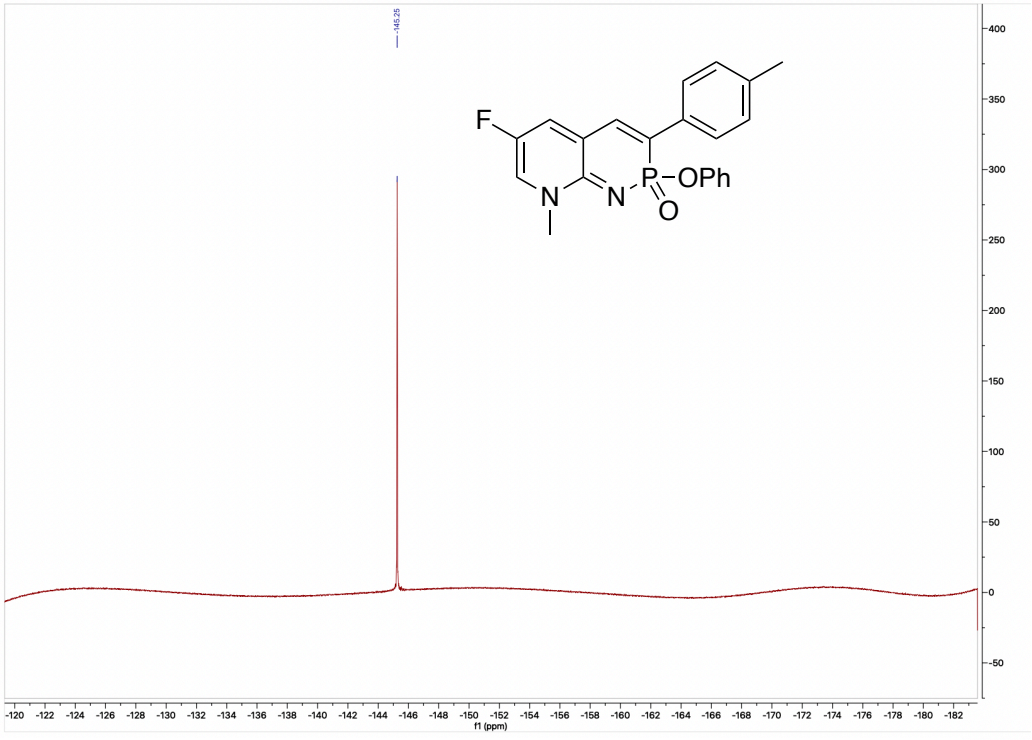

Figure A61 ^{19}F NMR Spectrum of Heterocycle **6e** in DMSO-d_6

APPENDIX B

SUPPLEMENTARY INFORMATION FOR CHAPTER III

Appendix B is the supplementary information for Chapter III of this dissertation. It includes experimental details, experimental data, spectra, and computational details relevant to the content of Chapter III.

Experimental Details

General. All oxygen- and water-free reactions were performed under an N_2 atmosphere using Schlenk techniques. Column chromatography was performed using silica gel (240–300 mesh), with solvent systems being referenced to the most abundant solvent. NMR spectra were acquired at room temperature on a Varian Inova 500 (^{1}H: 500 MHz, ^{13}C: 126 MHz, ^{19}F: 471 MHz, ^{31}P: 202 MHz), a Bruker Avance III HD 500 equipped with a Prodigy multinuclear cryoprobe (^{1}H: 500 MHz, ^{13}C: 126 MHz, ^{31}P: 202 MHz), or a Bruker Avance-III-HD 600 MHz (^{1}H: 599.98 MHz, ^{13}C: 150.87 MHz, ^{19}F: 565 MHz) spectrometer. ^{1}H and ^{13}C chemical shifts (δ) are expressed in ppm relative to residual $CHCl_3$ (^{1}H: 7.26, ^{13}C: 77.16), DMSO (^{1}H: 2.50, ^{13}C: 39.52), or acetone (^{1}H: 2.05, ^{13}C: 29.84, 206.26). ^{31}P NMR are referenced to 85% H_3PO_4 (δ 0 ppm) as an external reference, and ^{19}F NMR are referenced to $CFCl_3$ (δ 0 ppm) as an external standard. UV-vis spectra were recorded using an Agilent Technologies Cary 60 UV-vis spectrophotometer in $CHCl_3$. Fluorescence emission spectra were recorded using a Horiba Jobin Yvon FluoroMax-4 fluorimeter.

High-resolution mass spectra (HRMS) were recorded on a Waters XEVO G2-XS mass spectrometer.

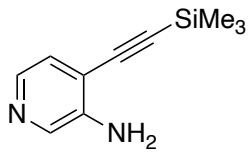

3-Amino-4-(2-trimethylsilyl)ethynylpyridine (4). 3-Amino-4-iodopyridine (1 g, 4.55 mmol, 1 equiv.), $Pd(PPh_3)_2Cl_2$ (95 mg, 0.14 mmol, 0.03 equiv.), and CuI (17 mg, 0.09 mmol, 0.02 equiv.) were combined in a round bottom flask. The flask was evacuated and backfilled with N_2 a total of three times. The flask was then charged with 33 mL of an N_2-sparged 1:10 mixture of THF:Et_3N. Trimethylsilylacetylene (3.20 mL, 22.5 mmol, 5 equiv.) was then added dropwise, and the reaction was stirred at room temperature for 1 h. The reaction was then quenched with EtOAc (5 mL) and filtered through a pad of celite. The filtrate was transferred to a separatory funnel and extracted with EtOAc (3x), dried (Na_2SO_4), filtered and concentrated *in vacuo*. The residue was then dry loaded onto a silica plug and flushed with hexanes to remove nonpolar impurities. The product was then eluted with EtOAc and concentrated *in vacuo* to afford **4** (853 mg, quantitative yield) as a brown solid. ^{1}H NMR (500 MHz, $CDCl_3$) δ 8.15 (br s, 1H), 7.92 (br s, 1H), 7.12 (d, J = 5.1 Hz, 1H), 4.23 (br s, 2H), 0.28 (s, 9H). ^{13}C NMR (126 MHz, $CDCl_3$) δ 143.67, 138.69, 136.99, 125.13, 114.34, 104.55, 98.89, -0.06. HRMS (ASAP) $[M+H]^+$ calcd for $C_{10}H_{15}N_2Si$ 191.1004, found 191.1013.

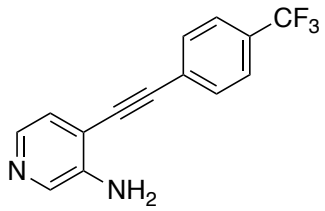

3-Amino-4-(2-(4-trifluoromethylphenyl)ethynyl)pyridine (5a). 3-Amino-4-iodopyridine (500 mg, 2.27 mmol, 1 equiv.), $Pd(PhCN)_2Cl_2$ (26 mg, 0.07 mmol, 0.03 equiv.), and CuI (17 mg, 0.09 mmol, 0.04 equiv.) were combined in a flame-dried round bottom flask. The flask was evacuated and backfilled with N_2 a total of three times. The flask was then charged with an N_2-sparged 2:3 mixture of THF:DIPA (10 mL). While stirring, P(*t*-Bu)$_3$ (10 wt% in hexanes, 0.4 mL, 0.136 mmol, 0.06 equiv.) was added via syringe, followed by dropwise addition of 4-ethynyl-(trifluoromethyl)benzene (0.535 mL, 3.27 mmol, 1.2 equiv.). The reaction was stirred at room temperature for 24 h. The reaction was then quenched with EtOAc (5 mL) and filtered through a pad of celite. The filtrate was transferred to a separatory funnel and extracted with EtOAc (3x), dried (Na_2SO_4), filtered and concentrated. The residue was dry loaded onto silica plug and rinsed with both hexanes and EtOAc to remove impurities. The product was then eluted in acetone to yield **5a** (534 mg, 90%) as a brown solid. ^{1}H NMR (500 MHz, $CDCl_3$) δ 8.21 (br s, 1H), 8.00 (br s, 1H), 7.65 (s, 4H), 7.22 (d, J = 4.9 Hz, 1H), 4.29 (br s, 2H). ^{13}C NMR (151 MHz, acetone-d_6) δ 145.94, 138.53, 138.31, 133.24, 130.87 (q, J = 30.5 Hz), 130.65, 127.88 (q, J = 271.3 Hz), 126.46 (q, J = 3.8 Hz), 125.71, 112.49, 96.40, 87.42. ^{19}F NMR (471 MHz, acetone-d_6) δ –63.35. HRMS (ASAP) $[M+H]^+$ calcd for $C_{14}H_{10}N_2F_3$ 263.0796, found 263.0952.

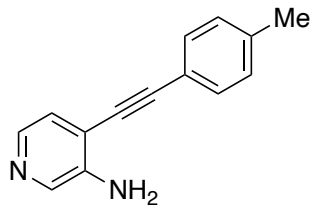

3-Amino-4-(2-(4-methylphenyl)ethynyl)pyridine (5b). 3-Amino-4-iodopyridine (500 mg, 2.77 mmol, 1 equiv.), 4-ethynyltoluene (0.64 mL, 5.5 mmol, 2.4 equiv.), $Pd(PPh_3)_2Cl_2$ (47 mg, 0.07 mmol, 0.03 equiv.), and CuI (9mg, 0.05 mmol, 0.02 equiv.) were combined in a round bottom flask. The flask was then evacuated and backfilled with N_2 a total of three times. The flask was then charged with an N_2-sparged 1:10 mixture of THF:Et_3N (18 mL) and the reaction stirred at room temperature for 4 h. The reaction was then quenched with EtOAc (5 mL) and filtered through a pad of celite. The filtrate was transferred to a separatory funnel and extracted with EtOAc (3x), dried (Na_2SO_4), filtered and concentrated *in vacuo*. The residue was dry loaded onto silica and purified by column chromatography (gradient of hexanes to EtOAc) to afford **5b** (286 mg, 61%) as a brown solid. ^{1}H NMR (500 MHz, $CDCl_3$) δ 8.16 (s, 1H), 7.97 (d, J = 5.0 Hz, 1H), 7.44 (d, J = 8.2 Hz, 2H), 7.20–7.17 (m, 3H), 4.23 (br s, 2H), 2.39 (s, 3H). ^{13}C NMR (126 MHz, $CDCl_3$) δ 143.08, 139.56, 139.25, 137.14, 131.73, 129.44, 125.11, 119.27, 115.13, 98.79, 82.78, 21.73. HRMS (ASAP) $[M+H]^+$ calcd for $C_{14}H_{13}N_2$ 209.1079, found 209.1110.

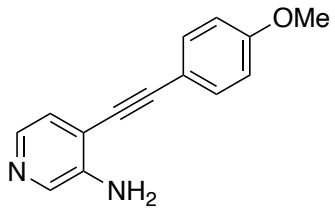

3-Amino-4-(2-(4-methoxyphenyl)ethynyl)pyridine (5c). Crude 4-ethynylanisole (443 mg, 3.35 mmol, 1.47 equiv.), 3-amino-4-iodopyridine (500 mg, 2.27 mmol, 1 equiv.), $Pd(PhCN)_2Cl_2$ (26 mg, 0.07 mmol, 0.03 equiv.), and CuI (17 mg, 0.09 mmol, 0.04 equiv.) were combined in a round bottom flask. The flask was evacuated and backfilled with N_2 a total of three times. The flask was then charged with an N_2-sparged 2:3 mixture of THF:DIPA (10.3 mL). While stirring, P(*t*-Bu)$_3$ (10 wt% in hexanes, 0.4 mL, 0.136 mmol, 0.06 equiv.) was added via syringe and the reaction was stirred at room temperature an additional 48 h. The reaction was then quenched with EtOAc (5mL) and filtered through a pad of celite. The filtrate was transferred to a separatory funnel and extracted with EtOAc (3x), dried (Na_2SO_4), filtered and concentrated *in vacuo*. The residue was dry loaded onto silica and purified by column chromatography (gradient of 30% EtOAc in hexanes to 100% EtOAc in hexanes) to afford **5c** (443 mg, 87%) as a brown solid. ^{1}H NMR (500 MHz, $CDCl_3$) δ 8.16 (s, 1H), 7.97 (s, 1H), 7.49 (d, J = 7.6 Hz, 2H), 7.19 (s, 1H), 6.91 (d, J = 7.6 Hz, 2H), 4.23 (br s, 2H), 3.84 (s, 3H). ^{13}C NMR (126 MHz, $CDCl_3$) δ 160.43, 143.09, 139.02, 136.89, 133.39, 125.10, 115.52, 114.37, 114.34, 98.90, 82.18, 55.52. HRMS (ASAP) $[M+H]^+$ calcd for $C_{14}H_{13}N_2O$ 225.1046, found 225.1028.

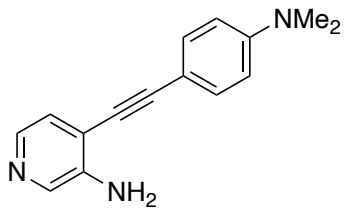

3-Amino-4-(2-(4-dimethylaminophenyl)ethynyl)pyridine (5d). 3-Amino-4-(2-trimethyl-silyl)ethynylpyridine (500 mg, 2.63 mmol, 1 equiv.) and K_2CO_3 (1.45 g, 10.5 mmol, 4 equiv.) were stirred in a 1:1 mixture of $CHCl_3$:MeOH (24 mL) at room

temperature for 2 h to afford deprotected 3-amino-4-ethynylpyridine. The reaction mixture was transferred to separatory funnel and washed with brine (3x), dried (Na_2SO_4) and condensed *in vacuo*. The crude material was then combined in a round bottom flask with 4-iodo-N,N-dimethylaniline (781 mg, 3.16 mmol, 1.2 equiv.), $Pd(PPh_3)_2Cl_2$ (56 mg, 0.08 mmol, 0.02 equiv.), and CuI (10 mg, 0.05 mmol, 0.02 equiv.). The flask was then evacuated and backfilled with N_2 a total of three times. The flask was then charged with an N_2 sparged 1:10 mixture of THF:Et_3N (17 mL) and stirred at room temperature for 4 h. The reaction was then quenched with EtOAc (5 mL) and filtered through a pad of celite. The filtrate was transferred to a separatory funnel and extracted with EtOAc (3x), dried (Na_2SO_4), filtered and concentrated *in vacuo*. Clean product solidified from crude residue upon crystallization from DCM with hexanes to afford **5d** (280 mg, 45%) as an orange solid. ^{1}H NMR (500 MHz, $CDCl_3$) δ 8.13 (br s, 1H), 7.95 (d, J = 5.1 Hz, 1H), 7.41 (d, J = 8.9 Hz, 1H), 7.17 (d, J = 5.0 Hz, 1H), 6.66 (d, J = 8.9 Hz, 2H), 4.21 (br s, 2H), 3.01 (s, 6H). ^{13}C NMR (151 MHz, $CDCl_3$) δ 150.72, 142.86, 139.17, 136.77, 133.06, 124.89, 116.26, 111.88, 108.77, 100.46, 81.56, 40.30. HRMS (ASAP) $[M+H]^+$ calcd for $C_{15}H_{16}N_3$ 238.1344, found 238.1362.

General Cyclization Procedure. The 3-amino-4-arylethynylpyridine (1 equiv.), $P(OPh)_3$ (4 equiv.), and imidazole (2.5 g) were combined neat in an oven-dried round bottom flask. The flask was capped and equipped with a bleed needle before being stirred in a sand bath at 150 °C for 2 h. After cooling to room temperature, the mixture was suspended in EtOAc and transferred to a separatory funnel. The organic layer was washed

DI water (2x) and brine (1x), dried (Na_2SO_4), filtered and condensed *in vacuo*. The crude product was then purified by column chromatography or by crystallization.

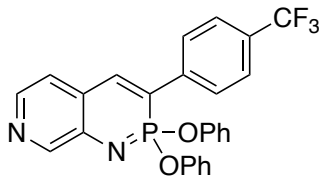

Imidate 6a. Following the general cyclization procedure, aminopyridine **5a** (150 mg, 0.57 mmol, 1 equiv.) and $P(OPh)_3$ (0.6 mL, 2.28 mmol, 4 equiv.) were reacted in imidazole (2.5 g) for 2 h. Column chromatography (gradient of CH_2Cl_2 to EtOAc) gave **6a** (106 mg, 39%) as a yellow solid. ^{1}H NMR (500 MHz, $CDCl_3$) δ 8.64 (s, 1H), 8.11 (s, 1H), 8.06 (d, J = 40.0 Hz, 1H), 7.91 (d, J = 8.0 Hz, 2H), 7.76 (d, J = 8.1 Hz, 2H), 7.23–7.17 (m, 5H), 7.11 (t, J = 7.4 Hz, 2H), 6.94 (d, J = 7.9 Hz, 4H). ^{13}C NMR (126 MHz, $CDCl_3$) δ 149.95 (d, J = 6.3 Hz), 147.41 (d, J = 9.2 Hz), 138.55, 138.05, 131.12, 130.86, 130.01, 128.26 (q, J = 31.8 Hz), 128.02 (d, J = 5.9 Hz), 126.39 (q, J = 4.1 Hz), 125.80, 125.12 (q, J = 272.0 Hz), 122.92 (d, J = 9.5 Hz), 120.75 (d, J = 5.0 Hz), 118.13, 117.10. ^{31}P NMR (202 MHz, $CDCl_3$) δ 25.10 (d, J = 39.7 Hz). ^{19}F NMR (471 MHz, $CDCl_3$) δ -62.60. HRMS (ASAP) $[M+H]^+$ calcd for $C_{26}H_{19}N_2O_2F_3P$ 479.1136, found 479.1130.

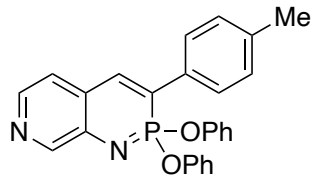

Imidate 6b. Following the general cyclization procedure, aminopyridine **5b** (194 mg, 0.93 mmol, 1 equiv.) and $P(OPh)_3$ (0.98 mL, 3.73 mmol, 4 equiv.) were reacted in

imidazole (2.5 g) for 2 h. Column chromatography (gradient of 12% EtOAc in hexanes to 100% EtOAc) gave **6b** (289 mg, 73%) as a yellow solid. ^{1}H NMR (500 MHz, $CDCl_3$) δ 8.60 (d, *J* = 1.0 Hz, 1H), 8.07 (d, *J* = 5.1 Hz, 1H), 7.99 (d, *J* = 40.7 Hz, 1H), 7.71 (d, *J* = 7.1 Hz, 2H), 7.30 (d, *J* = 7.9 Hz, 2H), 7.18 (t, *J* = 7.9 Hz, 4H), 7.14 (d, *J* = 5.1 Hz, 1H), 7.07 (t, *J* = 7.9 Hz, 2H), 6.95 (d, *J* = 7.8 Hz, 4H), 2.44 (s, 3H). ^{13}C NMR (126 MHz, $CDCl_3$) δ 150.09 (d, *J* = 5.7 Hz), 148.04 (d, *J* = 27.4 Hz), 145.71, 145.28 (d, *J* = 9.6 Hz), 139.34, 138.10, 131.85 (d, *J* = 3.8 Hz), 130.18, 129.84, 127.55 (d, *J* = 6.0 Hz), 125.54 (d, *J* = 1.8 Hz), 125.30, 122.64, 120.94 (d, *J* = 5.0 Hz), 119.07 (d, *J* = 127.7 Hz), 21.46. ^{31}P NMR (202 MHz, $CDCl_3$) δ 26.51 (d, *J* = 40.8 Hz). HRMS (ASAP) $[M+H]^+$ calcd for $C_{26}H_{22}N_2O_2P$ 425.1419, found 425.1414.

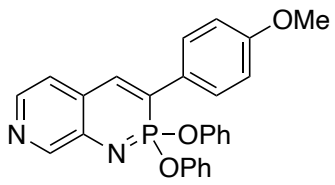

Imidate 6c. Following the general cyclization procedure, aminopyridine **5c** (340 mg, 1.52 mmol, 1 equiv.) and $P(OPh)_3$ (1.6 mL, 6 mmol, 4 equiv.) were reacted in imidazole (2.5 g) for 2 h. After cooling, the crude mixture was left at room temperature for 24 h for the product to precipitate. The solid was suspended in EtOAc and filtered, and the collected precipitate was washed with water and EtOAc in succession, and then dried overnight to afford **6c** (369 mg, 55%) as yellow, crystalline solid. ^{1}H NMR (500 MHz, $CDCl_3$) δ 8.58 (s, 1H), 8.05 (d, *J* = 5.2 Hz, 1H), 7.94 (d, *J* = 40.6 Hz, 1H), 7.78 (d, *J* = 8.4 Hz, 2H), 7.22-7.13 (m, 5H), 7.09 (t, *J* = 7.4 Hz, 2H), 7.04 (d, *J* = 8.5 Hz, 2H), 6.95 (d, *J* = 8.0 Hz, 4H), 3.90 (s, 3H). ^{13}C NMR (126 MHz, $CDCl_3$) δ 160.47, 150.07 (d, *J* = 6.0 Hz), 147.99, 147.78,

145.52, 144.38 (d, J = 9.6 Hz), 138.05, 129.85, 129.00 (d, J = 6.1 Hz), 127.07, 125.55, 122.57, 120.92 (d, J = 5.2 Hz), 118.87 (d, J = 126.8 Hz), 114.89, 55.57. ^{31}P NMR (202 MHz, acetone-d_6) δ 7.32 (d, J = 40.1 Hz). HRMS (ASAP) $[M+H]^+$ calcd for $C_{26}H_{22}N_2O_3P$ 441.1368 , found 441.1453.

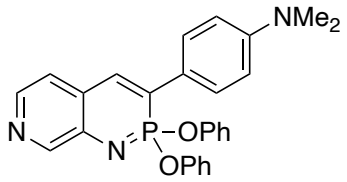

Imidate 6d. Following the general cyclization procedure, aminopyridine **5d** (250 mg, 1.05 mmol, 1 equiv.) and $P(OPh)_3$ (1.1 mL, 4.21 mmol, 4 equiv.) were reacted in imidazole (2.5 g) for 2 h. Column chromatography (gradient of 50% EtOAc in CH_2Cl_2 to 100% EtOAc) gave **5d** (328 mg, 69%) as a yellow-orange solid. ^{1}H NMR (500 MHz, $CDCl_3$) δ 8.55 (s, 1H), 8.03 (d, J = 5.1 Hz, 1H), 7.89 (d, J = 41.2 Hz, 1H), 7.76 (d, J = 7.7 Hz, 2H), 7.17 (t, J = 7.8 Hz, 4H), 7.11 (d, J = 5.2 Hz, 1H), 7.07 (t, J = 6.9 Hz, 2H), 6.97 (d, J = 8.8 Hz, 4H), 6.80 (d, J = 8.8 Hz, 2H), 3.06 (s, 6H). 13C NMR (126 MHz, acetone-d_6) δ 152.04, 151.19 (d, J = 5.5 Hz), 147.86 (d, J = 27.3 Hz), 145.97, 142.47 (d, J = 9.4 Hz), 138.82, 130.77, 129.25 (d, J = 6.6 Hz), 126.89 (d, J = 28.7 Hz), 126.43 (d, J = 1.4 Hz), 123.20 (d, J = 1.8 Hz), 122.22 (d, J = 4.3 Hz), 121.77 (d, J = 4.9 Hz), 119.91 (d, J = 124.6 Hz), 113.46, 40.30. ^{31}P NMR (202 MHz, acetone-d_6) δ 27.60 (d, J = 41.3 Hz). HRMS (ASAP) $[M+H]^+$ calcd for $C_{27}H_{25}N_3O_2P$ 454.1684, found 454.1714.

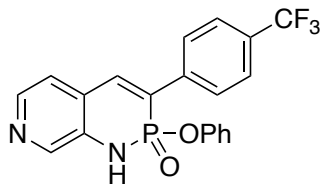

Amidate 2a. Imidate **6a** (403 mg, 0.96 mmol, 1 equiv.) was dissolved in THF (20 mL) in a round bottom flask. Water (20 drops) was added and the solution stirred at 60 °C for 72 h. After cooling, the reaction mixture was dried (Na_2SO_4), filtered, and condensed *in vacuo*. The crude residue was dry loaded onto silica and purified by flash column chromatography (gradient of EtOAc to MeOH) to afford **6a** (85 mg, 45%) as a light brown solid. ^{1}H NMR (500 MHz, $CDCl_3$) δ 8.99 (s, 1H), 8.48 (s, 1H), 8.27 (d, *J* = 5.0 Hz, 1H), 7.97 (d, *J* = 8.0 Hz, 2H), 7.75 (d, *J* = 8.2 Hz, 2H), 7.58 (d, *J* = 38.6 Hz, 1H), 7.21 (d, *J* = 5.0 Hz, 1H), 7.09 (t, *J* = 7.9 Hz, 2H), 6.99 (t, *J* = 6.8 Hz, 1H), 6.88 (d, *J* = 7.8 Hz, 2H). ^{13}C NMR (126 MHz, $CDCl_3$) δ 149.99 (d, *J* = 9.0 Hz), 142.20, 140.29 (d, *J* = 4.6 Hz), 140.03 (d, *J* = 9.6 Hz), 138.37 (d, *J* = 8.8 Hz), 135.10, 130.95 (q, *J* = 32.5 Hz), 129.74 (d, *J* = 1.6 Hz), 129.26 (d, *J* = 158.1 Hz), 128.56 (d, *J* = 6.4 Hz), 126.22 (q, *J* = 3.8 Hz), 125.52 (d, *J* = 1.8 Hz), 124.61 (d, *J* = 15.8 Hz), 122.96 (q, *J* = 272.9 Hz), 122.78, 121.13 (d, *J* = 4.2 Hz). ^{31}P NMR (202 MHz, $CDCl_3$) δ 8.86 (d, *J* = 38.7 Hz). ^{19}F NMR (471 MHz, $CDCl_3$) δ –62.84. HRMS (ASAP) $[M+H]^+$ calcd for $C_{20}H_{15}F_3N_2O_2P$ 403.0823, found 403.0851.

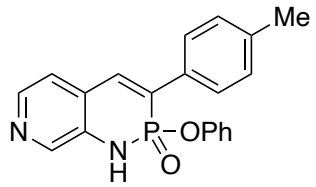

Amidate 2b. Imidate **6b** (692 mg, 1.63 mmol, 1 equiv.) was dissolved in THF (20 mL) in a round bottom flask. Water (5 drops) was added and the solution stirred at 60 °C for 24

h. After cooling, the reaction mixture was dried (Na_2SO_4), filtered, and condensed *in vacuo*. The crude residue was dry loaded onto silica and purified by flash column chromatography (gradient of EtOAc to acetone) to afford **2b** (120 mg, 21%) as a tan solid. ^{1}H NMR (500 MHz, $CDCl_3$) δ 9.45 (s, 1H), 8.46 (s, 1H), 8.21 (d, J = 5.0 Hz, 1H), 7.78 (d, J = 7.7 Hz, 2H), 7.51 (d, J = 39.5 Hz, 1H), 7.31 (d, J = 7.8 Hz, 2H), 7.14 (d, J = 5.0 Hz, 1H), 7.04 (t, J = 7.7 Hz, 2H), 6.94 (t, J = 7.3 Hz, 1H), 6.90 (d, J = 8.0 Hz, 2H), 2.43 (s, 3H). ^{13}C NMR (126 MHz, $CDCl_3$) δ 150.30 (d, J = 9.2 Hz), 141.74, 139.90 (d, J = 9.7 Hz), 139.72, 138.05, 135.18, 131.96 (d, J = 8.5 Hz), 130.29, 130.03, 129.54, 128.04 (d, J = 6.7 Hz), 125.18, 124.96 (d, J = 15.7 Hz), 122.46, 121.34 (d, J = 4.1 Hz), 21.50. ^{31}P NMR (202 MHz, $CDCl_3$) δ 10.15 (d, J = 39.6 Hz). HRMS (ASAP) $[M+H]^+$ calcd for $C_{20}H_{18}N_2O_2P$ 349.1106, found 349.1086.

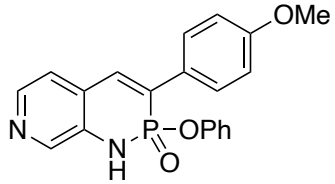

Amidate 2c. Imidate **6c** (360 mg, 0.817 mmol, 1 equiv.) was dissolved in THF (20 mL) in a round bottom flask. Water (20 drops) was added and the solution stirred at 60 °C for 72 h. After cooling, the reaction mixture was dried (Na_2SO_4), filtered, and condensed *in vacuo*. The crude residue was dry loaded onto silica and purified by flash column chromatography (gradient of EtOAc to MeOH) to afford **2c** (166 mg, 56%) as an orange solid. ^{1}H NMR (500 MHz, acetone-d_6) δ 8.51 (s, 1H), 8.18 (d, J = 5.0 Hz, 1H), 7.94 (d, J = 7.3 Hz, 2H), 7.76 (d, J = 39.0 Hz, 1H), 7.36 (d, J = 5.0 Hz, 1H), 7.18 (t, J = 7.8 Hz, 2H), 7.10–7.01 (m, 3H), 6.96 (d, J = 8.3 Hz, 2H), 3.86 (s, 3H). ^{13}C NMR (126 MHz, acetone-

d_6) δ 161.63, 151.65 (d, J = 9.0 Hz), 142.49, 140.02 (d, J = 9.0 Hz), 137.47 (d, J = 4.8 Hz), 136.20, 132.34, 130.39 (d, J = 1.8 Hz), 130.33, 128.47 (d, J = 9.1 Hz), 126.05 (d, J = 15.9 Hz), 125.84, 123.41, 122.12 (d, J = 4.1 Hz), 115.28, 55.82. ^{31}P NMR (202 MHz, acetone-d_6) δ 8.00 (d, J = 38.8 Hz). HRMS (ASAP) $[M+H]^+$ calcd for $C_{20}H_{18}N_2O_3P$ 365.1055, found 365.1039.

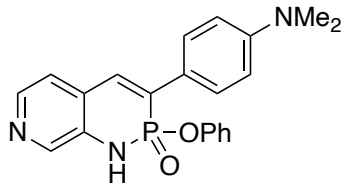

Amidate 2d. Imidate **6d** (150 mg, 0.33 mmol, 1 equiv.) was dissolved in MeCN (20 mL) in a round bottom flask. 30% H_2SO_4 (aq, 5 drops) was added and the solution stirred at 70 °C for 3 h. After cooling, the reaction mixture transferred to a separatory funnel and washed with water (2x) and brine (1x). The organic layer was then dried (Na_2SO_4), filtered, and condensed *in vacuo*. The residue was then crystallized from CH_2Cl_2 with hexanes to afford **2d** (40 mg, 32%) as a light brown solid. ^{1}H NMR (500 MHz, $CDCl_3$) δ 8.38 (s, 1H), 8.20 (d, J = 5.1 Hz, 1H), 7.81 (d, J = 7.6 Hz, 2H), 7.42 (d, J = 40.0 Hz, 1H), 7.19 (d, J = 5.2 Hz, 1H), 7.12 (t, J = 7.9 Hz, 2H), 7.00 (t, J = 7.4 Hz, 1H), 6.93 (d, J = 8.7 Hz, 2H), 6.79 (d, J = 8.8 Hz, 2H), 3.06 (s, 6H). ^{13}C NMR (126 MHz, acetone-d_6) δ 151.15, 150.82 (d, J = 9.4 Hz), 141.53, 138.71 (d, J = 8.7 Hz), 134.94 (d, J = 3.1 Hz), 133.27 (d, J = 5.1 Hz), 132.09, 129.38, 128.80 (d, J = 7.1 Hz), 125.64, 124.74 (d, J = 1.8 Hz), 122.42 (d, J = 9.5 Hz), 122.09, 121.19 (d, J = 4.0 Hz), 112.05, 39.34. ^{31}P NMR (202 MHz, acetone-d_6) δ 7.83 (d, J = 38.9 Hz). HRMS (ASAP) $[M+H]^+$ calcd for $C_{21}H_{21}N_3O_2P$ 378.1371, found 378.1390.

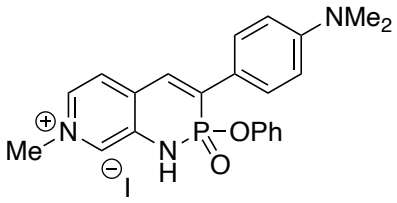

***N*-Methyl Pyridinium Heterocycle 2d'.** Amidate **2d** (35 mg, 0.09 mmol, 1 equiv.) was suspended in excess MeI (2.5 mL) in a bomb flask. The suspension was stirred at 110 °C for 3 h during which time a deep maroon color formed. After cooling, the flask was left to stand at room temperature for 30 min. The resultant precipitate was collected and washed with CH_2Cl_2 to give methylated heterocycle **2d'** (30 mg, 63%) as a dark red solid. ^{1}H NMR (500 MHz, DMSO-d_6) δ 11.12 (s, 1H), 8.39 (d, J = 6.3 Hz, 1H), 8.36 (s, 1H), 8.01 (d, J = 38.9 Hz, 1H), 7.95 (d, J = 6.3 Hz, 1H), 7.92 (d, J = 8.9 Hz, 2H), 7.28 (t, J = 7.7 Hz, 2H), 7.14 (t, J = 7.4 Hz, 1H), 6.94 (d, J = 8.0 Hz, 2H), 6.85 (d, J = 8.8 Hz, 2H), 4.26 (s, 3H), 3.04 (s, 6H). ^{13}C NMR (126 MHz, DMSO-d_6) δ 151.67, 149.77 (d, J = 9.5 Hz), 136.74, 136.37, 136.07, 135.23, 132.68 (d, J = 12.1 Hz), 131.36 (d, J = 16.5 Hz), 129.88, 129.32 (d, J = 7.5 Hz), 128.73 (d, J = 4.3 Hz), 125.50, 125.39, 120.79 (d, J = 4.0 Hz), 120.13, 112.05, 47.61. ^{31}P NMR (202 MHz, DMSO-d_6) δ 5.70 (d, J = 39.2 Hz). HRMS (ASAP) $[M+H]^+$ calcd for $C_{22}H_{24}IN_3O_2P$ 520.0651, found 520.0714.

Crystallographic Data

General. Diffraction intensities for **2a**–**2d, 2d'** and **6d** were collected at 173 K on a Bruker Apex2 CCD diffractometer using a *Incoatec* Cu *IμS* source, CuKα radiation, 1.54178 Å. Space groups were determined based on systematic absences (**2b**, **2c**, and **6d**) and intensity statistics (**2a, 2d** and **2d'**). Absorption corrections were applied by SADABS.[1] Structures were solved by direct methods and Fourier techniques and refined on F^2 using full matrix least-squares procedures. All non-H atoms were refined with anisotropic thermal parameters. H atoms in **2a**–**2c, 2d'** were found on the residual density maps and refined with isotropic thermal parameters. H atoms in **2d** and **6d** were refined in calculated positions in a rigid group model. The I atom in **2d'** is disordered over three positions. Refinement shown that occupation factors of the I atom in these positions are close to 0.89, 0.055 and 0.055. Occupation factors of the I atom in these positions were fixed at these values in the final refinement. The structure of **6d** was refined as a racimic twin; the Flack parameter is 0.32(4). All calculations were performed by the Bruker SHELXL-2014/7 package.[2]

*Crystallographic Data for **2a***: $C_{20}H_{14}F_3N_2O_2P$, M = 402.30.19, 0.12 x 0.06 x 0.02 mm, T = 173(2) K, Triclinic, space group *P*-1, a = 7.8008(4) Å, b = 8.1205(5) Å, c = 15.2905(9) Å, α = 95.240(4)°, β = 91.939(4)°, γ = 116.460(3)°, V = 860.49(9) Å^3, Z = 2, Dc = 1.553 Mg/m^3, μ(Cu) = 1.891 mm^{-1}, F(000) = 412, $2\theta_{max}$ = 136.97°, 10588 reflections, 3116 independent reflections [R_{int} = 0.0395], R1 = 0.0349, wR2 = 0.0948 and GOF = 1.048 for 3116 reflections (309 parameters) with I>2σ(I), R1 = 0.0393, wR2 = 0.0980 and GOF = 1.048 for all reflections, max/min residual electron density +0.334/–0.323 eÅ^{-3}. CCDC-2210396.

Crystallographic Data for ***2b***: $C_{20}H_{17}N_2O_2P$, M = 348.32, 0.12 x 0.17 x 0.20 mm, T = 173(2) K, Monoclinic, space group *C*2/*c*, *a* = 24.5418(15) Å, *b* = 10.0738(6) Å, *c* = 14.5824(9) Å, β = 107.984(2)°, *V* = 3429.1(4) Å^3, *Z* = 8, *D*c = 1.349 Mg/m^3, μ(Cu) = 1.550 mm^{-1}, F(000) = 1456, $2\theta_{max}$ = 133.41°, 11166 reflections, 3030 independent reflections [R_{int} = 0.0396], R1 = 0.0363, wR2 = 0.0989 and GOF = 1.027 for 3030 reflections (294 parameters) with I>2σ(I), R1 = 0.0375, wR2 = 0.1002 and GOF = 1.027 for all reflections, max/min residual electron density +0.291/ –0.441 eÅ^{-3}. CCDC-2210393.

Crystallographic Data for ***2c***: $C_{20}H_{17}N_2O_3P$, M = 364.32, 0.19 x 0.22 x 0.23 mm, T = 173(2) K, Monoclinic, space group *P*2$_1$/*n*, *a* = 9.4546(5) Å, *b* = 8.4853(5) Å, *c* = 21.5114(12) Å, β = 99.293(2)°, *V* = 1703.10(17) Å^3, *Z* = 4, *D*c = 1.421 Mg/m^3, μ(Cu) = 1.632 mm^{-1}, F(000) = 760, $2\theta_{max}$ = 133.30°, 16184 reflections, 3012 independent reflections [R_{int} = 0.0350], R1 = 0.0361, wR2 = 0.1056 and GOF = 1.063 for 3012 reflections (303 parameters) with I>2σ(I), R1 = 0.0364, wR2 = 0.1061 and GOF = 1.063 for all reflections, max/min residual electron density +0.377/ –0.470 eÅ^{-3}. CCDC-2210395.

Crystallographic Data for ***2d***: $C_{21}H_{20}N_3O_2P$, M = 377.37, 0.17 x 0.09 x 0.05 mm, T = 173(2) K, Triclinic, space group *P*-1, *a* = 8.9079(3) Å, *b* = 8.9507(3) Å, *c* = 12.5734(4) Å, α = 69.827(2)°, β = 83.619(2)°, γ = 79.828(2)°, *V* = 924.84(5) Å^3, *Z* = 2, *D*c = 1.355 Mg/m^3, μ(Cu) = 1.494 mm^{-1}, F(000) = 396, $2\theta_{max}$ = 133.29°, 9192 reflections, 3264 independent reflections [R_{int} = 0.0363], R1 = 0.0557, wR2 = 0.1625 and GOF = 1.055 for 3264 reflections (248 parameters) with I>2σ(I), R1 = 0.0601, wR2 = 0.1671 and GOF = 1.055 for all reflections, max/min residual electron density +0.647/–0.266 eÅ^{-3}. CCDC-2210397.

Crystallographic Data for ***2d'***: $C_{22}H_{23}IN_3O_2P$, M = 519.30, 0.08 x 0.07 x 0.06 mm, T = 173(2) K, Triclinic, space group *P*-1, *a* = 9.6055(5) Å, *b* = 10.0075(5) Å, *c* = 12.3140(7) Å, α = 75.385(3)°, β = 71.905(3)°, γ = 88.796(3)°, *V* = 1086.64(10) Å^3, *Z* = 2, *D*c = 1.587 Mg/m^3, μ(Cu) = 12.460 mm^{-1}, F(000) = 520, $2\theta_{max}$ = 133.29°, 10957 reflections, 3826 independent reflections [R_{int} = 0.0432], R1 = 0.0297, wR2 = 0.0749 and GOF = 1.063 for 3826 reflections (363 parameters) with I>2σ(I), R1 = 0.0307, wR2 = 0.0756 and GOF = 1.063 for all reflections, max/min residual electron density +0.921/–0.333 eÅ^{-3}. CCDC-2217960.

Crystallographic Data for ***6d***: $C_{27}H_{24}N_3O_2P$, M = 453.46, 0.16 x 0.12 x 0.01 mm, T = 173(2) K, Orthorhombic, space group *Pna*2$_1$, *a* = 20.1647(5) Å, *b* = 10.3875(2) Å, *c* = 22.0503(5) Å, *V* = 4618.67(18) Å^3, *Z* = 8, Z' =2, *D*c = 1.304 Mg/m^3, μ(Cu) = 1.290 mm^{-1}, F(000) = 1904, $2\theta_{max}$ = 133.83°, 64728 reflections, 8194 independent reflections [R_{int} = 0.1472], R1 = 0.0685, wR2 = 0.1724 and GOF = 1.036 for 8194 reflections (596 parameters) with I>2σ(I), R1 = 0.0813, wR2 = 0.1856 and GOF = 1.036 for all reflections, max/min residual electron density +1.371/–0.462 eÅ^{-3}. CCDC-2223323.

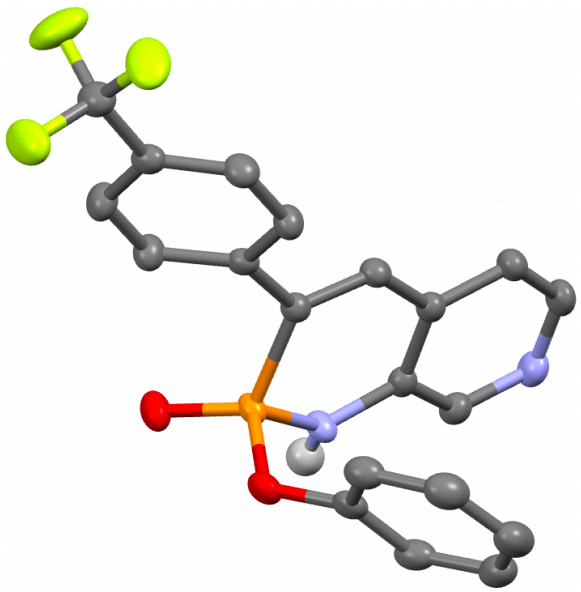

Figure B1. ORTEP drawing of pyridine-PN **2a**; thermal ellipsoids drawn at 30% probability.

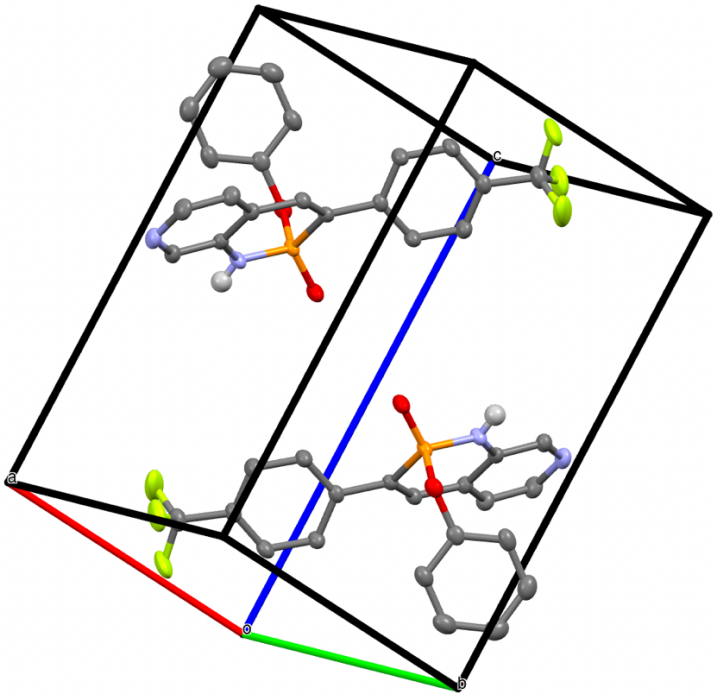

Figure B2. ORTEP drawing of the crystal packing of pyridine-PN **2a**; thermal ellipsoids drawn at 30% probability.

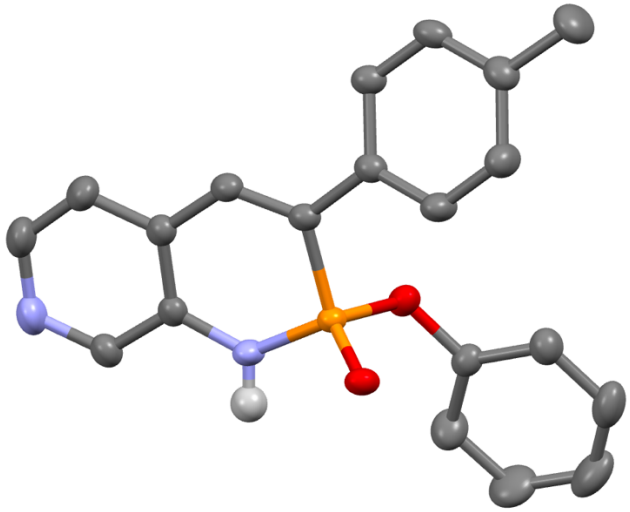

Figure B3. ORTEP drawing of pyridine-PN **2b**; thermal ellipsoids drawn at 30% probability.

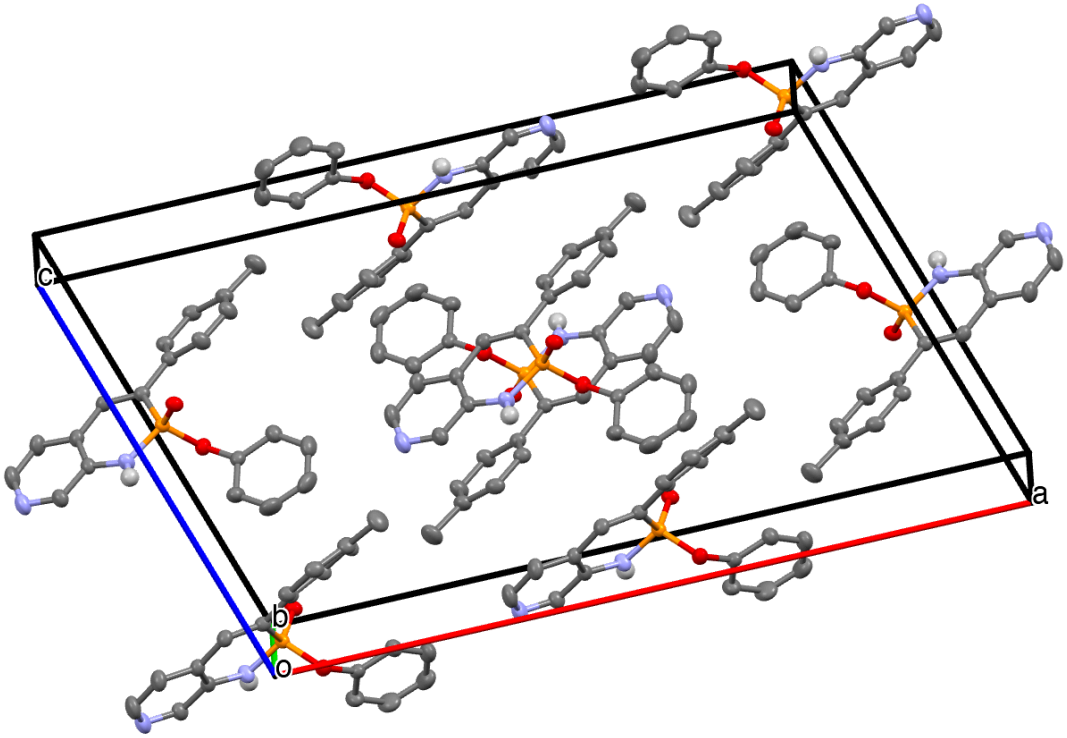

Figure B4. ORTEP drawing of the crystal packing of pyridine-PN **2b**; thermal ellipsoids drawn at 30% probability.

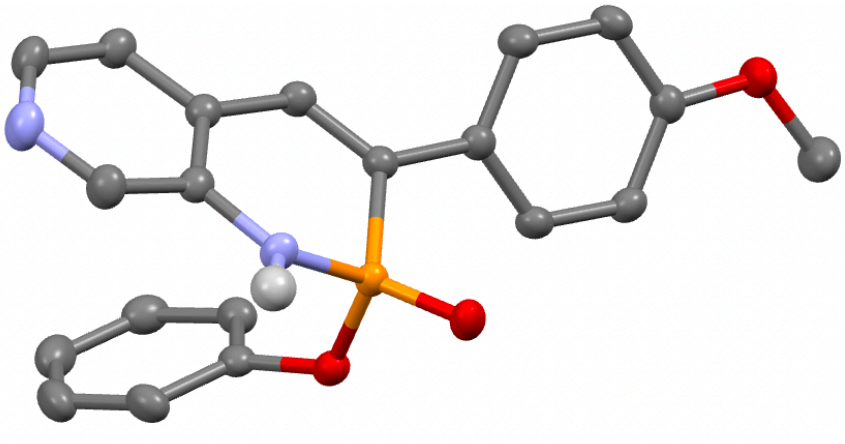

Figure B5. ORTEP drawing of pyridine-PN **2c**; thermal ellipsoids drawn at 30% probability.

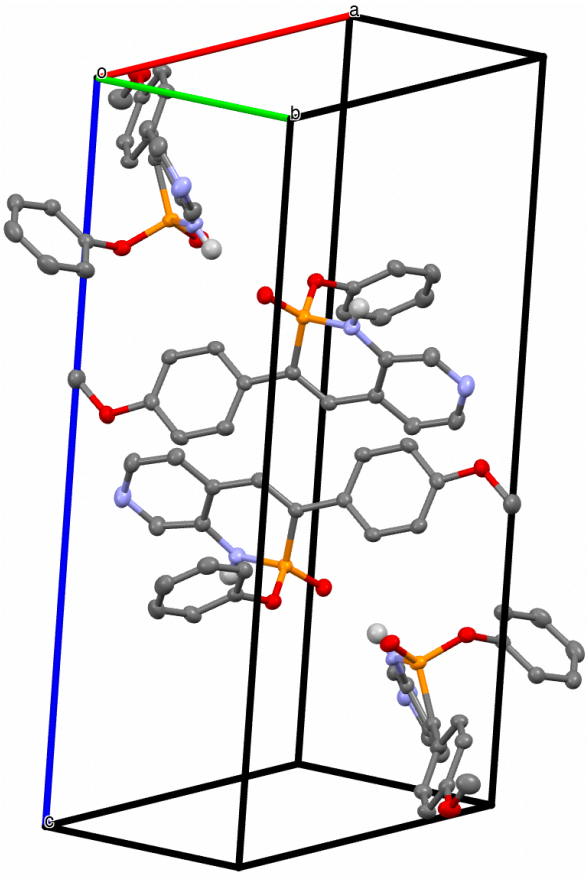

Figure B6. ORTEP drawing of the crystal packing of pyridine-PN **2c**; thermal ellipsoids drawn at 30% probability. No typical homodimerization observed.

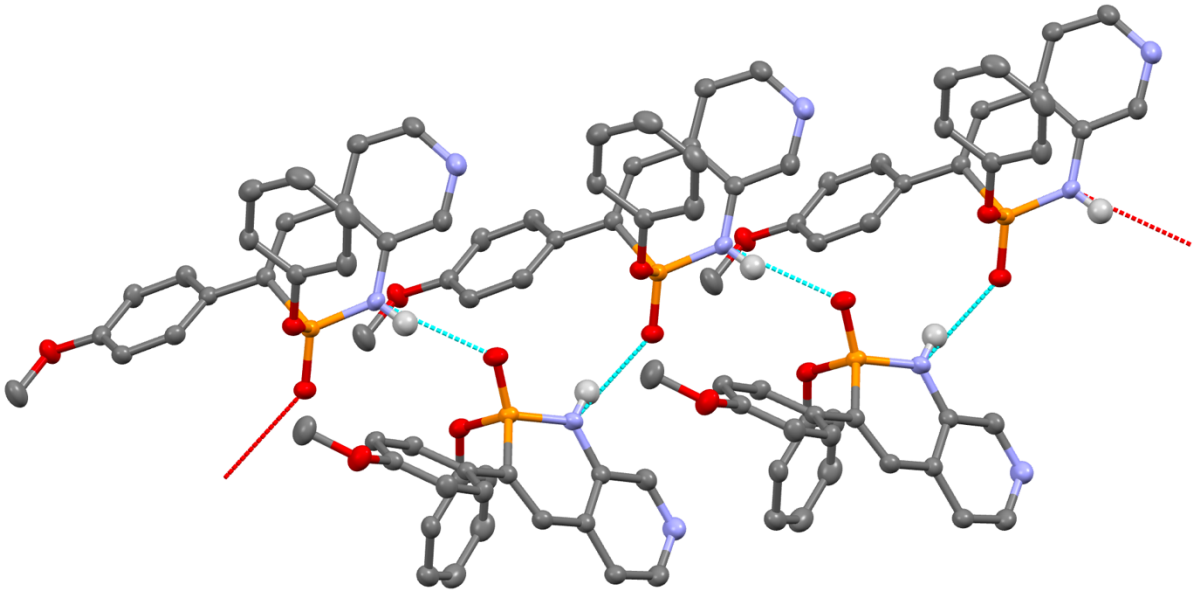

Figure B7. ORTEP drawing of the supramolecular head-to-tail polymer of pyridine-PN **2c**; thermal ellipsoids drawn at 30% probability.

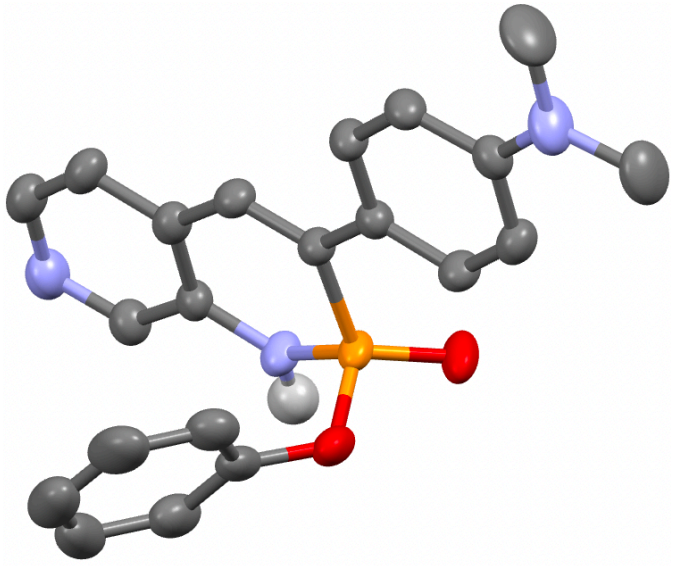

Figure B8. ORTEP drawing of pyridine-PN **2d**; thermal ellipsoids drawn at 30% probability.

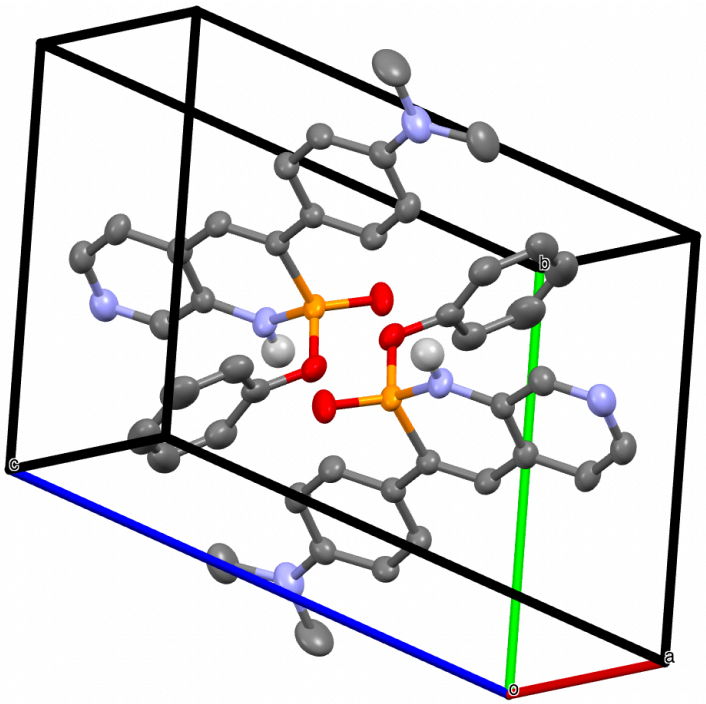

Figure B9. ORTEP drawing of the crystal packing of pyridine-PN **2d**; thermal ellipsoids drawn at 30% probability.

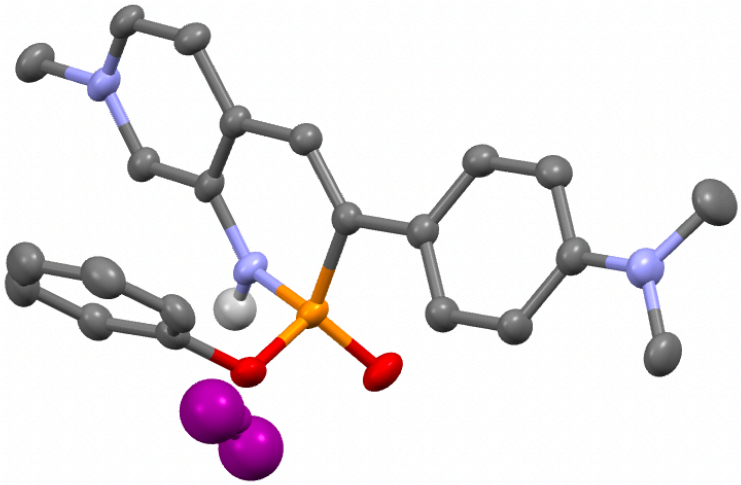

Figure B10. ORTEP drawing of N-methyl pyridinium-PN **2d'**; thermal ellipsoids drawn at 30% probability. The iodide anion is disordered.

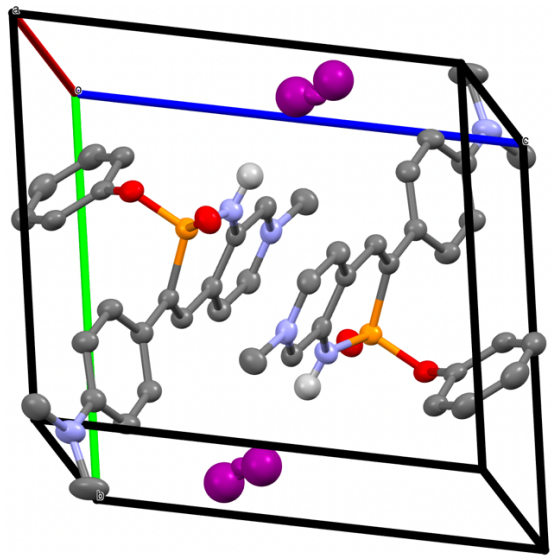

Figure B11. ORTEP drawing of the crystal packing of pyridinium-PN **2d'**; thermal ellipsoids drawn at 30% probability. The iodide anion is disordered.

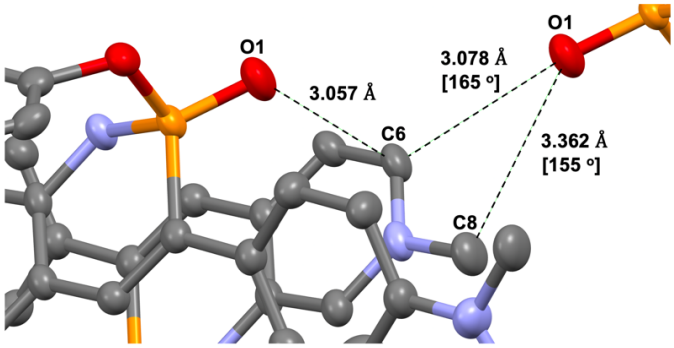

Figure B12. Close-up view showing the short P=O•••CH contacts in **2d'**.

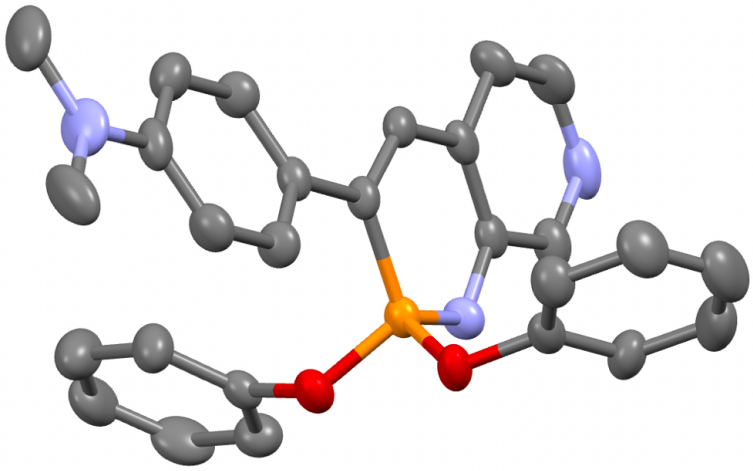

Figure B13. ORTEP drawing of pyridine-PN **6d**; thermal ellipsoids drawn at 30% probability

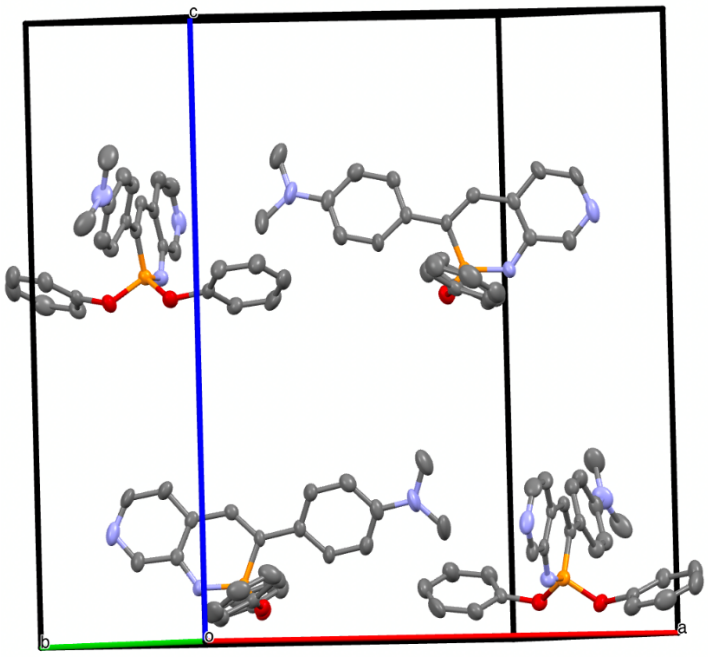

Figure B14. ORTEP drawing of the crystal packing of pyridine-PN **6d**; thermal ellipsoids drawn at 30% probability.

Stilbazole UV-Vis Comparison

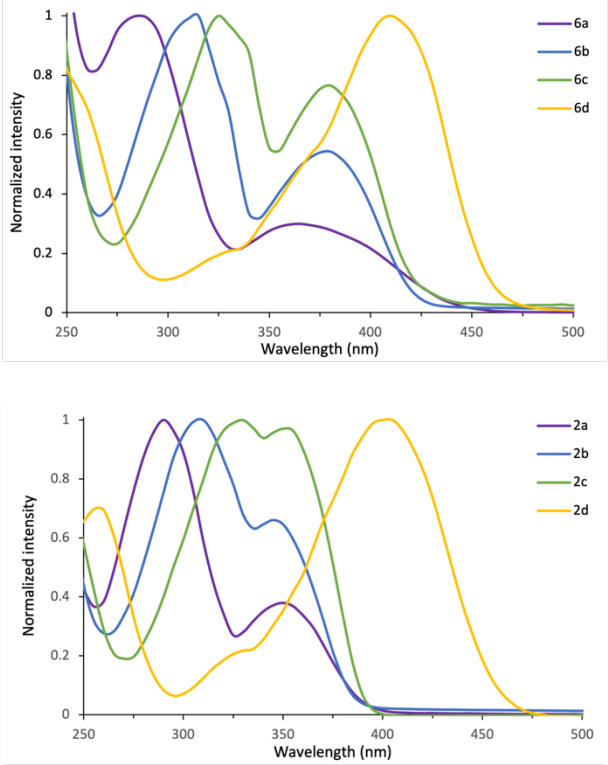

Figure B15. Electronic absorption spectra of imidates **6** (left) and amidates **2** (right) in anhydrous ethanol (~10^{-5} M) at room temperature.

Table B1. UV-Vis comparison of para-substituted stilbazole absorption data to imdates **6**

R	λ_{max} Stilbazole (nm)[a]	λ_{ICT} Imidate (nm)[b]	Δ (nm)
CF_3	305	365	60
Me	314	380	66
OMe	327	380	53

NMe_2	380	410	30

[a] Data collected in anhydrous ethanol as ~6 x 10^{-3} M solutions at room temperature; reported in reference [3]. [b] Data collected in anhydrous ethanol as ~10^{-5} M solutions at room temperature.

Table B2. UV-Vis comparison of para-substituted stilbazole absorption data to amidates **2**

R	λ_{max} Stilbazole (nm)[a]	λ_{ICT} Amidate (nm)[b]	Δ (nm)
CF_3	305	350	45
Me	314	345	31
OMe	327	350	23
NMe_2	380	400	20

[a] Data collected in anhydrous ethanol as ~6 x 10^{-3} M solutions at room temperature; reported in reference [3]. [b] Data collected in anhydrous ethanol as ~10^{-5} M solutions at room temperature.

Computational Data

Cartesian coordinates optimized at B3LYP-D3/6-311+G(d,p)

2a

	X	Y	Z
P	-1.67754	-1.03761	-2.00068
N	-3.29816	-1.20169	-1.55465
N	-5.85782	-0.60743	0.99646
C	4.16805	2.46405	-1.79974
O	-1.47769	-1.01457	-3.46536
O	-0.87321	-2.32053	-1.37061
C	-1.15938	0.36291	-0.98950
C	-1.96413	0.81527	0.00294
H	-1.60825	1.64778	0.60520
C	-3.27724	0.31329	0.34599
C	-3.92032	-0.66947	-0.43283
C	-5.21042	-1.07935	-0.06061
H	-5.72577	-1.82964	-0.65745
C	-5.24439	0.32028	1.74788
H	-5.79520	0.68411	2.60859
C	-3.97845	0.80385	1.45861
H	-3.52572	1.56155	2.08850
C	0.20020	0.90463	-1.21437

C	1.00836	1.24762	-0.11728
H	0.64820	1.07268	0.88919
C	2.27913	1.77269	-0.30582
H	2.89311	2.03557	0.54660
C	2.76801	1.95352	-1.60017
C	1.98762	1.59980	-2.69906
H	2.37090	1.73948	-3.70183
C	0.71334	1.07616	-2.51000
H	0.11289	0.80109	-3.36751
C	-0.76184	-2.53811	0.00373
C	0.43577	-2.20696	0.63011
H	1.23580	-1.77458	0.04270
C	0.57423	-2.43823	1.99669
H	1.50622	-2.18599	2.48967
C	-0.47745	-2.99277	2.72686
H	-0.36712	-3.16964	3.79028
C	-1.66763	-3.32814	2.08281
H	-2.48572	-3.76618	2.64276
C	-1.81422	-3.10742	0.71432
H	-2.72924	-3.36935	0.19944
H	-3.85849	-1.78364	-2.16494
F	4.32401	3.08555	-2.98906
F	4.53139	3.34281	-0.83595

F	5.07848	1.45605	-1.76419

2b

	X	Y	Z
P	-1.69233	-1.00040	-2.00682
N	-3.31095	-1.15994	-1.55032
N	-5.83056	-0.61532	1.05342
C	4.19385	2.52864	-1.81800
O	-1.50918	-0.97079	-3.47400
O	-0.89472	-2.30158	-1.39808
C	-1.15211	0.38177	-0.98238
C	-1.94556	0.81706	0.02756
H	-1.57759	1.63535	0.64177
C	-3.25531	0.31239	0.38073
C	-3.91520	-0.65199	-0.40722
C	-5.19960	-1.06653	-0.02347
H	-5.72576	-1.80334	-0.62777
C	-5.20156	0.29474	1.81302
H	-5.73703	0.64288	2.68996
C	-3.93825	0.78036	1.51401
H	-3.47331	1.52305	2.15292
C	0.21026	0.91236	-1.20924
C	1.02820	1.24898	-0.11845

H	0.67339	1.07393	0.89071
C	2.30544	1.75995	-0.31525
H	2.91994	2.00182	0.54610
C	2.81913	1.94684	-1.60367
C	2.00964	1.59210	-2.68766
H	2.38677	1.71498	-3.69776
C	0.73029	1.07894	-2.50307
H	0.13068	0.80619	-3.36234
C	-0.79396	-2.54599	-0.02886
C	0.38726	-2.20312	0.62224
H	1.18302	-1.73447	0.05735
C	0.51197	-2.46311	1.98495
H	1.43046	-2.19964	2.49718
C	-0.53658	-3.05765	2.68765
H	-0.43708	-3.25590	3.74845
C	-1.71071	-3.40278	2.01966
H	-2.52734	-3.86942	2.55831
C	-1.84333	-3.15310	0.65486
H	-2.74639	-3.41918	0.12118
H	-3.87909	-1.73209	-2.16230
H	4.66717	2.11476	-2.71152
H	4.13748	3.61470	-1.95069
H	4.84809	2.33586	-0.96464

2c

	X	Y	Z
P	-1.66313	-0.98817	-1.99848
N	-3.28491	-1.16821	-1.56322
N	-5.83066	-0.67905	1.02710
O	4.00982	2.53227	-1.84718
O	-1.45963	-0.96218	-3.46310
O	-0.85501	-2.27607	-1.37345
C	-1.15493	0.40619	-0.97390
C	-1.96603	0.82834	0.02843
H	-1.61983	1.65529	0.64372
C	-3.26803	0.29816	0.37274
C	-3.90586	-0.67588	-0.42162
C	-5.18419	-1.11546	-0.04705
H	-5.69254	-1.86046	-0.65658
C	-5.22320	0.24068	1.79234
H	-5.77036	0.57691	2.66676
C	-3.96714	0.75042	1.50256
H	-3.52033	1.49998	2.14641
C	0.20023	0.95407	-1.18943
C	1.00033	1.31352	-0.09692
H	0.63781	1.14358	0.91026

C	2.27505	1.84725	-0.26811
H	2.86244	2.10124	0.60368
C	2.78076	2.02447	-1.56050
C	2.00068	1.65303	-2.66277
H	2.41054	1.79005	-3.65587
C	0.73578	1.12103	-2.48210
H	0.15043	0.83403	-3.34645
C	4.85503	2.92902	-0.77321
H	5.76578	3.30511	-1.23595
H	4.39547	3.72482	-0.17652
H	5.10168	2.08083	-0.12480
C	-0.77734	-2.51826	-0.00284
C	0.38080	-2.14705	0.67393
H	1.17664	-1.65910	0.12573
C	0.48221	-2.40451	2.03902
H	1.38285	-2.11956	2.57116
C	-0.56653	-3.02471	2.71893
H	-0.48528	-3.22099	3.78166
C	-1.71700	-3.39825	2.02557
H	-2.53358	-3.88476	2.54642
C	-1.82596	-3.15125	0.65824
H	-2.71052	-3.43880	0.10505
H	-3.83752	-1.75028	-2.17998

2d

	X	Y	Z
P	7.28731	7.05151	7.12543
N	5.66942	6.88554	7.57889
N	3.16447	7.37754	10.20977
N	13.10140	10.46988	7.33447
O	7.46971	7.07375	5.65726
O	8.09054	5.75172	7.73629
C	7.82626	8.43575	8.14883
C	7.02915	8.85775	9.16498
H	7.39097	9.67511	9.78378
C	5.72760	8.33820	9.52327
C	5.06856	7.37425	8.73335
C	3.79309	6.94244	9.12372
H	3.27052	6.20477	8.51722
C	3.79137	8.28782	10.97047
H	3.26016	8.62394	11.85487
C	5.04769	8.78849	10.66591
H	5.51009	9.52965	11.30852
C	9.18529	8.95826	7.92366
C	9.98907	9.36012	9.00404
H	9.62054	9.24329	10.01689

C	11.26501	9.86589	8.82075
H	11.83702	10.14742	9.69374
C	11.82167	9.98857	7.52527
C	11.01472	9.57846	6.43945
H	11.37980	9.65480	5.42514
C	9.74105	9.06989	6.63721
H	9.16147	8.76331	5.77546
C	13.82511	11.05770	8.45087
H	14.80654	11.38318	8.10986
H	13.30259	11.92628	8.87499
H	13.98018	10.32726	9.25131
C	13.58712	10.71249	5.98449
H	14.61982	11.05443	6.03199
H	13.57031	9.79444	5.38978
H	12.99509	11.47397	5.45813
C	8.18743	5.51013	9.10532
C	9.35324	5.88318	9.76800
H	10.14038	6.37560	9.21130
C	9.47147	5.62571	11.13173
H	10.37757	5.91349	11.65299
C	8.43218	5.00371	11.82441
H	8.52659	4.80786	12.88617
C	7.27331	4.62955	11.14542

H	6.46322	4.14322	11.67651
C	7.14730	4.87699	9.77967
H	6.25539	4.59110	9.23739
H	5.10519	6.30858	6.96803
H	5.10519	6.30858	6.96803

References

1. Sheldrick, G. M. *Bruker/Siemens Area Detector Absorption Correction Program*, Bruker AXS, Madison, WI, 1998.

2. Sheldrick, G. M. Crystal structure refinement with SHELXL. *Acta Cryst.* **2015**, *C71*, 3–8.

3. Cao, C.-T.; Yan, L.; Cao, C. Determination and application of the exited-state substituent constants of pyridyl and substituted phenyl groups. *J. Phys. Org. Chem.* **2021**, *34*, e4246.

Copies of NMR Spectra

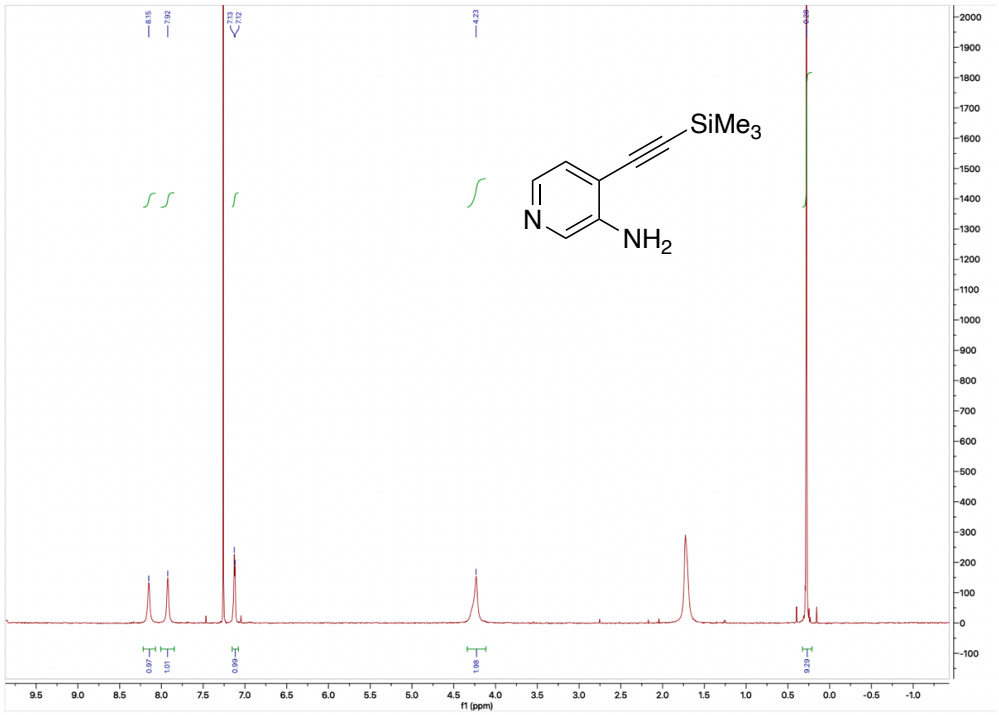

Figure B16 ^{1}H NMR Spectrum of **4** in $CDCl_3$

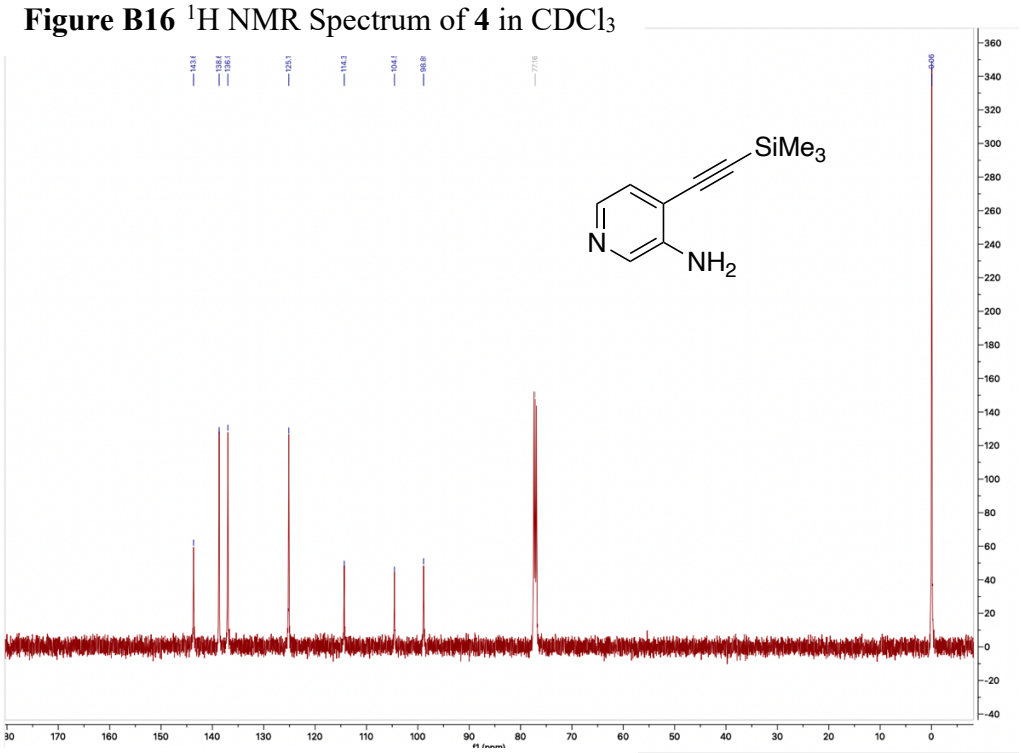

Figure B17 ^{13}C NMR Spectrum of **4** in $CDCl_3$

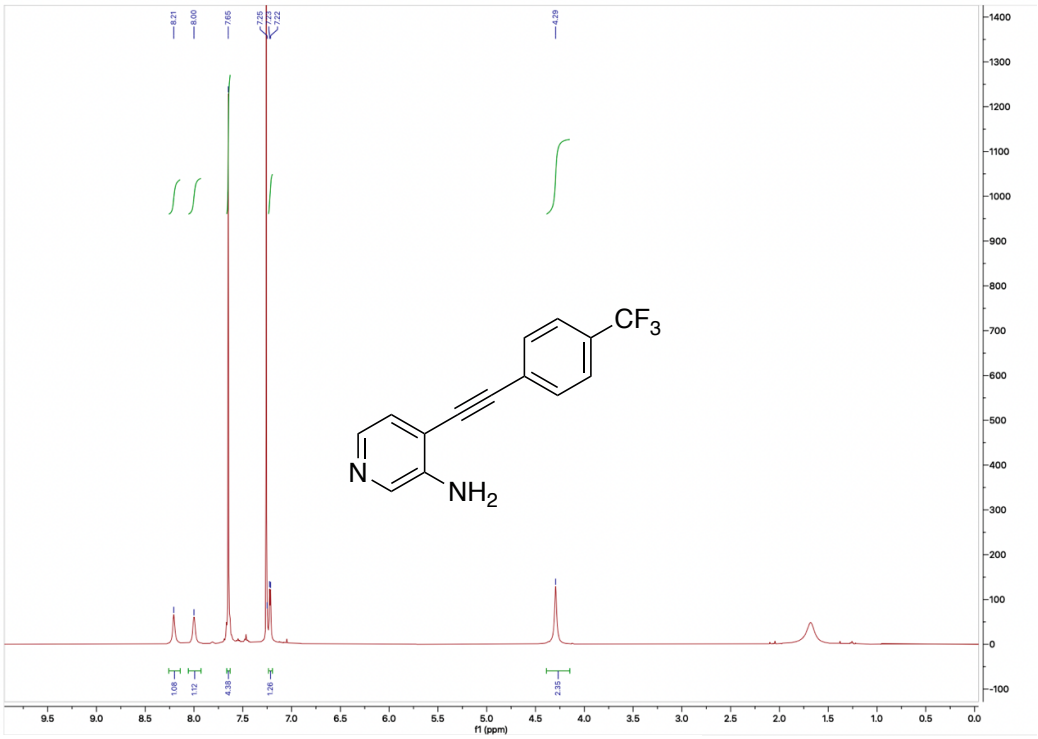

Figure B18 ^{1}H NMR Spectrum of **5a** in Acetone-d_6

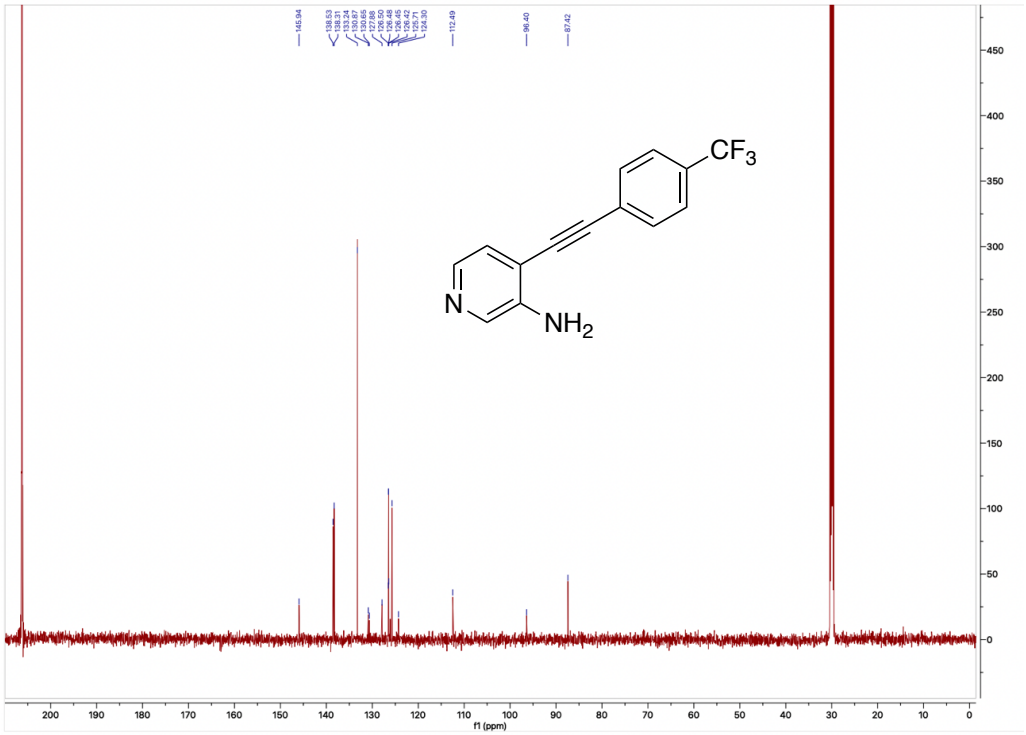

Figure B19 ^{13}C NMR Spectrum of **5a** in Acetone-d_6

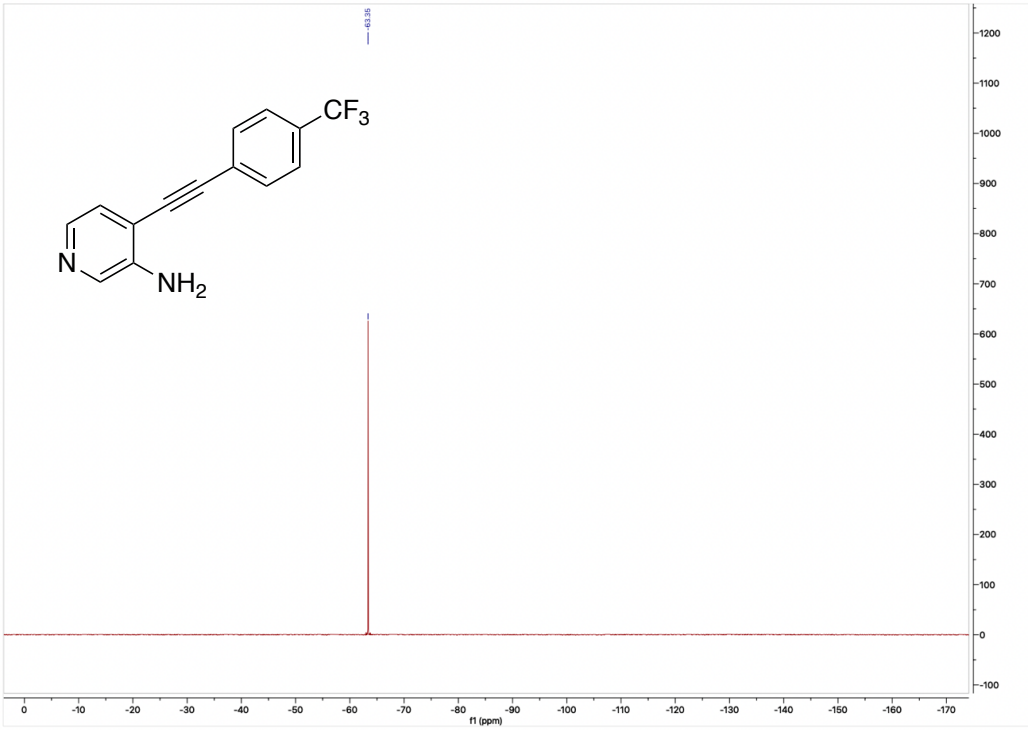

Figure B20 ^{19}F NMR Spectrum of **5a** in Acetone-d_6

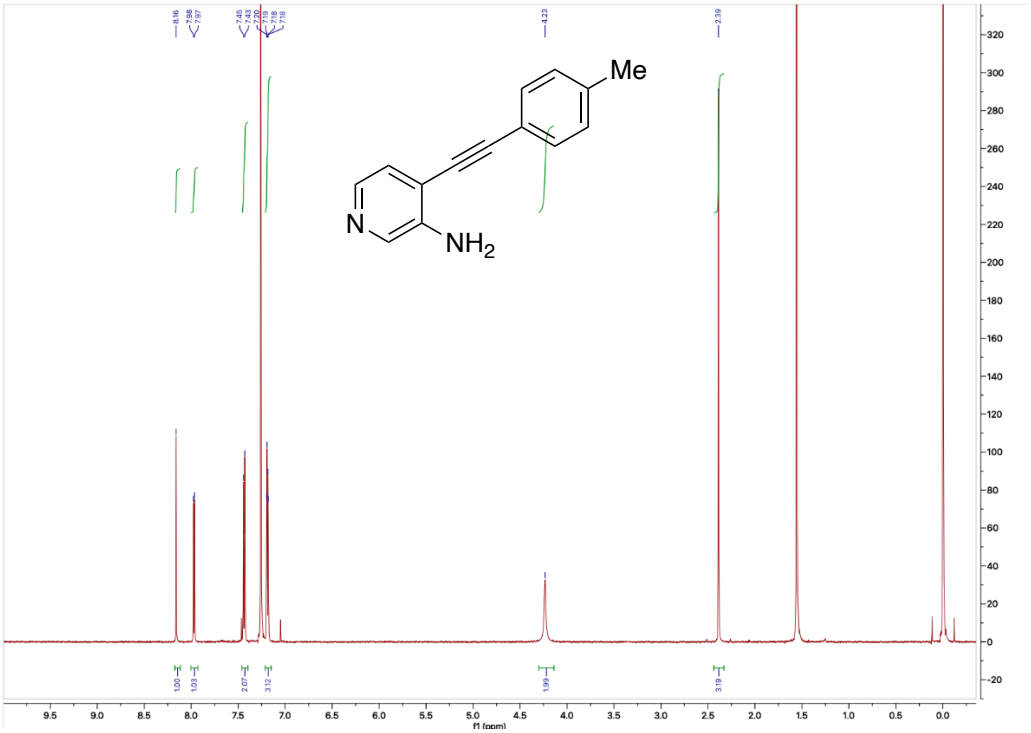

Figure B21 ^{1}H NMR Spectrum of **5b** in $CDCl_3$

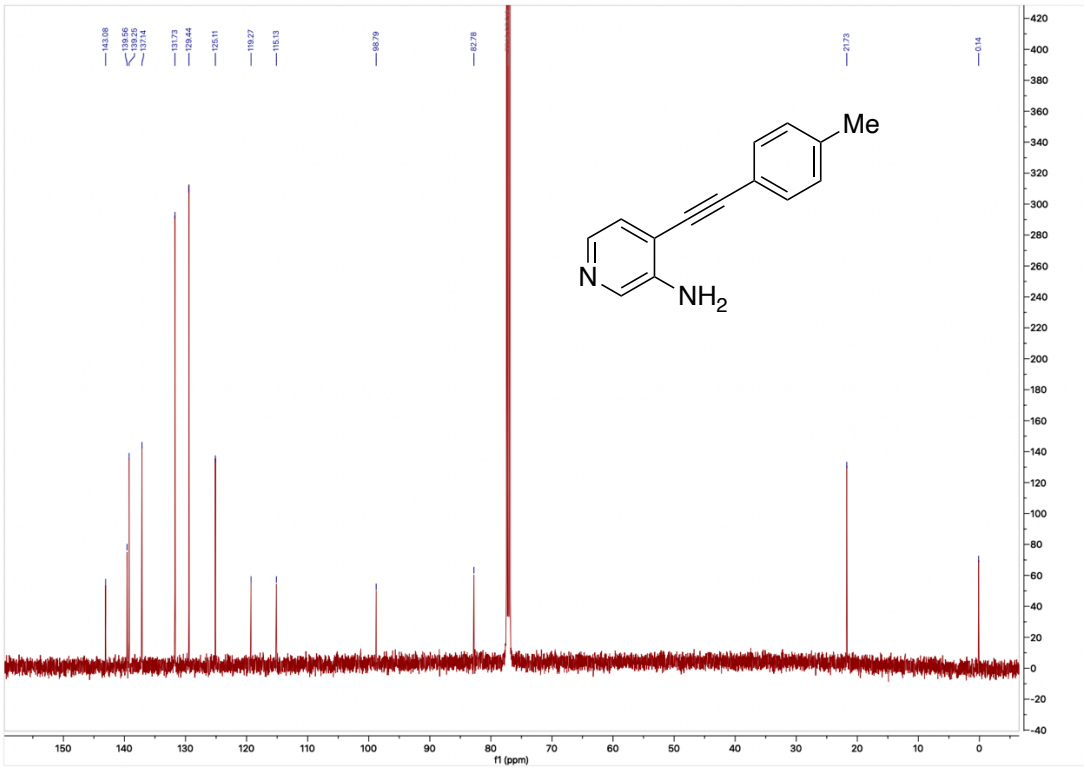

Figure B22 ^{13}C NMR Spectrum of **5b** in $CDCl_3$

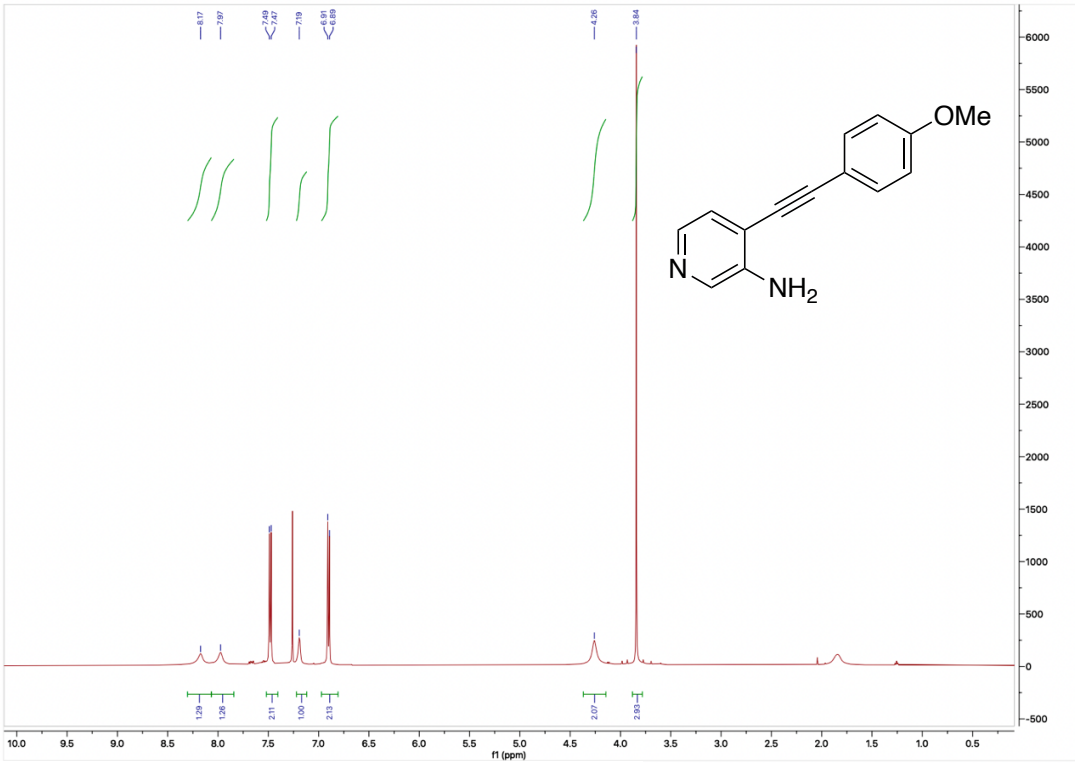

Figure B23 ^{1}H NMR Spectrum of **5c** in $CDCl_3$

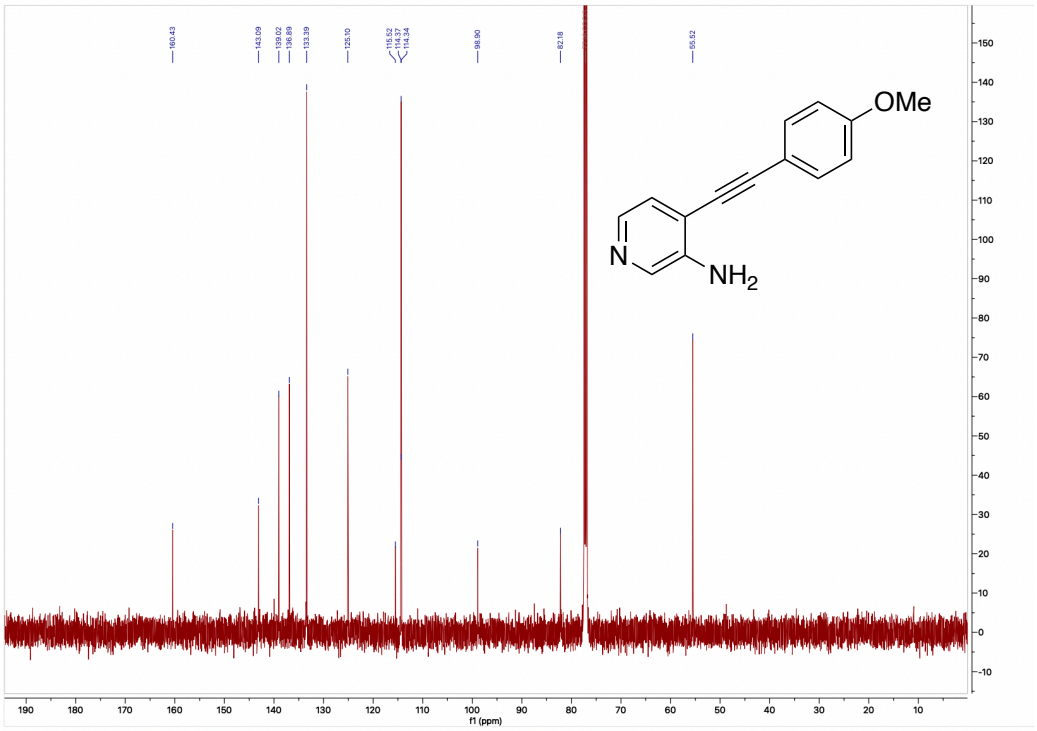

Figure B24 ^{13}C NMR Spectrum of **5c** in $CDCl_3$

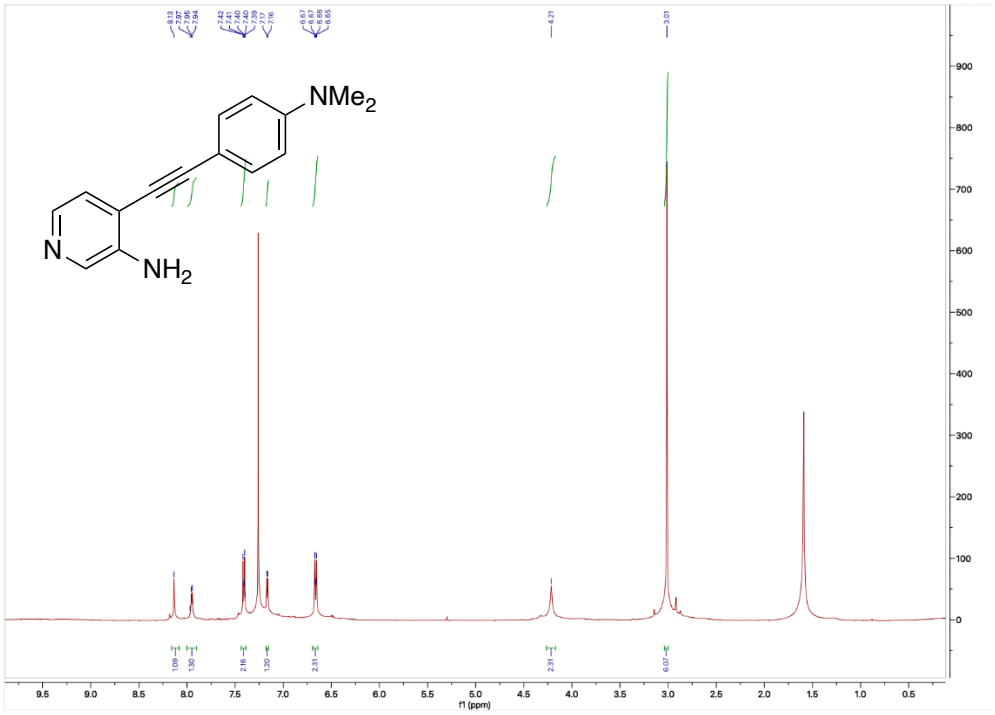

Figure B25 ^{1}H NMR Spectrum of **5d** in $CDCl_3$

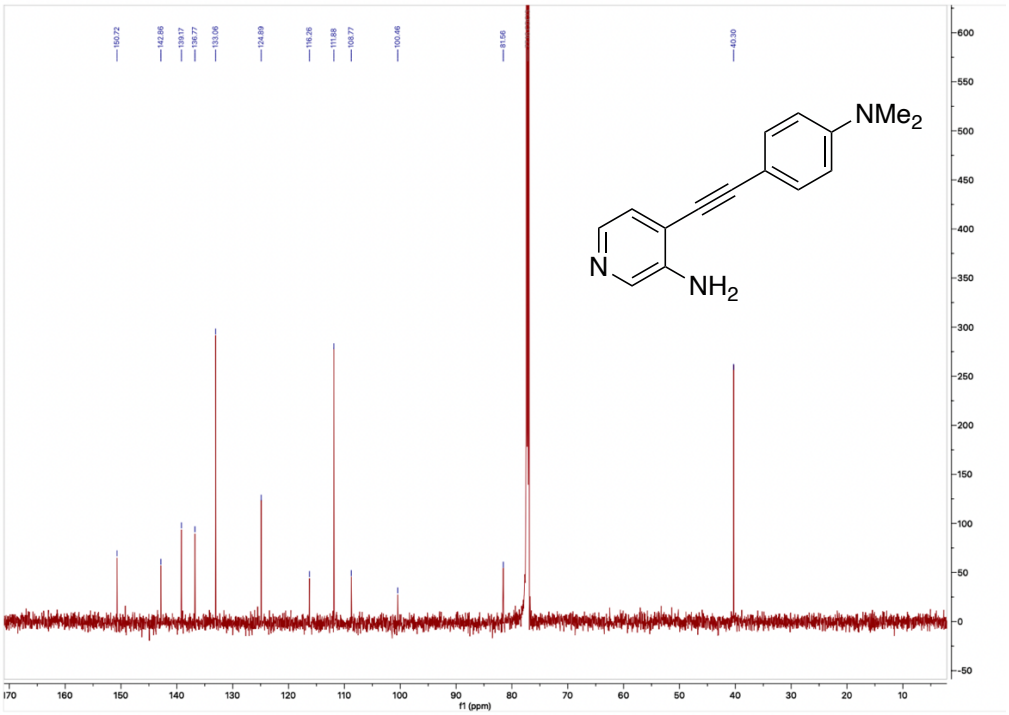

Figure B26 ^{13}C NMR Spectrum of **5d** in $CDCl_3$

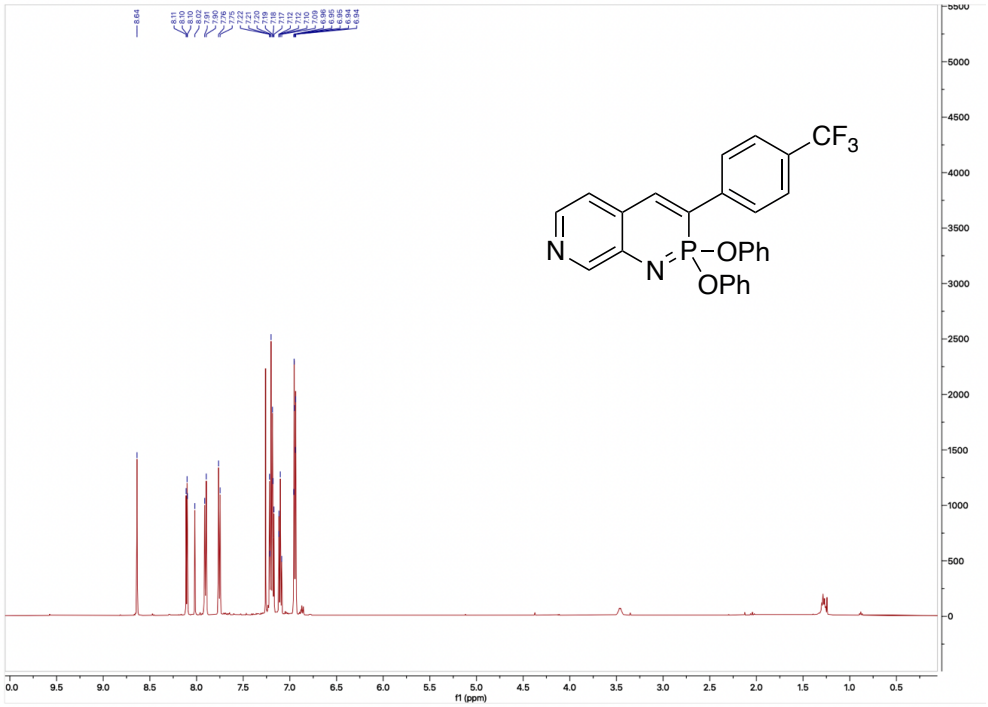

Figure B27 ^{1}H NMR Spectrum of **6a** in $CDCl_3$

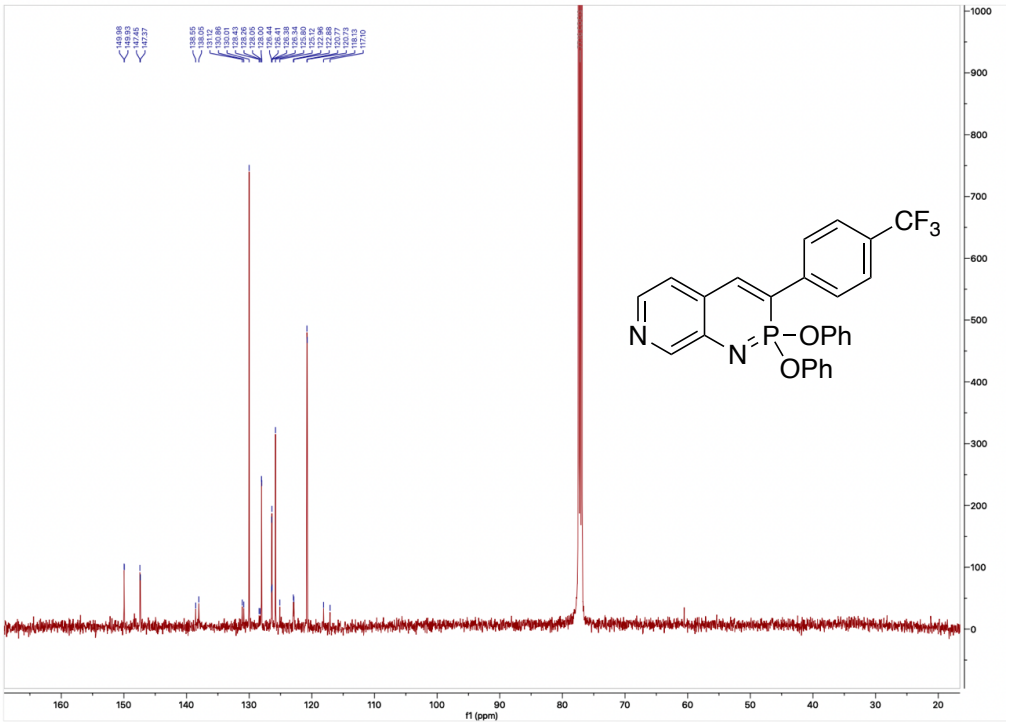

Figure B28 ^{13}C NMR Spectrum of **6a** in $CDCl_3$

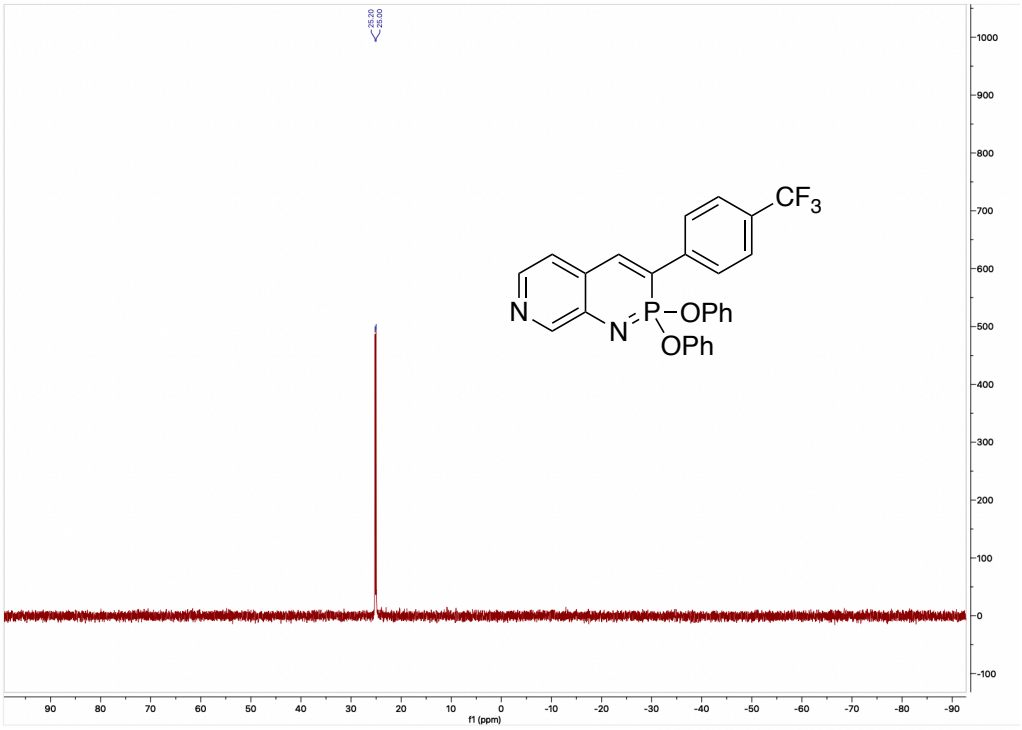

Figure B29 ^{31}P NMR Spectrum of **6a** in $CDCl_3$

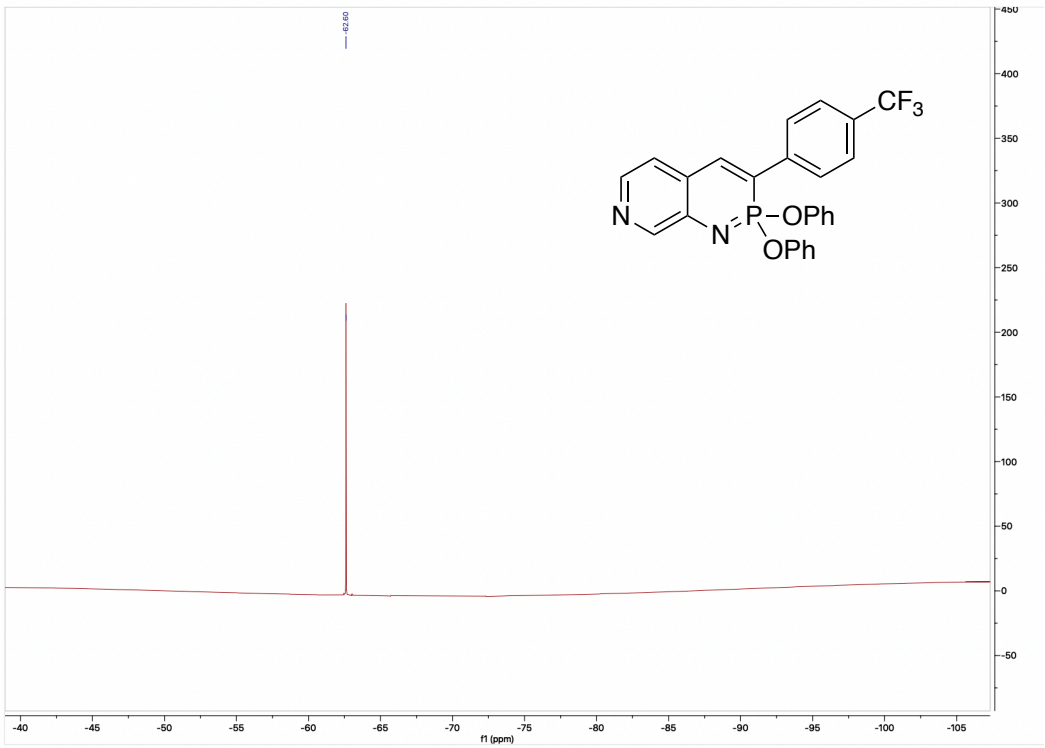

Figure B30 ^{19}F NMR Spectrum of **6a** in $CDCl_3$

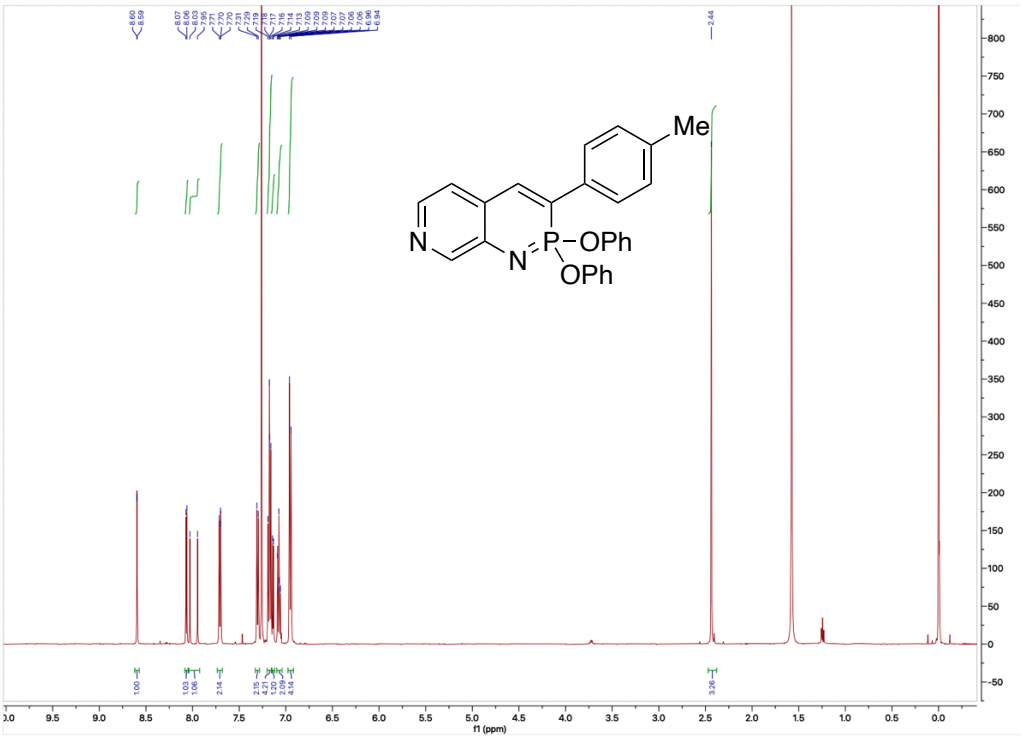

Figure B31 ^{1}H NMR Spectrum of **6b** in $CDCl_3$

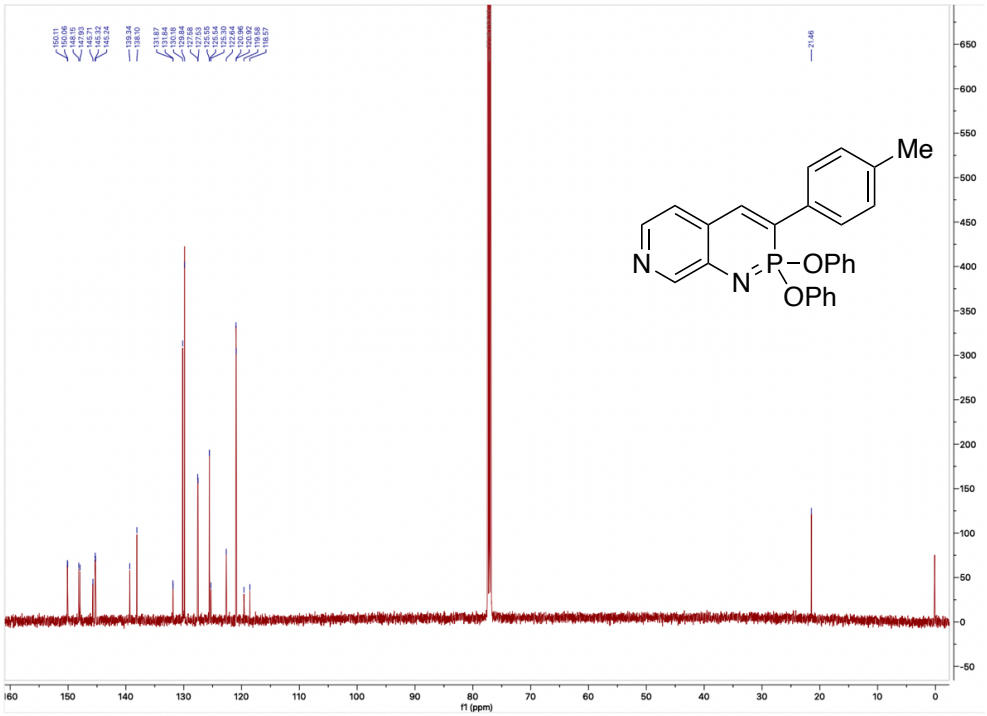

Figure B32 ^{13}C NMR Spectrum of **6b** in $CDCl_3$

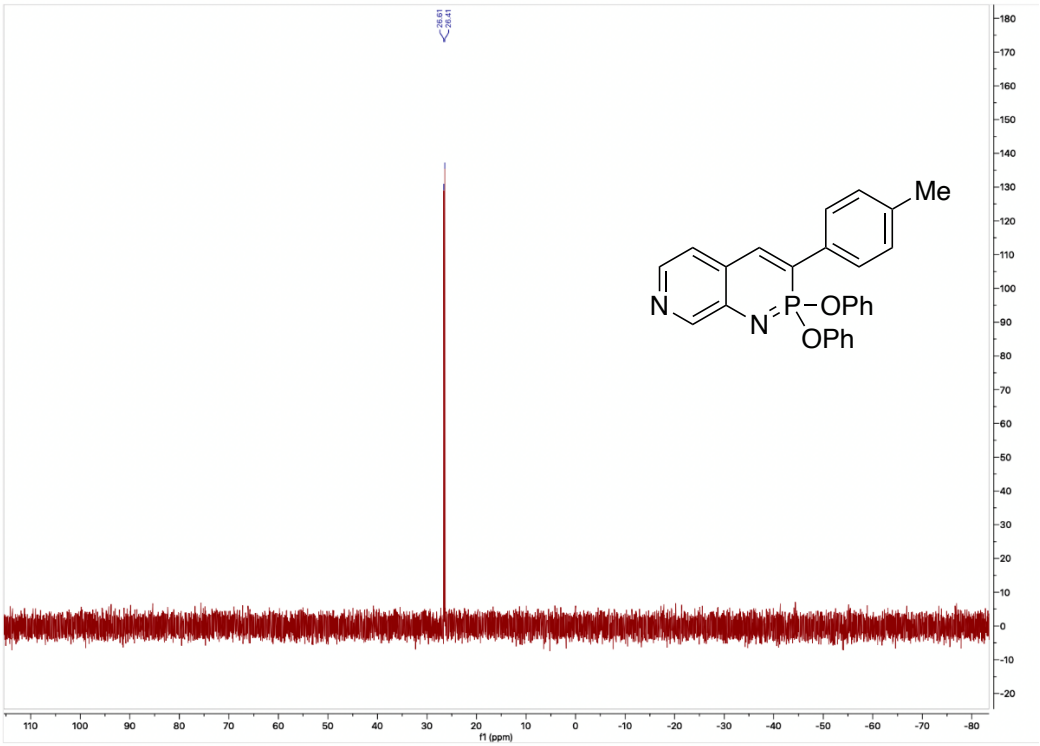

Figure B33 ^{31}P NMR Spectrum of **6b** in $CDCl_3$

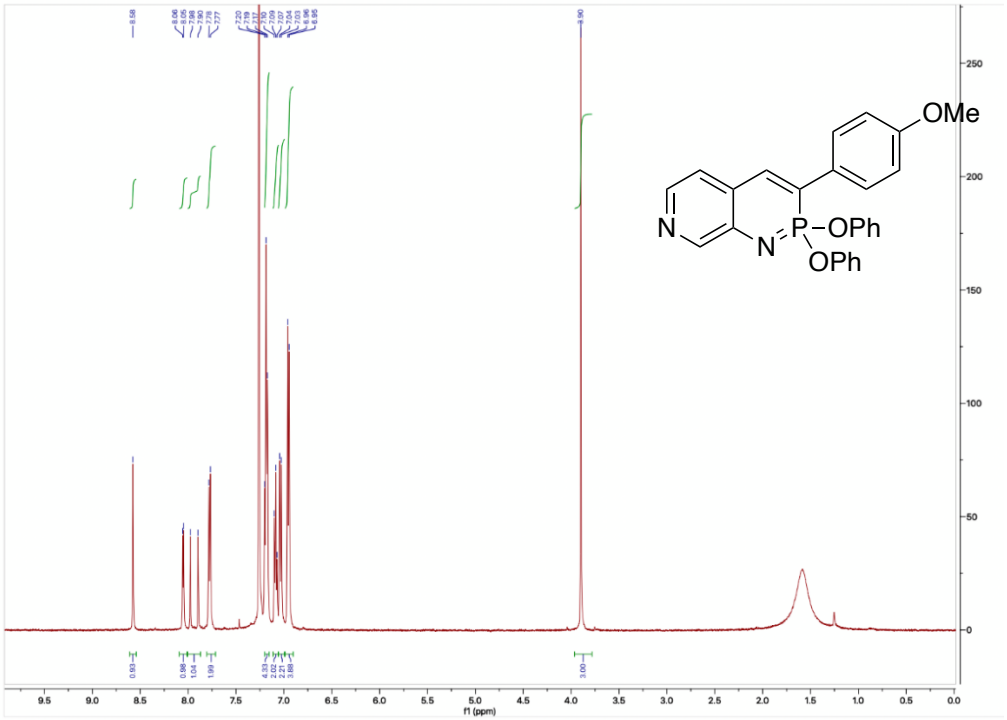

Figure B34 ^{1}H NMR Spectrum of **6c** in $CDCl_3$

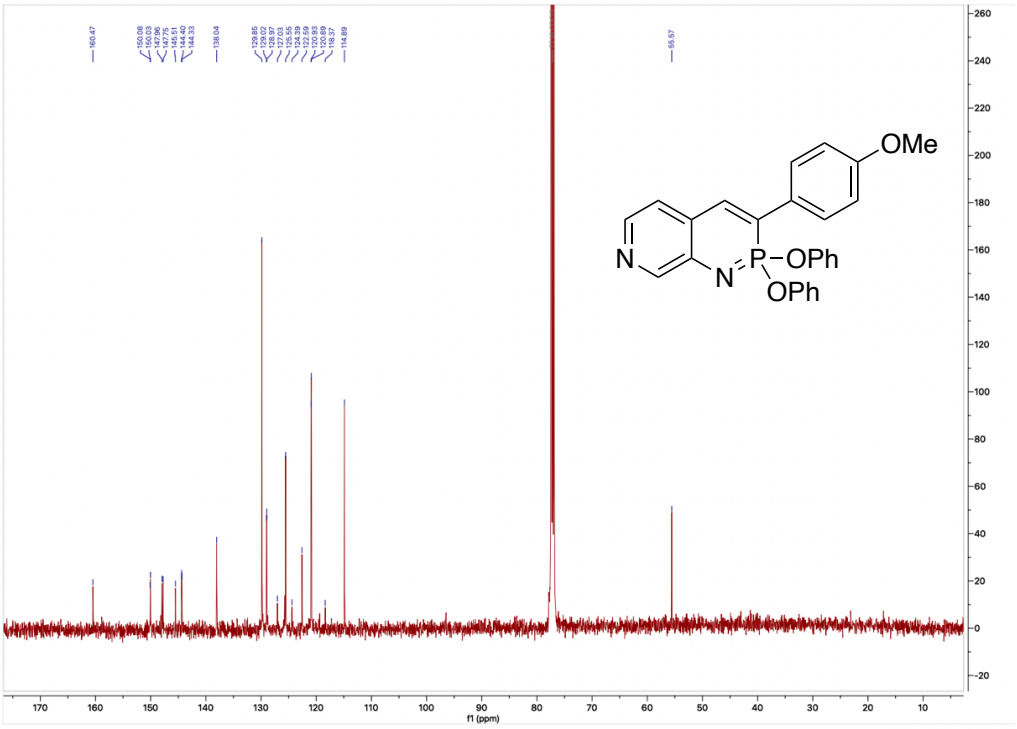

Figure B35 ^{13}C NMR Spectrum of **6c** in $CDCl_3$

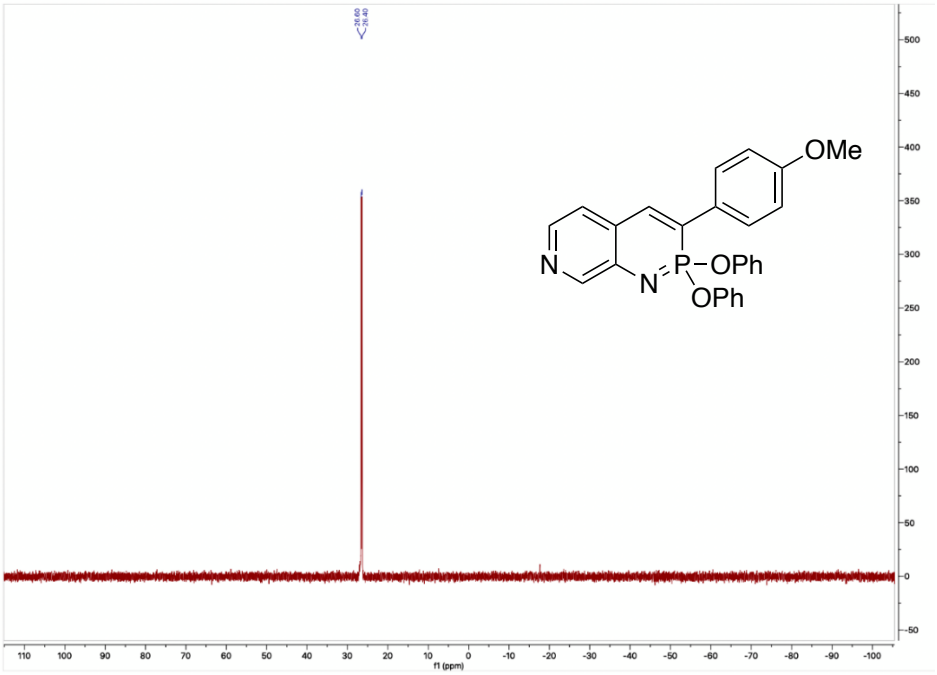

Figure B36 ^{31}P NMR Spectrum of **6c** in $CDCl_3$

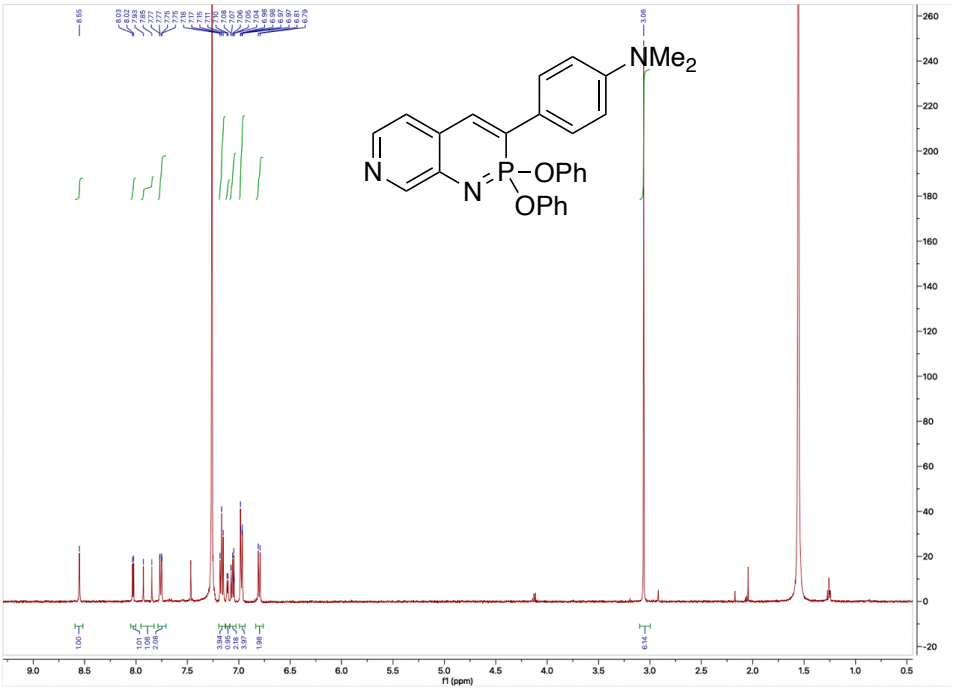

Figure B37 ^{1}H NMR Spectrum of **6d** in $CDCl_3$

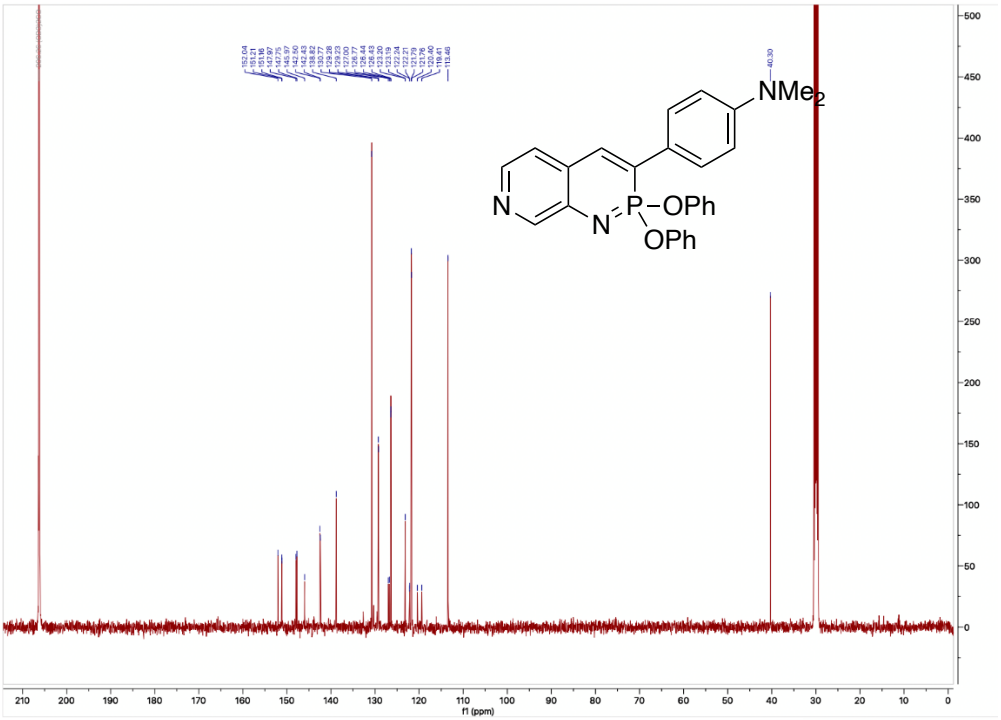

Figure B38 ^{13}C NMR Spectrum of **6d** in Acetone-d_6

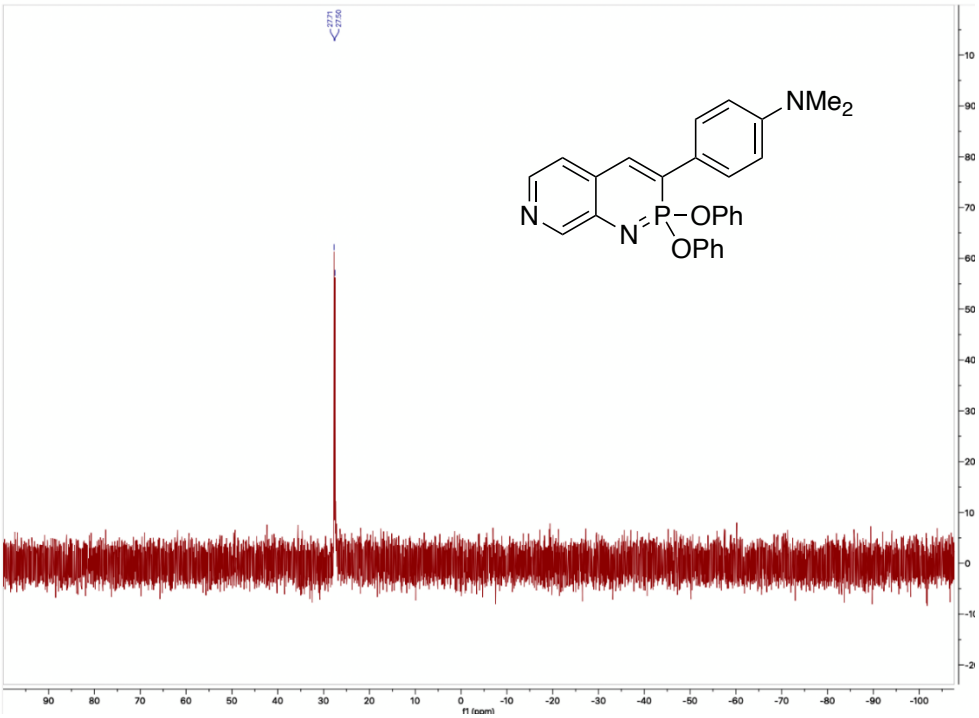

Figure B39 ^{31}P NMR Spectrum of **6d** in Acetone-d_6

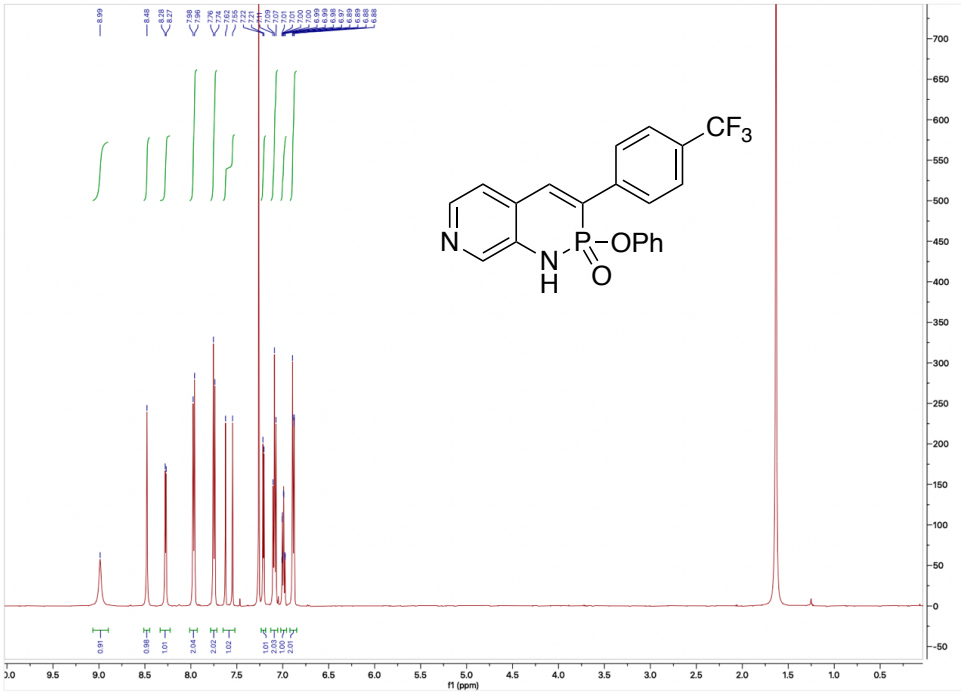

Figure B40 ^{1}H NMR Spectrum of **2a** in $CDCl_3$

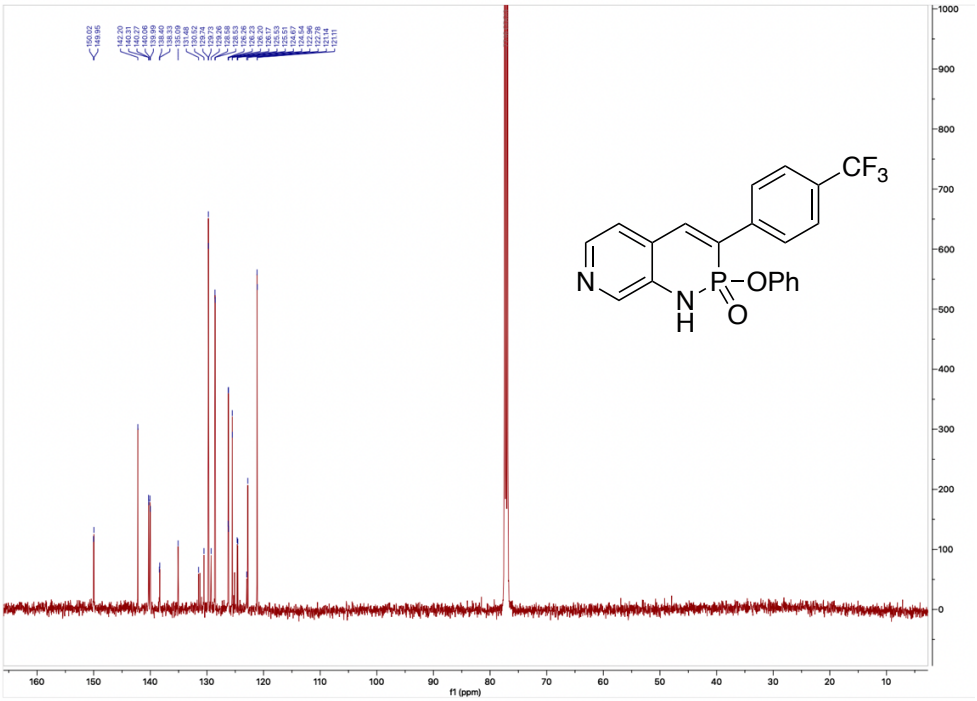

Figure B41 ^{13}C NMR Spectrum of **2a** in $CDCl_3$

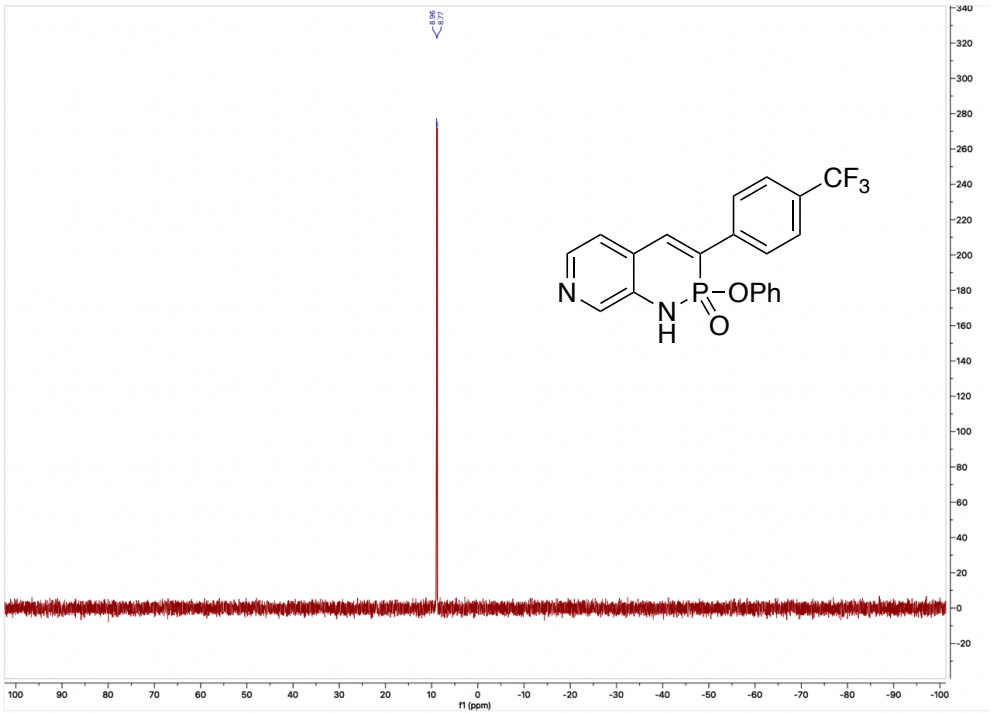

Figure B42 ^{31}P NMR Spectrum of **2a** in $CDCl_3$

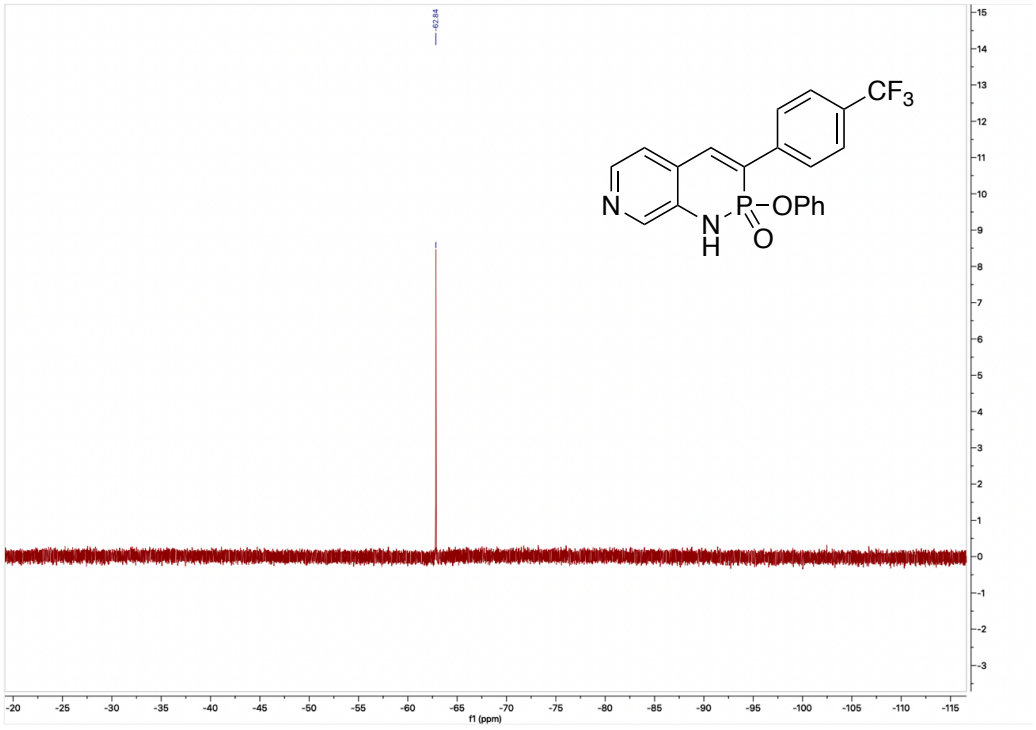

Figure B43 ^{19}F NMR Spectrum of **2a** in $CDCl_3$

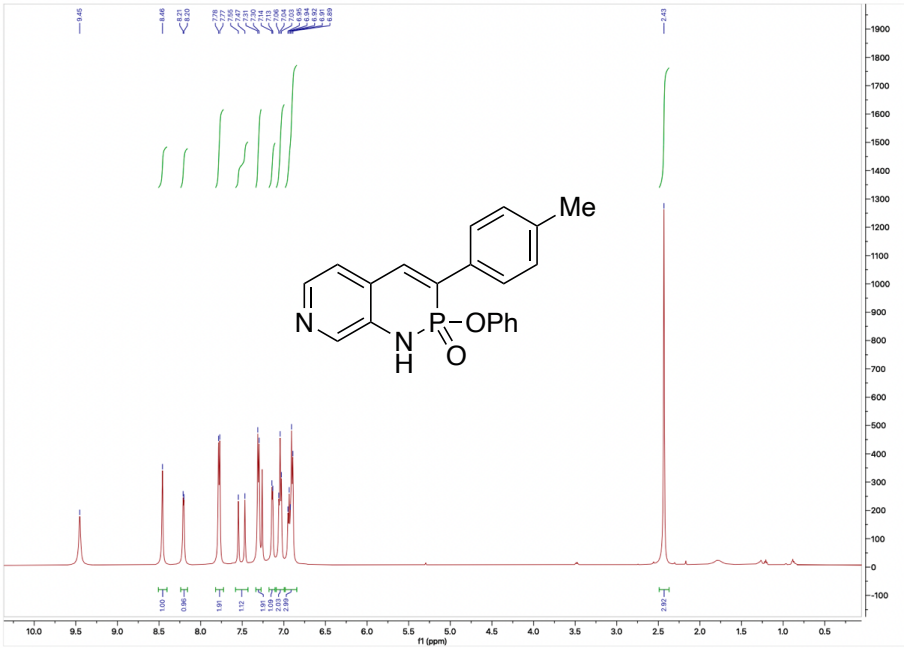

Figure B44 ^{1}H NMR Spectrum of **2b** in Acetone-d_6

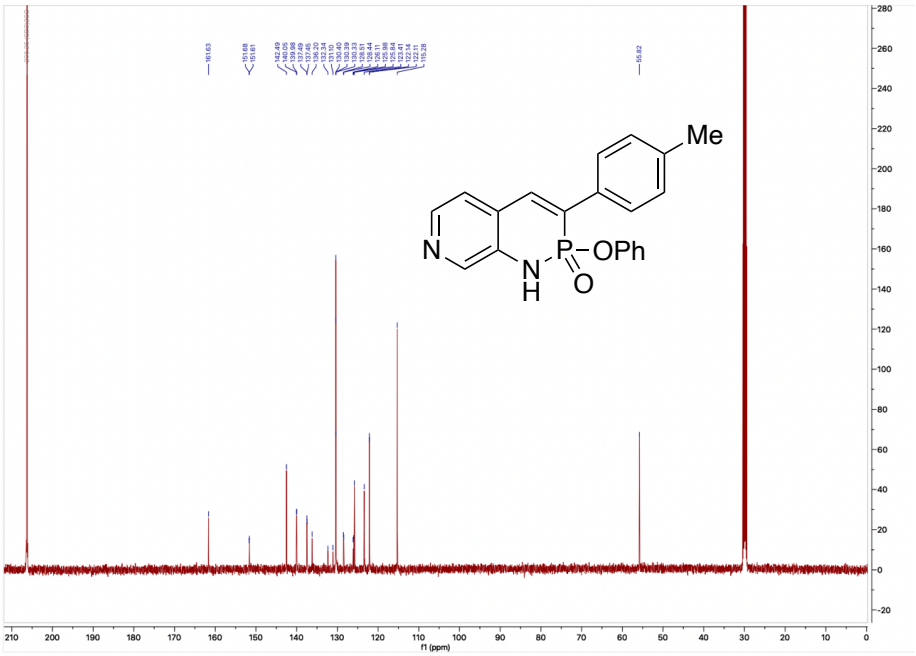

Figure B45 ^{13}C NMR Spectrum of **2b** in Acetone-d_6

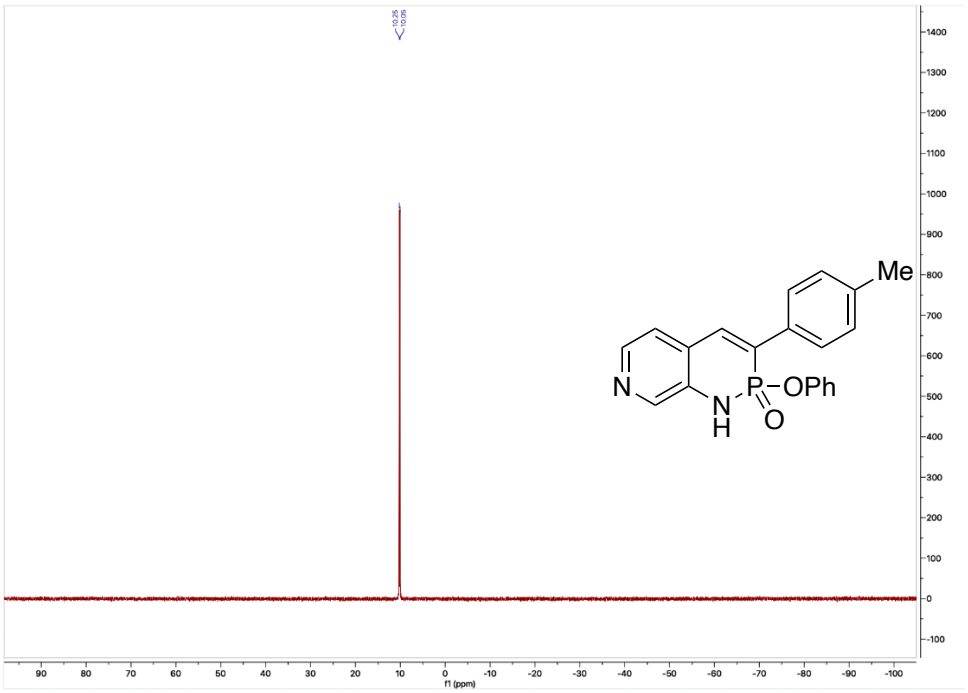

Figure B46 ^{31}P NMR Spectrum of **2b** in Acetone-d_6

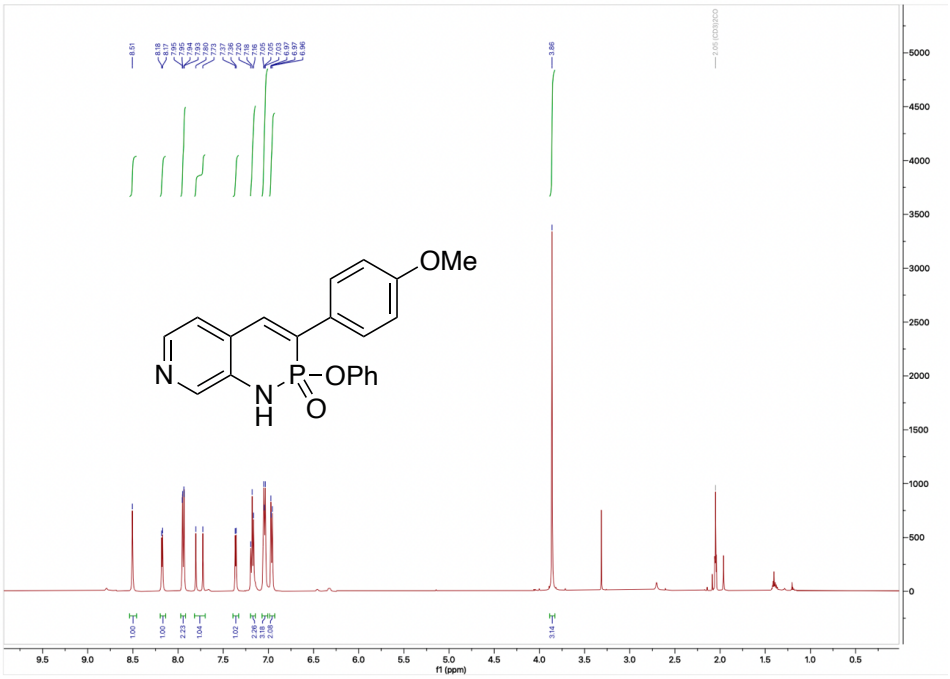

Figure B47 ^{1}H NMR Spectrum of **2c** in Acetone-d_6

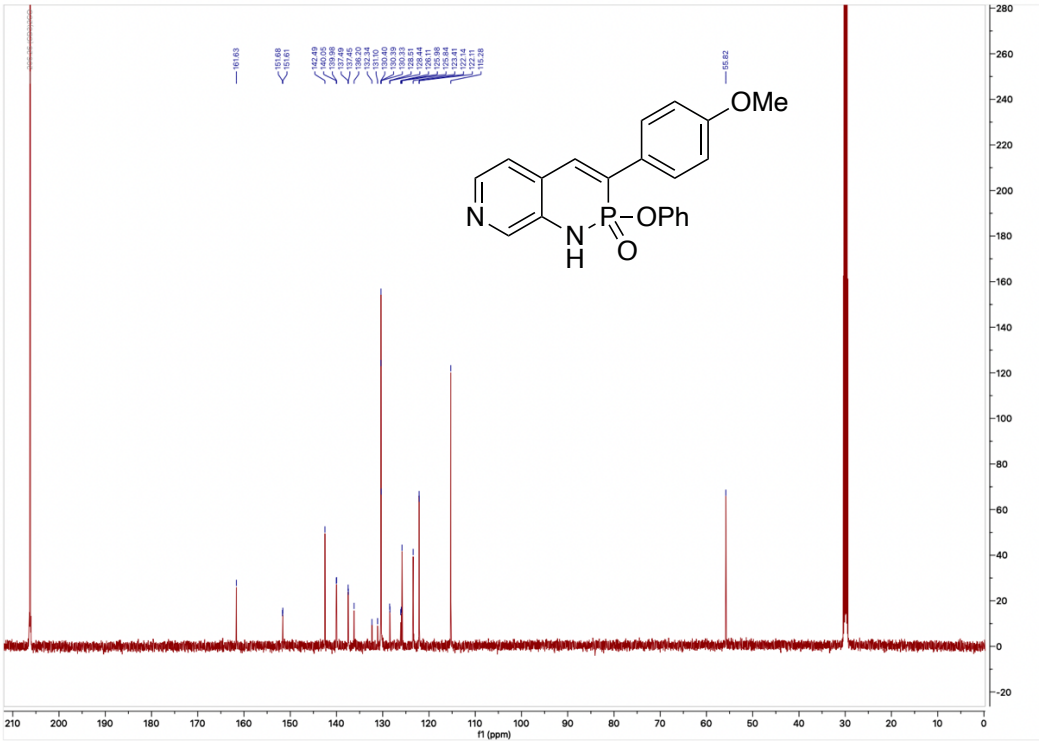

Figure B48 ^{13}C NMR Spectrum of **2c** in Acetone-d_6

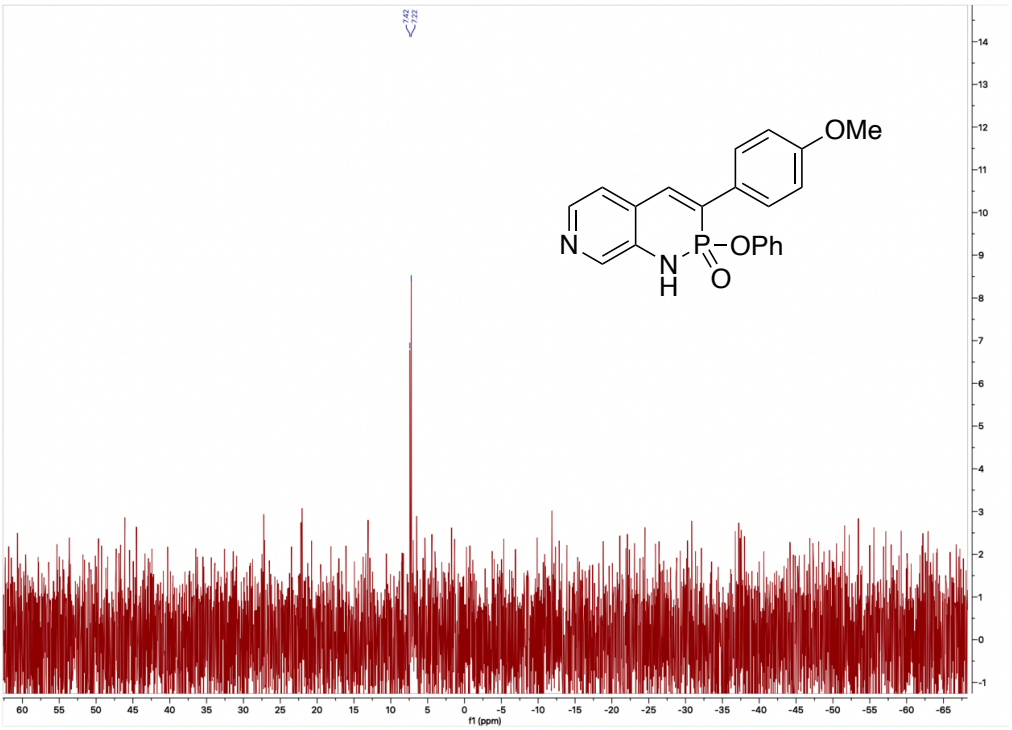

Figure B49 ^{31}P NMR Spectrum of **2c** in Acetone-d_6

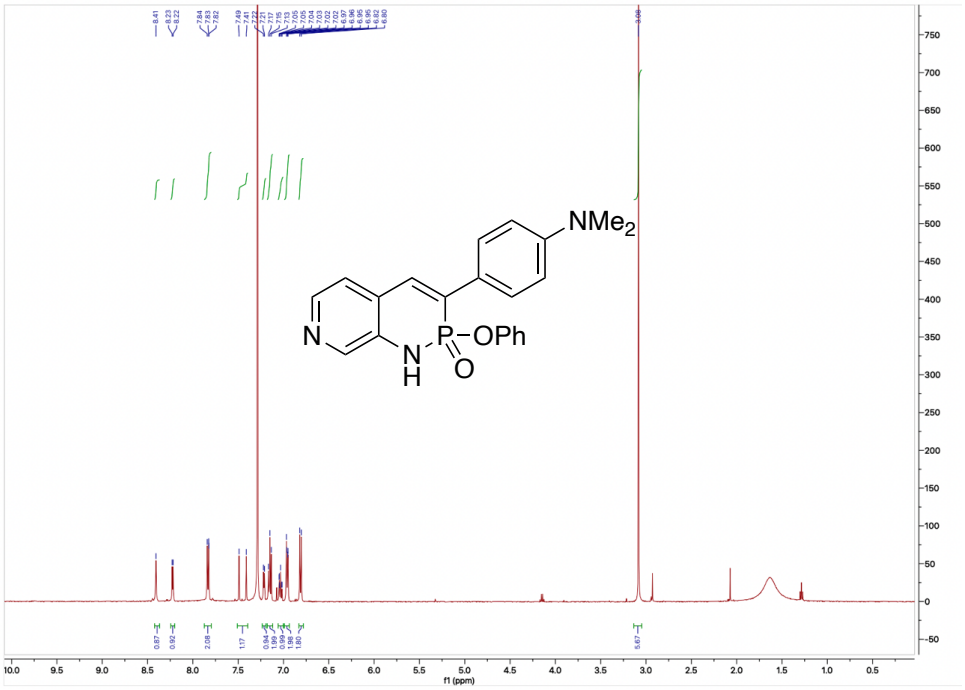

Figure B50 ^{1}H NMR Spectrum of **2d** in $CDCl_3$

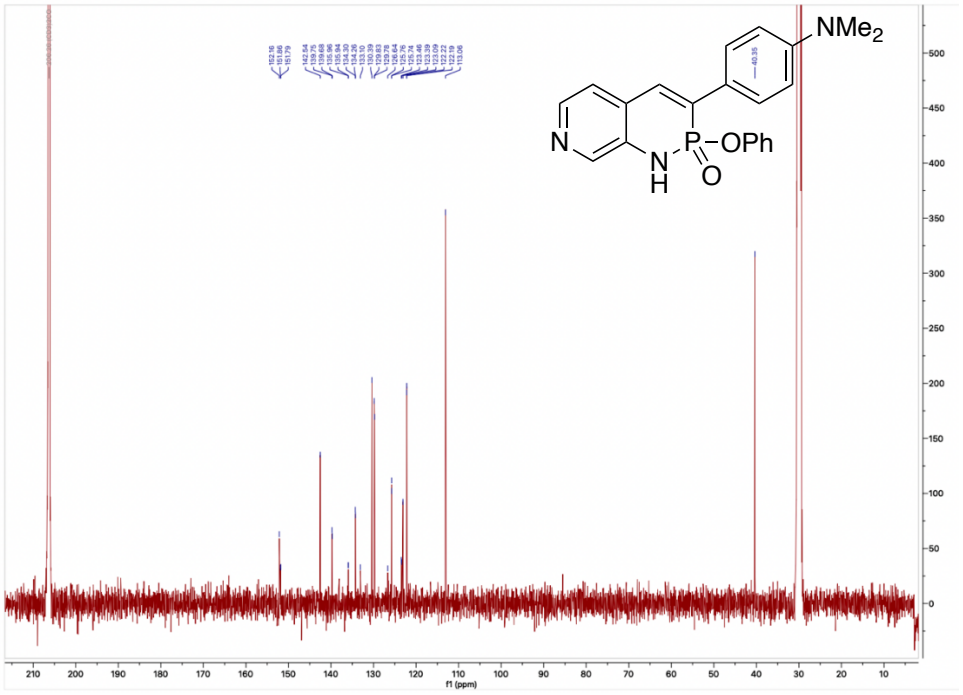

Figure B51 ^{13}C NMR Spectrum of **2d** in Acetone-d_6

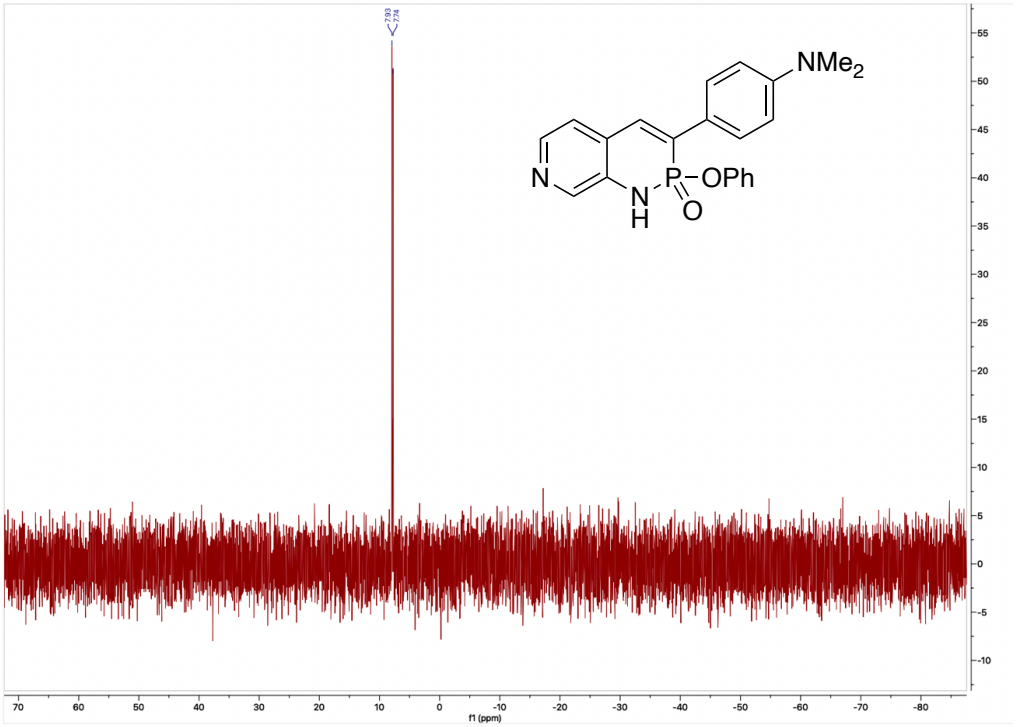

Figure B52 ^{31}P NMR Spectrum of **2d** in $CDCl_3$

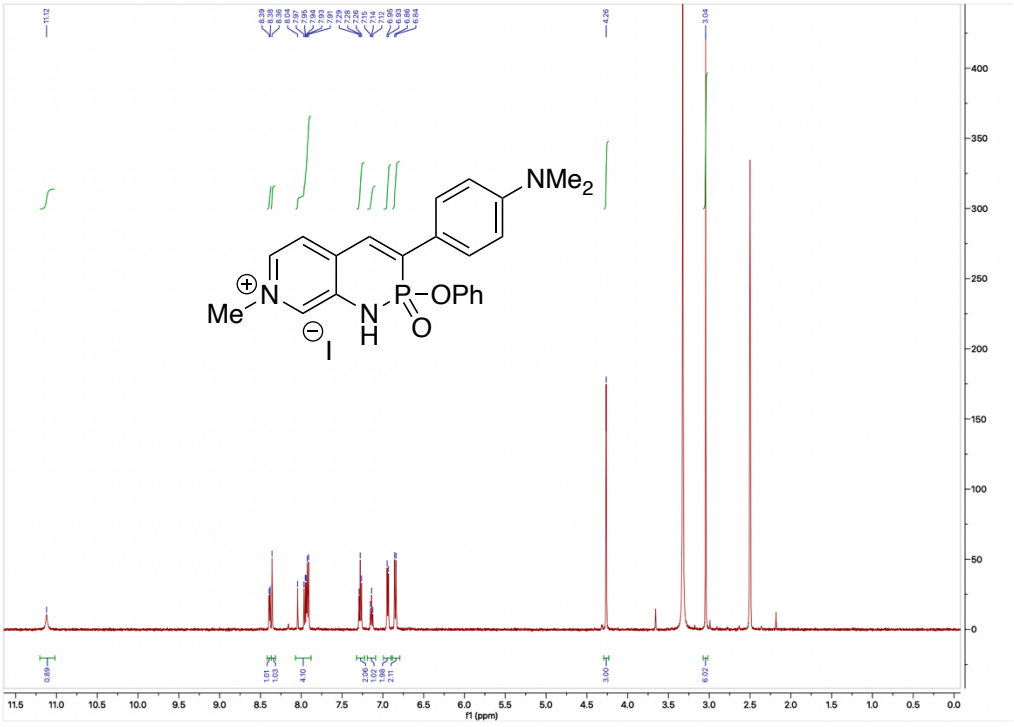

Figure B53 ^{1}H NMR Spectrum of **2d'** in DMSO-d_6

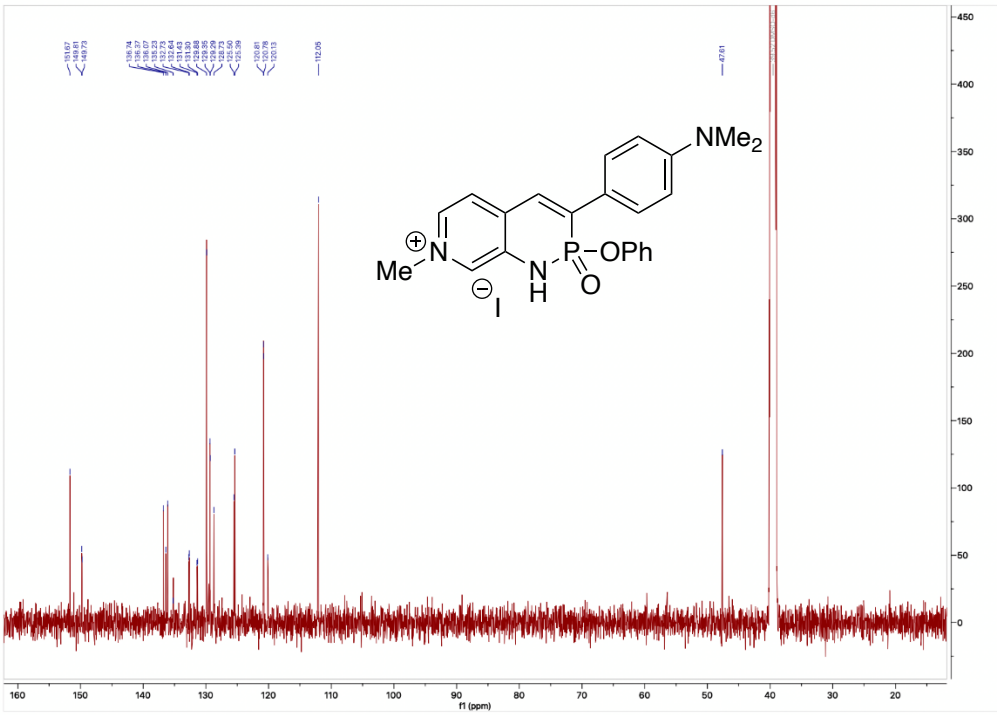

Figure B54 ^{13}C NMR Spectrum of **2d'** in DMSO-d_6

APPENDIX C

SUPPLEMENTARY INFORMATION FOR CHAPTER IV

Appendix C is the supplementary information for Chapter IV of this dissertation. It includes experimental details, experimental data, spectra, and computational details relevant to the content of Chapter IV.

General. Diffraction intensities for **2d** and **2e** were collected at 173 K on a Bruker Apex2 CCD diffractometer using MoKα radiation, λ= 0.71073 Å. Space groups were determined based on intensity statistics (**2d**) and systematic absences (**2e**). Absorption corrections were applied by SADABS.[1] Structures were solved by direct methods and Fourier techniques and refined on F^2 using full matrix least-squares procedures. All non-H atoms were refined with anisotropic thermal parameters. H atoms in both structures were refined in calculated positions in a rigid group model except the H atoms at the N atoms involved in forming H-bonds. These H atoms were found from the diffraction data and refined with isotropic thermal parameters. The standard N–H bond distance was used in the refinement as the target for corresponding bond length. In both structures the main molecules form dimer units via N–H···S H-bonds. Crystal structure of **2d** includes also solvent molecule CH_2Cl_2. Terminal Me-groups in **2e** are disordered over two positions in ratio 1:1. All calculations were performed by the Bruker SHELXL-2014 package.[2]

Crystallographic Data for **2d**: $C_{22}H_{17}Cl_2N_2PS$, M = 443.30, 0.24 x 0.18 x 0.12 mm, T = 173(2) K, Triclinic, space group *P*-1, *a* = 8.8716(14) Å, *b* = 10.6480(16) Å, *c* =

11.6935(18) Å, α = 83.063(2)°, β = 80.956(2)°, γ = 86.672(2)°, V = 1082.0(3) Å^3, Z = 2, D_c = 1.361 Mg m^{-3}, μ(Mo) = 0.481 mm^{-1}, F(000) = 456, $2\theta_{max}$ = 60.18°, 17797 reflections, 6236 independent reflections [R_{int} = 0.0291], R1 = 0.0454, wR2 = 0.1283 and GOF = 1.058 for 6236 reflections (257 parameters) with I>2σ(I), R1 = 0.0537, wR2 = 0.1354 and GOF = 1.060 for all reflections, max/min residual electron density +1.155/–0.652 eÅ^{-3}. CCDC 2034968.

Crystallographic Data for **2e**: $C_{25}H_{23}N_2PS$, M = 414.48, 0.23 x 0.23 x 0.11 mm, T = 173(2) K, Monoclinic, space group *C*2/*c*, *a* = 19.716(4) Å, *b* = 12.307(2) Å, *c* = 18.192(3) Å, β = 99.272(3)°, V = 4356.5(14) Å^3, Z = 8, D_c = 1.264 Mg m^{-3}, μ(Mo) = 0.236 mm^{-1}, F(000) = 1744, $2\theta_{max}$ = 60.042°, 24992 reflections, 6375 independent reflections [R_{int} = 0.0366], R1 = 0.0378, wR2 = 0.1027 and GOF = 1.020 for 6375 reflections (293 parameters) with I>2σ(I), R1 = 0.0450, wR2 = 0.1078 and GOF = 1.026 for all reflections, max/min residual electron density +0.458/ –0.256 eÅ^{-3}. CCDC 2034967.

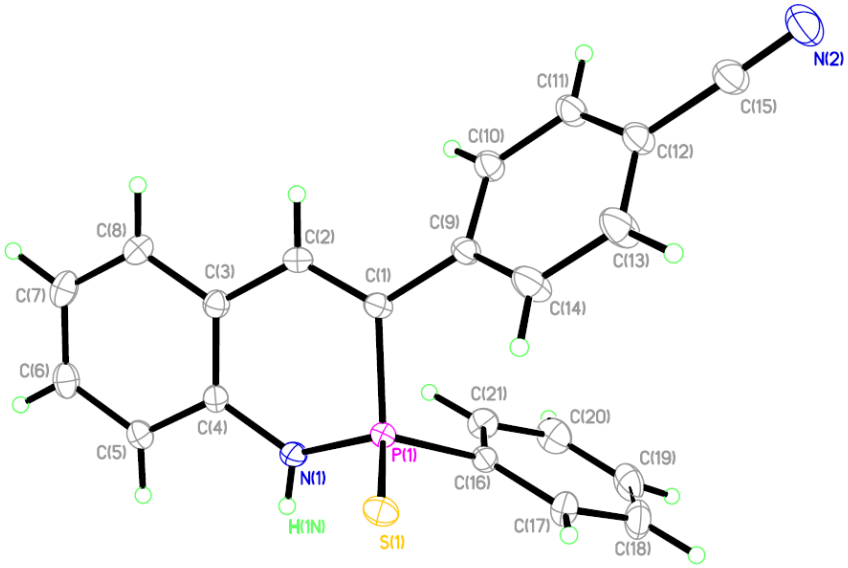

Figure C1. ORTEP drawing of thio-heterocycle **2d**; thermal ellipsoids drawn at 30% probability.

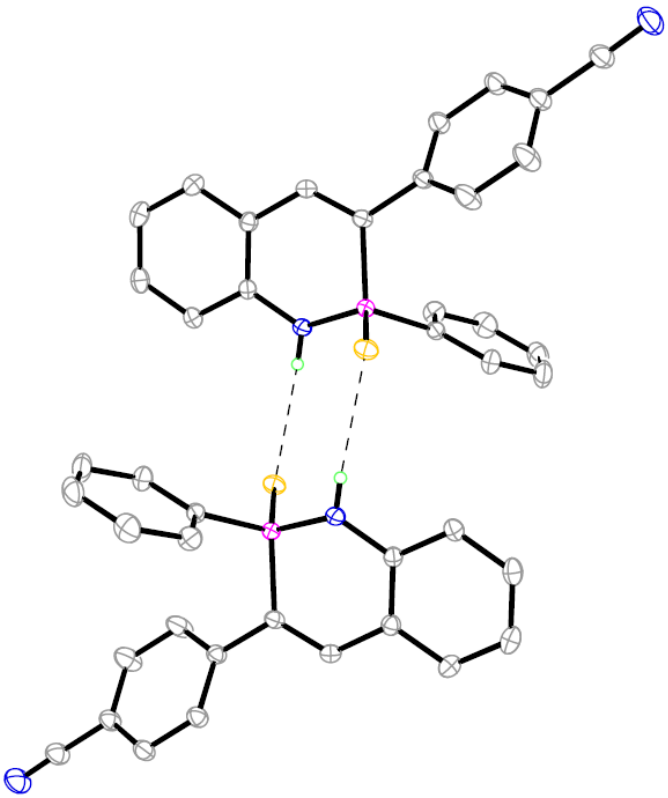

Figure C2. ORTEP drawing of the racemic dimer of thio-heterocycle **2d**; thermal ellipsoids drawn at 30% probability.

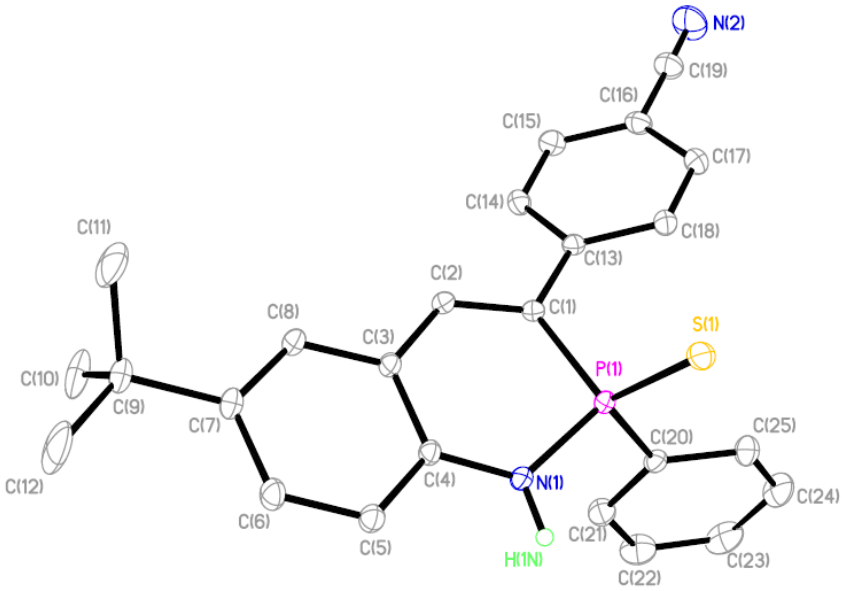

Figure C3. ORTEP drawing of thio-heterocycle **2e**; thermal ellipsoids drawn at 30% probability.

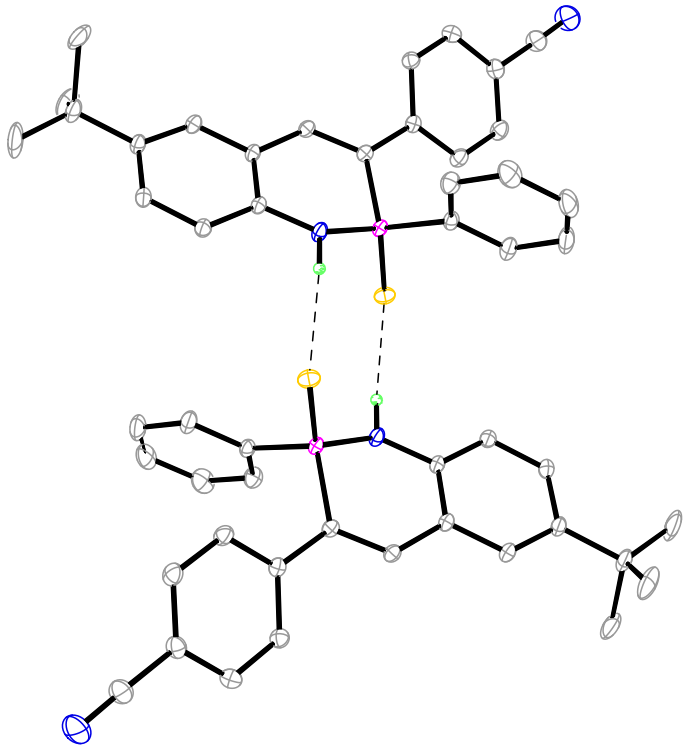

Figure C4. ORTEP drawing of the racemic dimer of thio-heterocycle **2e**; thermal ellipsoids drawn at 30% probability.

Comparison of the photophysical properties of 2c and 2e in $CHCl_3$ vs. MeCN

Table C1. Photophysical properties of heterocycles **2c** and **2e** in $CHCl_3$ and MeCN[a]

cmpd	solvent	λ_{abs} (nm)	λ_{em} (nm)	Stokes shift (nm)	Stokes shift (cm^{-1})
2c	MeCN	371	497	26	6834
	$CHCl_3$	373	492	19	6484
2e	MeCN	360	484	24	7116
	$CHCl_3$	350	470	20	7304

[a]All values collected using ca. 10^{-5} M solutions.

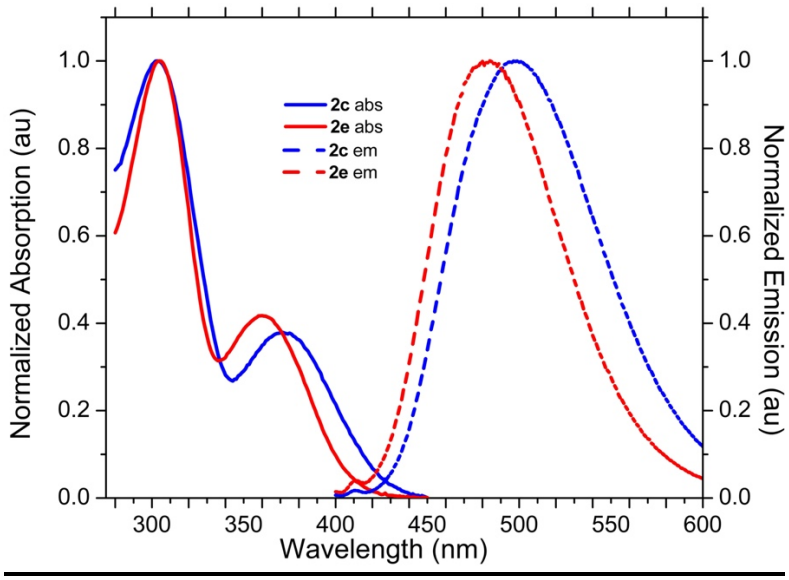

Figure C5. Stacked absorption and emission spectra of **2c** and **2e** in MeCN.

TD-DFT studies and coordinates for selected heterocycles 2

Ground state calculations:

The initial structures were optimized at the ground state using the functional PBE0[3,4] (25% full-range HF exchange) and TZVP basis set[5] as implemented in Gaussian 09.[6] In addition, all the ground state optimized structures were confirmed by frequency analysis and the number of imaginary frequencies was zero. TD-DFT vertical excitation calculations and geometry optimization of the first excited state (S_1) were performed at the same level of theory and the PCM solvation model[7,8] was used to account for the solvent effects of chloroform.

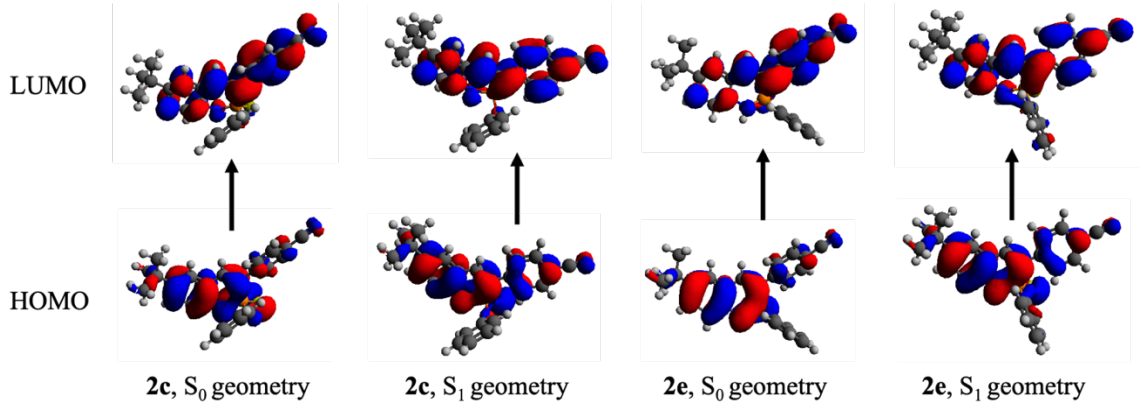

Figure C6. Frontier orbital plots (isovalue = 0.2) of heterocycles **2c** and **2e** in the optimized S_0 and S_1 structures calculated by DFT and TD-DFT methods at the PCM($CHCl_3$)-PBE0/TZVP level of theory, respectively.

Table S2: Calculated frontier orbitals and first excitation values for compounds **2c** and **2e**[a]

Compound	E_{HOMO}	E_{LUMO}	ΔE_{DFT}	S_0 to S_1 computed (nm), osc. strength

2c	–6.385	–2.995	3.390	366, 0.3008
2e	–6.266	–2.996	3.270	379, 0.2913

[a]Calculated at the PCM($CHCl_3$)-PBE0/TZVP level of theory; energy values reported in eV.

Ground state geometries

Cartesian coordinates for compound **2c**:

Zero-point correction = 0.421712 (Hartree/Particle)

Thermal correction to Energy = 0.449176

Thermal correction to Enthalpy = 0.450120

Thermal correction to Gibbs Free Energy = 0.361543

Sum of electronic and zero-point Energies = -1889.158422

Sum of electronic and thermal Energies = -1889.130957

Sum of electronic and thermal Enthalpies = -1889.130013

Sum of electronic and thermal Free Energies = -1889.218591

C	5.9109860000	-1.0127790000	1.1533730000
C	5.0355570000	-1.8264830000	0.1914770000
C	5.8782310000	-2.2674180000	-1.0123200000
C	4.5534540000	-3.0772420000	0.9234020000
C	3.8750230000	-0.9607620000	-0.2912030000
C	4.1298800000	0.2285300000	-0.9900630000
C	3.1157770000	1.0456670000	-1.4423340000
C	1.7816580000	0.7081810000	-1.2116480000

N	0.7623840000	1.5129150000	-1.6795590000
P	-0.9026400000	1.3908620000	-1.4009190000
C	-1.0061200000	-0.2540390000	-0.6674560000
C	-2.3262920000	-0.8359160000	-0.3580790000
C	-3.3835040000	-0.8088680000	-1.2726080000
C	-4.5954720000	-1.4010130000	-0.9689250000
C	-4.7803940000	-2.0320500000	0.2615900000
C	-6.0290760000	-2.6445490000	0.5766760000
N	-7.0368070000	-3.1420540000	0.8343530000
C	-3.7362490000	-2.0562460000	1.1881880000
C	-2.5300550000	-1.4590360000	0.8792290000
C	0.1312770000	-0.9026690000	-0.3258710000
O	-1.2645780000	2.4235910000	-0.1630650000
C	-0.7323110000	2.3172380000	1.1083410000
C	0.5478280000	2.7796580000	1.3788630000
C	1.0316030000	2.7193560000	2.6783080000
C	0.2401010000	2.2157260000	3.7010410000
C	-1.0455880000	1.7721210000	3.4204710000
C	-1.5373290000	1.8222950000	2.1245000000
S	-1.9364900000	1.9272820000	-2.9483300000
C	1.4890200000	-0.4795060000	-0.5275740000
C	2.5481010000	-1.2863390000	-0.0827700000
H	6.7510340000	-1.6187540000	1.5047120000

H	5.3363510000	-0.6881710000	2.0245830000
H	6.3226080000	-0.1225060000	0.6724890000
H	6.7174460000	-2.8853170000	-0.6803300000
H	6.2898970000	-1.4132420000	-1.5546170000
H	5.2798940000	-2.8533350000	-1.7145290000
H	5.4155870000	-3.6633620000	1.2506640000
H	3.9468950000	-3.7180320000	0.2778810000
H	3.9686850000	-2.8280810000	1.8129310000
H	5.1535950000	0.5278980000	-1.1865150000
H	3.3519020000	1.9591990000	-1.9789680000
H	1.0148430000	2.2389420000	-2.3353090000
H	-3.2475000000	-0.3279230000	-2.2329560000
H	-5.4050740000	-1.3814320000	-1.6884960000
H	-3.8824770000	-2.5329880000	2.1500590000
H	-1.7361450000	-1.4493370000	1.6170950000
H	0.0155770000	-1.8839840000	0.1309170000
H	1.1504390000	3.1905500000	0.5785580000
H	2.0315340000	3.0802630000	2.8916370000
H	0.6203960000	2.1775430000	4.7153260000
H	-1.6762230000	1.3921060000	4.2166050000
H	-2.5419540000	1.4919570000	1.8890350000
H	2.2871050000	-2.1993170000	0.4395920000

Cartesian coordinates for compound **2e**:

Zero-point correction = 0.417734 (Hartree/Particle)

Thermal correction to Energy = 0.444242

Thermal correction to Enthalpy = 0.445186

Thermal correction to Gibbs Free Energy = 0.359416

Sum of electronic and zero-point Energies = -1813.978974

Sum of electronic and thermal Energies = -1813.952466

Sum of electronic and thermal Enthalpies = -1813.951522

Sum of electronic and thermal Free Energies = -1814.037292

C	-5.5134060000	-2.5541420000	-0.3364810000
C	-5.7067050000	-1.0403170000	-0.2763330000
C	-6.4388910000	-0.5979280000	-1.5498110000
C	-6.5737670000	-0.7140440000	0.9466330000
C	-4.3789170000	-0.2953860000	-0.1682330000
C	-4.3630320000	1.1053570000	-0.1094380000
C	-3.1889360000	1.8214890000	-0.0055380000
C	-1.9601230000	1.1636360000	0.0437700000
N	-0.7727910000	1.8749150000	0.0828850000
P	0.6771600000	1.2807940000	0.7773640000
C	0.5353370000	-0.4516120000	0.2524370000
C	1.7461860000	-1.2836930000	0.1754320000
C	2.7880400000	-1.1676940000	1.1022840000

C	3.9099890000	-1.9690870000	1.0104470000
C	4.0192120000	-2.9096580000	-0.0150450000
C	5.1762550000	-3.7369800000	-0.1124530000
N	6.1114950000	-4.4067090000	-0.1932350000
C	2.9901670000	-3.0313820000	-0.9504710000
C	1.8753710000	-2.2217880000	-0.8555390000
C	-0.6930050000	-0.9575440000	0.0037130000
C	1.9441970000	2.0719940000	-0.2697400000
C	3.0220780000	2.7235510000	0.3176920000
C	3.9902660000	3.3150210000	-0.4819300000
C	3.8826180000	3.2541400000	-1.8639200000
C	2.8048500000	2.6030560000	-2.4522650000
C	1.8349930000	2.0117300000	-1.6584450000
S	0.9329160000	1.5958390000	2.6935360000
C	-1.9389530000	-0.2382240000	-0.0130420000
C	-3.1527770000	-0.9332340000	-0.1209270000
H	-6.4873560000	-3.0434320000	-0.4146000000
H	-5.0240540000	-2.9378290000	0.5626400000
H	-4.9238130000	-2.8545050000	-1.2068760000
H	-7.3959390000	-1.1204100000	-1.6368640000
H	-5.8453570000	-0.8225280000	-2.4397250000
H	-6.6457810000	0.4746140000	-1.5471510000
H	-7.5317180000	-1.2381960000	0.8821530000

H	-6.7845460000	0.3552260000	1.0203620000
H	-6.0773920000	-1.0217260000	1.8703510000
H	-5.2969050000	1.6559260000	-0.1408660000
H	-3.2171070000	2.9057080000	0.0404230000
H	-0.8792140000	2.8773600000	0.1634100000
H	2.7009890000	-0.4586020000	1.9178120000
H	4.7060270000	-1.8767210000	1.7395250000
H	3.0790830000	-3.7505850000	-1.7558930000
H	1.0983310000	-2.2967700000	-1.6076070000
H	-0.7640590000	-2.0266980000	-0.1886550000
H	3.0856060000	2.7640590000	1.4001820000
H	4.8301430000	3.8244290000	-0.0231240000
H	4.6408550000	3.7153430000	-2.4871630000
H	2.7207010000	2.5567080000	-3.5322540000
H	0.9900340000	1.5072400000	-2.1143230000
H	-3.0997850000	-2.0149650000	-0.1631400000

Excited state geometries

Cartesian coordinates for compound **2c**:

C	-6.0817380000	-0.6876210000	-1.3217830000
C	-5.1841790000	-1.7042300000	-0.5995640000
C	-5.9842810000	-2.3765590000	0.5264430000
C	-4.7676490000	-2.7777690000	-1.6023920000

C	-3.9939660000	-0.9738650000	0.0026500000
C	-4.2163960000	0.0404470000	0.9624980000
C	-3.1623760000	0.7246390000	1.5238190000
C	-1.8476450000	0.4407970000	1.1410920000
N	-0.8143850000	1.1775720000	1.6479910000
P	0.8565340000	0.8901360000	1.4861420000
C	0.9519070000	-0.4693090000	0.3531570000
C	2.2395580000	-1.0185130000	0.0618810000
C	3.4524530000	-0.3454340000	0.3753850000
C	4.6791450000	-0.8912070000	0.0895890000
C	4.7744910000	-2.1428310000	-0.5450510000
C	6.0350380000	-2.7020610000	-0.8532660000
N	7.0678480000	-3.1614550000	-1.1049920000
C	3.5879890000	-2.8264390000	-0.8714610000
C	2.3639850000	-2.2827880000	-0.5802090000
C	-0.2558430000	-0.9713650000	-0.1610030000
O	1.4310340000	2.2723410000	0.8177200000
C	1.0092160000	2.7149340000	-0.4369120000
C	0.0040700000	3.6666870000	-0.5014020000
C	-0.3790000000	4.1591260000	-1.7414810000
C	0.2402670000	3.7022200000	-2.8976240000
C	1.2494360000	2.7520500000	-2.8130240000
C	1.6435280000	2.2527040000	-1.5788190000

S	1.6567120000	0.7221410000	3.2698870000
C	-1.5725120000	-0.6010580000	0.2002740000
C	-2.6833290000	-1.2646170000	-0.3491330000
H	-6.9462250000	-1.2003300000	-1.7527470000
H	-5.5388830000	-0.1936700000	-2.1314950000
H	-6.4536410000	0.0825540000	-0.6431070000
H	-6.8462720000	-2.8999350000	0.1036170000
H	-6.3574170000	-1.6515220000	1.2525220000
H	-5.3698920000	-3.1059700000	1.0600470000
H	-5.6608620000	-3.2655470000	-1.9994860000
H	-4.1486190000	-3.5499100000	-1.1384630000
H	-4.2194490000	-2.3546800000	-2.4480110000
H	-5.2247590000	0.2909860000	1.2674530000
H	-3.3427670000	1.5071100000	2.2539420000
H	-1.0504800000	1.8715370000	2.3484210000
H	3.4318520000	0.6350500000	0.8359850000
H	5.5819520000	-0.3479400000	0.3424570000
H	3.6464840000	-3.7978100000	-1.3489130000
H	1.4780250000	-2.8569780000	-0.8183230000
H	-0.1855550000	-1.7558450000	-0.9055440000
H	-0.4596600000	4.0215190000	0.4112480000
H	-1.1611610000	4.9073520000	-1.8007000000
H	-0.0604840000	4.0900740000	-3.8640070000

H	1.7411830000	2.3977600000	-3.7117600000
H	2.4356880000	1.5179920000	-1.4992750000
H	-2.4799650000	-2.0472510000	-1.0689210000

Cartesian coordinates for compound **2e**:

C	-5.2454010000	-2.5083080000	-1.2165510000
C	-5.5172560000	-1.2050930000	-0.4686420000
C	-6.3164670000	-0.2728020000	-1.3922770000
C	-6.3575390000	-1.5261800000	0.7770540000
C	-4.2408030000	-0.5011010000	-0.0376460000
C	-4.3272730000	0.7241320000	0.6625370000
C	-3.1919690000	1.3923610000	1.0550970000
C	-1.9217980000	0.8739350000	0.7653650000
N	-0.8084620000	1.5748220000	1.1024290000
P	0.8466420000	1.1241470000	0.9314330000
C	0.7323760000	-0.5223570000	0.2341720000
C	1.9362480000	-1.2799130000	0.0910280000
C	3.2283240000	-0.6954830000	0.1699200000
C	4.3716320000	-1.4425130000	0.0338080000
C	4.2961200000	-2.8266270000	-0.2073050000
C	5.4701920000	-3.5968550000	-0.3648760000
N	6.4323650000	-4.2288720000	-0.4921100000
C	3.0269420000	-3.4290720000	-0.2941030000

C	1.8868680000	-2.6811520000	-0.1515210000
C	-0.5269840000	-0.9798410000	-0.1660090000
C	1.4745330000	2.2877820000	-0.3153180000
C	2.3029150000	3.3387390000	0.0697510000
C	2.7833580000	4.2216160000	-0.8875860000
C	2.4348640000	4.0599080000	-2.2214390000
C	1.6097020000	3.0069500000	-2.6054300000
C	1.1308250000	2.1177040000	-1.6585070000
S	1.6803210000	1.3182690000	2.7125620000
C	-1.7893170000	-0.3845480000	0.0941930000
C	-2.9764120000	-1.0163050000	-0.3019070000
H	-6.1960000000	-2.9642360000	-1.5026280000
H	-4.7076540000	-3.2295580000	-0.5959740000
H	-4.6712120000	-2.3407450000	-2.1313620000
H	-7.2406580000	-0.7674230000	-1.7035190000
H	-5.7428770000	-0.0256730000	-2.2890830000
H	-6.5881590000	0.6603930000	-0.8948850000
H	-7.2814370000	-2.0284710000	0.4773370000
H	-6.6311290000	-0.6248960000	1.3291730000
H	-5.8133400000	-2.1880330000	1.4552500000
H	-5.2941490000	1.1526000000	0.8948110000
H	-3.2655560000	2.3384680000	1.5809250000
H	-0.9461540000	2.4579950000	1.5809120000

H	3.3358220000	0.3725710000	0.3171240000
H	5.3406600000	-0.9617140000	0.0972110000
H	2.9540470000	-4.4971370000	-0.4642090000
H	0.9304800000	-3.1872320000	-0.1872400000
H	-0.5639620000	-1.9149580000	-0.7140930000
H	2.5735100000	3.4529730000	1.1141680000
H	3.4314280000	5.0375120000	-0.5884830000
H	2.8119400000	4.7503830000	-2.9673750000
H	1.3464420000	2.8745870000	-3.6486270000
H	0.5035180000	1.2861080000	-1.9622240000
H	-2.8797190000	-1.9595250000	-0.8247590000

4. References

1. Sheldrick, G. M. *Bruker/Siemens Area Detector Absorption Correction Program*, Bruker AXS, Madison, WI, 1998.

2. Sheldrick, G. M.; Crystal structure refinement with SHELXL. *Acta Cryst. C* **2015**, *71*, 3–8.

3. Adamo, C.; Barone, V. Toward reliable density functional methods without adjustable parameters: the PBE0 model. *J. Chem. Phys.* **1999**, *110*, 6158–6169.

4. Bremond, E.; Savarese, M.; Su, N. Q.; Perez-Jimenez, A. J.; Xu, X.; Sancho-Garcia, J. C.; Adamo, C. Benchmarking Density Functionals on Structural Parameters of Small-/Medium-Sized Organic Molecules. *J. Chem. Theory Comput.* **2016**, *12*, 459–465.

5. Schuafer, A.; Huber, C.; Ahlrichs, R. Fully optimized contracted Gaussian basissets of triple zeta valence quality for atoms Li to Kr. *J. Chem. Phys.* **1994**, *100*, 5829–5835.

6. Gaussian 16, Revision C.01, Frisch, M. J.; Trucks, G. W.; Schlegel, H. B.; Scuseria, G. E.; Robb, M. A.; Cheeseman, J. R.; Scalmani, G.; Barone, V.; Petersson, G. A.; Nakatsuji, H.; Li, X.; Caricato, M.; Marenich, A. V.; Bloino, J.; Janesko, B. G.; Gomperts, R.; Mennucci, B.; Hratchian, H. P.; Ortiz, J. V.; Izmaylov, A. F.; Sonnenberg, J. L.; Williams-Young, D.; Ding, F.; Lipparini, F.; Egidi, F.; Goings, J.; Peng, B.; Petrone, A.; Henderson, T.; Ranasinghe, D.; Zakrzewski, V. G.; Gao, J.; Rega, N.; Zheng, G.; Liang, W.; Hada, M.; Ehara, M.; Toyota, K.; Fukuda, R.; Hasegawa, J.; Ishida, M.; Nakajima, T.; Honda, Y.; Kitao, O.; Nakai, H.; Vreven, T.; Throssell, K.; Montgomery, J. A., Jr.; Peralta, J. E.; Ogliaro, F.; Bearpark, M. J.; Heyd, J. J.; Brothers, E. N.; Kudin, K. N.; Staroverov, V. N.;

Keith, T. A.; Kobayashi, R.; Normand, J.; Raghavachari, K.; Rendell, A. P.; Burant, J. C.; Iyengar, S. S.; Tomasi, J.; Cossi, M.; Millam, J. M.; Klene, M.; Adamo, C.; Cammi, R.; Ochterski, J. W.; Martin, R. L.; Morokuma, K.; Farkas, O.; Foresman, J. B.; Fox, D. J. Gaussian, Inc., Wallingford CT, 2016.

7. Miertuš, S.; Scrocco, E.; Tomasi, J.; Electrostatic interaction of a solute with a continuum. A direct utilization of AB initio molecular potentials for the prevision of solvent effects. *J. Chem. Phys.* **1981**, *55*, 117–129.

8. Barone, V.; Cossi, M.; Tomasi, J. Geometry optimization of molecular structure in solution by the polarizable continuum model. *J. Comput. Chem.* **1998**, *19*, 404–417.

Copies of NMR Spectra

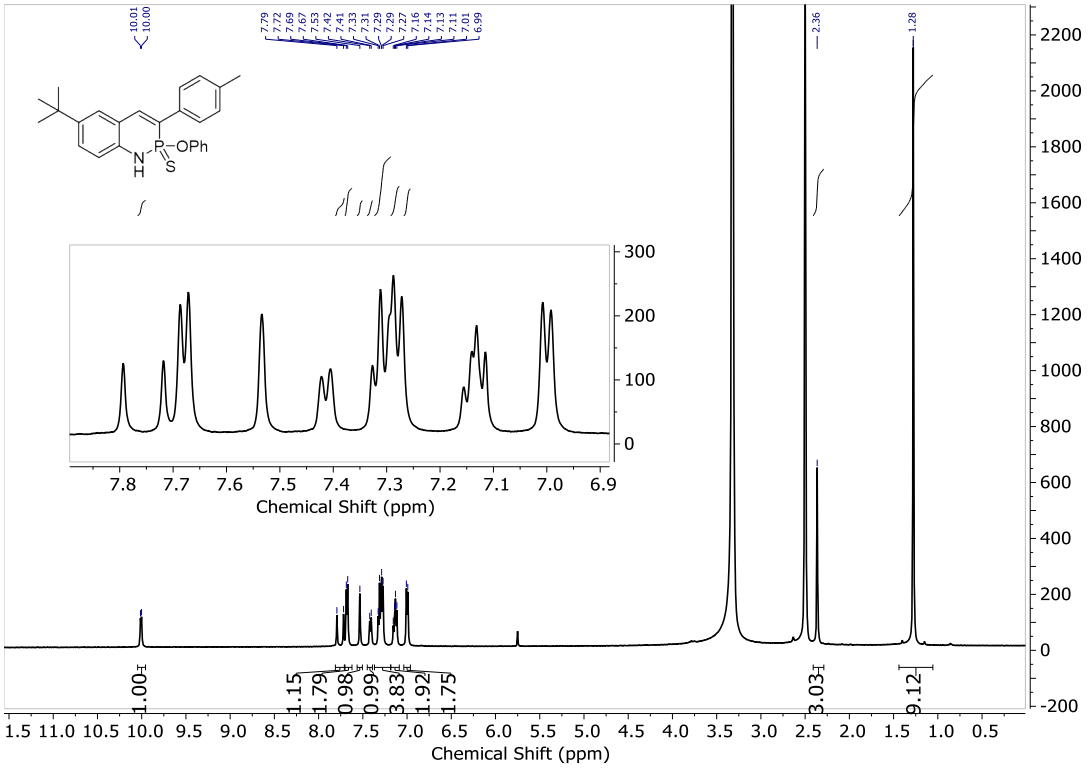

Figure C7 ^{1}H NMR spectrum of **2a** in DMSO-d_6.

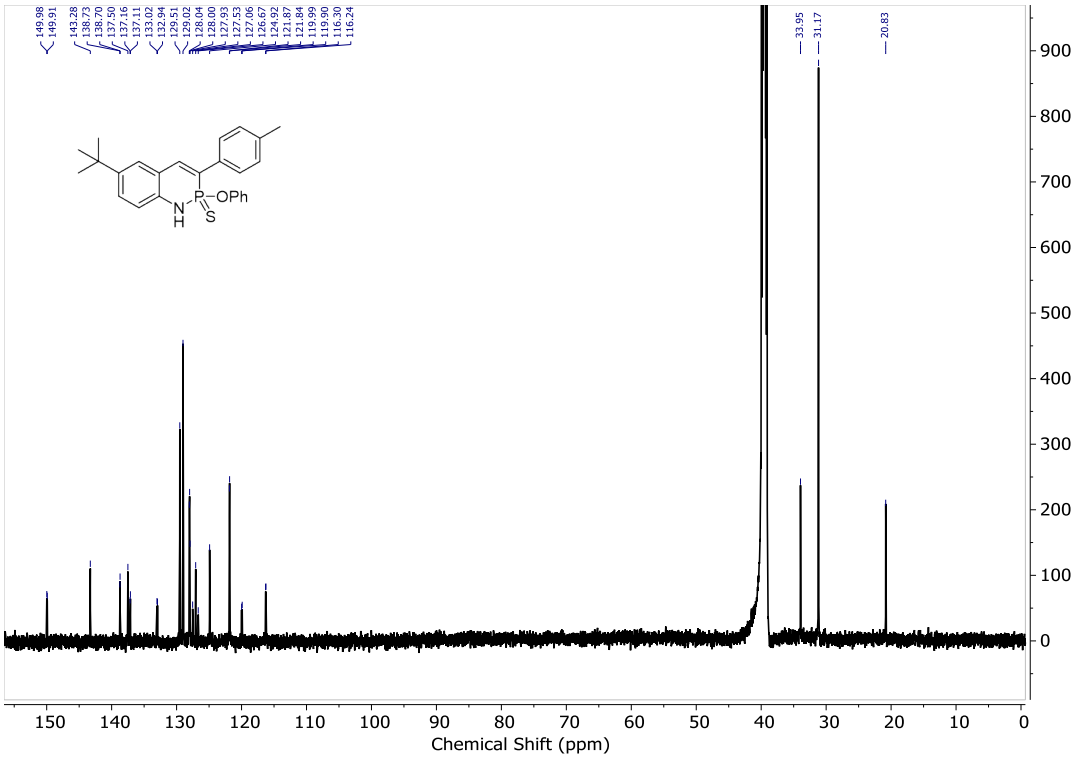

Figure C8 ^{13}C NMR spectrum of **2a** in DMSO-d_6.

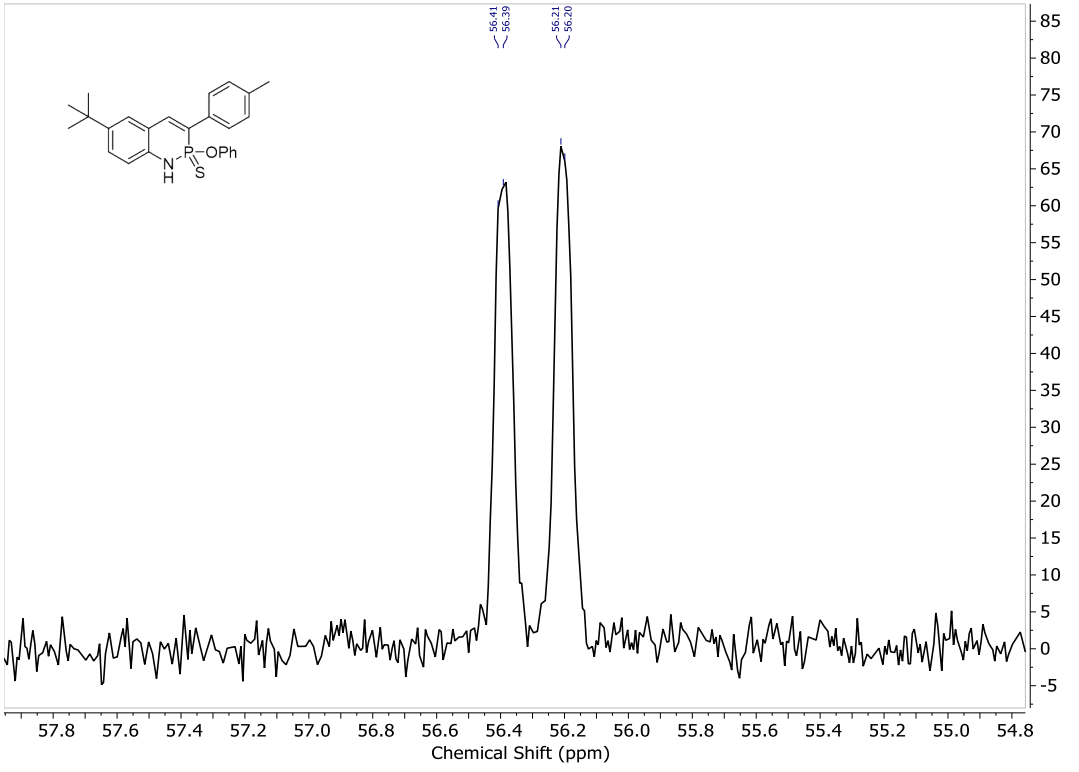

Figure C9 ^{31}P NMR spectrum of **2a** in DMSO-d_6.

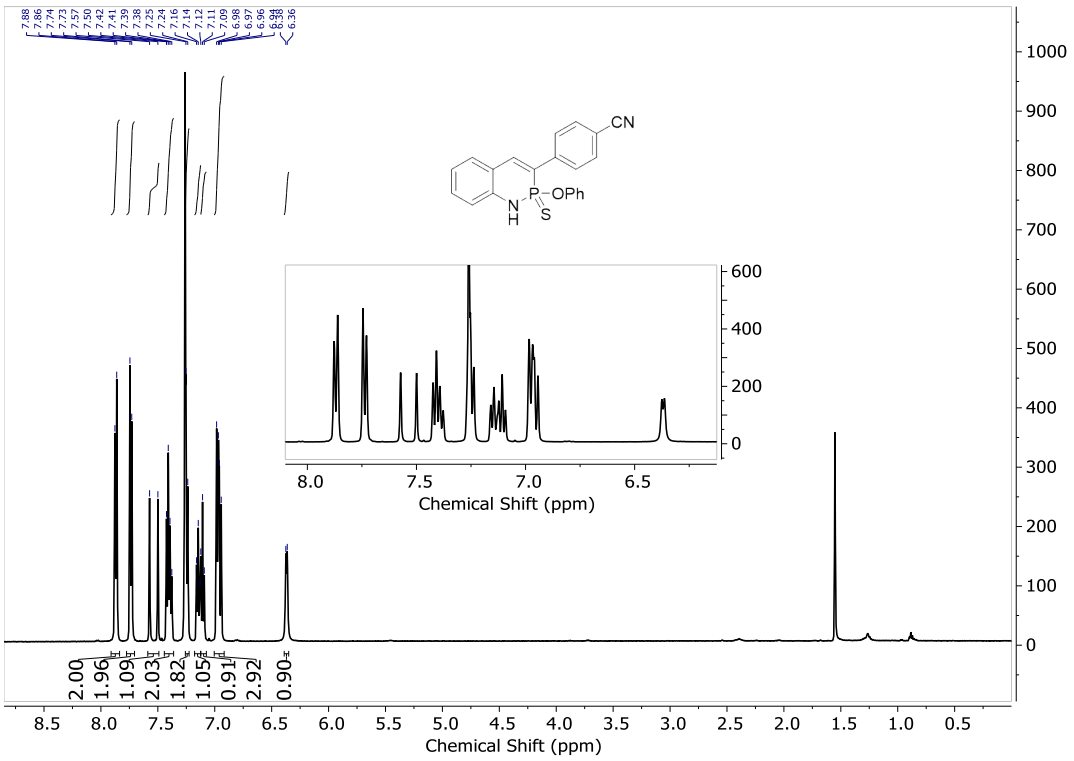

Figure C10 ^{1}H NMR spectrum of **2b** in $CDCl_3$.

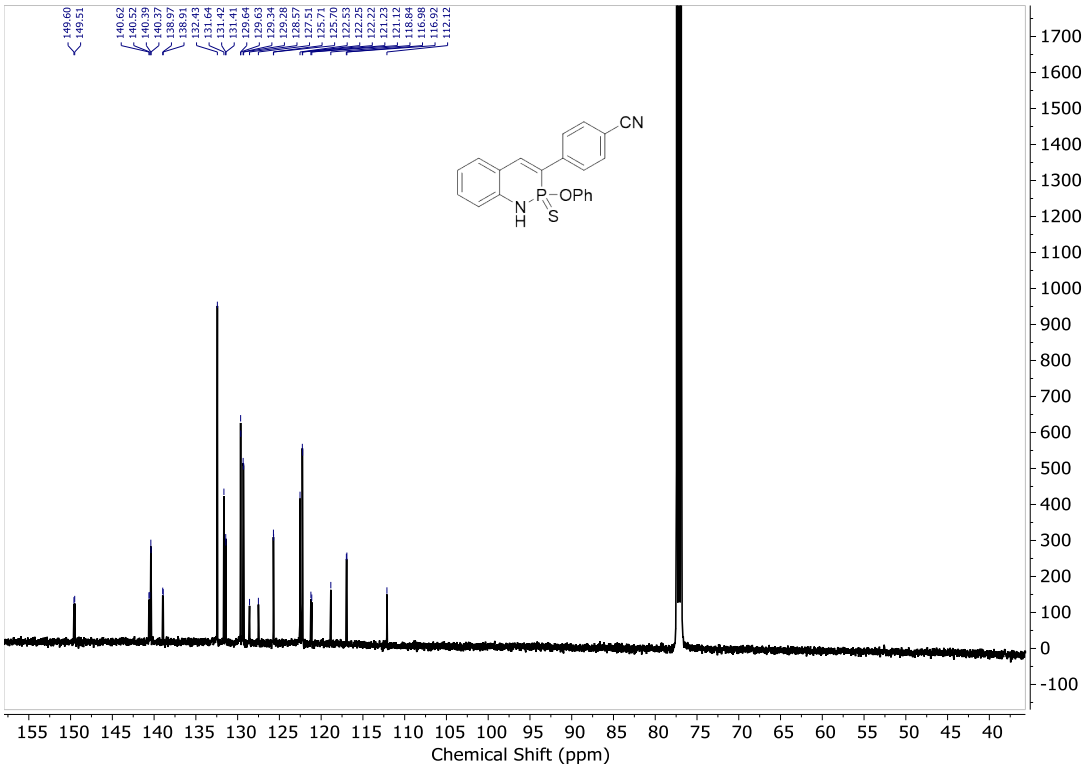

Figure C11 ^{13}C NMR spectrum of **2b** in $CDCl_3$.

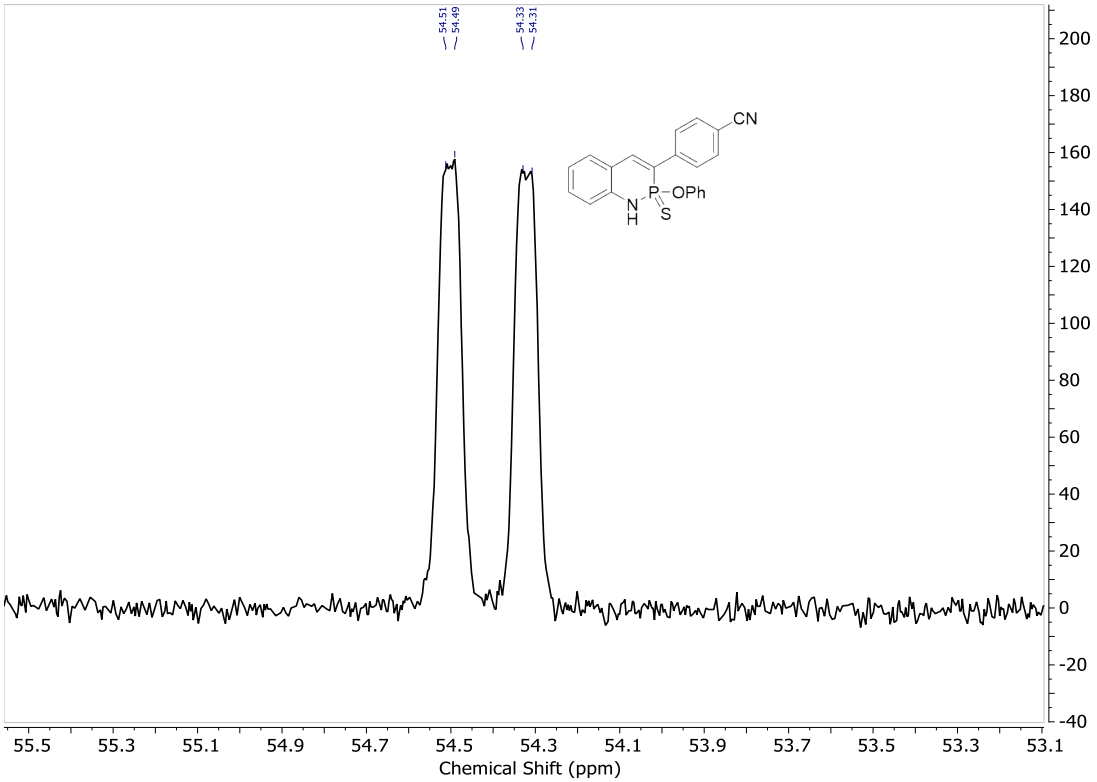

Figure C12 ^{31}P NMR spectrum of **2b** in $CDCl_3$.

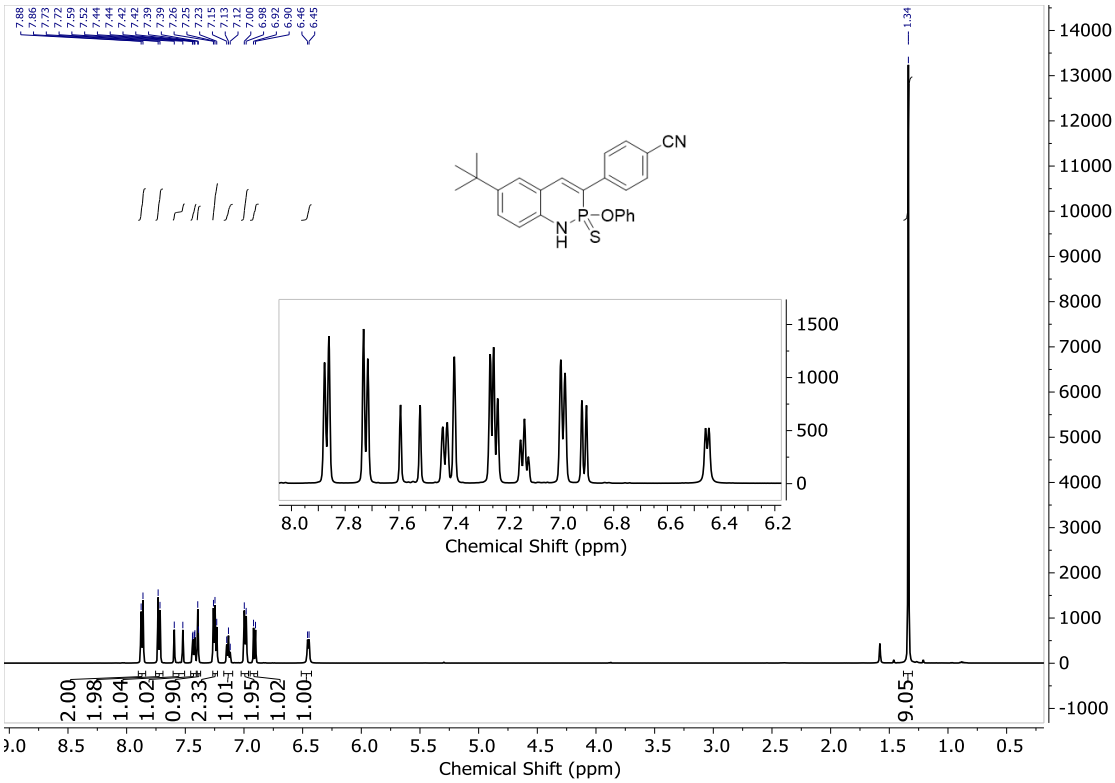

Figure C13 ^{1}H NMR spectrum of **2c** in $CDCl_3$.

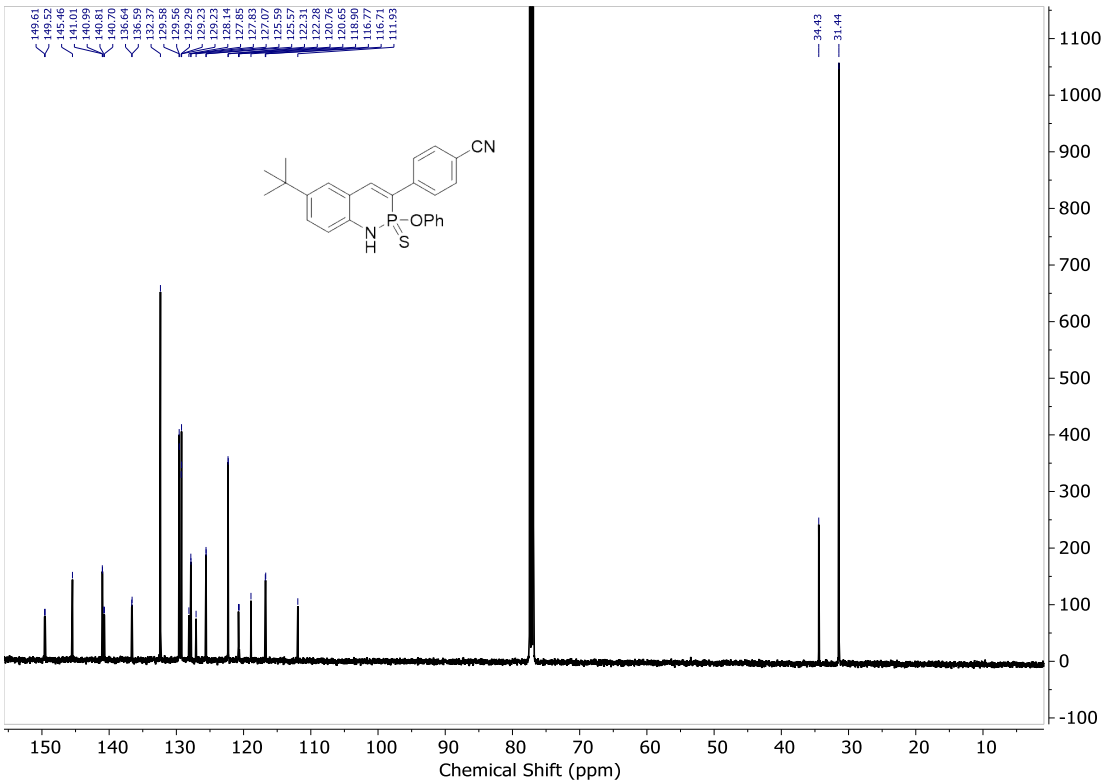

Figure C14 ^{13}C NMR spectrum of **2c** in $CDCl_3$.

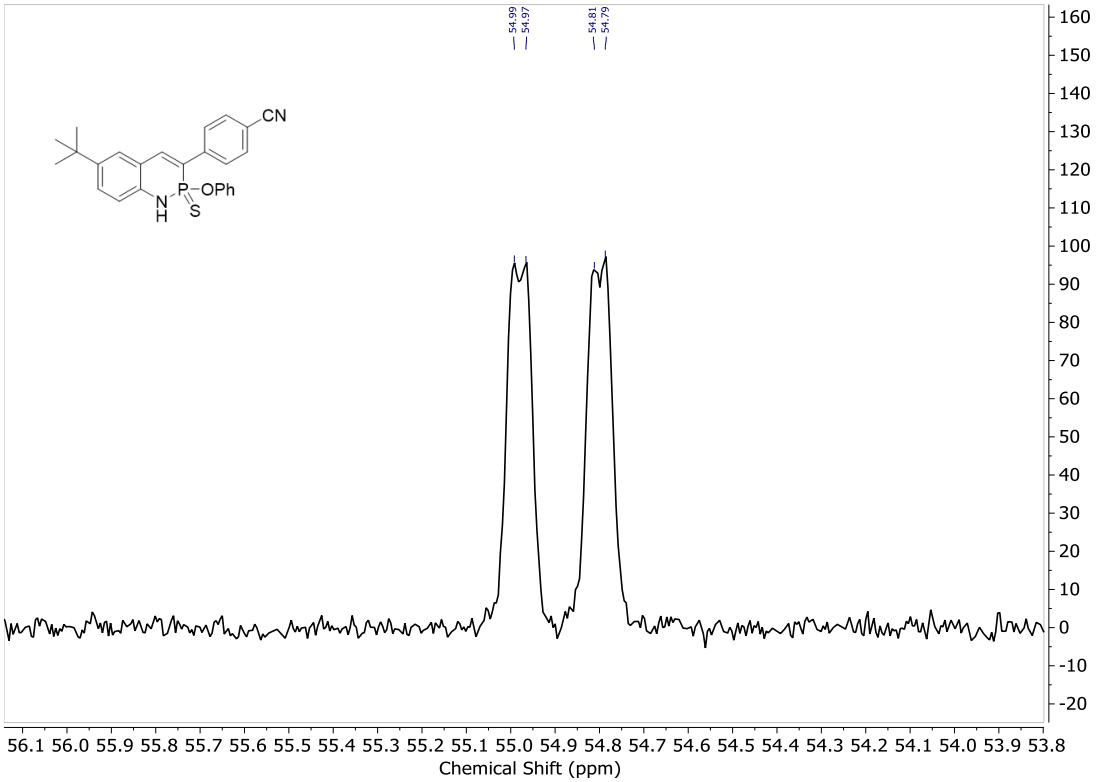

Figure C15 ^{31}P NMR spectrum of **2c** in $CDCl_3$.

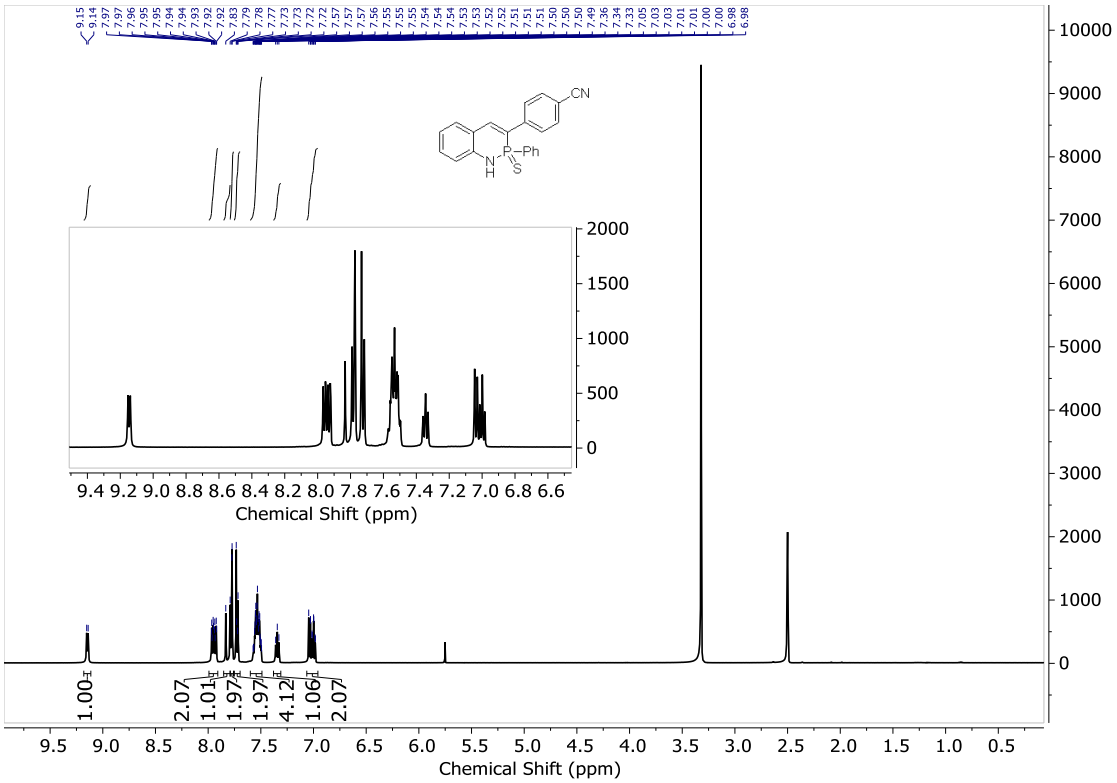

Figure C16 ^{1}H NMR spectrum of **2d** in DMSO-d_6.

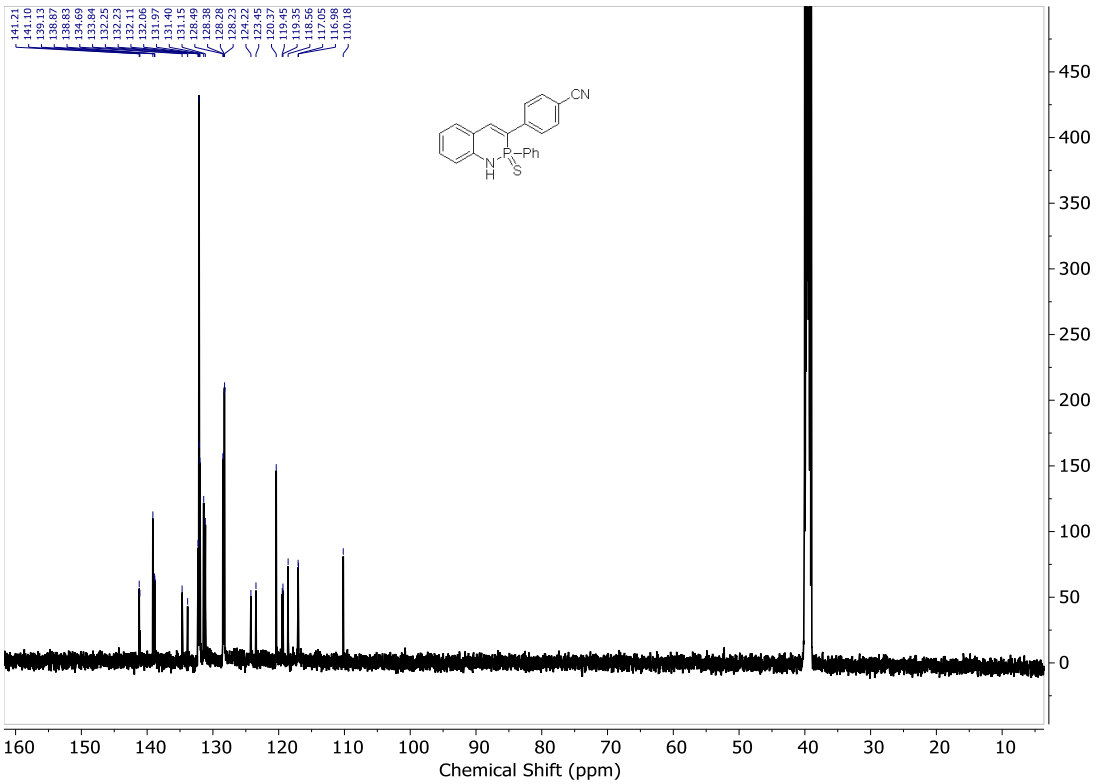

Figure C17 ^{13}C NMR spectrum of **2d** in DMSO-d_6.

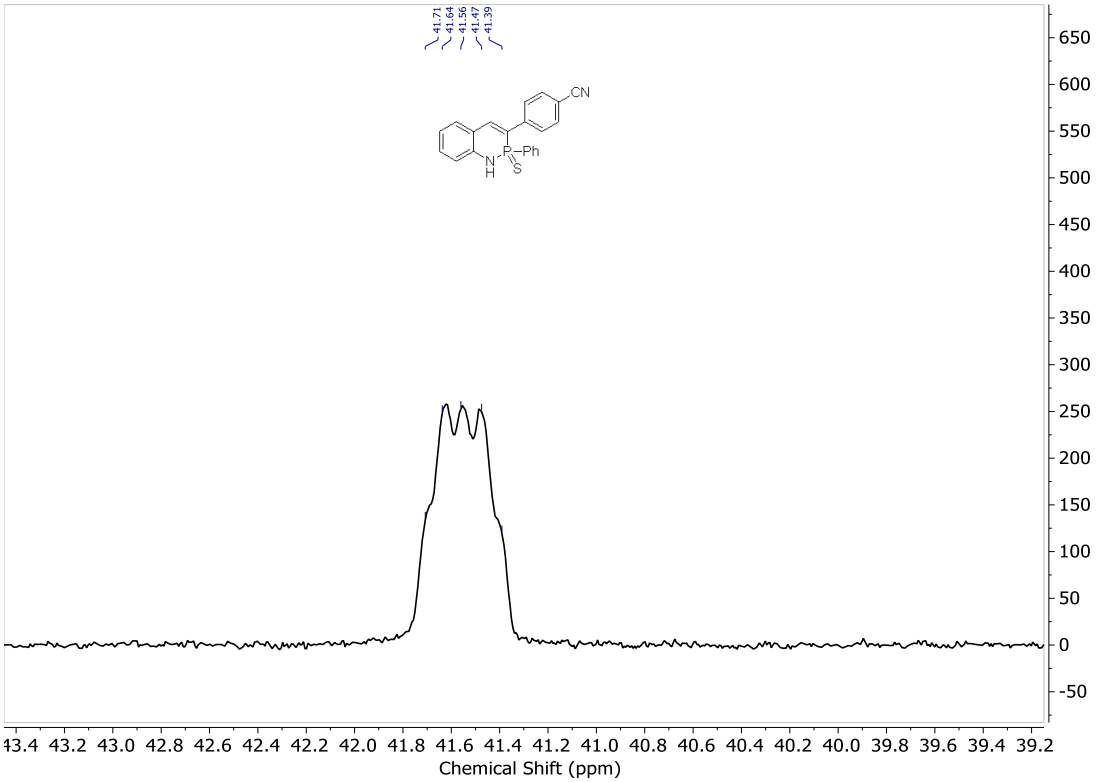

Figure C18 ^{31}P NMR spectrum of **2d** in DMSO-d_6.

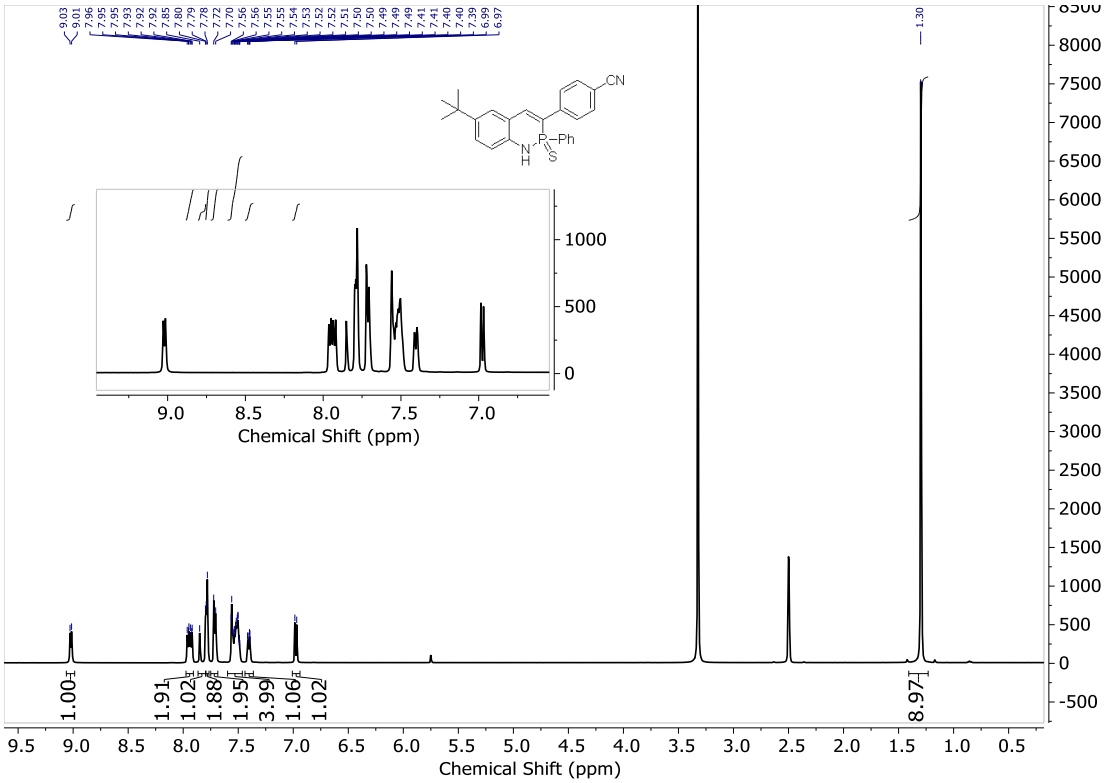

Figure C19 ^{1}H NMR spectrum of **2e** in DMSO-d_6.

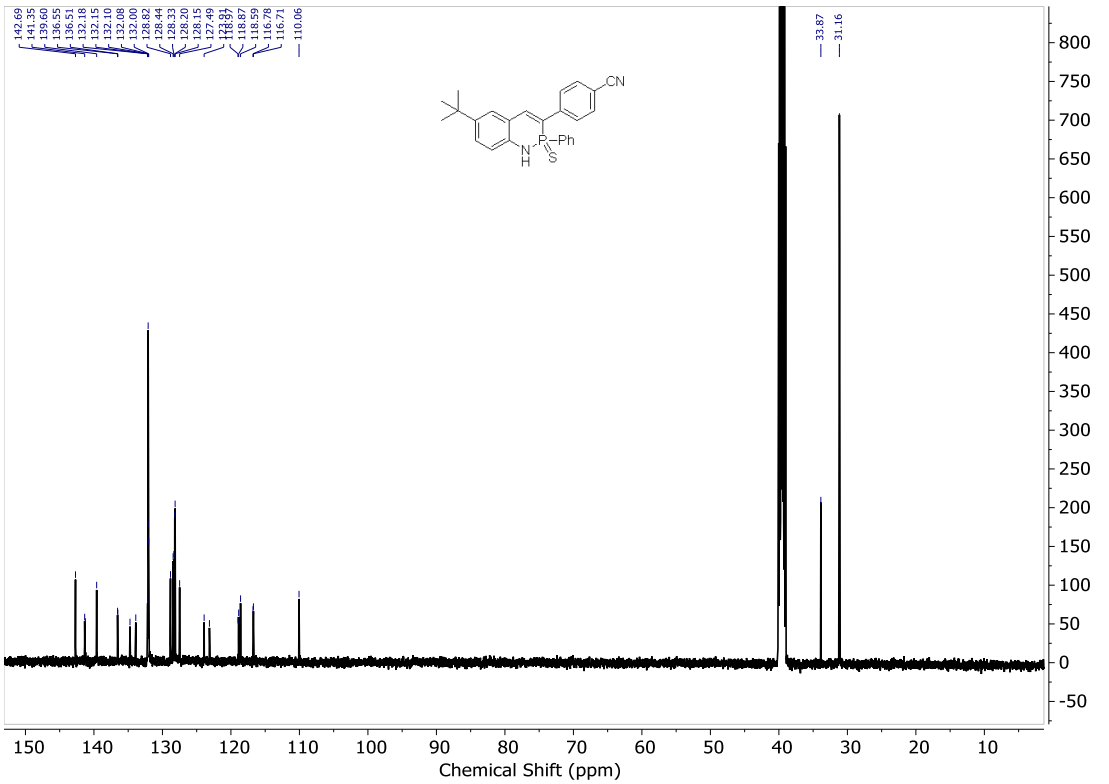

Figure C20 ^{13}C NMR spectrum of **2e** in DMSO-d_6.

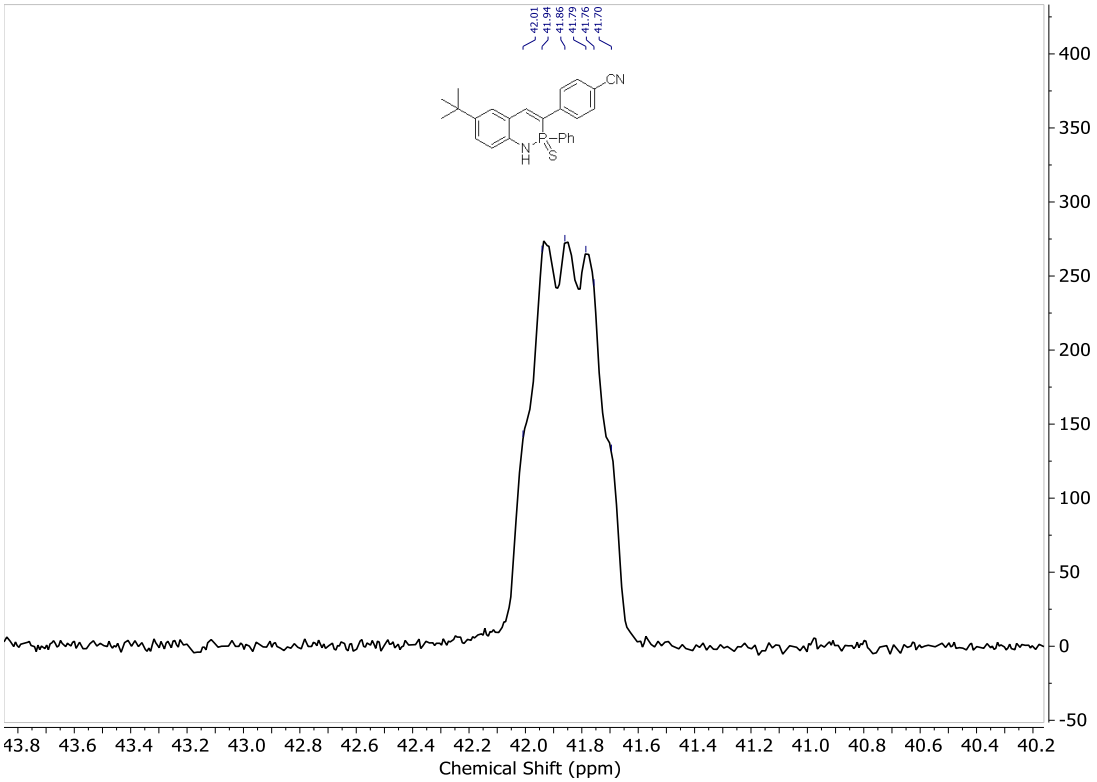

Figure C21 ^{31}P NMR spectrum of **2e** in DMSO-d_6.

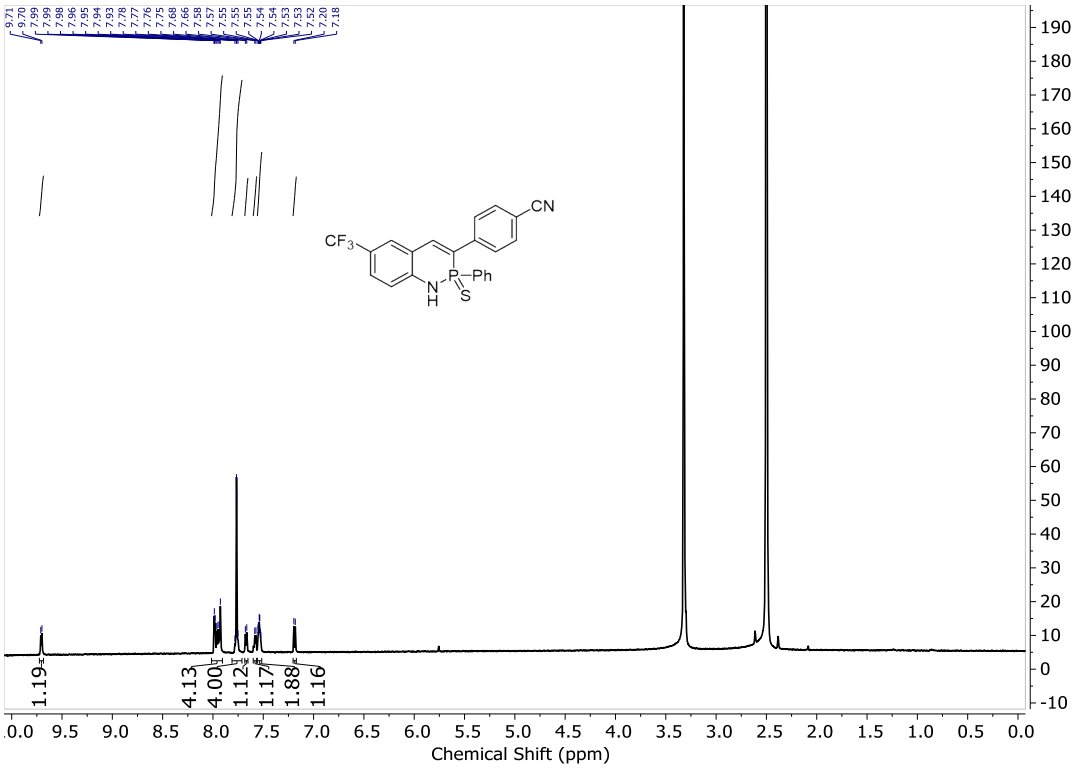

Figure C22 ^{1}H NMR spectrum of **2f** in DMSO-d_6.

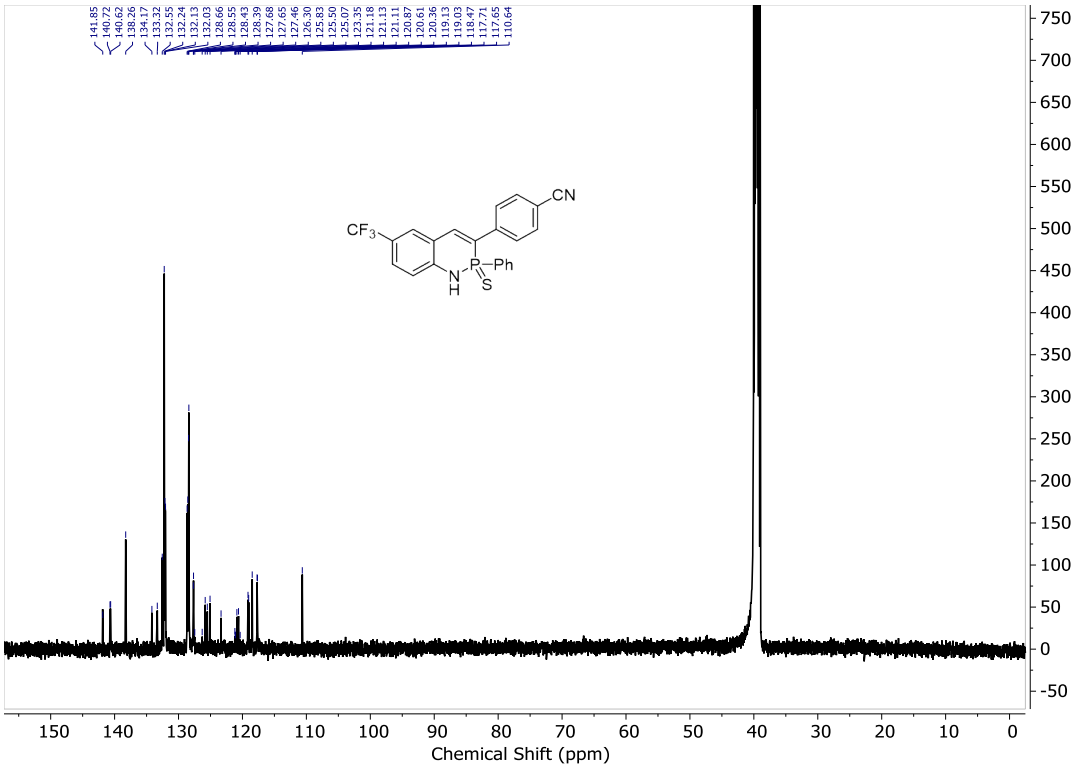

Figure C23 ^{13}C NMR spectrum of **2f** in DMSO-d_6.

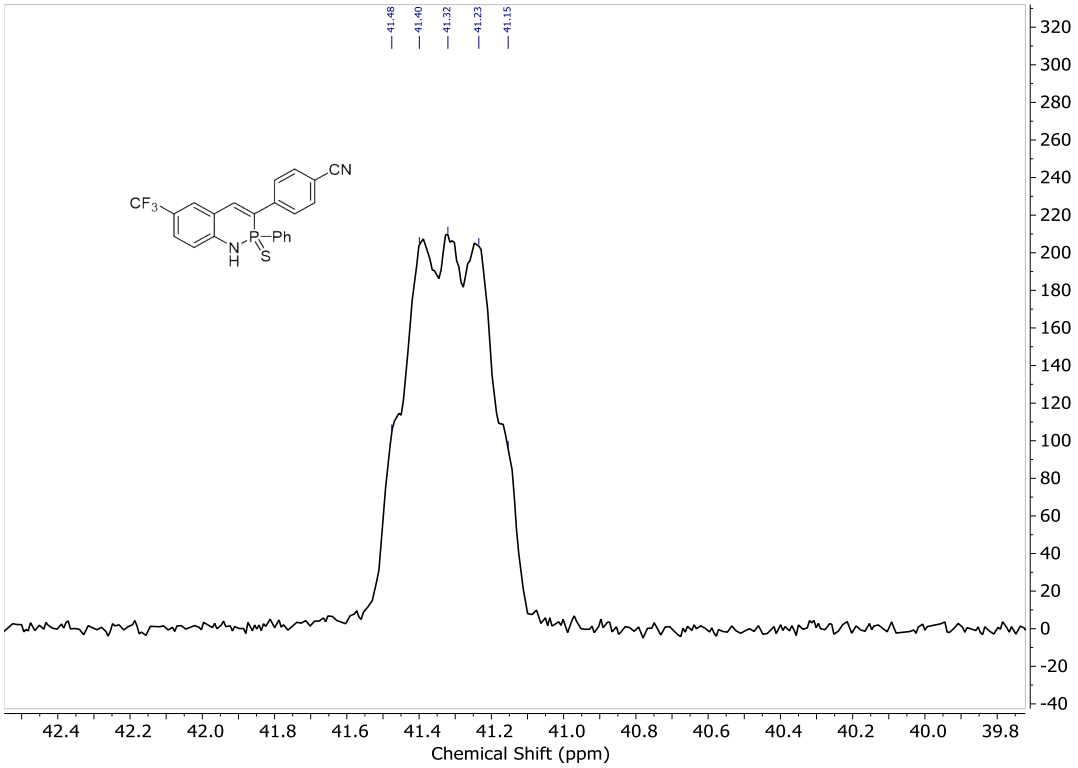

Figure C24 ^{31}P NMR spectrum of **2f** in DMSO-d_6.

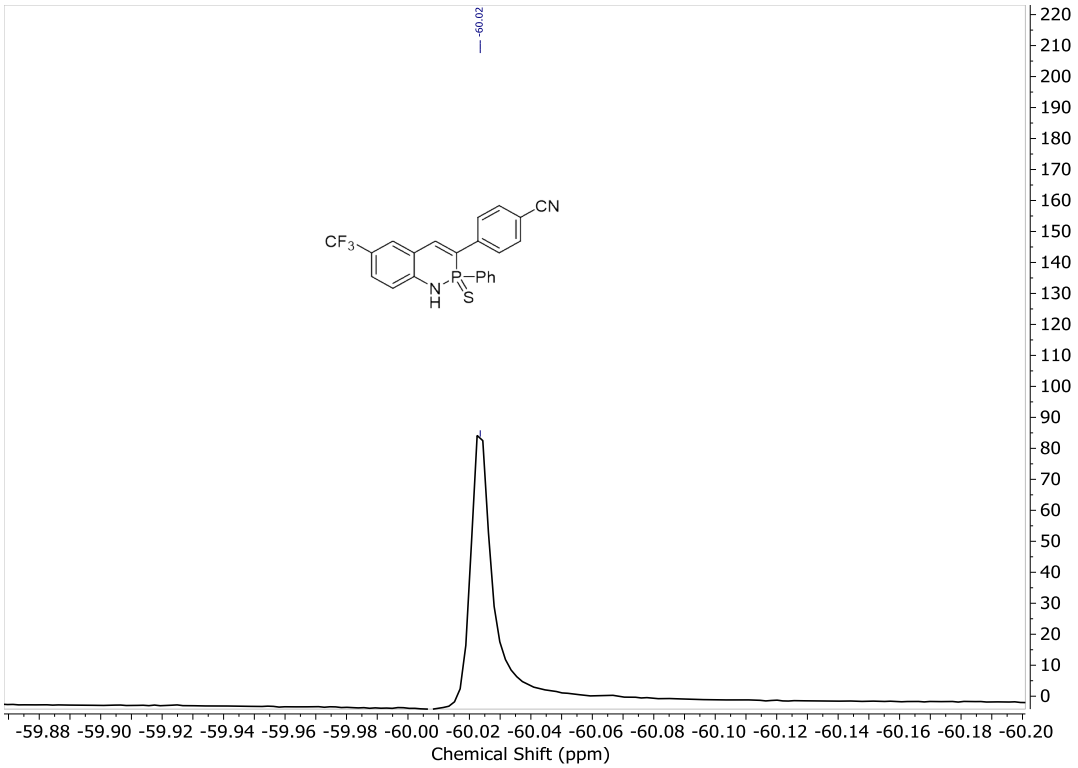

Figure C25 ^{19}F NMR spectrum of **2f** in DMSO-d_6.

REFERENCES CITED

Chapter I.

1 G. Brugnatelli, *G. Fis. Chim. Storia Nat. Med. Ed Arti*, 1818, **1**, 117–129.
2 E. Kabir and M. Uzzaman, *Results Chem.*, 2022, **4**, 100606.
3 F. Ullah, S. Ullah, M. F. A. Khan, M. Mustaqeem, R. N. Paracha, M. F. Rehman, F. Kanwal, S. S. Hassan and S. Bungau, *Molecules*, 2022, **27**, 6631–6649.
4 J. Jampilek, *Molecules*, 2019, **24**, 3839–3843.
5 O. Ostroverkhova, *Chem. Rev.*, 2016, **116**, 13279–13412.
6 M. M. Heravi and V. Zadsirjan, *RSC Adv.*, 2020, **10**, 44247–44311.
7 S. S. M. Fernandes, M. C. R. Castro, D. Ivanou, A. Mendes and M. M. M. Raposo, *Coatings*, 2022, **12**, 34–46.
8 S. Kumar, *J. Heterocycl. Chem.*, 2019, **56**, 1168–1230.
9 R. Iftikhar, F. Z. Khan and N. Naeem, *Mol. Divers.*, 2023, DOI:10.1007/s11030-022-10597-0.
10 E. Peris, *Chem. Rev.*, 2018, **118**, 9988–10031.
11 S. C. Sau, P. K. Hota, S. K. Mandal, M. Soleilhavoup and G. Bertrand, *Chem. Soc. Rev.*, 2020, **49**, 1233–1252.
12 K. Mezgebe and E. Mulugeta, *RSC Adv.*, 2022, **12**, 25932–25946.
13 C. Reus and T. Baumgartner, *Dalton Trans.*, 2016, **45**, 1850–1855.
14 T. Baumgartner, *Acc. Chem. Res.*, 2014, **47**, 1613–1622.
15 M. Stolar and T. Baumgartner, *Chem. – Asian J.*, 2014, **9**, 1212–1225.
16 X. He and T. Baumgartner, *RSC Adv.*, 2013, **3**, 11334–11350.
17 T. Baumgartner and R. Réau, *Chem. Rev.*, 2006, **106**, 4681–4727.
18 X.-D. Jiang, J. Zhao, D. Xi, H. Yu, J. Guan, S. Li, C.-L. Sun and L.-J. Xiao, *Chem. – Eur. J.*, 2015, **21**, 6079–6082.
19 C. Müller, Z. Freixa, M. Lutz, A. L. Spek, D. Vogt and P. W. N. M. van Leeuwen, *Organometallics*, 2008, **27**, 834–838.
20 C. Müller, E. A. Pidko, M. Lutz, A. L. Spek and D. Vogt, *Chem. – Eur. J.*, 2008, **14**, 8803–8807.
21 A. Fukazawa, S. Suda, M. Taki, E. Yamaguchi, M. Grzybowski, Y. Sato, T. Higashiyama and S. Yamaguchi, *Chem. Commun.*, 2016, **52**, 1120–1123.
22 V. Jancik, F. Cortés-Guzmán, R. Herbst-Irmer and D. Matínez-Otero, *Chem. – Eur. J.*, 2017, **23**, 6964–6968.
23 A. B. Chaplin, J. A. Harrison and P. J. Dyson, *Inorg. Chem.*, 2005, **44**, 8407–8417.
24 S. S. Krishnamurthy, *Phosphorus Sulfur Silicon Relat. Elem.*, 1994, **87**, 101–111.
25 J. Liebig, *Justus Liebigs Ann. Chem.*, 1834, **11**, 139–150.
26 P. v. R. Schleyer and A. J. Kos, *Tetrahedron*, 1983, **39**, 1141–1150.
27 K. Dimroth, *Acc. Chem. Res.*, 1982, **15**, 58–64.
28 T. Delouche, E. Caytan, M. Cordier, T. Roisnel, G. Taupier, Y. Molard, N. Vanthuyne, B. Le Guennic, M. Hissler, D. Jacquemin and P.-A. Bouit, *Angew. Chem. Int. Ed.*, 2022, **61**, e202205548.

29 C. Müller, D. Wasserberg, J. J. M. Weemers, E. A. Pidko, S. Hoffmann, M. Lutz, A. L. Spek, S. C. J. Meskers, R. A. J. Janssen, R. A. van Santen and D. Vogt, *Chem. – Eur. J.*, 2007, **13**, 4548–4559.
30 D. G. Gilheany, *Chem. Rev.*, 1994, **94**, 1339–1374.
31 A. Schenk and A. Michaelis, *Ber. Dtsch. Chem. Ges.*, 1888, **21**, 1497–1504.
32 G. Märkl and D. Matthes, *Angew. Chem. Int Ed. Engl.*, 1972, **11**, 1019–1020.
33 C. Bourdieu and A. Foucaud, *Tetrahedron Lett.*, 1986, **27**, 4725–4726.
34 T. Kobayashi and M. Nitta, *Chem. Lett.*, 1985, **14**, 1459–1462.
35 J. Barluenga, F. Lopez and F. Palacios, *J. Chem. Res. Synposes*, 1985, **7**, 221.
36 J. C. Williams, J. A. Kuczkowski, N. A. Portnoyz, K. S. Yong, J. D. Wander and A. M. Aguiar, *Tetrahedron Lett.*, 1971, **12**, 4749–4752.
37 W. Tang and Y.-X. Ding, *J. Org. Chem.*, 2006, **71**, 8489–8492.
38 Y. Sun and N. Cramer, *Chem. Sci.*, 2018, **9**, 2981–2985.
39 J. P. Bard, D. W. Johnson and M. M. Haley, *Synlett*, 2020, **31**, 1862–1877.
40 T. Eicher, S. Hauptmann, and A. Speicher, *The Chemistry of Heterocycles*, John Wiley & Sons, Ltd, 2nd edn., 2003, vol. 1, ch. 2, pp. 5–16.
41 M. Häring, *Helv. Chim. Acta*, 1960, **43**, 1826–1840.
42 A. I. Bokanov and B. I. Stepanov, *Russ. Chem. Rev.*, 1977, **46**, 855–860.
43 L. D. Freedman and H. S. Freeman, *Chem. Rev.*, 1987, **87**, 289–306.
44 J. J. Skolimowski, L. D. Quin and A. N. Hughes, *J. Org. Chem.*, 1989, **54**, 3493–3496.
45 Y. Zhi-Gang and Z. De-Feng, *Chin. J. Chem.*, 2010, **21**, 71–78.
46 W. Ye, X. Li, B. Ding, C. Wang, M. Shrestha, X. Ma, Y. Chen and H. Tian, *J. Org. Chem.*, 2020, **85**, 3879–3886.
47 M. J. S. Dewar and V. P. Kubba, *J. Am. Chem. Soc.*, 1960, **82**, 5685–5688.
48 M. J. S. Dewar, V. P. Kubba and R. Pettit, *J. Chem. Soc. Resumed*, 1958, 3073–3076.
49 I. G. M. Campbell and J. K. Way, *J. Chem. Soc.*, 1960, 5034–5041.
50 H. Yamamoto, T. Kobayashi and M. Nitta, *Heterocycles*, 1998, **48**, 1903–1915.
51 J. M. Alvarez-Gutirrez and F. López-Ortiz, *Tetrahedron Lett.*, 1996, **37**, 2841–2844.
52 N. Avarvari, P. Le Floch and F. Mathey, *J. Am. Chem. Soc.*, 1996, **118**, 11978–11979.
53 G. Märkl, S. Dietl, M. L. Ziegler and B. Nuber, *Angew. Chem. Int. Ed. Engl.*, 1988, **27**, 389–391.
54 N. Avarvari, P. Le Floch, L. Ricard and F. Mathey, *Organometallics*, 1997, **16**, 4089–4098.
55 U. Rhörig, N. Mézailles, N. Maigrot, L. Ricard, F. Mathey and P. Le Floch, *Eur. J. Inorg. Chem.*, **2000**, 2565–2571.
56 D. Zhao, C. Nimphius, M. Lindale and F. Glorius, *Org. Lett.*, 2013, **15**, 4504–4507.
57 S. Park, B. Seo, S. Shin, J.-Y. Son and P. H. Lee, *Chem. Commun.*, 2013, **49**, 8671–8673.
58 Y. Sun and N. Cramer, *Angew. Chem. Int. Ed.*, 2017, **56**, 364–367.
59 Q. Yao, J. Chen, H. Song, F. Huang and B. Shi, *Angew. Chem. Int. Ed.*, 2022, **61**, e202202892.

60 V. G. Zaitsev, D. Shabashov and O. Daugulis, *J. Am. Chem. Soc.*, 2005, **127**, 13154–13155.
61 L. Zeng, S. Tang, D. Wang, Y. Deng, J.-L. Chen, J.-F. Lee and A. Lei, *Org. Lett.*, 2017, **19**, 2170–2173.
62 R. Huang, M. Wang, H. Deng, J. Xu, H. Yan, Y. Zhao and Z. Shi, *Sci. Adv.*, 2023, **9**, eade8638.
63 G. C. Morrison, R. O. Waite and J. Shavel, *J. Heterocycl. Chem.*, 1966, **3**, 540–540.
64 S. Kh. Nurtdinov, I. V. Tsivunina, V. I. Savran, N. M. Ismagilova, T. V. Zykova and V. S. Tsivunin, *Zh. Obshch. Khim.*, 1981, **51**, 1549.
65 W. H.-L. Wai Tan, C. Bourdieu and A. Foucaud, *Tetrahedron*, 1990, **46**, 6715–6730.
66 C. Bourdieu and A. Foucaud, *Tetrahedron Lett.*, 1987, **28**, 4673–4674.
67 J. Barluenga, F. Lopez and F. Palacios, *Tetrahedron Lett.*, 1987, **28**, 4327–4328.
68 C. Bedel and A. Foucaud, *Tetrahedron Lett.*, 1991, **32**, 2619–2620.
69 E. Fluck, F. Rosche, G. Heckmann and F. Weller, *Heteroat. Chem.*, 1995, **6**, 355–363.
70 W. Tang, Y. Ding and Y.-X. Ding, *Tetrahedron*, 2008, **64**, 10507-10511.
71 J.-H. Yan, Q.-Y. Li, J. Boutin, M. P. Renard, Y.-X. Ding, X.-J. Hao, W.-M. Zhao and M.-W. Wang, *Acta. Pharmacol. Sin.*, 2008, **6**, 752–758.
72 Z.-Q. Lin, W.-Z. Wang, S.-B. Yan and W.-L. Duan, *Angew. Chem. Int. Ed.*, 2015, **54**, 6265–6269.
73 L. Liu, A.-A. Zhang, Y. Wang, F. Zhang, Z. Zuo, W.-X. Zhao, C.-L. Feng and W. Ma, *Org. Lett.*, 2015, **17**, 2046–2049.
74 Y.-N. Ma, X. Zhang and S. Yang, *Chem. – Eur. J.*, 2017, **23**, 3007–3011.
75 Y.-H. Chen, X.-L. Qin and F.-S. Han, *Chem. Commun.*, 2017, **53**, 5826–5829.
76 C. L. Vonnegut, A. M. Shonkwiler, M. M. Khalifa, L. N. Zakharov, D. W. Johnson and M. M. Haley, *Angew. Chem. Int. Ed.*, 2015, **54**, 13318–13322.
77 J. P. Bard, H. J. Bates, C.-L. Deng, L. N. Zakharov, D. W. Johnson and M. M. Haley, *J. Org. Chem.*, 2020, **85**, 85–91.
78 J. P. Bard, J. L. Mancuso, C.-L. Deng, L. N. Zakharov, D. W. Johnson and M. M. Haley, *Supramol. Chem.*, 2020, **32**, 49–55.
79 C.-L. Deng, J. P. Bard, L. N. Zakharov, D. W. Johnson and M. M. Haley, *Org. Lett.*, 2019, **21**, 6427–6431.
80 C.-L. Deng, J. P. Bard, L. N. Zakharov, D. W. Johnson and M. M. Haley, *J. Org. Chem.*, 2019, **84**, 8131–8139.
81 N. A. Takaesu, E. Ohta, L. N. Zakharov, D. W. Johnson and M. M. Haley, *Organometallics*, 2017, **36**, 2491–2493.
82 C.-L. Deng, J. P. Bard, J. A. Lohrman, J. E. Barker, L. N. Zakharov, D. W. Johnson and M. M. Haley, *Angew. Chem. Int. Ed.*, 2019, **58**, 3934–3938.
83 J. P. Bard, C.-L. Deng, H. C. Richardson, J. M. Odulio, J. E. Barker, L. N. Zakharov, P. H.-Y. Cheong, D. W. Johnson and M. M. Haley, *Org. Chem. Front.*, 2019, **6**, 1257–1265.
84 J. P. Bard, J. N. McNeill, G. I. Warren, L. N. Zakharov, D. W. Johnson and M. M. Haley, *Isr. J. Chem.*, 2021, **61**, 217–221.

85 J. N. McNeill, L. J. Karas, J. P. Bard, K. Fabrizio, L. N. Zakharov, S. N. MacMillan, C. K. Brozek, J. I. Wu, D. W. Johnson and M. M. Haley, *Chem. – Eur. J.*, 2022, **28**, e202200472.
86 J. N. McNeill, M. A. Kascoutas, L. J. Karas, L. N. Zakharov, J. I. Wu, D. W. Johnson and M. M. Haley, *Chem. – Eur. J.*, 2023, **29**, e202203918.
87 T. J. Grahame and R. B. Schlesinger, *Inhalation Toxicol.*, 2005, **17**, 15–27.
88 H. A. Fargher, N. Lau, L. N. Zakharov, M. M. Haley, D. W. Johnson and M. D. Pluth, *Chem. Sci.*, 2019, **10**, 67–72.
89 B. W. Tresca, A. C. Brueckner, M. M. Haley, P. H.-Y. Cheong and D. W. Johnson, *J. Am. Chem. Soc.*, 2017, **139**, 3962–3965.
90 M. D. Hartle, R. J. Hansen, B. W. Tresca, S. S. Prakel, L. N. Zakharov, M. M. Haley, M. D. Pluth and D. W. Johnson, *Angew. Chem. Int. Ed.*, 2016, **55**, 11480–11484.
91 B. W. Tresca, R. J. Hansen, C. V. Chau, B. P. Hay, L. N. Zakharov, M. M. Haley and D. W. Johnson, *J. Am. Chem. Soc.*, 2015, **137**, 14959–14967.
92 J. P. Bard, S. G. Bolton, H. J. Howard, J. N. McNeill, T. P. de Faria, L. N. Zakharov, D. W. Johnson, M. D. Pluth and M. M. Haley, *J. Org. Chem*., 2023, DOI: 10.1021/acs.joc.3c01927.
93 G. Signore, R. Nifosì, L. Albertazzi, B. Storti and R. Bizzarri, *J. Am. Chem. Soc.*, 2010, **132**, 1276–1288.
94 G. Niu, W. Liu, B. Zhou, H. Xiao, H. Zhang, J. Wu, J. Ge and P. Wang, *J. Org. Chem.*, 2016, **81**, 7393–7399.
95 D. Aristova, R. Selin, H. S. Heil, V. Kosach, Y. Slominsky, S. Yarmoluk, V. Pekhnyo, V. Kovalska, R. Henriques, A. Mokhir and S. Chernii, *ACS Omega*, 2022, **7**, 47734–47746.
96 Z. Li, J. Zou, and X. Chen, *Adv. Mater.*, 2022, **35**, 2209529.
97 J. Park, S. J. Kim, H. Kwon, E. Jin, K. Yoon, H. Kim, S. Shadman, W. Choe, J. Kim and Y. S. Park, *Chem. Commun.*, 2021, **57**, 12147–12150.
98 H. Deng, M. Wang, Y. Liang, X. Chen, T. Wang, J. J. Wong, Y. Zhao, K. N. Houk and Z. Shi, *Chem*, 2022, **8**, 569–579.
99 G. Märkl and P. Kreitmeier, in *Phosphorus-Carbon Heterocyclic Chemistry*, ed François Mathey, Elsevier Science, Amsterdam, 1st edn, 2001, ch. 5.3, pp 535-630.
100 G. Märkl and G. Dorfmeister, *Tetrahedron Lett.*, 1987, **28**, 1093–1096.
101 G. Märki and S. Pflaum, *Tetrahedron Lett.*, 1986, **27**, 4415–4418.
102 G. Märkl and G. Dorfmeister, *Tetrahedron Lett.*, 1986, **27**, 4419–4422.
103 R. Appel, M. Groβe-bley, H. Souady and W. Steglich, *Phosphorus Sulfur Relat. Elem.*, 1987, **30**, 757–757.
104 U. J. Vogelbacher, M. Ledermann, T. Schach, G. Michels, U. Hees and M. Regitz, *Angew. Chem. Int. Ed. Engl.*, 1988, **27**, 272–274.
105 M. Regitz, O. J. Scherer and R. Appel, *Multiple bonds and low coordination in phosphorus chemistry*, G. Thieme Verlag; Thieme Medical Publishers, Stuttgart, New York, 1990.
106 I. Gutman and J. H. Potgieter, *J. Chem. Educ.*, 1994, **71**, 222.
107 R. Appel and M. Poppe, *Angew. Chem. Int. Ed. Engl.*, 1989, **28**, 53–54.
108 G. Märkl and C. Dörges, *Angew. Chem. Int. Ed. Engl.*, 1991, **30**, 106–107.

109 G. Märkl, C. Dörges, T. Riedl, F.-G. Klärner and C. Lodwig, *Tetrahedron Lett.*, 1990, **31**, 4589.
110 G. Märkl and S. Dorsch, *Tetrahedron Lett.*, 1995, **36**, 3839–3842.
111 V. A. Galishev, V. N. Sakharov, T. S. Dolgushina, L. Tamm and A. A. Petrov, *Zh. Obshc. Khim.*, 1986, **56**, 1661–1663.
112 G. Märkl, Ch. Dörges, H. Nöth and K. Polborn, *Tetrahedron Lett.*, 1990, **31**, 6999–7002.
113 G. Frison, A. Sevin, N. Avarvari, F. Mathey and P. Le Floch, *J. Org. Chem.*, 1999, **64**, 5524–5529.
114 K. Karaghiosoff, H. Klehr and A. Schmidpeter, *Chem. Ber.*, 1986, **119**, 410–419.
115 M. M. Hansmann, *Chem. – Eur. J.*, 2018, **24**, 11573–11577.
116 H. Huang, Z. Wei, J. Hou, R. Wang, G. Tao, M. Wang, Z. Duan and F. Mathey, *Eur. J. Org. Chem.*, **2018**, 2863–2869.
117 M. Habib Mebazaa and M. Simalty, *Tetrahedron Lett.*, 1972, **13**, 4363–4366.
118 M. Simalty and H. Chahine, *Bull. Soc. Chim.*, 1968, **12**, 4938–4943.
119 L. D. Quin, C. C. Henderson, N. S. Rao and J. C. Kisalus, *Synthesis*, 1984, **1984**, 1074–1075.
120 L. D. Quin and J. C. Kisalus, *Phosphorus Sulfur Relat. Elem.*, 1985, **22**, 35–39.
121 L. D. Quin and B. G. Marsi, *Heteroat. Chem.*, 1990, **1**, 93–107.
122 J. Barluenga, F. Lopez and F. Palacios, *J. Chem Soc., Chem. Commun.*, 1985, 1681–1682.
123 J. Barluenga, F. Palacios, F. J. González and S. Fustero, *J. Chem. Soc., Chem. Commun.*, 1988, 1596–1597.
124 J. Barluenga, F. López and F. Palacios, *J. Organomet. Chem.*, 1990, **382**, 61–67.
125 J. Barluenga, F. López and F. Palacios, *J. Chem. Soc. Chem. Commun.*, 1986, 1574–1575.
126 M. Alajarin, C. Lopez-Leonardo, R. Raja and R.-A. Orenes, *Org. Lett.*, 2011, **13**, 5668–5671.
127 U. Heim, H. Pritzkow, U. Fleischer, H. Grützmacher, M. Sanchez, R. Réau and G. Bertrand, *Chem. – Eur. J.*, 1996, **2**, 68–74.
128 X. Liu, T. K. W. Ong, S. Selvaratnam, J. J. Vittal, A. J. P. White, D. J. Williams and P.-H. Leung, *J. Organomet. Chem.*, 2002, **643–644**, 4–11.
129 L. Zhang, W. Yu, C. Liu, Y. Xu, Z. Duan and F. Mathey, *Organometallics*, 2015, **34**, 5697–5702.
130 Z. Chen, C. S. Wannere, C. Corminboeuf, R. Puchta and P. v. R. Schleyer, *Chem. Rev.*, 2005, **105**, 3842–3888.
131 E. Elguero, I. Alkorta and J. Elguero, *Heteroatom. Chem.*, 2018, **29**, e21441.

Chapter II.

1 M. J. S. Dewar, V. P. Kubba, *J. Am. Chem. Soc.* **1960**, *82*, 5685–5688.
2 I. G. M. Campbell, J. K. Way, *J. Chem. Soc.* **1960**, 5034–5041.
3 J. P. Bard, D. W. Johnson, M. M. Haley, *Synlett* **2020**, *31*, 1862–1877.
4 J. P. Bard, C.-L. Deng, H. C. Richardson, J. M. Odulio, J. E. Barker, L. N. Zakharov, P. H.-Y. Cheong, D. W. Johnson, M. M. Haley, *Org. Chem. Front.* **2019**, *6*, 1257–1265.

5 C. L. Vonnegut, A. M. Shonkwiler, M. M. Khalifa, L. N. Zakharov, D. W. Johnson, M. M. Haley, *Angew. Chem. Int. Ed.* **2015**, *54*, 13318–13322; *Angew. Chem.* **2015**, *127*, 13516–13520.
6 J. P. Bard, H. J. Bates, C.-L. Deng, L. N. Zakharov, D. W. Johnson, M. M. Haley, *J. Org. Chem.* **2020**, *85*, 85–91.
7 J. Park, S. J. Kim, H. Kwon, E. Jin, K. Yoon, H. Kim, S. Shadman, W. Choe, J. Kim, Y. S. Park, *Chem. Commun.* **2021**, *57*, 12147–12150.
8 J. P. Bard, J. L. Mancuso, C.-L. Deng, L. N. Zakharov, D. W. Johnson, M. M. Haley, *Supramol. Chem.* **2020**, *32*, 49–55.
9 C.-L. Deng, J. P. Bard, L. N. Zakharov, D. W. Johnson, M. M. Haley, *Org. Lett.* **2019**, *21*, 6427–6431.
10 C.-L. Deng, J. P. Bard, L. N. Zakharov, D. W. Johnson, M. M. Haley, *J. Org. Chem.* **2019**, *84*, 8131–8139.
11 N. A. Takaesu, E. Ohta, L. N. Zakharov, D. W. Johnson, M. M. Haley, *Organometallics* **2017**, *36*, 2491–2493.
12 J. R. Quinn, S. C. Zimmerman, J. E. Del Bene, I. Shavitt, *J. Am. Chem. Soc.* **2007**, *129*, 934–941.
13 S. C. Zimmerman, B. F. Duerr, *J. Org. Chem.* **1992**, *57*, 2215–2217.
14 G. G. Hammes, A. C. Park, *J. Am. Chem. Soc.* **1969**, *91*, 956–961.
15 Z. Wang, B. S. Gelfand, T. Baumgartner, *Angew. Chem. Int. Ed.* **2016**, *55*, 3481–3485; *Angew. Chem.* **2016**, *128*, 3542–3546.
16 R. Ahmed, A. Altieri, D. M. D'Souza, D. A. Leigh, K. M. Mullen, M. Papmeyer, A. M. Z. Slawin, J. K. Y. Wong, J. D. Woollins, *J. Am. Chem. Soc.* **2011**, *133*, 12304–12310.
17 S. C. C. van der Lubbe, A. Haim, T. van Heesch, C. Fonseca Guerra, *J. Phys. Chem. A* **2020**, *124*, 9451–9463.
18 J. Reynisson, E. Mcdonald, *J. Comput. Aided Mol. Des.* **2004**, *18*, 421–431.
19 C. Seillan, P. Marsal, O. Siri, *Org. Biomol. Chem.* **2010**, *8*, 3882–3887.
20 F. Tomas, J. L. M. Abboud, J. Laynez, R. Notario, L. Santos, S. O. Nilsson, J. Catalan, R. M. Claramunt, J. Elguero, *J. Am. Chem. Soc.* **1989**, *111*, 7348–7353.
21 I. Alkorta, P. Goya, J. Elguero, S. Singh, *Natl. Acad. Sci. Lett.* **2007**, *30*, 139–159.
22 H. B. Schlegel, P. Gund, E. M. Fluder, *J. Am. Chem. Soc.* **1982**, *104*, 5347–5351.
23 L. Wei, S.-T. Han, T.-T. Jin, T.-G. Zhan, L.-J. Liu, J. Cui, J.; K.-D. Zhang, *Chem. Sci.* **2021**, *12*, 1762–1771.
24 A. Altieri, F. G. Gatti, E. R. Kay, D. A. Leigh, D. Martel, F. Paolucci, A. M. Z. Slawin, J. K. Y. Wong, *J. Am. Chem. Soc.* **2003**, *125*, 8644–8654.
25 H. M. Coubrough, B. Balonova, C. M. Pask, B. A. Blight, A. J. Wilson, *ChemistryOpen* **2020**, *9*, 40–44.
26 C.-H. Wu, Y. Zhang, K. van Rickley, J. I-C. Wu, *Chem. Commun.* **2018**, *54*, 3512–3515.
27 C.-H. Wu, L. J. Karas, H. Ottosson, J. I.-C. Wu, *Proc. Natl. Acad. Sci. USA* **2019**, *116*, 20303–20308.
28 J. I. Wu, J. E. Jackson, P. v. R. Schleyer, *J. Am. Chem. Soc.* **2014**, *136*, 13526–13529.

29 V. Saez Talens, J. Davis, C.-H. Wu, Z. Wen, F. Lauria, K. B. S. S. Gupta, R. Rudge, M. Boraghi, A. Hagemeijer, T. T. Trinh, P. Englebienne, I. K. Voets, J. I. Wu, R. E. Kieltyka, *J. Am. Chem. Soc.* **2020**, *142*, 19907–19916.
30 V. Saez Talens, P. Englebienne, T. T. Trinh, W. E. M. Noteborn, I. K.; Voets, R. E. Kieltyka, *Angew. Chem. Int. Ed.* **2015**, *54*, 10502–10506; *Angew. Chem.* **2015**, *127*, 10648–10652.

Chapter III.

1 Y. Fu, N. S. Finney, *RSC Adv.* **2018**, *8*, 29051–29061.
2 J. Strahan, B. C. Popere, P. Khomein, C. A. Pointer, S. M. Martin, A. N. Oldacre, S. Thayumanavan, E. R. Young, *Dalton Trans.* **2019**, *48*, 8488–8501.
3 M. H. Lim, S. J. Lippard, *Acc. Chem. Res.* **2007**, *40*, 41–51.
4 Y. Liu, B. Jiang, L. Zhao, L. Zhao, Q. Wang, C. Wang, B. Xu, *SAA* **2021**, *261*, 120009.
5 Y. Shiraishi, S. Sumiya, K. Manabe, T. Hirai, *ACS Appl. Mater. Interfaces* **2011**, *3*, 4649–4656.
6 J. Joniak, H. Stankovičová, J. Filo, K. Gaplovská-Kyselá, V. Garaj, M. Cigáň, *Sens. Actuators B Chem.* **2020**, *307*, 127646.
7 B. Zhang, L. Xu, Y. Zhou, W. Zhang, Y. Wang, Y. Zhu, *Luminescence* **2020**, *35*, 305–311.
8 L. Huang, W. Sheng, L. Wang, X. Meng, H. Duan, L. Chi, *RSC Adv.* **2021**, *11*, 23597–23606.
9 B. Hak Jhun, K. Ohkubo, S. Fukuzumi, Y. You, *J. Mater. Chem. C* **2016**, *4*, 4556–4567.
10 C. L. Vonnegut, A. M. Shonkwiler, M. M. Khalifa, L. N. Zakharov, D. W. Johnson, M. M. Haley, *Angew. Chem. Int. Ed.* **2015**, *54*, 13318–13322; *Angew. Chem.* **2015**, *127*, 13516–13520.
11 J. P. Bard, D. W. Johnson, M. M. Haley, *Synlett* **2020**, *31*, 1862–1877.
12 J. N. McNeill, L. J. Karas, J. P. Bard, K. Fabrizio, L. N. Zakharov, S. N. MacMillan, C. K. Brozek, J. I. Wu, D. W. Johnson, M. M. Haley, *Chem. Eur. J.* **2022**, *28*, e202200472.
13 C.-L. Deng, J. P. Bard, L. N. Zakharov, D. W. Johnson, M. M. Haley, *Org. Lett.* **2019**, *21*, 6427–6431.
14 J. P. Bard, C.-L. Deng, H. C. Richardson, J. M. Odulio, J. E. Barker, L. N. Zakharov, P. H.-Y. Cheong, D. W. Johnson, M. M. Haley, *Org. Chem. Front.* **2019**, *6*, 1257–1265.
15 S. E. Krikorian, *J. Phys. Chem.* **1982**, *86*, 1875–1881.
16 C.-L. Deng, J. P. Bard, J. A. Lohrman, J. E. Barker, L. N. Zakharov, D. W. Johnson, M. M. Haley, *Angew. Chem. Int. Ed.* **2019**, *58*, 3934–3938; *Angew. Chem.* **2019**, *131*, 3974–3978.
17 Z. R. Grabowski, K. Rotkiewicz, W. Rettig, *Chem. Rev.* **2003**, *103*, 3899–4032.
18 M. Tasior, I. Bald, I. Deperasińska, P. J. Cywiński, D. T. Gryko, *Org. Biomol. Chem.* **2015**, *13*, 11714–11720.
19 A. M. El-Zohry, E. A. Orabi, M. Karlsson, B. Zietz, *J. Phys. Chem. A* **2021**, *125*, 2885–2894.

20 S. Lee, M. Jen, T. Jang, G. Lee, Y. Pang, *Sci. Rep.* **2022**, *12*, 6557.
21 S. Yalcin, L. Thomas, M. Tian, N. Seferoglu, H. Ihmels, Y. Dede, *J. Org. Chem.* **2014**, *79*, 3799–3808.
22 H. Nerenz, M. Meier, W. Grahn, A. Reisner, E. Schmälzlin, S. Stadler, K. Meerholz, C. Bräuchle, P. G. Jones, *J. Chem. Soc., Perkin Trans. 2* **1998**, 437–448.
23 K. Anandhan, M. Cerón, V. Perumal, P. Ceballos, P. Gordillo-Guerra, E. Pérez-Gutiérrez, A. E. Castillo, S. Thamotharan, M. J. Percino, *RSC Adv.* **2019**, *9*, 12085–12096.
24 S. Nigam, S. Rutan, *Appl. Spectrosc.* **2001**, *55*, 362A-370A.
25 J. Seo, S. Kim, S. Y. Park, *J. Am. Chem. Soc.* **2004**, *126*, 11154–11155.
26 C. Hansch, A. Leo, R. W. Taft, *Chem. Rev.* **1991**, *91*, 165–195.
27 J. R. W. McLay, J. J. Sutton, G. E. Shillito, C. B. Larsen, G. S. Huff, N. T. Lucas, K. C. Gordon, *Inorg. Chem.* **2021**, *60*, 130–139.
28 W. H. Melhuish, *J. Phys. Chem.* **1961**, *65*, 229–235.
29 R. B. Moffett, *J. Org. Chem.* **1970**, *35*, 3596–3600.
30 C.-T. Cao, L. Yan, C. Cao, *J. Phys. Org. Chem.* **2021**, *34*, e4246.
31 M. F. Pepitone, G. G. Jernigan, J. S. Melinger, O.-K. Kim, *Org. Lett.* **2007**, *9,* 801–804.
32 C. Thomas, A. Milet, F. Peruch, B. Bibal, *Polym. Chem.* **2013**, *4*, 3491–3498.
33 A. M. Genaev, G. E. Salnikov, K. Y. Koltunov, *Chem. Heterocycl. Comp.* **2020**, *56*, 892–897.
34 Gaussian 16, Revision C.01, M. J. Frisch, G. W. Trucks, H. B. Schlegel, G. E. Scuseria, M. A. Robb, J. R. Cheeseman, G. Scalmani, V. Barone, G. A. Petersson, H. Nakatsuji, X. Li, M. Caricato, A. V. Marenich, J. Bloino, B. G. Janesko, R. Gomperts, B. Mennucci, H. P. Hratchian, J. V. Ortiz, A. F. Izmaylov, J. L. Sonnenberg, D. Williams-Young, F. Ding, F. Lipparini, F. Egidi, J. Goings, B. Peng, A. Petrone, T. Henderson, D. Ranasinghe, V. G. Zakrzewski, J. Gao, N. Rega, G. Zheng, W. Liang, M. Hada, M. Ehara, K. Toyota, R. Fukuda, J. Hasegawa, M. Ishida, T. Nakajima, Y. Honda, O. Kitao, H. Nakai, T. Vreven, K. Throssell, J. A. Montgomery, Jr., J. E. Peralta, F. Ogliaro, M. J. Bearpark, J. J. Heyd, E. N. Brothers, K. N. Kudin, V. N. Staroverov, T. A. Keith, R. Kobayashi, J. Normand, K. Raghavachari, A. P. Rendell, J. C. Burant, S. S. Iyengar, J. Tomasi, M. Cossi, J. M. Millam, M. Klene, C. Adamo, R. Cammi, J. W. Ochterski, R. L. Martin, K. Morokuma, O. Farkas, J. B. Foresman, and D. J. Fox, Gaussian, Inc., Wallingford CT, 2016.

Chapter IV.

1 K. S. Gayen, N. Chatterjee, *Asian J. Org. Chem.* **2020**, *9*, 508–528.
2 T. Ozturk, E. Ertas, O. Mert, *Chem. Rev*. **2007**, *107*, 5210–5278.
3 J. O. Moon, J. W. Lee, M. G. Choi, S. Ahn, S. K. Chang, *Tetrahedron Lett.* **2012**, *53*, 6594–6597.
4 M. G. Choi, Y. H. Kim, J. E. Namgoong, S. K. Chang, *Chem. Commun.* **2009**, 3560–3562.
5 J. E. Park, M. G. Choi, S. K. Chang, *Inorg. Chem.* **2012**, *51*, 2880–2884.

6 F. Carta, A. Maresca, A. Scozzafava, C. T. Supuran, *Bioorgan. Med. Chem.* **2012**, *20*, 2266–2273.
7 S. Eor, J. Hwang, M. G. Choi, S. K. Chang, *Org. Lett.* **2011**, *13*, 370–373.
8 Q. Q. Zhang, J. F. Ge, Q. F. Xu, X. B. Yang, X. Q. Cao, N. J. Li, J. M. Lu, *Tetrahedron Lett.* **2011**, *52*, 595–597.
9 S. Cha, J. Hwang, M. G. Choi, S. K. Chang, *Tetrahedron Lett.* **2010**, *51*, 6663–6665.
10 T. E. Ali, *Arkivoc* **2013**, *2014*, 21–91.
11 M. Yamashita, Preparation, Structure, and Biological Properties of Phosphorus Heterocycles with a C–P Ring System. In *Bioactive Heterocycles II*; Springer: Berli, Germany, **2007**, *8*, pp. 173–222.
12 L. D. Quin, F. H. Osman, R. O. Day, A. N. Hughes, X.-P. Wu, L. Q. Wang, *New J. Chem.* **1989**, *13*, 375–381.
13 J. P. Bard, D. W. Johnson, M. M. Haley, *Synlett* **2020**, *31*, 1862-1877.
14 J. P. Bard, H. J. Bates, C.-L. Deng, L. N. Zakharov, D. W. Johnson, M. M. Haley, *J. Org. Chem.* **2020**, *85*, 85–91.
15 J. P. Bard, C.-L. Deng, H. C. Richardson, J. M. Odulio, J. E. Barker, L. N. Zakharov, P. H.-Y. Cheong, D. W. Johnson, M. M. Haley, *Org. Chem. Front.* **2019**, *6*, 1257–1265.
16 H. Teichmann, G. Hilgetag, *Angew. Chem., Int. Ed. Engl.* **1967**, *6*, 1013–1023.
17 L. M. Gregoret, S. D. Rader, R. J. Fletterick, F. E. Cohen, *Proteins Struct. Dyn. Bioinf.* **1991**, *9*, 99–107.
18 P. Zhou, F. Tian, F. Lv, Z. Shang, *Proteins Struct. Dyn. Bioinf.* **2009**, *76*, 151–163.
19 A. Maciejewski, R. P. Steer, *Chem. Rev.* **1993**, *93*, 67–98.
20 K. J. Falk, R. P. Steer, *J. Am. Chem. Soc.* **1989**, *111*, 6518–6524.
21 R. P. Steer, V. Ramamurthy, *Acc. Chem. Res.* **1988**, *21*, 380−386.
22 H. Saadeh, T. Goodson, L. Yu, *Macromolecules* **1997**, *30*, 4608−4612.
23 A. M. Brouwer, *Pure Appl. Chem.* **2011**, *83*, 2213–2228.
24 S. R. Meech, D. J. Phillips, *Photochem.* **1983**, *23*, 193–217.
25 M. D. Ediger, R. S. Moog, S. G. Boxer, M. D. Fayer, *P. Chem. Phys. Lett.* **1982**, *88*, 123–127